CERN-THESIS-2012-421

Alma Mater Studiorum · Università di Bologna

Dottorato di ricerca in Fisica
Ciclo XXIV

Settore Concorsuale di afferenza: 02/A1
Settore Scientifico disciplinare: FIS/04

Measurement of branching fractions and $\mathcal{CP}$ violation for charmless charged two-body B decays at LHCb

Presentata da:
Stefano Perazzini

Relatore:
Chiar.mo Prof. Domenico Galli
Corelatore:
Dott. Vincenzo Vagnoni

Coordinatore Dottorato:
Chiar.mo Prof. Fabio Ortolani

Esame finale anno 2012

Contents

Introduction

One of the most intriguing questions of modern physics is why the universe that we observe is composed of matter. It is believed that at the time of the Big Bang equal amounts of matter and anti-matter were created, hence during the first instants after the Big Bang matter and anti-matter were equally populating the early universe. Then, particles and anti-particles started to annihilate each other until a universe exclusively composed of matter was left. Such a phenomenon can be explained if there exists some kind of asymmetry which differentiates the behaviour of matter and anti-matter particles. The first experiment revealing the presence of such an asymmetry dates back to 1964, when it was discovered that the so-called $\mathcal{CP}$ symmetry was violated by weak interactions using neutral kaon decays.

In the last decade $\mathcal{CP}$ violation has been extensively studied also using decays of B and D hadrons. In the Standard Model of particle physics, the violation of the $\mathcal{CP}$ symmetry is parameterized by a complex phase entering the elements of the so-called Cabibbo-Kobayashi-Maskawa (CKM) matrix. The family of charmless charged two body B decays, $B \to h^+h'^-$ decays, where B can be either a B^0 meson, a B_s^0 meson or a Λ_b baryon, while h and h' stand for π, K or p is matter of great interest, as such decays are sensitive probes of the CKM matrix and have the potential to reveal the presence of New Physics. In contrast to the case of other theoretically clean measurements of $\mathcal{CP}$ violation in the B sector, a simple interpretation of the $\mathcal{CP}$ violating observables of the charmless two-body B decays in terms of CKM phases is not possible. This is because these decays receive significant contributions not only from tree-level transitions, but also from QCD and Electroweak penguin diagrams. Such "penguin pollution" poses several problems for a clean measurement of CKM phases using these decays. On the other hand, the presence of loops inside the penguin diagrams has interesting implications, since they could be affected by sizable contributions from New Physics. One promising way to exploit the presence of penguins for these decays as a resource rather than a limitation consists in combining the measurements of the $B^0 \to \pi^+\pi^-$ and $B_s^0 \to K^+K^-$ time-dependent $\mathcal{CP}$ asymmetries, assuming the invariance of the strong interaction dynamics under the exchange of the $d \leftrightarrow s$ quarks (U-spin symmetry) in the decay graphs of these modes. In this way it is possible to determine the CKM angle γ, without the need of any dynamical assumption. Due to the possible presence of New Physics in the penguin loops, a measurement of γ using these decays could differ appreciably from that determined using other B decays governed by pure tree amplitudes. As $U-$spin symmetry is not exactly conserved, the measurement of the direct $\mathcal{CP}$ asymmetries of the $B^0 \to K^+\pi^-$ and $B_s^0 \to \pi^+K^-$ decays is also important to constrain the size of symmetry breaking effects. In addition the comparison of the branching fractions of the $U-$spin related modes provides valuable information about the theoretical modelling of strong interaction contributions in hadronic B decays.

The analyses carried out in this sector at the B-Factories and at the Tevatron have been able

to detect for the first time the presence of direct $\mathcal{CP}$ violation in the $B^0 \to K^+\pi^-$ decay and to measure the time-dependent $\mathcal{CP}$ asymmetry in $B^0 \to \pi^+\pi^-$. While for the former the measurements of BaBar and Belle are in good agreement, in the latter case only the measurements of the mixing-induced $\mathcal{CP}$ asymmetry coefficient agree well, while those of the direct $\mathcal{CP}$ asymmetry coefficient are quite different, with an agreement at the level of 2.4σ only. The CDF experiment has also observed the $B_s^0 \to K^+K^-$, $B_s^0 \to \pi^+K^-$, $\Lambda_b \to p\pi^-$ and $\Lambda_b \to pK^-$ decays, and more recently has published a 3σ evidence for the rare decay $B^0 \to \pi^+\pi^-$.

In this thesis the status-of-the-art of the LHCb measurements in this sector is presented. LHCb is one of the four main experiments operating at the Large Hadron Collider (LHC), specifically devoted to the measurement of $\mathcal{CP}$ violation and rare decays of beauty and charm hadrons.

In the first chapter the framework of $\mathcal{CP}$ violation within the Standard Model, the rôle of the CKM matrix with its basic formalism and the current experimental status are introduced. Then an overview of the theoretical tools commonly used to deal with hadronic B decays is given with a dedicated part on B hadron phenomenology, where the relation between $\mathcal{CP}$ violation and the CKM matrix is outlined. Then, after a brief summary of the relevant observables and the current measurements of $B \to h^+h'^-$ decays, a strategy for the extraction of the angle γ from the analysis of these decays is discussed in some detail.

In the second chapter the LHCb detector is described, focusing on the physics constraints and the technologies adopted for each sub-detector, and giving a brief summary of sub-detector performances.

The third chapter is dedicated to the measurement of the direct $\mathcal{CP}$ asymmetries of the $B^0 \to K^+\pi^-$ and $B_s^0 \to \pi^+K^-$ decays performed using the data collected at $\sqrt{s} = 7$ TeV by LHCb during 2010, corresponding to an integrated luminosity of about 37 pb^{-1}. The optimization of the event selection, the calibration of the particle identification, the extraction of the $\mathcal{CP}$ asymmetries from data and the evaluation of the systematic uncertainties are discussed in detail.

In the fourth chapter, an update of the analysis presented in the third chapter is reported, using a data sample collected during the first part of 2011, corresponding to an integrated luminosity of about 320 pb^{-1}. In addition, the measurement of the branching fractions of the rare modes $B^0 \to K^+K^-$ and $B_s^0 \to \pi^+\pi^-$ is presented.

Finally, in the fifth chapter we report the measurement of the branching fractions of the $B_s^0 \to K^+K^-$, $B^0 \to \pi^+\pi^-$ and $B_s^0 \to \pi^+K^-$ decays, as well as that of the ratio between the branching fractions of the $\Lambda_b \to p\pi^-$ and $\Lambda_b \to pK^-$ decays.

Chapter 1

$\mathcal{CP}$ violation and charmless charged two-body B decays

The violation of the $\mathcal{CP}$ symmetry, i.e. the non-invariance of fundamental interactions under the combined transformation of charge conjugation ($\mathcal{C}$) and parity ($\mathcal{P}$), is one of the most important topics in modern physics. Under $\mathcal{C}$, particles turn into antiparticles, by conjugation of their internal quantum numbers (*e.g.* $Q \to -Q$ for the electromagnetic charge). Under $\mathcal{P}$, spatial coordinates are reversed, changing the handedness of the reference frame ($\vec{x} \to -\vec{x}$). If $\mathcal{CP}$ were an exact symmetry of Nature, the behaviour of matter and antimatter would be the same. Among the fundamental forces, gravitational, electromagnetic and strong interactions respect $\mathcal{C}$ and $\mathcal{P}$ and, therefore, also their combination $\mathcal{CP}$. In contrast, weak interactions violate both $\mathcal{C}$ and $\mathcal{P}$ symmetries, as for example W bosons couple only to left-handed particles and their $\mathcal{CP}$ counterpart, right-handed antiparticles, but neither to right-handed particles nor to left-handed antiparticles. However, it was initially thought that weak interactions preserved the $\mathcal{CP}$ symmetry, until it was firstly discovered in 1964 that also $\mathcal{CP}$ was violated in neutral kaon decays [1]. In the last decade $\mathcal{CP}$ violation has been extensively studied also using decays of B and D hadrons.

The phenomenon of $\mathcal{CP}$ violation can be observed as arising in the flavour mixing of neutral mesons (*i.e.* the transformation of a neutral meson into its $\mathcal{CP}$ counterpart), or directly from the decay diagrams (when the decay rate of a particle to a final state differs from that of the corresponding antiparticle to the charge conjugate final state), or finally in the interference between mixing and decay. $\mathcal{CP}$ violation is nowadays a well established experimental fact in several K^0 and B^0 decays [1, 2, 6–14]. Recently, an evidence of direct $\mathcal{CP}$ violation in the decays of D^0 mesons has been claimed by the LHCb collaboration [5] and another evidence in B_s^0 decays has been found as the result of the work presented in this thesis.

It is well known that $\mathcal{CP}$ violation is a key ingredient to explain the observed baryon asymmetry of the Universe [15]. However, it is believed that the observed baryon asymmetry is too large to be generated by the size of $\mathcal{CP}$ violation present in the Standard Model (SM). The simplest way to explain such a discrepancy is to postulate the existence of new elementary particles and interactions lying beyond SM, leading to additional sources of $\mathcal{CP}$ violation which could be associated to high energy scales, not directly accessible by particle colliders so far. Such "New Physics" could also manifest itself as a small deviation of some observables from their SM predictions, and for this reason $\mathcal{CP}$ violation represents a very relevant field to be explored with

constantly increasing precision. Any improvement in the experimental accuracy and theoretical understanding in this sector can play a crucial role in quest for physics beyond the SM.

1.1 The CKM matrix

In the SM, the $\mathcal{CP}$ symmetry is broken by complex phases in the Yukawa couplings of quark fields with the Higgs scalar:

$$\mathcal{L}_Y = -Y^d_{ij}\overline{Q^I_{Li}}\phi D^I_{Rj} - Y^u_{ij}\overline{Q^I_{Li}}\phi^\dagger U^I_{Rj} + h.c., \tag{1.1}$$

where $Y^{u,d}$ are 3×3 complex matrices, ϕ is the Higgs field, i and j are generation labels. Q^I_L are left-handed quark doublets, and D^I_R and U^I_R are respectively generic right-handed down-type and up-type quark singlets in the weak-eigenstate basis. When the symmetry group of the Standard Model electroweak interaction, $SU(2)_L\times U(1)_Y$, is broken assigning a vacuum expectation value to the Higgs field, $\langle\phi\rangle = \left(0, v/\sqrt{2}\right)$, Eq. (1.1) yields mass terms for the quarks. The physical states are thus obtained diagonalizing the Yukawa matrix using four matrices:

$$M^f_{diag} = \frac{v}{\sqrt{2}} V^f_L Y^f V^{f\dagger}_R, \tag{1.2}$$

where $v/\sqrt{2}$ is the vacuum expectation value for the Higgs scalar and $f = u, d$. As a consequence of this diagonalization, weak-eigenstates and mass-eigentstates of quarks become mixed and the charged current interactions for quarks are then given by:

$$\mathcal{L}_{W^\pm} = \frac{g}{\sqrt{2}}\overline{U_{Li}}\gamma^\mu \left(V^u_L V^{d\dagger}_L\right)_{ij} D_{Lj} W^+_\mu + h.c., \tag{1.3}$$

where g is the electroweak coupling constant. The product of the two V^f_L matrices contains the couplings of an up-type antiquark and a down-type quark to the charged W bosons and is called Cabibbo-Kobayashi-Maskawa (CKM) matrix [16, 17]:

$$V_{CKM} \equiv V^u_L V^{d\dagger}_L = \begin{pmatrix} V_{ud} & V_{us} & V_{ub} \\ V_{cd} & V_{cs} & V_{cb} \\ V_{td} & V_{ts} & V_{tb} \end{pmatrix} \tag{1.4}$$

The Feynman diagrams describing charged-current weak interactions between up-type and down-type quarks can be represented as shown in Fig. 1.1 where the various elements of CKM matrix modify the strenghts of the couplings. Before describing how the CKM matrix accounts for $\mathcal{CP}$ violation we will present its main properties.

1.1.1 Properties of the CKM matrix

The first important feature of the CKM matrix is its unitarity, required since processes involving quarks will not be invariant under a change of the quark field basis representation. Such a condition determines the number of free parameters of the matrix. A generic $N\times N$ unitary matrix depends on $N(N-1)/2$ mixing angles and $N(N+1)/2$ complex phases. In the CKM case, dealing with a mixing matrix between the quark flavour eigenstates, the Lagrangian allows to redefine the phase of each quark field such that:

$$\begin{cases} U \to e^{-i\varphi_U} U \\ D \to e^{-i\varphi_D} D \end{cases} \Rightarrow V_{UD} \to e^{i\varphi_U} V_{UD} e^{-i\varphi_D} \tag{1.5}$$

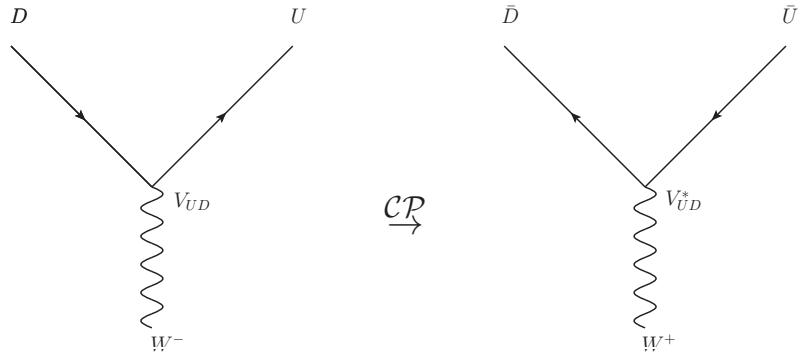

Figure 1.1: Basic Feynman diagrams for charged-current weak interaction processes between up-type (U) and down-type (D) quarks. On the left the interaction diagram between quarks mediated by negative vector boson (W^-) is represented. On the right its $\mathcal{CP}$ conjugate diagram is reported. The V_{CKM} factor V_{UD} modifying the strngth of the coupling is also shown.

In this way $2N-1$ unphysical phases of the CKM cancel out. As a consequence any $N \times N$ complex matrix describing mixing between N generations of quarks has:

$$\underbrace{\frac{1}{2}N\left(N-1\right)}_{\text{mixing angles}} + \underbrace{\frac{1}{2}\left(N-1\right)\left(N-2\right)}_{\text{physical complex phases}} = \left(N-1\right)^2 \tag{1.6}$$

free parameters. The interesting case $N = 2$ leads to a mixing matrix with only one free parameter, named the Cabibbo angle θ_C [16]:

$$V_C = \begin{pmatrix} \cos\theta_C & \sin\theta_C \\ -\sin\theta_C & \cos\theta_C \end{pmatrix} \tag{1.7}$$

The nature of V_C allowed to explain the suppression of flavour changing neutral current (FCNC) and historically had put the basis for the discovery of the charm quark [18, 19].

In the case $N = 3$, the resulting number of free parameters is four: three mixing angles and one complex phase. This phase alone is responsible for $\mathcal{CP}$ violation in the weak interactions of the SM. Among the various possible conventions, a standard choice to parameterize V_{CKM} is the following:

$$V_{CKM} = \begin{pmatrix} c_{12}c_{13} & s_{12}c_{13} & s_{13}e^{-i\delta} \\ -s_{12}c_{23} - c_{12}s_{23}s_{13}e^{i\delta} & c_{12}c_{23} - s_{12}s_{23}s_{13}e^{i\delta} & s_{23}c_{13} \\ s_{12}s_{23} - c_{12}c_{23}s_{13}e^{i\delta} & -c_{12}s_{23} - s_{12}c_{23}s_{13}e^{i\delta} & c_{23}c_{13} \end{pmatrix} \tag{1.8}$$

where $s_{ij} = \sin\theta_{ij}$, $c_{ij} = \cos\theta_{ij}$ and δ is the $\mathcal{CP}$ violating phase. All the θ_{ij} angles can be chosen to lie in the first quadrant, so $s_{ij}, c_{ij} \geq 0$, and the mixing between two quarks generation i, j vanishes if the corresponding θ_{ij} is equal to zero. In particular, in the case $\theta_{13} = \theta_{23} = 0$ the third generation would decouple and the CKM matrix would take the form of V_C in Eq. (1.7). The presence of a complex phase in the mixing matrix is a necessary but not sufficient condition

for $\mathcal{CP}$ violation. As pointed out in [20], another key condition is:

$$\left(m_t^2 - m_c^2\right)\left(m_t^2 - m_u^2\right)\left(m_c^2 - m_u^2\right)\left(m_b^2 - m_s^2\right)\left(m_b^2 - m_d^2\right)\left(m_s^2 - m_d^2\right) \times J_{CP} \neq 0 \qquad (1.9)$$

where

$$J_{CP} = \left|\Im\left(V_{i\alpha}V_{j\beta}V_{i\beta}^*V_{j\alpha}^*\right)\right| \qquad (i \neq j, \alpha \neq \beta) \qquad (1.10)$$

is the "Jarlskog parameter". This condition is related to the fact that according to Eq. (1.5) it would be possible to remove the CKM phase if any of two quarks with the same charge were degenerated in mass. As a consequence the origin of $\mathcal{CP}$ violation is deeply connected to the "flavour problem", with the origin of quark masses hierarchy, and number of fermion generations. J_{CP} can be interpreted as a measurement of the entity of $\mathcal{CP}$ violation in the SM. Its value does not depend on the phase convention of the quark fields, Eq. (1.5), and within the standard parameterization in Eq. (1.8) it can be written as:

$$J_{CP} = s_{12}s_{13}s_{23}c_{12}c_{23}c_{13}^2 \sin\delta. \qquad (1.11)$$

Experimentally one has $J_{CP} = \mathcal{O}\left(10^{-5}\right)$, which states that $\mathcal{CP}$ violation in Standard Model is very small. Various extensions of the SM foresee new sources of flavour mixing which could enhance the strength of the violation.

1.1.2 Experimental knowledge of $|V_{ij}|$

The determination of the CKM matrix elements is possible using the following tree-level processes:

$|V_{ud}|$ - Nuclear beta decays ($d \to ue\bar{\nu}_e$ transitions);

$|V_{us}|$ - Semileptonic kaons decays $K \to \pi l\bar{\nu}$ ($s \to ul\bar{\nu}$ transitions);

$|V_{ub}|$ - Exclusive and inclusive semileptonic B-hadron decays ($b \to ul\bar{\nu}$ transitions);

$|V_{cd}|$ - Semileptonic D-hadron decays $D \to \pi l\bar{\nu}$ ($c \to dl\bar{\nu}$ transitions) and charm production from ν interaction with matter;

$|V_{cs}|$ - Semileptonic D decays ($c \to sl\bar{\nu}$ transitions) and leptonic D_s decays ($D_s \to l\bar{\nu}$)

$|V_{cb}|$ - Exclusive and inclusive semileptonic B decays to charm ($b \to cl\bar{n}u$ transitions);

$|V_{tb}|$ - Branching ratio of $t \to Wb$ decay (assuming CKM matrix unitarity) and single top-quark-production cross section;

The magnitudes of V_{td} and V_{ts} are not measurable using tree-level processes. The cleanest way to obtain them is to extract $|V_{td}/V_{ts}|$ from $B^0 - \bar{B}^0$ and $B_s^0 - \bar{B}_s^0$ oscillation processes, which are mediated by box diagrams where top quarks circulate as virtual states. Tab. 1.1 summarizes the current values of each $|V_{ij}|$ [21]. Fig. 1.2 shows in a pictorial way how flavour-changing processes between quarks are governed by the CKM matrix: the size of the boxes represents the order of magnitude of the corresponing transition. Experimental information lead to the following consideration: transitions within the same generation imply V_{CKM} elements of $\mathcal{O}(1)$; those between the first and second generations are suppressed by a factor $\mathcal{O}(10^{-1})$; those between the second and third generations are suppressed by a factor $\mathcal{O}(10^{-2})$; and those between the first and third generations are strongly suppressed by a factor $\mathcal{O}(10^{-3})$.

CKM matrix element	Experimental value
$\|V_{ud}\|$	0.97425 ± 0.00022
$\|V_{us}\|$	0.2252 ± 0.0009
$\|V_{cd}\|$	0.230 ± 0.011
$\|V_{cs}\|$	1.023 ± 0.036
$\|V_{cb}\|$	$(40.6 \pm 1.3) \times 10^{-3}$
$\|V_{ub}\|$	$(3.89 \pm 0.44) \times 10^{-3}$
$\|V_{td}\|$	$(8.4 \pm 0.6) \times 10^{-3}$
$\|V_{ts}\|$	$(38.7 \pm 2.1) \times 10^{-3}$
$\|V_{tb}\|$	0.88 ± 0.07

Table 1.1: Experimental knowledge of the magnitudes of the CKM matrix elements [21].

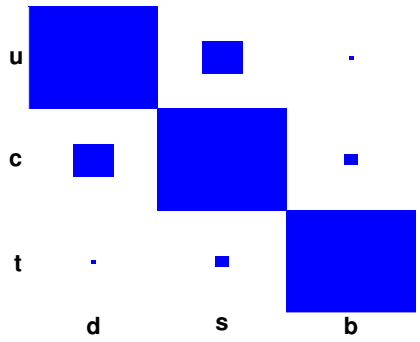

Figure 1.2: Graphical representation of of the order of magnitude of the CKM matrix elements. The size of the boxes represents the order of magnitude, as reported in the text, of the corresponding element.

1.1.3 Wolfenstein parameterization of the CKM matrix

Starting from the observed hierarchy relations among the matrix terms $|V_{ij}|$, thanks to the experimental information available on their magnitude, it can be stated that:

$$s_{12} = 0.22 \gg s_{23} = \mathcal{O}(10^{-2}) \gg s_{13} = \mathcal{O}(10^{-3}) \tag{1.12}$$

using the standard parameterization in Eq. (1.8). In order to quantify the relations illustrated in Fig. 1.2 it is useful to introduce the "Wolfenstein parameterization" [22] of the CKM matrix. Defining:

$$s_{12} = \lambda = \frac{|V_{us}|}{\sqrt{|V_{ud}|^2 + |V_{us}|^2}}, \quad s_{23} = A\lambda^2 = \lambda \left|\frac{V_{cb}}{V_{us}}\right|, \quad s_{13}e^{-i\delta} = A\lambda^3 (\rho - i\eta) = V_{ub} \tag{1.13}$$

the CKM matrix in Eq. (1.8) can be re-written as a power expansion of the parameter $\lambda = \sin\theta_C$ (where θ_C is the Cabibbo angle defined in Eq. (1.7)):

$$V_{CKM} = \begin{pmatrix} 1-\lambda^2/2 & \lambda & A\lambda^3(\rho - i\eta) \\ -\lambda & 1-\lambda^2/2 & A\lambda^2 \\ A\lambda^3(1-\rho-i\eta) & -A\lambda^2 & 1 \end{pmatrix} + \mathcal{O}\left(\lambda^4\right) \tag{1.14}$$

For certain processes, in particular when $\mathcal{CP}$ violation is expected to be very small, it could be useful to further expand the parameterization to the subsequent order, obtaining:

$$\begin{aligned}
&V_{ud} = 1 - \frac{1}{2}\lambda^2 - \frac{1}{8}\lambda^4 + \mathcal{O}(\lambda^6), \quad V_{us} = \lambda + \mathcal{O}(\lambda^7), \quad V_{ub} = A\lambda^3(\rho - i\eta), \\
&V_{cd} = -\lambda + \frac{1}{2}A^2\lambda^5\left[1 - 2(\rho + i\eta)\right] + \mathcal{O}(\lambda^7), \quad V_{cs} = 1 - \frac{1}{2}\lambda^2 - \frac{1}{8}\lambda^4(1 + 4A^2) + \mathcal{O}(\lambda^6), \\
&V_{cb} = A\lambda^2 + \mathcal{O}(\lambda^8), \quad V_{td} = A\lambda^3\left[1 - (\rho + i\eta)\left(1 - \frac{1}{2}\lambda^2\right)\right] + \mathcal{O}(\lambda^7), \\
&V_{ts} = -A\lambda^2 + \frac{1}{2}A\lambda^4\left[1 - 2(\rho + i\eta)\right] + \mathcal{O}(\lambda^6), \quad V_{tb} = 1 - \frac{1}{2}A^2\lambda^4 + \mathcal{O}(\lambda^6).
\end{aligned} \tag{1.15}$$

It can be noted that

- $V_{ub} \equiv A\lambda^3(\rho - i\eta)$ by definition does not receive any correction;
- $V_{us} = \lambda$ and $V_{cb} = A\lambda^2$ to a very high accuracy;
- contributions to $\mathcal{CP}$ violation (*i.e.* the presence of an imaginary term) from V_{cs} and V_{cb} are suppressed at least by a factor λ^6 and λ^8, respectively;
- contributions to $\mathcal{CP}$ violation from V_{td} and V_{ts} are at the level of λ^5 and λ^4, respectively.

It is useful to define:

$$\bar{\rho} \equiv \rho\left(1 - \frac{1}{2}\lambda^2\right), \qquad \bar{\eta} \equiv \eta\left(1 - \frac{1}{2}\lambda^2\right) \tag{1.16}$$

that allows one to write:

$$V_{td} = A\lambda^3(1 - \bar{\rho} - i\bar{\eta}). \tag{1.17}$$

Using Eq. (1.14) the "Jarlskog parameter" introduced in Eq. (1.11) becomes:

$$J_{CP} = \lambda^6 A^2 \eta, \tag{1.18}$$

directly related to the $\mathcal{CP}$ violating parameter η.

1.1.4 Unitary triangles

The unitarity of the CKM matrix $V_{CKM}V_{CKM}^\dagger = V_{CKM}^\dagger V_{CKM} = \mathbb{I}$, leads to a set of 12 equations relating the matrix elements: 6 for diagonal terms equal to 1 and 6 for the off-diagonal terms equal to 0. The equations for the off-diagonal terms can be represented as triangles in the

complex plane, all having the same area $J_{CP}/2$:

$$\underbrace{V_{ud}V_{us}^*}_{\mathcal{O}(\lambda)} + \underbrace{V_{cd}V_{cs}^*}_{\mathcal{O}(\lambda)} + \underbrace{V_{td}V_{ts}^*}_{\mathcal{O}(\lambda^5)} = 0, \tag{1.19}$$

$$\underbrace{V_{us}V_{ub}^*}_{\mathcal{O}(\lambda^4)} + \underbrace{V_{cs}V_{cb}^*}_{\mathcal{O}(\lambda^2)} + \underbrace{V_{ts}V_{tb}^*}_{\mathcal{O}(\lambda^2)} = 0, \tag{1.20}$$

$$\underbrace{V_{ud}V_{ub}^*}_{(\rho+i\eta)A\lambda^3} + \underbrace{V_{cd}V_{cb}^*}_{-A\lambda^3} + \underbrace{V_{td}V_{tb}^*}_{(1-\rho-i\eta)A\lambda^3} = 0, \tag{1.21}$$

$$\underbrace{V_{ud}^*V_{cd}}_{\mathcal{O}(\lambda)} + \underbrace{V_{us}^*V_{cs}}_{\mathcal{O}(\lambda)} + \underbrace{V_{ub}^*V_{cb}}_{\mathcal{O}(\lambda^5)} = 0, \tag{1.22}$$

$$\underbrace{V_{cd}^*V_{td}}_{\mathcal{O}(\lambda^4)} + \underbrace{V_{cs}^*V_{ts}}_{\mathcal{O}(\lambda^2)} + \underbrace{V_{cb}^*V_{tb}}_{\mathcal{O}(\lambda^2)} = 0, \tag{1.23}$$

$$\underbrace{V_{ud}^*V_{td}}_{(1-\rho-i\eta)A\lambda^3} + \underbrace{V_{us}^*V_{ts}}_{-A\lambda^3} + \underbrace{V_{ub}^*V_{tb}}_{(\rho+i\eta)A\lambda^3} = 0. \tag{1.24}$$

In these equations we emphasized the values of each product $V_{ij}V_{kl}^*$ at the leading order in λ as obtained from Eq. (1.14), representing the length of the corresponding triangle sides. Only two out of the six unitary triangles have sides of the same order of magnitude: they are described by Eqs. (1.21) and (1.24), and represented in Figs. 1.3 (left) and 1.3 (right). Let us focus on the triangle corresponding to Eq. (1.21). To the level of approximation of Eq. (1.14) it satisfies this relation:

$$[(\rho + i\eta) + (-1) + (1 - \rho - i\eta)]\, A\lambda^3 = 0, \tag{1.25}$$

while to the next order, using Eqs. (1.15) and (1.16) one gets:

$$[(\bar{\rho} + i\bar{\eta}) + (-1) + (1 - \bar{\rho} - i\bar{\eta})]\, A\lambda^3 + \mathcal{O}(\lambda^7) = 0. \tag{1.26}$$

Normalizing to the common factor $A\lambda^3$, we obtain the triangle of Fig. 1.3: it is usually referred to as "The Unitary Triangle" (UT). Its importance will be discussed in next sections. Here below we can show how its sides and angles are related to the CKM matrix elements. About its sides, using Eqs. (1.15) one can see that:

$$R_b \equiv \sqrt{\bar{\rho}^2 + \bar{\eta}^2} = \left(1 - \frac{\lambda^2}{2}\right) \frac{1}{\lambda} \frac{|V_{ub}|}{|V_{cb}|}, \tag{1.27}$$

$$R_t \equiv \sqrt{(1 - \bar{\rho})^2 + \bar{\eta}^2} = \frac{1}{\lambda} \frac{|V_{td}|}{|V_{cb}|}, \tag{1.28}$$

while its angles are related to the CKM elements through:

$$V_{ub} = A\lambda^3 \left(\frac{R_b}{1 - \lambda^2/2}\right) e^{-i\gamma}, \tag{1.29}$$

$$V_{td} = A\lambda^3 R_t e^{-i\beta}, \tag{1.30}$$

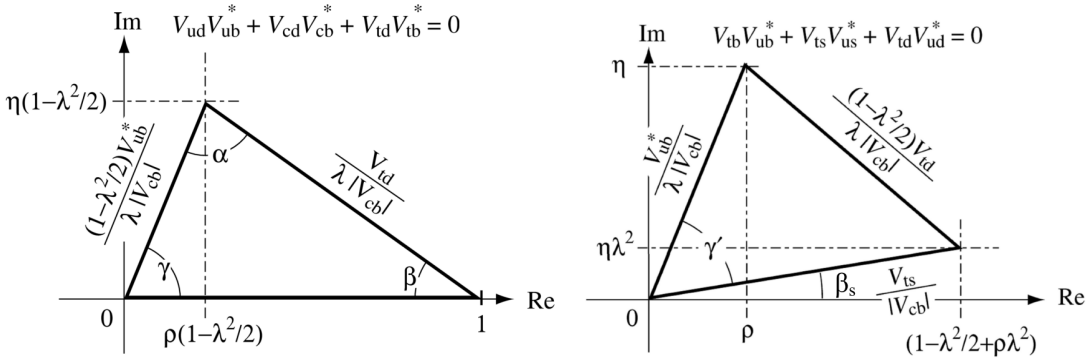

Figure 1.3: Representation in the complex plane of the unitary triangles described in the text: on the left the UT corresponding to Eq. (1.21); on the right the triangle corresponding to Eq. (1.24) is reported.

where in fact the angles γ and β appear. It is useful, in order to better understand the processes where such angles are involved, to write:

$$\alpha \equiv \arg\left(-\frac{V_{td}V_{tb}^*}{V_{ud}V_{ub}^*}\right) = \arg\left(-\frac{1-\bar{\rho}-i\bar{\eta}}{\bar{\rho}+i\bar{\eta}}\right), \tag{1.31}$$

$$\beta \equiv \arg\left(-\frac{V_{cd}V_{cb}^*}{V_{td}V_{tb}^*}\right) \equiv \phi_d/2 = \arg\left(\frac{1}{1-\bar{\rho}-i\bar{\eta}}\right), \tag{1.32}$$

$$\gamma \equiv \arg\left(-\frac{V_{ud}V_{ub}^*}{V_{cd}V_{cb}^*}\right) = \arg\left(\bar{\rho}+i\bar{\eta}\right). \tag{1.33}$$

From Eq. (1.29) we can also see that the $\mathcal{CP}$ violating phase δ is equal to the γ angle of the UT. The other non squashed triangle has similar characteristics with respect to the UT. Expanding Eq. (1.24) we obtain:

$$\left\{\left[1-\rho-i\eta-\lambda^2\left(\frac{1}{2}-\rho-i\eta\right)\right]+\left[-1+\lambda^2\left(\frac{1}{2}-\rho-i\eta\right)\right]+[\rho+i\eta]\right\}A\lambda^3+\mathcal{O}(\lambda^7)=0. \tag{1.34}$$

Dividing again by the common factor $A\lambda^3$ we obtain a triangle with the apex placed in the point (ρ,η) instead of $(\bar{\rho},\bar{\eta})$, and tilted by an angle:

$$\beta_s \equiv \phi_s/2 = \arg\left(\frac{V_{ts}V_{tb}^*}{V_{cs}V_{cb}^*}\right). \tag{1.35}$$

1.1.5 Experimental determination of the UT

Here we briefly discuss the experimental status of the UT. More details about the method and the results can be found in Refs. [23, 24]. The method relies on information from both experimentally and theoretically determined input parameters. The experimental information about the constraints on the UT parameters can be obtained from the following measurements:

$|\mathbf{V_{ub}}|\,/\,|\mathbf{V_{cb}}|$: The measurements of branching fractions of semi-leptonic decays governed by $b \to ul\bar{\nu}$ and $b \to cl\bar{\nu}$ transitions give information about the magnitudes of V_{ub} and V_{cb}

respectively. The ratio between these two quantities is proportional to the side of the UT between the γ and α angles.

Δm_d: This parameter represents the frequency of $B^0 - \bar{B}^0$ mixing. It is proportional to the magnitude of V_{td} and thus to the side of the UT between the β and α angles. However, the relation between Δm_d and V_{td} is affected by large theoretical uncertainties, thus the ratio $\Delta m_s/\Delta m_d$ is also used as a constraint for the UT.

$\Delta m_s/\Delta m_d$: Δm_s is the analog of Δm_d in the case of $B_s^0 - \bar{B}_s^0$ mixing and its value is proportional to V_{ts}. The relation between $\Delta m_s/\Delta m_d$, V_{ts} and V_{td} contains some theoretical parameters that can be estimated more precisely than in the case of Δm_d.

β: This angle can be determined from time-dependent measurements of the $B^0 \to J/\psi K^0$ decays. Its relation with the $\bar{\rho}$ and $\bar{\eta}$ parameters is reported in Eq. (1.32).

ε_K: This parameter is related to $\mathcal{CP}$ violation in the neutral kaon system.

α: This angle of the UT can be measured from the analysis of $B \to \pi\pi$ and $B \to \rho\rho$ decays. Decay amplitudes and $\mathcal{CP}$ asymmetries of these channels are related to $V_{td}V_{tb}^*$ and $V_{ud}V_{ub}^*$ sides of the UT.

γ: The determination of this angle is performed by means of $B \to D^{(*)}K^{(*)}$ decays, whose transitions are mediated by V_{ub} and V_{cb}.

$\sin(2\beta+\gamma)$: Time-dependent decay rates of $B \to D^{(*)}\pi$ channels contain terms proportional to $\sin(2\beta+\gamma)$.

The determination of the UT parameters can be formulated in the following way. The unkowns $\bar{\rho}$ and $\bar{\eta}$ are related to a set of N observables x_i by M relations $c_j = \phi_j(x_1, ..., x_N, \bar{\rho}, \bar{\eta})$ ($j \in \{1, M\}$). The joint p.d.f. for $\bar{\rho}$ and $\bar{\eta}$ can be determined applying the Bayes theorem. The conditional distribution $\mathbf{f}$ for $\bar{\rho}$ and $\bar{\eta}$, given the measurements x_i of the input observables and the constraint relations c_j, can be written as:

$$\mathbf{f}(\bar{\rho}, \bar{\eta}|x_1, .., x_N, c_1, ..., c_M) \propto f(c_1, ..., c_M|\bar{\rho}, \bar{\eta}, x_1, ..., x_N) \cdot f_0(\bar{\rho}, \bar{\eta}) \cdot g_0(x_1, ..., x_N), \quad (1.36)$$

where f in the right part is the probability to obtain the relation values c_1, ...,c_M for a given set of values of $\bar{\rho}$, $\bar{\eta}$ and measurements of the x_i; f_0 is the *a priori* p.d.f. for the unknown $\bar{\rho}$ and $\bar{\eta}$; $g_0(x_1, ..., x_N)$ is the *a priori* p.d.f. for the input observables $x_1...x_N$ determined from experimental measurements and theoretical calculations. The p.d.f. for the values c_1, ...,c_M, given the values of $\bar{\rho}$, $\bar{\eta}$ and of the observables x_1, ...,x_N, is thus given by:

$$f(c_1, ..., c_M|\bar{\rho}, \bar{\eta}, x_1, ..., x_N) = \prod_{j=1,M} \delta(c_j - \phi_j(x_1, ..., x_N, \bar{\rho}, \bar{\eta})), \quad (1.37)$$

where the symbol $\delta(\cdot)$ is the Dirac delta function. In the end the joint distribution for $\bar{\rho}$ and $\bar{\eta}$ in Eq. (1.36) becomes:

$$\mathbf{f}(\bar{\rho}, \bar{\eta}|x_1, .., x_N, c_1, ..., c_M) \propto \prod_{j=1,M} \delta(c_j - \phi_j(x_1, ..., x_N, \bar{\rho}, \bar{\eta})) \cdot f_0(\bar{\rho}, \bar{\eta}) \cdot \prod_{j=1,N} f_i(x_i), \quad (1.38)$$

where the $f_i\,(x_i)$ represent the distributions of the observables x_i determined from experimental measurements and theoretical computations. The method to determine the final joint p.d.f. for $\bar{\rho}$ and $\bar{\eta}$ consists in a Monte Carlo generation of $\bar{\rho}$ and $\bar{\eta}$ values, weighted by the constraint relations.

Tab. 1.2 reports the input values and the full fit results for the observables described in the beginning of this section. The full fit results for the parameters $\bar{\rho}$ and $\bar{\eta}$ are:

$$\bar{\rho} = 0.132 \pm 0.020, \qquad \bar{\eta} = 0.358 \pm 0.012 \tag{1.39}$$

Fig. 1.4 shows the 68% probability intervals of the UT parameters obtained from the full fit, together with the 68% and 95% contours for the $\bar{\rho}$ and $\bar{\eta}$ parameters [23].

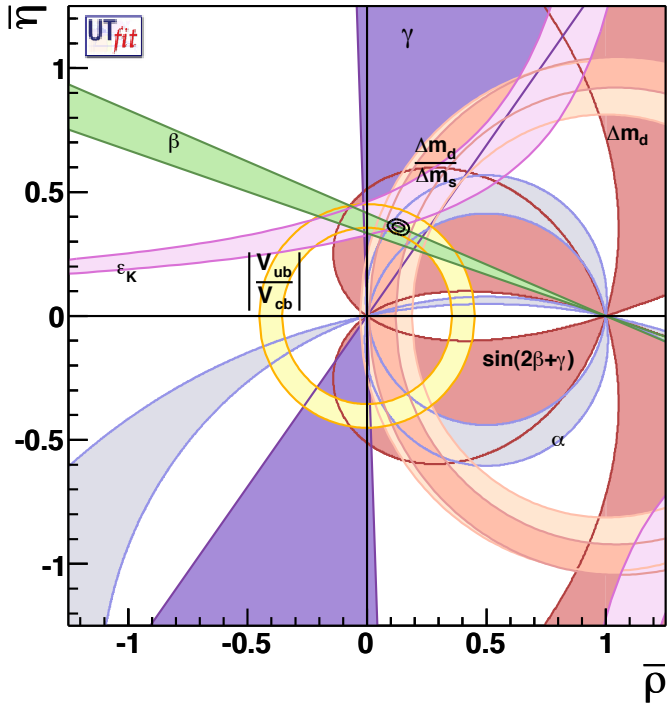

Figure 1.4: 68% probability regions for the parameters of the UT obtained from the method described in the text. The 68% and 95% contours for the $\bar{\rho}$ and $\bar{\eta}$ parameters are also shown.

1.2 Hadronic two-body B decays

Non-leptonic B meson decays play a key rôle in the exploration of $\mathcal{CP}$ violation, as various CKM matrix elements enter the Feynman diagrams governing such decays. Before looking at the experimental strategy to extract such quantities from hadronic B decays, we have to discuss the theoretical tools to deal with them.

A generic two-body hadronic B decay is mediated by $b \to q_1\bar{q}_2 d(s)$ transitions, where $q_{1,2} \in \{u, d, c, s\}$. The Feynman diagrams contributing to such transitions can be divided into two

Parameter	Input value	Full fit result
$\lvert V_{ub}\rvert$	0.00376 ± 0.00020	0.00364 ± 0.00011
$\lvert V_{cb}\rvert$	0.04083 ± 0.00045	0.04117 ± 0.00043
Δm_d	(0.507 ± 0.005) ps^{-1}	(0.507 ± 0.005) ps^{-1}
Δm_s	(17.77 ± 0.12) ps^{-1}	(17.77 ± 0.12) ps^{-1}
α	$(91.4 \pm 6.1)^\circ$	$(87.8 \pm 3.0)^\circ$
$\sin(2\beta)$	0.654 ± 0.026	0.705 ± 0.018
$\cos(2\beta)$	0.87 ± 0.13	0.71 ± 0.018
γ	$(-106 \pm 11)^\circ$ and $(74 \pm 11)^\circ$	$(69.8 \pm 3.0)^\circ$
$2\beta + \gamma$	$(-90 \pm 56)^\circ$ and $(94 \pm 52)^\circ$	$(114.7 \pm 3.1)^\circ$
$\lvert\varepsilon_K\rvert$	$(2.22994 \pm 0.0104974) \times 10^{-3}$	$(2.22854 \pm 0.00998004) \times 10^{-3}$

Table 1.2: Input values and the UT fit results for the observables described in the text.

groups: tree-level topologies and penguing (or loop-level) topologies. Accordingly to the flavour content of the final state we can divide the two-body hadronic decays into:

- $q_1 \neq q_2 \in \{u, c\}$: transitions mediated obly by tree-level topologies;
- $q_1 = q_2 \in \{u, c\}$: transition mediated by both tree-level and penguin topologies;
- $q_1 = q_2 \in \{d, s\}$: transition mediated only by penguin topologies.

As shown in Figs. 1.6 and 1.7, penguin contributions consist of gluon-mediated diagrams and electroweak diagrams (where both $W^\pm$ and Z bosons show up).

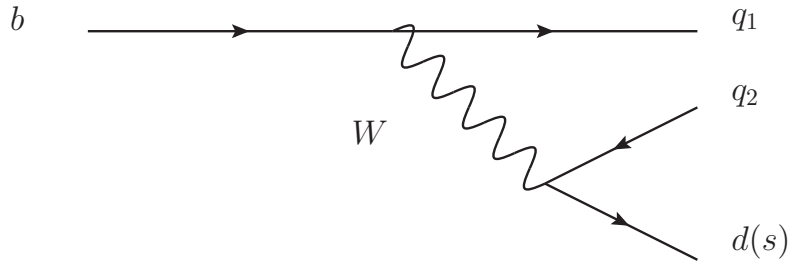

Figure 1.5: Feynman diagram governing the tree level transition of a non-leptonic B hadron decay. For the q_1 and q_2 quarks the relation $q_1 \neq q_2 \in \{u, c\}$ holds.

1.2.1 Hadronic matrix elements

In order to describe the weak decays of hadrons, it is necessary to take into account also the strong interactions binding together their constituent quarks. Thanks to the asymptotic freedom

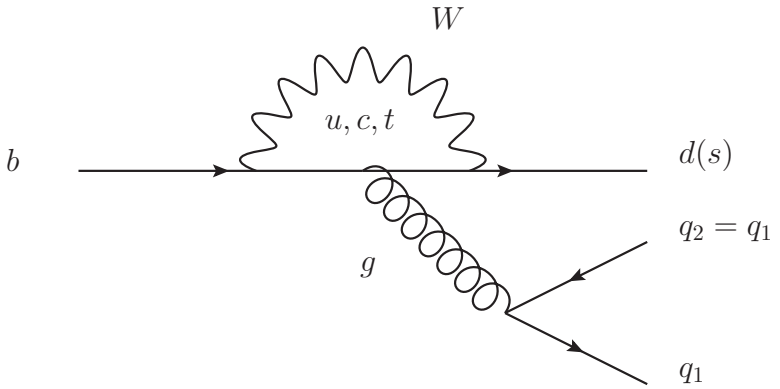

Figure 1.6: Feynman diagram governing the QCD penguin topology of a non-leptonic B hadron decay. For the q_1 and q_2 quarks the relation $q_1 = q_2 \in \{u, d, c, s\}$ holds.

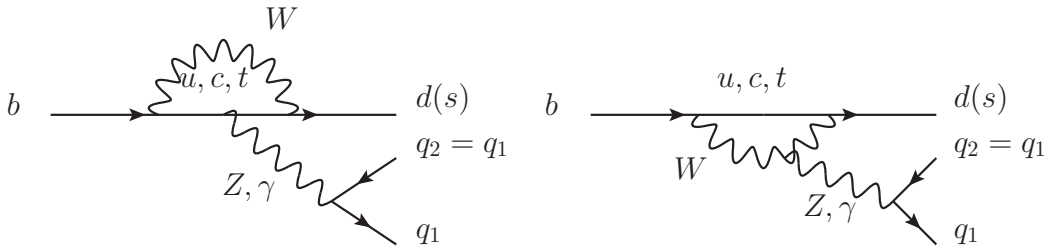

Figure 1.7: Feynman diagrams governing the EW penguin topology of a non-leptonic B hadron decay. For the q_1 and q_2 quarks the relation $q_1 = q_2 \in \{u, d, c, s\}$ holds.

of QCD one could treat the short-distance corrections, that is the contribution of hard gluons at energies of the order $\mathcal{O}(M_W)$ down to hadronic scales ≥ 1 GeV, in perturbation theory. The formal framework used to exploit such property is the so called Operator Product Expansion (OPE) [25, 26].

Operator product expansion allows to write the transition matrix elements in the following way:

$$\langle f| \mathcal{H}_{eff} |i\rangle = \frac{G_F}{\sqrt{2}} \lambda_{CKM} \sum_k C_k(\mu) \langle f| Q_k(\mu) |i\rangle \tag{1.40}$$

where short-distance contributions, represented by perturbative Wilson coefficients functions $C_k(\mu)$, and long-distance contributions, represented by non-perturbative hadronic matrix elements $\langle f| Q_k(\mu) |i\rangle$, can be disentangled. G_F is the Fermi constant, λ_{CKM} is a factor arising from CKM matrix element entering the weak interaction vertices and μ is an appropriate renormalization scale.

The simplest case where the OPE technique can be applied is the description of pure tree

transitions, as shown in Fig. 1.5, and neglecting QCD contributions:

$$\begin{aligned}\mathcal{H}_{eff} &= \frac{G_F}{\sqrt{2}}\lambda_{CKM}\frac{M_W^2}{k^2-M_W^2}\left(\bar{r}^{\alpha}q_2^{\alpha}\right)_{V-A}\left(\bar{q}_1^{\beta}b^{\beta}\right)_{V-A} \\ &= -\frac{G_F}{\sqrt{2}}\lambda_{CKM}\left(\bar{r}^{\alpha}q_2^{\alpha}\right)_{V-A}\left(\bar{q}_1^{\beta}b^{\beta}\right)_{V-A}+\mathcal{O}\left(\frac{k^2}{M_W^2}\right),\end{aligned} \tag{1.41}$$

where $r \in \{,s\}$, $V-A$ refers to the vector-axial Lorentz current $\gamma^{\mu}(1-\gamma_5)$, the term $\mathcal{O}\left(\frac{k^2}{M_W^2}\right)$ can be easilly neglected as the transferred momentum k^2 is of the order of quark masses and thus $k^2 \ll M_W^2$, and the indices α and β label the $SU(3)_C$ color of quarks. As no QCD corrections are considered, Eq. (1.41) represents the case where we have just one Wilson coefficient $C_1(\mu)=1$ and the decay is governed by a "current-current" effective hamiltonian:

$$Q_1 \equiv \left(\bar{r}^{\alpha}q_2^{\alpha}\right)_{V-A}\left(\bar{q}_1^{\beta}b^{\beta}\right)_{V-A}. \tag{1.42}$$

If we now turn on QCD, we have to distinguish between factorizable and non-factorizable QCD corrections. In the former case QCD corrections are due to the exchange of gluons within the two quark currents, $\bar{r}q_2$ and $\bar{q}_1 b$, and thus their contribution results in a different renormalization of C_1. The latter case represents long-distance strong interactions, with the exchange of gluons between the two quark currents, and enters in our effective hamiltonian via another hadronic matrix element:

$$Q_2 \equiv \left(\bar{r}^{\alpha}q_2^{\beta}\right)_{V-A}\left(\bar{q}_1^{\beta}b^{\alpha}\right)_{V-A}. \tag{1.43}$$

In the end the effective hamiltonian used to describe tree-level weak-interaction decays with QCD corrections can be written as:

$$\mathcal{H}_{eff} = \frac{G_F}{\sqrt{2}}\lambda_{CKM}\left[C_1(\mu)\,O_1 + C_2(\mu)\,O_2\right]. \tag{1.44}$$

Now that we stated the basic method to deal with QCD corrections in weak decay processes, we can apply it to the entire set of Feynman diagrams governing a generic hadronic two-body B decay, represented in Fig. 1.9. In a compact way we can write [27, 28]:

$$\mathcal{H}_{eff} = \frac{G_F}{\sqrt{2}}\left\{V_{ur}^*V_{ub}\sum_{k=1}^{2}C_k(\mu)\,Q_k^{ur} + V_{cr}^*V_{cb}\sum_{k=1}^{2}C_k(\mu)\,Q_k^{cr} - V_{tr}^*V_{tb}\sum_{k=3}^{10}C_k(\mu)\,Q_k^{r}\right\} \tag{1.45}$$

where we made explicit the λ_{CKM} term ($r \in \{d,s\}$). The various Q_k^{jr} and Q_k^r are:

- Current-current operators for tree-level processes ($j \in \{u,c\}$):

$$\begin{aligned}Q_1^{jr} &= \left(\bar{r}_{\alpha}j_{\alpha}\right)_{V-A}\left(\bar{j}_{\beta}b_{\beta}\right)_{V-A} \\ Q_2^{jr} &= \left(\bar{r}_{\alpha}j_{\alpha}\right)_{V-A}\left(\bar{j}_{\beta}b_{\beta}\right)_{V-A}\end{aligned} \tag{1.46}$$

- QCD penguin operators ($q' \in \{u, d, s, c, b\}$):

$$\begin{aligned} Q_3^r &= (\bar{r}_\alpha b_\alpha)_{V-A} \sum_{q'} \left(\bar{q}'_\beta q'_\beta\right)_{V-A} \\ Q_4^r &= (\bar{r}_\alpha b_\beta)_{V-A} \sum_{q'} \left(\bar{q}'_\beta q'_\alpha\right)_{V-A} \\ Q_5^r &= (\bar{r}_\alpha b_\alpha)_{V-A} \sum_{q'} \left(\bar{q}'_\beta q'_\beta\right)_{V+A} \\ Q_6^r &= (\bar{r}_\alpha b_\beta)_{V-A} \sum_{q'} \left(\bar{q}'_\beta q'_\alpha\right)_{V+A} \end{aligned} \tag{1.47}$$

- EW penguin operators ($e_{q'}$ is the electrical quark charges, $q' \in \{u, d, s, c, b\}$):

$$\begin{aligned} Q_7^r &= \frac{3}{2} (\bar{r}_\alpha b_\alpha)_{V-A} \sum_{q'} e_{q'} \left(\bar{q}'_\beta q'_\beta\right)_{V+A} \\ Q_8^r &= \frac{3}{2} (\bar{r}_\alpha b_\beta)_{V-A} \sum_{q'} e_{q'} \left(\bar{q}'_\beta q'_\alpha\right)_{V+A} \\ Q_9^r &= \frac{3}{2} (\bar{r}_\alpha b_\alpha)_{V-A} \sum_{q'} e_{q'} \left(\bar{q}'_\beta q'_\beta\right)_{V-A} \\ Q_{10}^r &= \frac{3}{2} (\bar{r}_\alpha b_\beta)_{V-A} \sum_{q'} e_{q'} \left(\bar{q}'_\beta q'_\alpha\right)_{V-A} \end{aligned} \tag{1.48}$$

The current-current, QCD and EW penguin operators are related to the tree, QCD and EW penguin processes shown in Figs. 1.5 1.6 and 1.7. The way Wilson coefficients are calculated is a technical detail that goes beyond the scope of of this thesis, as it deals with QCD renormalization effects. Thus we just summarize their order of magnitude at the renormalization scale $\mu = \mathcal{O}(m_b)$. The Wilson coefficients of the current-current operators satisfy $C_1(\mu) = \mathcal{O}\left(10^{-1}\right)$ and $C_2(\mu) = \mathcal{O}(1)$, whereas those of the penguin operators are $\mathcal{O}\left(10^{-2}\right)$ [26, 29].
It should be noted that penguin topologies with internal charm- and up-quark exchanges are not explicitly present in Eq. (1.45), while those with internal t quarks are represented by the terms with $Q_3, \ldots, Q_{10}$ operators. Naïvely speaking, the penguin diagrams with internal u and c quarks have been absorbed into the current-current operator during the calculation of Wilson coefficients, as explicitly demonstrated in [27, 28]. The effect of such absorption may also have important phenomenological consequences as pointed out in [30, 31].
Since the ratio of the QED and QCD couplings $\alpha/\alpha_s = \mathcal{O}\left(10^{-2}\right)$ is very small, we would expect naïvely that EW penguins should play a minor rôle in comparison with QCD penguins. This would actually be the case if the top quark were not "heavy". However, since the Wilson coefficient C_9 increases strongly with m_t, we obtain interesting EW penguin effects in several B decays. Of particular interest for this thesis is the impact of EW penguins on the $B \to K\pi$ system [32, 33].

In the end, using the unitarity of CKM matrix ($V_{tr}^* V_{tb} = -V_{ur}^* V_{ub} - V_{cr}^* V_{cb}$), Eq. (1.45) can be written in the more compact way:

$$\mathcal{H}_{eff} = \frac{G_F}{\sqrt{2}} \left\{ \sum_{j=u,c} V_{jr}^* V_{jb} \left[\sum_{k=1}^{2} C_k(\mu) Q_k^{jr} + \sum_{k=3}^{10} C_k(\mu) Q_k^r \right] \right\} \tag{1.49}$$

Such method results to be "universal", *i.e.* it can be applied to all B decays governed by the same corresponding quark-level transitions ($b \to q_1\bar{q}_2 d(s)$). Within this formalism, differences between various exclusive decay modes come only from the hadronic matrix elements associated with the four-quark operators.
The last remark concerns the way the hadronic matrix elements can be computed, as it represents the most challenging task and the principal source of theoretical uncertainties. Without entering the details, here we summarize different approaches that are commonly used in order to deal with non-leptonic B decays.

QCD factorization: Within this framework, one starts from the physical idea that factorization should hold for hadrons containing a heavy quark Q with $m_Q \gg \Lambda_{QCD}$ [34], and a formalism to calculate the relevant amplitudes at the leading order of a Λ_{QCD}/m_Q expansion is provided [35];

Perturbative hard-scattering approach: pQCD was developed independently in [36], and differs from the QCD factorization formalism in some technical aspects;

Soft collinear effective theory: SCET represents an interesting technique for factorization proofs and has received a lot of attention in the recent literature and led to various applications [37];

QCD light-cone sum-rule: Non-leptonic B decays can also be studied within the QCD light-cone sum-rule approaches [38].

1.2.2 Decay amplitudes

Using the formalism described in the previous section, we can write the matrix element of a generic $\bar{B} \to \bar{f}$ decay as follows:

$$\begin{aligned} A\left(\bar{B} \to \bar{f}\right) &= \left\langle \bar{f} \right| \mathcal{H}_{eff} \left| \bar{B} \right\rangle \\ &= \frac{G_F}{\sqrt{2}} \left\{ \sum_{j=u,c} V_{jr}^* V_{jb} \left[\sum_{k=1}^{2} C_k\left(\mu\right) \left\langle \bar{f} \right| Q_k^{jr} \left| \bar{B} \right\rangle + \sum_{k=3}^{10} C_k\left(\mu\right) \left\langle \bar{f} \right| Q_k^{r} \left| \bar{B} \right\rangle \right] \right\}, \end{aligned} \tag{1.50}$$

while for its $\mathcal{CP}$ conjugate decay:

$$\begin{aligned} A\left(B \to f\right) &= \left\langle f \right| \mathcal{H}_{eff}^{\dagger} \left| B \right\rangle \\ &= \frac{G_F}{\sqrt{2}} \left\{ \sum_{j=u,c} V_{jr} V_{jb}^* \left[\sum_{k=1}^{2} C_k\left(\mu\right) \left\langle f \right| Q_k^{jr\dagger} \left| B \right\rangle + \sum_{k=3}^{10} C_k\left(\mu\right) \left\langle f \right| Q_k^{r\dagger} \left| B \right\rangle \right] \right\}. \end{aligned} \tag{1.51}$$

Now, making use of the invariance of strong interactions under $\mathcal{CP}$ and that we have $\left(\mathcal{CP}\right)^{\dagger}\left(\mathcal{CP}\right) = \mathbb{I}$ we obtain:

$$\begin{aligned} \left(\mathcal{CP}\right) Q_k^{jr} \left(\mathcal{CP}\right)^{\dagger} &= Q_k^{jr} \\ \left(\mathcal{CP}\right) Q_k^{r} \left(\mathcal{CP}\right)^{\dagger} &= Q_k^{r} \\ \left(\mathcal{CP}\right) \left| f \right\rangle &= e^{i\phi_f} \left| \bar{f} \right\rangle \\ \left(\mathcal{CP}\right) \left| B \right\rangle &= e^{i\phi_B} \left| \bar{f} \right\rangle, \end{aligned} \tag{1.52}$$

and hence:

$$A\left(B\to f\right)=e^{i\left(\phi_B-\phi_f\right)}\times \\ \times\frac{G_F}{\sqrt{2}}\left\{\sum_{j=u,c}V_{jr}V_{jb}^*\left[\sum_{k=1}^{2}C_k\left(\mu\right)\left\langle\bar{f}\right|Q_k^{jr\dagger}\left|\bar{B}\right\rangle+\sum_{k=3}^{10}C_k\left(\mu\right)\left\langle\bar{f}\right|Q_k^{r\dagger}\left|\bar{B}\right\rangle\right]\right\}. \quad (1.53)$$

Consequently:

$$\begin{aligned}A\left(\bar{B}\to\bar{f}\right) &= e^{i\varphi_1}\left|A_1\right|e^{i\delta_1}+e^{i\varphi_2}\left|A_2\right|e^{i\delta_2}\\ A\left(B\to f\right) &= e^{i\left(\phi_B-\phi_f\right)}\times\left[e^{-i\varphi_1}\left|A_1\right|e^{i\delta_1}+e^{-i\varphi_2}\left|A_2\right|e^{i\delta_2}\right],\end{aligned} \quad (1.54)$$

where $\varphi_{1,2}$ denotes $\mathcal{CP}$ violating phases coming from the CKM elements $V_{jr}V_{jb}^*$, and $\left|A_{1,2}\right|e^{i\delta 1,2}$ are the $\mathcal{CP}$-conserving strong amplitude coming from:

$$\left|A\right|e^{i\delta}\sim\sum_k\underbrace{C_k\left(\mu\right)}_{\text{pert. QCD}}\times\underbrace{\left\langle\bar{f}\right|Q_k\left(\mu\right)\left|\bar{B}\right\rangle}_{\text{non-pert.}} \quad (1.55)$$

It should be noted that this generic amplitudes for any hadronic two-body B decay can always be written in a way such that they contain at most two weak CKM amplitudes.

1.3 Direct $\mathcal{CP}$ asymmetries

Now, using Eqs. (1.54) we obtain the following $\mathcal{CP}$-violating asymmetry:

$$\mathcal{A}_{\mathcal{CP}}\equiv\frac{\Gamma\left(\bar{B}\to\bar{f}\right)-\Gamma\left(B\to f\right)}{\Gamma\left(\bar{B}\to\bar{f}\right)+\Gamma\left(B\to f\right)}=\frac{\left|A\left(\bar{B}\to\bar{f}\right)\right|^2-\left|A\left(B\to f\right)\right|^2}{\left|A\left(\bar{B}\to\bar{f}\right)\right|^2+\left|A\left(B\to f\right)\right|^2}= \\ =\frac{2\left|A_1\right|\left|A_2\right|\sin\left(\delta_1-\delta_2\right)\sin\left(\varphi_1-\varphi_2\right)}{\left|A_1\right|^2+2\left|A_1\right|\left|A_2\right|\cos\left(\delta_1-\delta_2\right)\cos\left(\varphi_1-\varphi_2\right)+\left|A_2\right|^2}. \quad (1.56)$$

A non vanishing $\mathcal{CP}$ asymmetry $\mathcal{A}_{\mathcal{CP}}$ arises from interference between the two weak amplitudes, and requires both a non-trivial weak phase difference $\varphi_1-\varphi_2$ and a non-trivial strong phase difference $\delta_1-\delta_2$. This kind of $\mathcal{CP}$ violation is referred to as "direct" $\mathcal{CP}$ violation, as it originates directly at the amplitude level of the considered decay. Since $\varphi_1-\varphi_2$ is in general given by one of the angles of the UT, the goal is to determine this quantity from the measured value of $\mathcal{A}_{\mathcal{CP}}$. Unfortunately, the extraction of $\varphi_1-\varphi_2$ from $\mathcal{A}_{\mathcal{CP}}$ is affected by hadronic uncertainties, arising from the strong amplitudes $\left|A_{1,2}\right|e^{i\delta 1,2}$.

A part from the most obvious - but most challenging - strategy of calculating the hadronic matrix elements using the theoretical tools listed at the end of Sec. 1.2.1, an experimental approach can be used to deal with their uncertainties. A widely used strategy consists in searching for fortunate cases, where relations between decay amplitudes of different channels allow one to eliminate hadronic matrix elements. This strategy has been widely used in the extraction of the γ angle of the UT from tree-level governed decays $B_u^{\pm}\to K^{\pm}\left\{D^0,\bar{D}^0,D_+^0\right\}$ [39], and $B_d\to K^{*0}\left\{D^0,\bar{D}^0,D_+^0\right\}$ [40] decays, where D_+^0 stands for the $\mathcal{CP}$-even eigenstate of the neutral D-meson system. Such strategy results to be very challenging from the experimental point of view as the corresponding CKM triangles are quite flattened. An alternative consists in deriving

amplitude relations using the flavor symmetries of strong interactions, *i.e.* $SU(2)$ and $SU(3)$. Thanks to this it is possible to eliminate all the uncertainties connected to factorization and the infinite mass limit. Use of isospin relations is based on the assumption of invariance of strong interactions under the quark-flavour exchange $u \leftrightarrow d$. Such assumptions, corroborated by the observation of almost degenerated mass-eigenstates of quarks u and d, has been proven to be valid to a few percent accuracy. It has been used for the extraction of the α angle of the UT from $B \to \pi\pi, \rho\pi, \pi K$ inclusive decays. However, the effectiveness of this approach is currently limited by the number of unknown isospin parameters. Even with a more complete experimental information, it would still be important to complement this strategy with information on amplitudes from $SU(3)$ or factorization. Otherwise, the possible presence of new physics effects may remain undetected in full fits of $SU(2)$ amplitudes [41]. Of particular interest for this thesis is the $SU(3)$ symmetry assumption. $SU(3)$-based amplitude relations come from an extension of the $SU(2)$ approach, including the invariance of strong interactions under the flavour exchange $d \leftrightarrow s$. Several strategies based on $SU(3)$ symmetry have been proposed to cancel out the hadronic uncertainties. Still, the limited number of currently precise measurements available makes it necessary to introduce additional dynamical assumptions to further reduce the number of hadronic parameters. These assumptions usually rely on the additional knowledge of the strong matrix elements from the factorization approach. In Sec. 1.6 a strategy to use $SU(3)$ symmetry to extract the γ angle from two-body charmless B decays, first proposed in [42], will be discussed.

1.4 Mixing of neutral B mesons

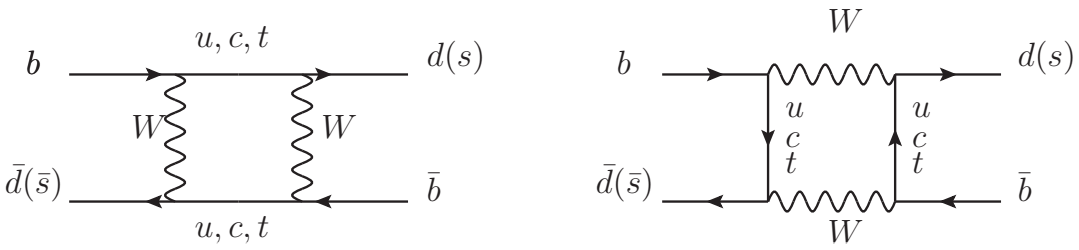

Figure 1.8: Box diagrams contributing to $\bar{B}^0 - B^0$ and $\bar{B}^0_s - B^0_s$ mixing.

$\mathcal{CP}$ violation for neutral B mesons is characterized by interference effects between $B^0_q - \bar{B}^0_q$ mixing and decay processes, the so called "mixing-induced" $\mathcal{CP}$ violation. Within the SM the phenomenon of neutral meson mixing arises from the box-diagrams shown in Fig 1.8. Because of this transitions, at any time t the B meson can be seen as a superpositions of states:

$$|B_q(t)\rangle = a(t)\left|B^0_q\right\rangle + b(t)\left|\bar{B}^0_q\right\rangle + c_1(t)\,|f_1\rangle + c_2(t)\,|f_2\rangle + c_3(t)\,|f_3\rangle \ldots \tag{1.57}$$

where the $\left|B^0_q\right\rangle$ and $\left|\bar{B}^0_q\right\rangle$ represent the particle and antiparticle state of the B^0_q meson; the f_i represent all possible final states where the mesons is allowed to decay into; $c_i(t)$ are the coefficients of each final state. In the case of a time range much larger than the typical strong interaction scale, we can make use of the so called Weisskopf-Wigner approximation, that allows

one to use a much simplified formalism [43]:

$$|\psi(t)\rangle = a(t)\,|B\rangle + b(t)\,\left|\bar{B}\right\rangle \tag{1.58}$$

with $|a(t)|^2 + |b(t)|^2 = 1$. The simplified time evolution is determined by a 2×2 effective Hamiltonian. Such Hamiltonian is not Hermitian, as otherwise mesons would not oscillate and not decay, but it can be expressed in terms of Hermitian matrices $\mathbf{M}$ and $\mathbf{\Gamma}$:

$$\mathbf{H} = \mathbf{M} - \frac{i}{2}\mathbf{\Gamma} = \begin{pmatrix} M & M_{12} \\ M_{12}^* & M \end{pmatrix} - \frac{i}{2}\begin{pmatrix} \Gamma & \Gamma_{12} \\ \Gamma_{12}^* & \Gamma \end{pmatrix}. \tag{1.59}$$

The diagonal elements of $\mathbf{H}$ are associated with flavour-conserving transitions, while off-diagonal elements are associated with flavour-changing transitions. The statement that diagonal elements of H are equal arises from the assumption of $\mathcal{CPT}$ invariance[1] [44]. The $\mathbf{M}$ matrix represents transitions via dispersive intermediate state ("off-shell" transitions), and $\mathbf{\Gamma}$ represents transitions via absorptive intermediate states ("on-shell" transition). The time evolution of a neutral B meson results to be described by a Schrödinger equation of the form:

$$i\frac{d}{dt}\begin{pmatrix} a(t) \\ b(t) \end{pmatrix} = \mathbf{H}\begin{pmatrix} a(t) \\ b(t) \end{pmatrix} \tag{1.60}$$

Solving the eigenvalue equation of $\mathbf{H}$ we obtain two eigenstates of well-defined masses $M_{H,L}$ and widths $\Gamma_{H,L}$:

$$\begin{aligned} |B_H\rangle &= \frac{p\,|B\rangle + q\,\left|\bar{B}\right\rangle}{\sqrt{|p|^2 + |q|^2}} \\ |B_L\rangle &= \frac{p\,|B\rangle - q\,\left|\bar{B}\right\rangle}{\sqrt{|p|^2 + |q|^2}}. \end{aligned} \tag{1.61}$$

The eigenvalues are:

$$\begin{aligned} \lambda_H &= M - \frac{i}{2}\Gamma + \frac{q}{p}\left(M_{12} - \frac{i}{2}\Gamma_{12}\right) \\ \lambda_L &= M - \frac{i}{2}\Gamma - \frac{q}{p}\left(M_{12} - \frac{i}{2}\Gamma_{12}\right), \end{aligned} \tag{1.62}$$

where

$$\left(\frac{q}{p}\right) = \sqrt{\frac{M_{12}^* - (i/2)\,\Gamma_{12}^*}{M_{12} - (i/2)\,\Gamma_{12}}}. \tag{1.63}$$

If we now assume a B meson generated in a pure particle state, *i.e.* $b(0) = 0$, and a $\bar{B}$ meson generated in a pure anti-particle state, *i.e.* $a(0) = 0$ we obtain, using Eq. (1.61), that their time evolution becomes:

$$\begin{aligned} |B(t)\rangle &= g_+(t)\,|B\rangle + \frac{q}{p}g_-(t)\,\left|\bar{B}\right\rangle \\ \left|\bar{B}(t)\right\rangle &= g_+(t)\,\left|\bar{B}\right\rangle + \frac{p}{q}g_-(t)\,|B\rangle \end{aligned} \tag{1.64}$$

[1] $\mathcal{T}$ represents the operator that changes the time flow direction ($t \to -t$).

where

$$g_+(t) = \left(\frac{e^{-i\lambda_H t} + e^{-i\lambda_L}}{2}\right), \qquad g_-(t) = \left(\frac{e^{-i\lambda_H t} - e^{-i\lambda_L}}{2}\right). \tag{1.65}$$

Consequently the decay rate to a final state f and its $\mathcal{CP}$ conjugate $\bar{f}$ are:

$$\begin{aligned}
\Gamma_{B\to f}(t) &= |A_f|^2 \cdot |g_+(t) + \lambda_f g_-(t)|^2 \\
\Gamma_{\bar{B}\to f}(t) &= |A_f|^2 \left|\frac{p}{q}\right|^2 \cdot |\lambda_f g_+(t) + g_-(t)|^2 \\
\Gamma_{\bar{B}\to \bar{f}}(t) &= \left|\bar{A}_{\bar{f}}\right|^2 \cdot \left|g_+(t) + \bar{\lambda}_{\bar{f}} g_-(t)\right|^2 \\
\Gamma_{B\to \bar{f}}(t) &= \left|\bar{A}_{\bar{f}}\right|^2 \left|\frac{q}{p}\right|^2 \cdot \left|\bar{\lambda}_{\bar{f}} g_+(t) + g_-(t)\right|^2
\end{aligned} \tag{1.66}$$

where:

$$\lambda_f = \frac{q}{p}\frac{\bar{A}_f}{A_f}, \qquad \bar{\lambda}_{\bar{f}} = \frac{p}{q}\frac{A_{\bar{f}}}{\bar{A}_{\bar{f}}} \tag{1.67}$$

are the $\mathcal{CP}$ violating parameters of the processes, and

$$\begin{aligned}
A_f &= A(B\to f) = \langle f|\,\mathcal{H}_{eff}\,|B\rangle, \qquad & \bar{A}_f &= A\left(\bar{B}\to f\right) = \langle f|\,\mathcal{H}_{eff}\,\left|\bar{B}\right\rangle \\
\bar{A}_{\bar{f}} &= A\left(\bar{B}\to \bar{f}\right) = \left\langle \bar{f}\right|\mathcal{H}_{eff}\,|\bar{B}\rangle, \qquad & A_{\bar{f}} &= A\left(B\to \bar{f}\right) = \left\langle \bar{f}\right|\mathcal{H}_{eff}\,|B\rangle
\end{aligned} \tag{1.68}$$

are the instantaneous decay amplitudes of B and $\bar{B}$ to final states f and $\bar{f}$.

1.4.1 Mixing parameters

Defining $M_{12} \equiv |M_{12}|\, e^{i\varphi_M}$ and $\Gamma_{12} \equiv |\Gamma_{12}|\, e^{i\varphi_\Gamma}$ we can write:

$$\begin{aligned}
\lambda_H - \lambda_L &= 2\sqrt{\left(M_{12} - \frac{i}{2}\Gamma_{12}\right)\left(M_{12}^* - \frac{i}{2}\Gamma_{12}^*\right)} \\
&= 2\,|M_{12}|\sqrt{1 - \frac{|\Gamma_{12}|^2}{4\,|M_{12}|^2} - i\frac{|\Gamma_{12}|}{|M_{12}|}\cos(\varphi_M - \varphi_\Gamma)}
\end{aligned} \tag{1.69}$$

From the evaluation of the absorptive part of the box-diagrams shown in Fig. 1.8, which are dominated by top-quark mediated transitions, we obtain [45]:

$$\frac{\Gamma_{12}}{M_{12}} \propto \frac{m_b^2}{m_t^2} = \mathcal{O}\left(10^{-3}\right). \tag{1.70}$$

In this way we can expand Eq. (1.69) in terms of $|\Gamma_{12}|\,/\,|M_{12}|$, neglecting second order term, as:

$$\lambda_H - \lambda_L \approx \underbrace{2\,|M_{12}|}_{\Delta M} - \frac{i}{2}\underbrace{\frac{|\Gamma_{12}|}{|M_{12}|}\cos(\varphi_M - \varphi_\Gamma)}_{\Delta\Gamma}. \tag{1.71}$$

In the end we can write:

$$\begin{aligned}
\lambda_H &= M + \frac{\Delta M}{2} - \frac{i}{2}\left(\Gamma + \frac{\Delta\Gamma}{2}\right) \\
\lambda_L &= M - \frac{\Delta M}{2} - \frac{i}{2}\left(\Gamma - \frac{\Delta\Gamma}{2}\right).
\end{aligned} \tag{1.72}$$

Now, inserting Eqs. (1.72) in Eqs. (1.66) we can write:

$$\begin{aligned}
\Gamma_{B\to f}(t) &= |A_f|^2 \left[I_+(t) + I_-(t)\right], \\
\Gamma_{\bar{B}\to f}(t) &= |A_f|^2 \left|\frac{p}{q}\right|^2 \left[I_+(t) - I_-(t)\right], \\
\Gamma_{\bar{B}\to \bar{f}}(t) &= \left|\bar{A}_{\bar{f}}\right|^2 \left[\bar{I}_+(t) + \bar{I}_-(t)\right], \\
\Gamma_{B\to \bar{f}}(t) &= \left|\bar{A}_{\bar{f}}\right|^2 \left|\frac{q}{p}\right|^2 \left[\bar{I}_+(t) - \bar{I}_-(t)\right],
\end{aligned} \tag{1.73}$$

where:

$$\begin{aligned}
I_+(t) &= \left(1 + |\lambda_f|^2\right)\cosh\left(\frac{\Delta\Gamma}{2}t\right) - 2\Re(\lambda_f)\sinh\left(\frac{\Delta\Gamma}{2}t\right), \\
I_-(t) &= \left(1 - |\lambda_f|^2\right)\cos(\Delta M t) - 2\Im(\lambda_f)\sin(\Delta M t), \\
\bar{I}_+(t) &= \left(1 + \left|\bar{\lambda}_{\bar{f}}\right|^2\right)\cosh\left(\frac{\Delta\Gamma}{2}t\right) - 2\Re\left(\bar{\lambda}_{\bar{f}}\right)\sinh\left(\frac{\Delta\Gamma}{2}t\right), \\
\bar{I}_-(t) &= \left(1 - \left|\bar{\lambda}_{\bar{f}}\right|^2\right)\cos(\Delta M t) - 2\Im\left(\bar{\lambda}_{\bar{f}}\right)\sin(\Delta M t).
\end{aligned} \tag{1.74}$$

1.4.2 $\mathcal{CP}$ violating parameters

The parameter p can be written as:

$$\frac{q}{p} = \sqrt{\frac{4|M_{12}|^2 e^{-2i\varphi_M} + |\Gamma_{12}|^2 e^{-2i\varphi_\Gamma}}{4|M_{12}|^2 + |\Gamma_{12}|^2 - 4|M_{12}||\Gamma_{12}|\sin(\varphi_M - \varphi_\Gamma)}}, \tag{1.75}$$

and using the same approximation as in (1.70):

$$\frac{q}{p} = \sqrt{1 + \frac{|\Gamma_{12}|}{|M_{12}|}\sin(\varphi_M - \varphi_\Gamma)e^{-i(\varphi_M)}} \approx e^{-i\varphi_M}, \tag{1.76}$$

Calculating the dispersive part of the box-diagrams shown in Fig. 1.8 one has [45]:

$$M_{12} \propto \left(V_{tq}^* V_{tb}\right)^2 e^{i(\pi - \varphi_B)} \tag{1.77}$$

and thus

$$\frac{q}{p} = e^{-i\left(\pi + 2\arg\left(V_{tq}^* V_{tb}\right) - \varphi_B\right)}. \tag{1.78}$$

About the istantaneous decay amplitudes in Eqs. (1.84) we can write:

$$\begin{aligned}
\bar{A}_f &= \langle f|\,\mathcal{H}_{eff}\,|\bar{B}\rangle = \\
&= \langle f|\,\frac{G_F}{\sqrt{2}}\left\{\sum_{j=u,c} V_{jr}^* V_{jb}\left[\sum_{k=1}^{2} C_k(\mu)\,Q_k^{jr}(\mu) + \sum_{k=3}^{10} C_k(\mu)\,Q_k^{r}(\mu)\right]\right\}|\bar{B}\rangle
\end{aligned} \tag{1.79}$$

and, applying the same condition of Eqs. (1.52),

$$A_{\bar{f}} = e^{i(\varphi_B - \varphi_f)} \times \\ \times \left\langle \bar{f} \right| \frac{G_F}{\sqrt{2}} \left\{ \sum_{j=u,c} V_{jr} V_{jb}^* \left[\sum_{k=1}^{2} C_k(\mu) Q_k^{jr}(\mu) + \sum_{k=3}^{10} C_k(\mu) Q_k^r(\mu) \right] \right\} \left| \bar{B} \right\rangle . \tag{1.80}$$

Of particular interest is the case where the final state is a $\mathcal{CP}$ eigenstate, yielding to $\left\langle \bar{f} \right| = \langle f|$ and $\varphi_f \in \{0, \pi\}$. Consequently, $A_{\bar{f}} = \pm A_f$ and the ratio between the two instantaneous decay amplitudes $\bar{A}_f$ and A_f results to be:

$$\frac{\bar{A}_f}{A_f} = \pm e^{i\varphi_B} \left[\frac{\sum_{j=u,c} V_{jr}^* V_{jb} \langle f| \mathcal{Q}^{jr} \left| \bar{B} \right\rangle}{\sum_{j=u,c} V_{jr} V_{jb}^* \langle f| \mathcal{Q}^{jr} \left| \bar{B} \right\rangle} \right], \tag{1.81}$$

where:

$$\mathcal{Q}^{jr} \equiv \sum_{k=1}^{2} C_k(\mu) Q_k^{jr} + \sum_{k=3}^{10} C_k(\mu) Q_k^r. \tag{1.82}$$

In general the amplitude ratio (1.81) suffers from large hadronic uncertainties, introduced by the hadronic matrix elements. However, if the decay of interest is dominated by a single CKM amplitude, we can write:

$$\begin{cases} \bar{A}_f = e^{i\varphi_{CKM}} \left(|A_{strong}| e^{i\delta} \right) \\ A_f = e^{i\varphi_B} e^{-i\varphi_{CKM}} \left(|A_{strong}| e^{i\delta} \right) \end{cases} \Rightarrow \frac{\bar{A}_f}{A_f} = e^{-i\varphi_B} e^{2i\varphi_{CKM}} \tag{1.83}$$

where A_{strong} and δ are the strong amplitude and the $\mathcal{CP}$ conserving phase respectively, and $\varphi_{CKM} = \arg\left(V_{jr}^* V_{jb} \right)$. In the end, from Eqs. (1.78) and (1.83) we can compute the $\mathcal{CP}$ violating parameter λ_f:

$$\lambda_f = \mp e^{-2i(\varphi_q - \varphi_{CKM})}. \tag{1.84}$$

1.4.3 Time-dependent $\mathcal{CP}$ asymmetry

Continuing to consider the particular case where $f = \bar{f}$, if we use the first two decay rates in Eqs. (1.73) to write a $\mathcal{CP}$ asymmetry, we obtain:

$$\begin{aligned} \mathcal{A}_{\mathcal{CP}}(t) &= \frac{\Gamma_{\bar{B} \to f}(t) - \Gamma_{B \to f}(t)}{\Gamma_{\bar{B} \to f}(t) + \Gamma_{B \to f}(t)} \\ &= \frac{\left(|\lambda_f|^2 - 1 \right) \cos(\Delta M t) + 2\Im(\lambda_f) \sin(\Delta M t)}{\left(|\lambda_f|^2 + 1 \right) \cosh\left(\frac{\Delta\Gamma}{2} t \right) - 2\Re(\lambda_f) \sinh\left(\frac{\Delta\Gamma}{2} t \right)} \\ &= \frac{\mathcal{A}^{dir} \cos(\Delta M t) + \mathcal{A}^{mix} \sin(\Delta M t)}{\cosh\left(\frac{\Delta\Gamma}{2} t \right) - \mathcal{A}^{\Delta\Gamma} \sinh\left(\frac{\Delta\Gamma}{2} t \right)} \end{aligned} \tag{1.85}$$

where we made use of $|q/p| \approx 1$ and we defined:

$$\mathcal{A}^{dir} = \frac{|\lambda_f|^2 - 1}{|\lambda_f|^2 + 1}, \quad \mathcal{A}^{mix} = \frac{2\Im(\lambda_f)}{|\lambda_f|^2 + 1}, \quad \mathcal{A}^{\Delta\Gamma} = \frac{2\Re(\lambda_f)}{|\lambda_f|^2 + 1}. \tag{1.86}$$

The three quantities satisfy the relation:

$$\left|\mathcal{A}^{dir}\right|^2 + \left|\mathcal{A}^{mix}\right|^2 + \left|\mathcal{A}^{\Delta\Gamma}\right|^2 = 1. \tag{1.87}$$

$\mathcal{A}^{dir}$ is analog of the direct $\mathcal{CP}$ asymmetry in Eq. (1.56). In the case of $\mathcal{A}^{dir} \neq 0$ we can speak of $\mathcal{CP}$ violation in the decay process. It should be noted that with the assumption used in Eq. (1.83), the strong phases entering the decay amplitudes $\bar{A}_f$ and A_f can be simplified, yielding $\mathcal{A}^{dir} = 0$. $\mathcal{A}^{mix}$ relies on the phase of the $\mathcal{CP}$ violating parameter λ_f. If it differs from zero it means that we have the so called "mixing-induced" $\mathcal{CP}$ violation, arising from the interference between $B - \bar{B}$ mixing and decay processes. Again, in the case of a single dominant phase in the amplitudes, the direct $\mathcal{CP}$ asymmetry cancels and the determination of A^{mix} allows one to extract the $\mathcal{CP}$ violating phase $\varphi_q - \varphi_{CKM}$. In addition, considering the case where $\Delta\Gamma = 0$ the time dependent $\mathcal{CP}$ asymmetry $\mathcal{A}_{\mathcal{CP}}$ satisfies:

$$\mathcal{A}_{\mathcal{CP}}(t)|_{\Delta\Gamma=0} = \pm \sin(\varphi_q - \varphi_{CKM}) \sin(\Delta M t) \tag{1.88}$$

1.5 Phenomenology of charmless two-body B decays

The family of charmless two-body B decays comprises several modes, providing many different ways for testing the SM picture of $\mathcal{CP}$ violation. In the studies presented in this thesis, we will take into account 8 channels (not counting the $\mathcal{CP}$-conjugate ones): $B^0 \to \pi^+\pi^-$, $B^0 \to K^+\pi^-$, $B^0 \to K^+K^-$, $B_s^0 \to K^+K^-$, $B_s^0 \to \pi^+K^-$, $B_s^0 \to \pi^+\pi^-$, $\Lambda_b \to p\pi^-$ and $\Lambda_b \to pK^-$. For each of these channels, relevant observables include branching ratios, charge CP asymmetries and, in the case of neutral B mesons, time dependent CP asymmetries. These channels, referred to as $B \to h^+h'^-$, have been extensively studied at the B factories [2, 46, 47, 54] and the Tevatron [3, 4, 48–53].

The theoretical framework used to extract CKM related quantities from these decays is the same discussed in previous sections. In contrast to the case of other theoretically clean measurements of $\mathcal{CP}$ violation in the B sector, a simple interpretation of the $\mathcal{CP}$ violating observables of the charmless two-body B decays in terms of CKM phases is not possible. This because of sizeable QCD ($b \to d(s)+g$ transitions) and EW ($b \to d(s)+\gamma, Z^0$ transitions) penguin constribution, in addition to the simple $b \to u+W^+$ tree-level transition. Such penguin pollution poses several problems for a clean measurement of CKM phases using these decays, arising from hadronic matrix elements. On the other hand, the presence of loops inside the penguin diagrams has interesting implications, since they could be affected by sizable contributions from NP.

One promising way to exploit the presence of penguins for these decays, as a powerful resource rather than a limitation, was first suggested in 1999 in [42], and recentrly revisited in [55]. The strategy consists in combining the measurement of the $B^0 \to \pi^+\pi^-$ and $B_s^0 \to K^+K^-$ time-dependent $\mathcal{CP}$ asymmetries. Assuming of invariance of the strong interaction dynamics under the exchange of the $d \leftrightarrow s$ quarks ($U-spin$ symmetry) in the decay graphs of these modes, it is possible to eliminate the hadronic matrix elements entering the time-dependent $\mathcal{CP}$ asymmetries. Once the QCD effects will be ruled out with this strategy, the determination of the angle $\gamma = \arg(V_{ub}^*)$ will be possible, without the need of any dynamical assumption typical of hadronic matrix elements calculation. Due to the possible presence of new particles in the penguin loops, a measurement of γ with these decays could differ appreciably from the one determined by using other B decays governed by pure tree amplitudes [56].

1.5.1 $B^0_{(s)} \to h^+h'^-$ decays amplitudes

The SM topologies responsible of charmless two-body $B_{d,s}$ mesons decays are depicted in Fig. 1.9, and the ones contributing to each decay mode are summarized in Tab. 1.3.

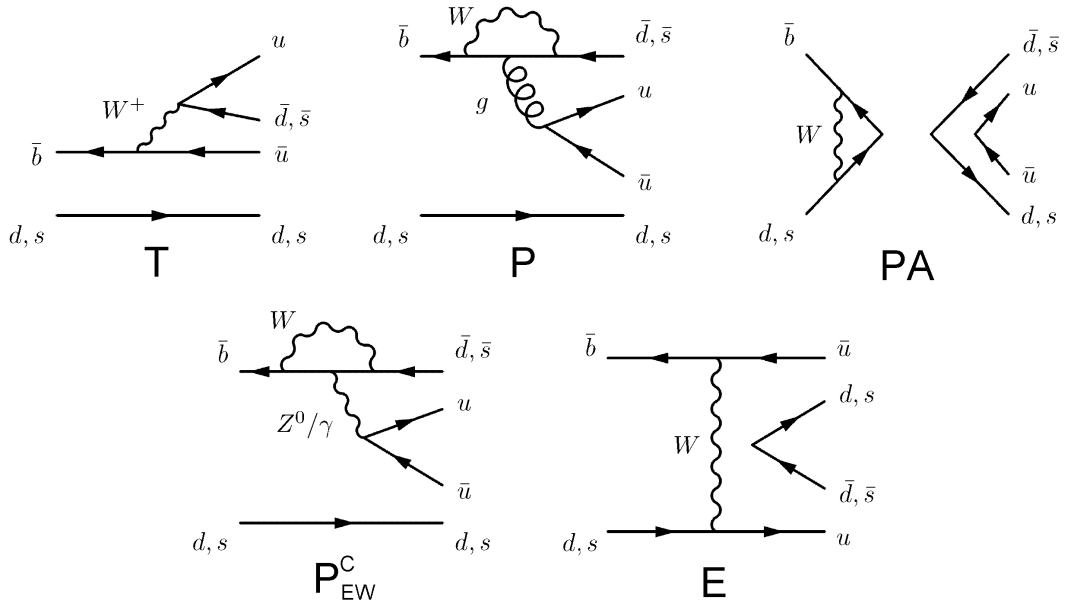

Figure 1.9: Diagrams contributing to the amplitudes of charmless $B^0_{(s)}$ decays to two charged mesons: Tree (T), Penguin (P), Penguin Annihilation (PA), Colour-suppressed Electroweak Penguin (P^C_{EW}) and Exchange (E).

Decay	Topology contributions
$B^0 \to \pi^+\pi^-$	T, P, P^C_{EQ}, PA, E
$B^0 \to K^+\pi^-$	T, P, P^C_{EQ}
$B^0_s \to K^+K^-$	T, P, P^C_{EQ}, PA, E
$B^0_s \to \pi^+K^-$	T, P, P^C_{EQ}
$B^0 \to K^+K^-$	PA, E
$B^0_s \to \pi^+\pi^-$	PA, E

Table 1.3: Diagrams contributing to the amplitudes of each charmless $B^0_{(s)}$ decay to two charged mesons. See the caption of Fig. 1.9 for the definitions.

It is useful to show the following relations among the various decay channels:

$$\underbrace{B^0 \to \pi^+\pi^-}_{T+P+\frac{2}{3}P^C_{EW}+PA+E} \qquad d \longleftrightarrow s \qquad \underbrace{B^0_s \to K^+K^-}_{T+P+\frac{2}{3}P^C_{EW}+PA+E} \tag{1.89}$$

$$\underbrace{B^0 \to K^+\pi^-}_{T+P+\frac{2}{3}P^C_{EW}} \qquad d \longleftrightarrow s \qquad \underbrace{B^0_s \to \pi^+K^-}_{T+P+\frac{2}{3}P^C_{EW}} \tag{1.90}$$

$$\underbrace{B^0 \to K^+\pi^-}_{T+P+\frac{2}{3}P^C_{EW}} \qquad d \overset{\text{spect.}}{\longleftrightarrow} s \qquad \underbrace{B^0_s \to K^+K^-}_{T+P+\frac{2}{3}P^C_{EW}+PA+E} \tag{1.91}$$

$$\underbrace{B^0 \to \pi^+\pi^-}_{T+P+\frac{2}{3}P^C_{EW}+PA+E} \qquad d \overset{\text{spect.}}{\longleftrightarrow} s \qquad \underbrace{B^0_s \to \pi^+K^-}_{T+P+\frac{2}{3}P^C_{EW}} \tag{1.92}$$

where we emphasized the diagrams contributing to the transitions and how the channels are interconnected by $SU(3)$ symmetry. With the label "spect." it is meant that the two considered transitions differ just for the valence quarks of the B mesons that do not participate to the weak processes governing the decay (spectator quarks).

Notably, $B^0 \to \pi^+\pi^-$ and $B^0_s \to \pi^+K^-$ differ by the interchange of the spectator quarks, which in the former case is a d while in the latter is a s. For this reason, their strong interaction dynamics are connected by the $U-$spin symmetry. However, $U-$spin symmetry is not fully satisfied, because the diagrams refferred to as PA and E contribute to the $B^0 \to \pi^+\pi^-$ decay but not to the $B^0_s \to \pi^+K^-$ decay. In any case such contributions are expected to be small and their size can be probed by means of $B^0 \to K^+K^-$ and $B^0_s \to \pi^+\pi^-$ decays, which proceed only through PA and E topologies. Analogous considerations should be performed for the $B^0_s \to K^+K^-$ and $B^0 \to K^+\pi^-$ decays. On the other hand, both $B^0 \to \pi^+\pi^-$ and $B^0_s \to K^+K^-$, as well as $B^0 \to K^+\pi^-$ and $B^0_s \to \pi^+K^-$ decays are fully $U-$spin symmetric: no dynamical assumptions that some topologies do not contribute significantly, as in the previous cases, are needed.

1.5.1.1 $B^0 \to \pi^+\pi^-$

The decay $B^0 \to \pi^+\pi^-$ originates from $\bar{b} \to \bar{u}u\bar{d}$ quark-level transitions, as emphasized Fig. 1.9. Using the formalism introduced in Sec. 1.2.2 the decay amplitude can be written as:

$$A\left(B^0 \to \pi^+\pi^-\right) = \lambda_u^{(d)}\left(A_T^u + A_P^u\right) + \lambda_c^{(d)}A_P^c + \lambda_t^{(d)}A_P^t \tag{1.93}$$

where A_T^u represents the amplitude due to tree-level processes, while A_P^j represent the amplitudes due to QCD and electroweak penguin topologies with internal j quarks ($j \in \{u, c, t\}$). The quantities $\lambda_j^{(d)}$ are the usual CKM factors $\lambda_j^{(d)} \equiv V_{jd}V_{jb}^*$. If we make use of the unitarity of CKM matrix and of the generalized Wolfenstein parameterization of Eqs. (1.15), we obtain:

$$A\left(B^0 \to \pi^+\pi^-\right) = \left(1 - \frac{\lambda^2}{2}\right)\mathcal{C}\left[e^{i\gamma} - de^{i\theta}\right] \tag{1.94}$$

where

$$\mathcal{C} \equiv \lambda^3 A R_b\left(A_T^u + A_P^u - A_P^t\right) \tag{1.95}$$

$\times 10^{-6}$	BaBar	Belle	CLEO	CDF	World Average
$\mathcal{B}\left(B^0 \to \pi^+\pi^-\right)$	$5.5 \pm 0.4 \pm 0.3$	$5.1 \pm 0.2 \pm 0.2$	$4.5^{+1.4+0.5}_{-1.2-0.4}$	$5.10 \pm 0.33 \pm 0.36$	5.16 ± 0.22
$\mathcal{B}\left(B^0 \to K^+\pi^-\right)$	$19.1 \pm 0.6 \pm 0.6$	$19.9 \pm 0.4 \pm 0.8$	$18.0^{+2.3+1.2}_{-2.1-0.9}$	–	19.4 ± 0.06
$\mathcal{B}\left(B^0 \to K^+K^-\right)$	$0.04 \pm 0.15 \pm 0.08$	$0.09^{+0.18}_{-0.13} \pm 0.01$	< 0.8	$0.23 \pm 0.10 \pm 0.10$	$0.15^{+0.11}_{-0.10}$
$\mathcal{B}\left(B_s^0 \to K^+K^-\right)$	–	$38^{+10}_{-9} \pm 7$	–	$24.4 \pm 1.4 \pm 4.6$	26.5 ± 4.4
$\mathcal{B}\left(B_s^0 \to \pi^+K^-\right)$	–	< 26	$5.0 \pm 0.7 \pm 0.8$	–	5.0 ± 1.1
$\mathcal{B}\left(B_s^0 \to \pi^+\pi^-\right)$	–	< 12	–	$0.57 \pm 0.15 \pm 0.10$	–
$\mathcal{B}\left(\Lambda_b \to p\pi^-\right)$	–	–	–	$3.1 \pm 0.6 \pm 0.7$	–
$\mathcal{B}\left(\Lambda_b \to pK^-\right)$	–	–	–	$5.0 \pm 0.7 \pm 1.0$	–

Table 1.4: Measurements of the branching fractions of all the charmless two-body B hadron decays in units of 10^{-6} [4, 49, 58, 59].

and

$$de^{i\theta} \equiv \frac{1}{(1-\lambda^2/2)\,R_b}\left(\frac{A_P^c - A_P^t}{A_T^u + A_P^u - A_P^t}\right) \tag{1.96}$$

The quantities A, λ, R_b and γ are those defined in Secs. 1.1.3 and 1.1.4. As a consequence, the $\mathcal{CP}$ violating parameter λ_f defined in Eq. (1.67) becomes:

$$\lambda_f = -e^{-2i\beta}\left[\frac{e^{i\gamma} - de^{i\theta}}{e^{-i\gamma} - de^{i\theta}}\right] \tag{1.97}$$

Inserting Eq. (1.97) into Eqs. (1.86) we obtain

$$\begin{aligned}
\mathcal{A}_{\pi\pi}^{dir} &= -\left[\frac{2d\sin\theta\sin\gamma}{1 - 2d\cos\theta\cos\gamma + d^2}\right] \\
\mathcal{A}_{\pi\pi}^{mix} &= \left[\frac{\sin(2\beta+2\gamma) - 2d\cos\theta\sin(2\beta+\gamma) + d^2\sin 2\beta}{1 - 2d\cos\theta\cos\gamma + d^2}\right]
\end{aligned} \tag{1.98}$$

where β denotes the $B^0 - \bar{B}^0$ mixing phase. The quantity $\mathcal{A}^{\Delta\Gamma}$ have been considered 0 as $\Delta\Gamma_d$ results to be small [21]. From Eqs. (1.98) one has that the $\mathcal{CP}$ violating observables $\mathcal{A}_{\pi\pi}^{dir}$ and $\mathcal{A}_{\pi\pi}^{mix}$ depend on the quantities d, θ, γ and β.

The branching fraction of the $B^0 \to \pi^+\pi^-$ mode was measured by different experiments and the values are reported in Tab. 1.4. B-Factories also provided a measurement of time-dependent $\mathcal{CP}$ asymmetries, and the current values are [2, 47]:

$$\mathcal{A}_{\pi\pi}^{dir} = \begin{cases} 0.25 \pm 0.08 \pm 0.02 & \text{BaBar} \\ 0.55 \pm 0.08 \pm 0.05 & \text{Belle} \end{cases} \tag{1.99}$$

$$\mathcal{A}_{\pi\pi}^{mix} = \begin{cases} -0.68 \pm 0.10 \pm 0.03 & \text{BaBar} \\ -0.61 \pm 0.10 \pm 0.04 & \text{Belle} \end{cases} \tag{1.100}$$

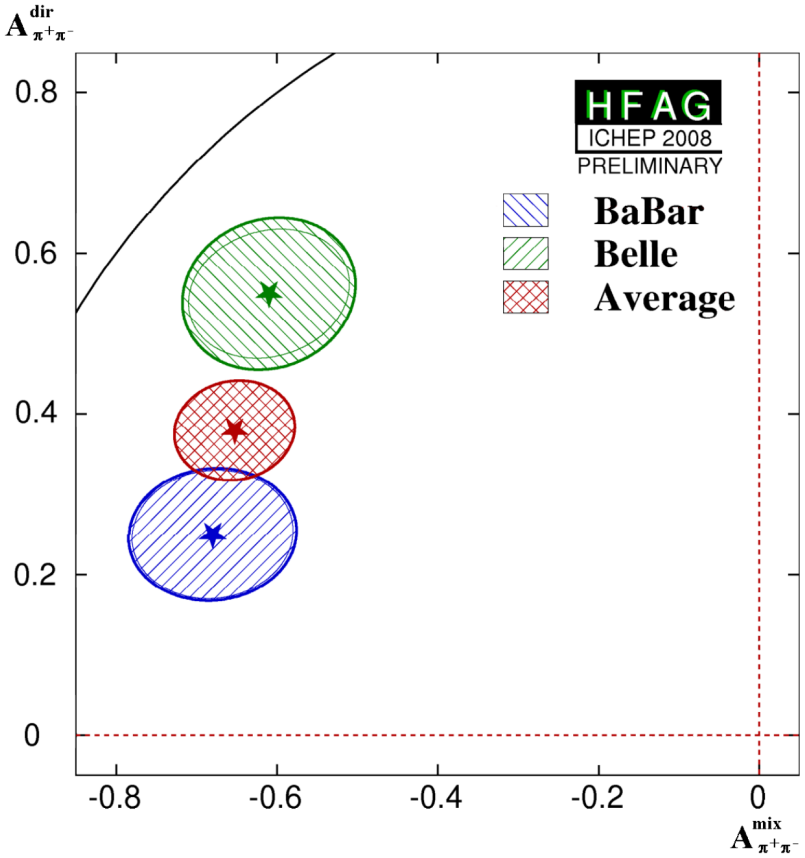

Figure 1.10: Representation of the measurements of the direct and mixing-induced $\mathcal{CP}$ violating asymmetries for the $B^0 \to \pi^+\pi^-$ decay, performed by BaBar [2] and Belle [47]. The contours correspond to the 60.7% C.L. regions.

The results from the B-Factories for $\mathcal{A}^{mix}_{\pi\pi}$ are fully consistent, whereas for $\mathcal{A}^{dir}$ there is some discrepancy, as also shown in Fig. 1.10. For this reason a third measurement of the time-dependent $\mathcal{CP}$ asymmetries of the $B^0 \to \pi^+\pi^-$ would be desirable.

1.5.1.2 $B^0 \to K^+\pi^-$

The $B^0 \to K^+\pi^-$ decay channel receives contributions both from tree and from penguin topologies depicted in Fig. 1.9, but not from PA and E topologies. Within the usual formalism and exploiting the CKM matrix unitarity, the decay amplitude of this channel can be written as:

$$A\left(B^0 \to K^+\pi^-\right) = -P\left[1 - re^{i\delta}e^{i\gamma}\right] \tag{1.101}$$

Where P describes the penguin amplitudes, r describes the amplitude ratios between tree and penguin amplitudes, and δ is the $\mathcal{CP}$ conserving hadronic phase.

The quark level transitions responsible of tree amplitudes are $\bar{b} \to \bar{u}u\bar{s}$, and contain a CKM factor $V^*_{ub}V_{us}$. On the other hand penguin amplitudes, dominated by a loop diagram with virtual

top quark, contain a CKM factor $V_{tb}^* V_{ts}$. Consequently, because of the ratio $V_{ub}^* V_{us} / V_{tb}^* V_{ts} \approx 0.02$, QCD penguin amplitudes are expected to dominate the decay process. EW penguin topologies can contribute to the amplitude only in the color-suppressed mode, thus are expected to play a minor rôle. The present measurements of the $B^0 \to K^+\pi^-$ branching ratio are reported in Tab. 1.4. As $B^0 \to K^+\pi^-$ is a flavour specific decay the instantaneous amplitude $A_{\bar{f}} \equiv A\left(B^0 \to K^-\pi^+\right)$ and $\bar{A}_f \equiv A\left(\bar{B}^0 \to K^+\pi^-\right)$ are zero. As a consequence the $\mathcal{CP}$ violating parameters in Eqs. (1.67) satisfy the relation $\lambda_f = \bar{\lambda}_{\bar{f}} = 0$. Consequently the decay rates are:

$$\begin{aligned}
\Gamma_{B^0\to K^+\pi^-}(t) &= |A_f|^2 \left[\cosh\left(\frac{\Delta\Gamma}{2}t\right) + \cos(\Delta M t)\right], \\
\Gamma_{B^0\to K^-\pi^+}(t) &= \left|\bar{A}_{\bar{f}}\right|^2 \left[\cosh\left(\frac{\Delta\Gamma}{2}t\right) - \cos(\Delta M t)\right], \\
\Gamma_{\bar{B}^0\to K^+\pi^-}(t) &= |A_f|^2 \left[\cosh\left(\frac{\Delta\Gamma}{2}t\right) - \cos(\Delta M t)\right], \\
\Gamma_{\bar{B}^0\to K^-\pi^+}(t) &= \left|\bar{A}_{\bar{f}}\right|^2 \left[\cosh\left(\frac{\Delta\Gamma}{2}t\right) + \cos(\Delta M t)\right].
\end{aligned} \tag{1.102}$$

If we define the time dependet asymmetry as in Eq. (1.85) we obtain a quantity independent of time:

$$\begin{aligned}
\mathcal{A}_{K^+\pi^-}^{\mathcal{CP}} &= \frac{\left[\Gamma_{B^0\to K^-\pi^+}(t) + \Gamma_{\bar{B}^0\to K^-\pi^+}(t)\right] - \left[\Gamma_{\bar{B}^0\to K^+\pi^-}(t) + \Gamma_{B^0\to K^+\pi^-}(t)\right]}{\left[\Gamma_{B^0\to K^-\pi^+}(t) + \Gamma_{\bar{B}^0\to K^-\pi^+}(t)\right] + \left[\Gamma_{\bar{B}^0\to K^+\pi^-}(t) + \Gamma_{B^0\to K^+\pi^-}(t)\right]} \\
&= \frac{\left|\bar{A}_{\bar{f}}\right|^2 - |A_f|^2}{\left|\bar{A}_{\bar{f}}\right|^2 + |A_f|^2} = \frac{2r\sin(\delta)\sin(\gamma)}{1 + 2r\cos(\delta)\cos(\gamma) + r^2}
\end{aligned} \tag{1.103}$$

which is analogous to Eq. (1.56). It is important to note that $\mathcal{A}_{K^+\pi^-}^{\mathcal{CP}}$ is a function of the γ angle of the UT and of the hadronic parameters r and δ. Thus the direct $\mathcal{CP}$ asymmetry of $B^0 \to K^+\pi^-$ contains informations about the γ angle. The current measurements of the direct $\mathcal{CP}$ asymmetry are reported in Tab. 1.5.

	BaBar	Belle	CLEO	CDF	World Average
$\mathcal{A}_{\mathcal{CP}}\left(B^0 \to K^+\pi^-\right)$	$-0.107 \pm 0.016^{+0.006}_{-0.004}$	$-0.094 \pm 0.018 \pm 0.008$	$-0.04 \pm 0.16 \pm 0.02$	$-0.086 \pm 0.023 \pm 0.009$	$-0.098^{+0.012}_{-0.011}$
$\mathcal{A}_{\mathcal{CP}}\left(B_s^0 \to \pi^+K^-\right)$	–	–	–	$0.39 \pm 0.15 \pm 0.08$	0.38 ± 0.17

Table 1.5: Current measurements of the direct $\mathcal{CP}$ asymmetries of the $B^0 \to K^+\pi^-$ and $B_s^0 \to \pi^+K^-$ decays as measured by Babar [2], Belle [54], CLEO [84] and CDF [48, 52] experiments. The average of the results is performed by HFAG [60].

1.5.1.3 $B_s^0 \to K^+K^-$

The decay $B_s^0 \to K^+K^-$ is the fully U-spin counterpart of $B^0 \to \pi^+\pi^-$, *i.e.* in order to get the decay diagrams for this decay one have to substitute any d quark with an s quark in the

$B^0 \to \pi^+\pi^-$ decay diagrams. On the other hand, just changing the s spectator quark of this decay with a d quark we obtain the $B^0 \to K^+\pi^-$ decay. Thus, also $B^0 \to K^+\pi^-$ results to be U-spin related to $B_s^0 \to K^+K^-$, but only in the case of small contributions from penguin annihilation (PA) and exchange (E) topologies depicted in Fig. 1.9.

Because of the different CKM factors entering the diagrams in the $B_s^0 \to K^+K^-$ decay, the penguin processes are dominant. In analogy to Eq. (1.94) we can write:

$$A\left(B_s^0 \to K^+K^-\right) = \lambda\mathcal{C}'\left[e^{i\gamma} + \frac{1}{\varepsilon}d'e^{i\theta'}\right] \tag{1.104}$$

where $\varepsilon \equiv \lambda^2/\left(1-\lambda^2/2\right)$; $\mathcal{C}'$, d' and θ' are the counterpart of $\mathcal{C}$, d and θ in the case of $B^0 \to \pi^+\pi^-$. Calculating the time-dependent $\mathcal{CP}$ asymmetry terms, we obtain:

$$\begin{aligned}
\mathcal{A}_{KK}^{dir} &= -\left[\frac{2d'\sin\theta'\sin\gamma}{1-2d'\cos\theta'\cos\gamma+d'^2}\right],\\
\mathcal{A}_{KK}^{mix} &= +\left[\frac{\sin\left(2\beta_s+2\gamma\right)-2d'\cos\theta'\sin\left(2\beta_s+\gamma\right)+d'^2\sin 2\beta_s}{1-2d'\cos\theta'\cos\gamma+d'^2}\right],\\
\mathcal{A}_{\Delta\Gamma}^{KK} &= -\left[\frac{d'^2\sin 2\beta_s+2\varepsilon d'\cos\theta'\cos\left(2\beta_s+\gamma\right)+\varepsilon^2\cos\left(2\beta_s+2\gamma\right)}{d'^2+2\varepsilon d'\cos\theta'\cos\gamma+\varepsilon^2 d'^2}\right].
\end{aligned} \tag{1.105}$$

In analogy to the case of the $B^0 \to \pi^+\pi^-$ decay the observables $\mathcal{A}_{KK}^{dir}$ and $\mathcal{A}_{KK}^{mix}$ results to be functions of d', θ', β_s and γ. For this decay only the branching ratio is experimentally known as reported in Tab. 1.4. It is worth noting that the lifetime of this decay measured by CDF [61] and LHCb [62]:

$$\tau_{KK} = \begin{cases} 1.53 \pm 0.18 \pm 0.02 \quad \text{ps} & \text{CDF} \\ 1.440 \pm 0.096 \pm 0.010 \quad \text{ps} & \text{LHCb} \end{cases} \tag{1.106}$$

can be used as a constraint for β_s [55].

1.5.1.4 $B_s^0 \to \pi^+K^-$

The $B_s^0 \to \pi^+K^-$ is the fully U-spin counterpart of $B^0 \to K^+\pi^-$, and is the "spectator" U-spin counterpart of $B^0 \to \pi^+\pi^-$. Within the usual formalism and exploiting the CKM matrix unitarity, the decay amplitude of this channel can be written as:

$$A\left(B_s^0 \to \pi^+K^-\right) = P_s\sqrt{\varepsilon}\left[1 + \frac{1}{\varepsilon}r_s e^{i\delta_s}e^{i\gamma}\right]. \tag{1.107}$$

As this channel is a "flavour specific" decay, the same considerations on its time-evolution which are valid for the $B^0 \to K^+\pi^-$ decay also hold in this case. Consequently for the direct $\mathcal{CP}$ asymmetry we have:

$$\mathcal{A}_{\mathcal{CP}} = \frac{2r_s\sin\left(\delta_s\right)\sin\left(\gamma\right)}{1+2r_s\cos\left(\delta_s\right)\cos\left(\gamma\right)+r_s^2} \tag{1.108}$$

Only the CDF experiment has performed measurements with this channel. They are reported in Tab. 1.4 (branching ratio) and Tab. 1.5 (direct $\mathcal{CP}$ asymmetry).

1.5.1.5 $B^0 \to K^+K^-$ and $B_s^0 \to \pi^+\pi^-$

Within the SM the amplitudes of these decays are governed by PA and E topologies shown in Fig. 1.9. The first evidence of the $B_s^0 \to \pi^+\pi^-$ decay has been obtained by CDF [3], and the corresponding branching ratio is reported in Tab. 1.4.

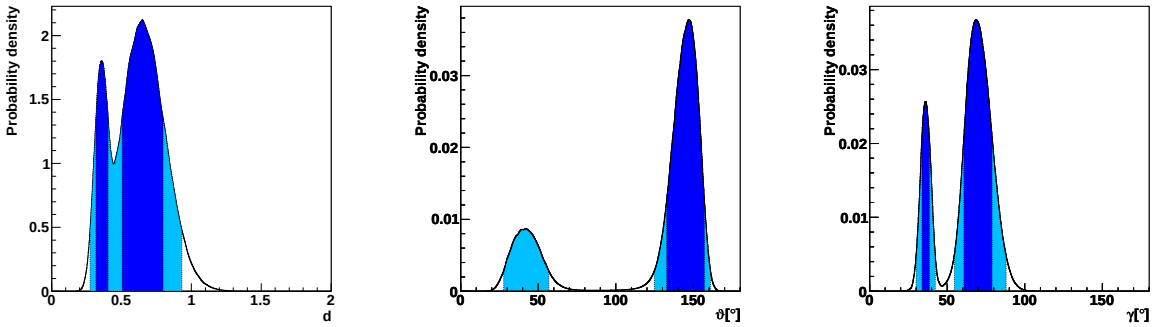

Figure 1.11: From left to right: p.d.f.'s for d, ϑ and γ obtained by using the current experimental measurements. 68% (dark) and 95% (light) probability intervals are also indicated.

1.6 Angle γ from present $B^0 \to h^+h'^-$ measurements

As we have seen the direct and mixing-induced $\mathcal{CP}$ coefficients $\mathcal{A}^{dir}_{\pi^+\pi^-}$ and $\mathcal{A}^{mix}_{\pi^+\pi^-}$ are experimentally known, while $\mathcal{A}^{dir}_{K^+K^-}$ and $\mathcal{A}^{mix}_{K^+K^-}$ are still unmeasured. Employing the U-spin symmetry, the value of $\mathcal{A}^{dir}_{K^+K^-}$ can be estimated to be equal to that of $\mathcal{A}^{\mathcal{CP}}_{K^+\pi^-}$, which is already well measured. This requires that penguin annihilation and exchange topologies do not give significant contributions to the decay amplitudes, a fact that can be eventually probed by measuring the branching fractions of the $B^0 \to K^+K^-$ and $B^0_s \to \pi^+\pi^-$ decays [42]. In this case we have a closed system of three equations and three unknowns. It is then possible to determine d, ϑ and γ by using the currently available measurements.

In order to infer a joint p.d.f. for d, ϑ and γ we will make use of a Bayesian approach implemented in the software packages developed by the UTfit Collaboration [23, 24]. The problem is in fact analogous to the one of inferring a p.d.f. for the CKM parameters $\bar{\rho}$ and $\bar{\eta}$, given a set of measurements and theoretical predictions related to them by analytical constraints. We do not need to rely on the full validity of the U-spin symmetry, and so we allow for a non-factorizable breaking of the U-spin relations $d = d'$ and $\vartheta = \vartheta'$ of up to 20% and $\pm 20°$ respectively, similar to what is done in Ref. [55], i.e. $\hat{\xi}$ and $\Delta\vartheta$ are varied uniformly in the ranges:

$$\hat{\xi} = d'/d \in [0.8,\, 1.2], \tag{1.109}$$

and

$$\Delta\vartheta = \vartheta' - \vartheta \in [-20°,\, 20°]. \tag{1.110}$$

By integrating out two variables in turn from the joint p.d.f. we obtain the one dimensional p.d.f.'s for d, ϑ and γ shown in Fig. 1.11. Due to the non-linearity of the system of equations, it is apparent in the plots that two solutions are present. However, it can be shown that the two solutions are well separated in the (d, ϑ, γ) space, and it turns out that the solution which has the central value of $\gamma \simeq 70°$ corresponding to the SM expectation could be easily isolated by imposing a requirement like $\vartheta > 90°$. Although non-factorizable effects might have a relevant impact on ϑ, it is not expected that they will change the sign of the cosine of this strong phase, which is predicted to be negative by factorization [55]. Consequently, the solution with $\vartheta \simeq 40°$

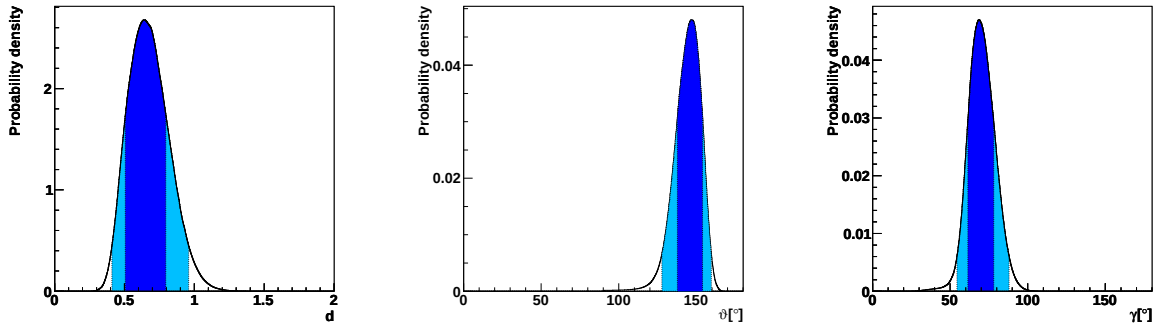

Figure 1.12: From left to right: p.d.f.'s for d, ϑ and γ obtained by using the current experimental measurements, and imposing $\vartheta > 90°$ in order to isolate the SM solution for γ. 68% (dark) and 95% (light) probability intervals are also indicated.

can be excluded through this argument, and thus we are justified to employ the constraint $\vartheta > 90°$. In this way we get the p.d.f.'s shown in Fig. 1.12. The corresponding 68% probability intervals for d, ϑ and γ are reported in Tab. 1.6.

The 68% probability interval $\gamma = (70 \pm 8)°$ that we obtain is fully consistent with the current average $\gamma = (74 \pm 11)°$ [23], determined from pure tree decays at the B factories, or with the indirect prediction from UT fits assuming the SM validity $\gamma = (69.6 \pm 3.1)°$ [23]. Furthermore, we have also obtained probability intervals for the hadronic parameters d and ϑ, that can be used to drive theory in correctly modelling the underlying hadron dynamics involved in the decays under study.

It is also interesting to see how the sensitivity depends on the size of U-spin breaking that is allowed. Fig. 1.13 shows the variations of the 68% and 95% probability intervals for γ as a function of the size of U-spin breaking, separately in $\hat{\xi}$ and $\Delta\vartheta$. The half-width of the 68% (95%) probability interval increases from about 5° (11°) in the case of zero non-factorizable U-spin breaking effects, up to 9° (18°) and 14° (25°) for breakings of 50% on $\hat{\xi}$ and $\pm 50°$ on $\Delta\vartheta$ respectively.

We can also predict probability intervals for $\mathcal{A}^{dir}_{K^+K^-}$ and also, by relying on the current knowledge of the B^0_s mixing phase ϕ_s, for $\mathcal{A}^{mix}_{K^+K^-}$. Such predictions have been obtained by assuming an additional independent U-spin breaking of 20% and $\pm 20°$ respectively on the hadronic parameters entering the expressions of $\mathcal{A}^{dir}_{K^+K^-}$ and $\mathcal{A}^{mix}_{K^+K^-}$, in order to take into account U-spin breaking effects also while exchanging the values of $\mathcal{A}^{mix}_{K^+K^-}$ and $\mathcal{A}^{\mathcal{CP}}_{K^+\pi^-}$. For this reason, the prediction of $\mathcal{A}^{dir}_{K^+K^-}$ is not simply equal to the measurement of $\mathcal{A}^{\mathcal{CP}}_{K^+\pi^-}$, but has a larger uncertainty.

All the relevant inputs and the predictions for the parameters of interest are summarized in Tab. 1.6. The p.d.f.'s for $\mathcal{A}^{dir}_{K^+K^-}$ and $\mathcal{A}^{mix}_{K^+K^-}$ are shown in Fig. 1.14.

1.7 Extraction of γ and ϕ_s

Eqs. (1.98) and (1.105) constitute a system of four equations with seven unknowns: d, ϑ, ϕ_d, γ, d', ϑ' and ϕ_s. However, ϕ_d is well measured by the B factories, $\phi_d = (0.768 \pm 0.028)$ rad [23],

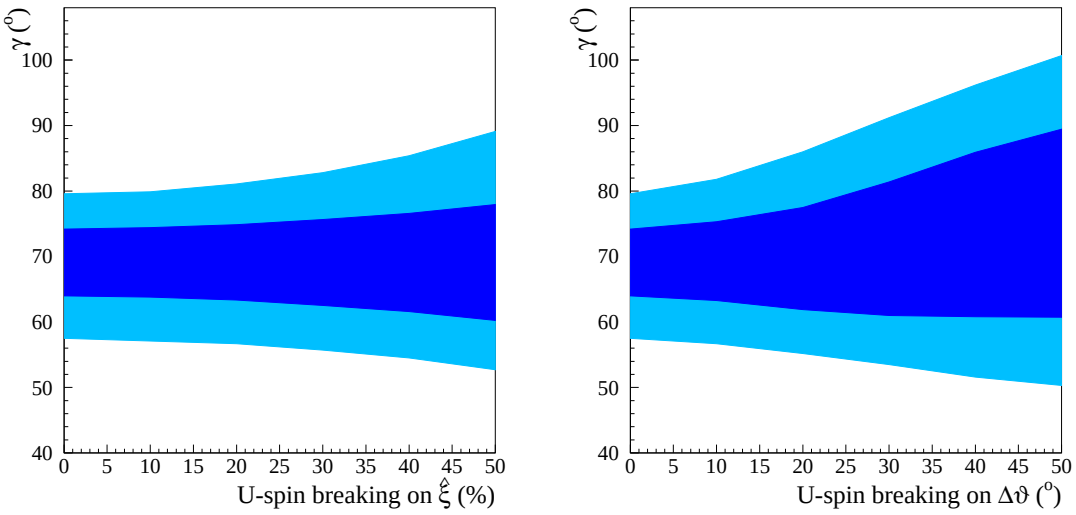

Figure 1.13: Variation of the 68% (dark) and 95% (light) probability intervals for γ as a function of the size of U-spin breaking that is allowed, separately in $\hat{\xi}$ and $\Delta\vartheta$. The plots are obtained by using the current experimental measurements, and imposing $\vartheta > 90^\circ$ in order to isolate the SM solution for γ.

Inputs	
ϕ_d	(0.768 ± 0.028) rad
ϕ_s	(-0.0366 ± 0.0015) rad
$\mathcal{A}^{dir}_{\pi^+\pi^-}$	0.38 ± 0.06
$\mathcal{A}^{mix}_{\pi^+\pi^-}$	-0.65 ± 0.07
$\mathrm{Corr}(\mathcal{A}^{dir}_{\pi^+\pi^-}, \mathcal{A}^{mix}_{\pi^+\pi^-})$	0.08
$\mathcal{A}^{\mathcal{CP}}_{K^+\pi^-}$	-0.098 ± 0.012
Predictions	
d	0.65 ± 0.15
ϑ	$(146 \pm 8)^\circ$
γ	$(70 \pm 8)^\circ$
$\mathcal{A}^{dir}_{K^+K^-}$	-0.09 ± 0.04
$\mathcal{A}^{mix}_{K^+K^-}$	0.150 ± 0.035
$\mathrm{Corr}(\mathcal{A}^{dir}_{K^+K^-}, \mathcal{A}^{mix}_{K^+K^-})$	-0.02

Table 1.6: Experimental inputs and predictions in terms of 68% probability intervals for the various parameters of interest.

and will be further refined by LHCb [63], while ϕ_s is expected to be very small in the SM. By assuming the validity of the U-spin symmetry, which leads to the identities $d = d'$ and $\vartheta = \vartheta'$, just three unknowns are left, and the system is fully solvable. It is then possible to determine simultaneously d, ϑ and γ. Furthermore, since we have more equations than unknowns, we can exploit the additional equation in order to make a measurement of ϕ_s from these channels

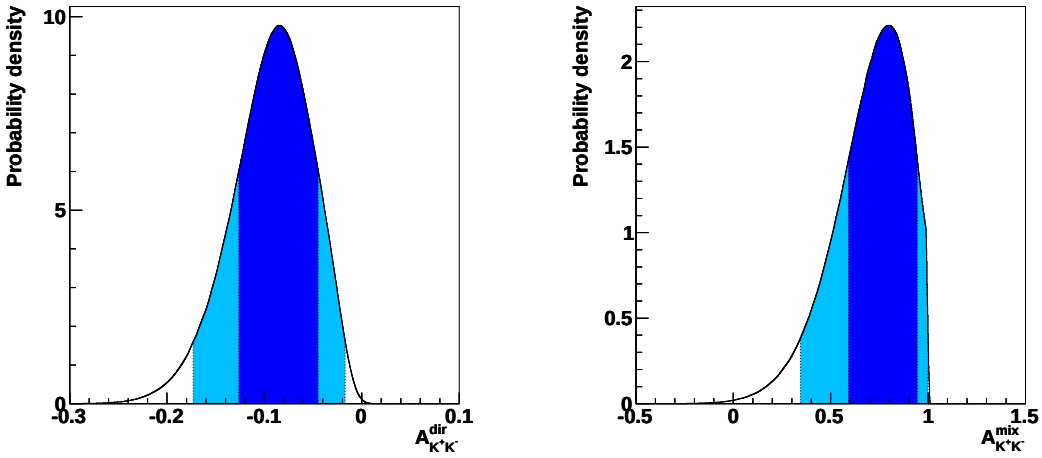

Figure 1.14: P.d.f.'s for $\mathcal{A}^{dir}_{K^+K^-}$ (left) and $\mathcal{A}^{mix}_{K^+K^-}$ (right) obtained by using the current experimental measurements and imposing $\vartheta > 90^\circ$ in order to isolate the SM solution for γ. 68% (dark) and 95% (light) probability intervals are also indicated.

alone. It is important to note, as we will show, that it is not necessary to rely on the U-spin symmetry validity *tout-court*, since meaningful results can be obtained also in the case when large non-factorizable U-spin breaking effects are taken into account.

As detailed in Ref. [55], first insights into U-spin breaking effects can be already obtained from present data using the measurements of the charge asymmetries and branching fractions of the U-spin related decay modes $B^0 \to K^+\pi^-$ and $B^0_s \to \pi^+K^-$. The validity of the U-spin symmetry leads to the identities $r = r_s$ and $\delta = \delta_s$ in Eqs. (1.101) and (1.107), as well as to the relation:

$$\frac{\mathcal{A}^{\mathcal{CP}}_{\pi^+K^-}}{\mathcal{A}^{\mathcal{CP}}_{K^+\pi^-}} \simeq -\left|\frac{P_s}{P}\right|^2 \frac{\mathcal{BR}(B^0 \to K^+\pi^-)}{\mathcal{BR}(B^0_s \to \pi^+K^-)}. \tag{1.111}$$

It is then possible to obtain experimental insights into U-spin breaking effects by writing

$$\left|\frac{P_s}{P}\right|_{\rm exp} = \left|\frac{P_s}{P}\right| \sqrt{\left[\frac{r_s}{r}\right]\left[\frac{\sin\delta_s}{\sin\delta}\right]} = 1.06 \pm 0.28, \tag{1.112}$$

that is in good agreement with the QCD sum-rule results of Ref. [57]

$$\left|\frac{P_s}{P}\right|^{\rm QCDSR}_{\rm fact} = 1.02^{+0.11}_{-0.10}, \tag{1.113}$$

although the experimental errors are still large. This quantity will be eventually measured with great precision at LHCb, thus providing a much more stringent test.

LHCb will measure all the four $\mathcal{CP}$ violating observables $\mathcal{A}^{dir}_{\pi^+\pi^-}$, $\mathcal{A}^{mix}_{\pi^+\pi^-}$, $\mathcal{A}^{dir}_{K^+K^-}$ and $\mathcal{A}^{mix}_{K^+K^-}$ with high precision. In particular, the determination of $\mathcal{A}^{mix}_{KK}$ will open a new avenue to the measurement of the B^0_s mixing phase ϕ_s [55].

Hypothetical LHCb measurements	
	Scenario B
ϕ_d	(0.768 ± 0.020) rad
$\mathcal{A}^{dir}_{\pi^+\pi^-}$	0.38 ± 0.04
$\mathcal{A}^{mix}_{\pi^+\pi^-}$	-0.65 ± 0.04
$\mathcal{A}^{\mathcal{CP}}_{K^+\pi^-}$	-0.100 ± 0.008
$\mathcal{A}^{mix}_{K^+K^-}$	0.150 ± 0.035
Sensitivities	
	Scenario B
d	0.63 ± 0.13
ϑ	$(146 \pm 7)^\circ$
γ	$(70 \pm 7)^\circ$
ϕ_s	(-0.03 ± 0.05) rad

Table 1.7: Hypothetical LHCb measurements corresponding to an integrated luminosity $L = 2\,\text{fb}^{-1}$, and consequent sensitivities on d, ϑ, γ and ϕ_s.

As U-spin symmetry predicts that $\mathcal{A}^{dir}_{K^+K^-}$ and $\mathcal{A}^{\mathcal{CP}}_{K^+\pi^-}$ shall assume the same value — neglecting exchange and annihilation topologies in the $\mathcal{A}^{dir}_{K^+K^-}$ decay amplitude, which are already quite constrained by current measurements of the branching fractions of the $B^0 \to K^+K^-$ and $B^0_s \to \pi^+\pi^-$ decays — we find that an optimal strategy consists of substituting the direct $\mathcal{CP}$ asymmetry term $\mathcal{A}^{dir}_{K^+K^-}$ with $\mathcal{A}^{\mathcal{CP}}_{K^+\pi^-}$, due to the much smaller statistical error achievable on $\mathcal{A}^{\mathcal{CP}}_{K^+\pi^-}$. LHCb will further constrain the size of the exchange and penguin annihilation amplitudes contributing to the $B^0_s \to K^+K^-$, by considerably improving the measurements of the $B^0 \to K^+K^-$ and $B^0_s \to \pi^+\pi^-$ branching ratios.

By following the procedure outlined in the previous section, using the values of Tab. 1.7 as inputs, we obtain the central values and the sensitivities for d, ϑ, γ and ϕ_s reported in the same table, corresponding to an integrated luminosity $L = 2\,\text{fb}^{-1}$. The corresponding p.d.f.'s are shown in Fig. 1.15. We emphasize that we are taking into account U-spin breaking effects as large as 20% for d and $\pm 20^\circ$ for ϑ, independently varied in the expressions of $\mathcal{A}^{\mathcal{CP}}_{K^+\pi^-}$ and $\mathcal{A}^{dir}_{K^+K^-}$, in order to consider sizable U-spin breaking effects not only with respect to the $B^0 \to \pi^+\pi^-$ channel but also between $B^0 \to K^+\pi^-$ and $B^0_s \to K^+K^-$.

Note that we can achieve a good precision not only on γ, but also on ϕ_s. The $\mathcal{CP}$ measurements from these channels will be important, first in order to give an independent confirmation of the baseline ϕ_s measurement from the $B^0_s \to J/\psi\phi$ decay, secondly to allow for an unambiguous determination of ϕ_s in conjuction with $B^0_s \to J/\psi\phi$. In particular, as pointed out in Ref. [55], we will be able to distinguish between the cases of $\phi_s = 0^\circ$ and $\phi_s = 180^\circ$, which is important for the search of NP.

We have also studied the dependence of the sensitivities to γ and ϕ_s as functions of the size of non-factorizable U-spin breaking that is allowed. Fig. 1.16 shows the variations of the 68% and 95% probability intervals for γ and ϕ_s separately as functions of $\hat{\xi}$ and $\Delta\vartheta$. It is apparent that the dependence on the amount of U-spin breaking is significantly more pronounced for γ than for ϕ_s.

Further information useful to constrain NP will come from the measurement of $\Delta\Gamma_s$, which can be also performed using $B^0_s \to K^+K^-$ decays. With an integrated luminosity $L = 2\,\text{fb}^{-1}$,

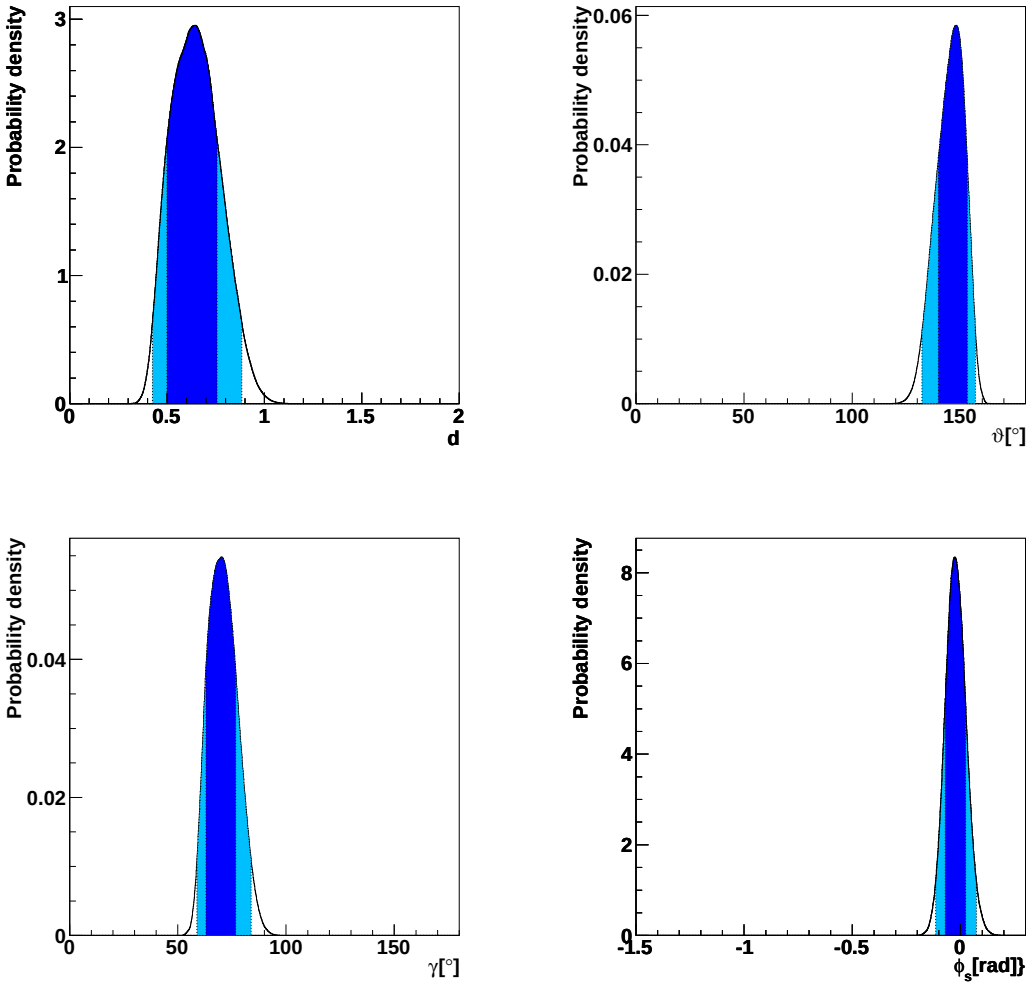

Figure 1.15: P.d.f.'s for d (top left), ϑ (top right), γ (bottom left) and ϕ_s (bottom right) obtained by using the hypothetical LHCb measurements shown in Tab. 1.7, with sensitivities corresponding to an integrated luminosity $L = 2\,\text{fb}^{-1}$. The condition $\vartheta > 90°$ was imposed in order to isolate the SM solution for γ. 68% (dark) and 95% (light) probability intervals are also indicated.

LHCb expects a statistical error on $\Delta\Gamma_s$ of about 0.02 ps^{-1}. In the presence of NP, $\Delta\Gamma_s$ is modified as follows [64]:

$$\Delta\Gamma_s = \Delta\Gamma_s^{SM} \cos(\phi_s), \tag{1.114}$$

i.e. NP effects can reduce the observed value of $\Delta\Gamma_s$ with respect to the SM expectation.

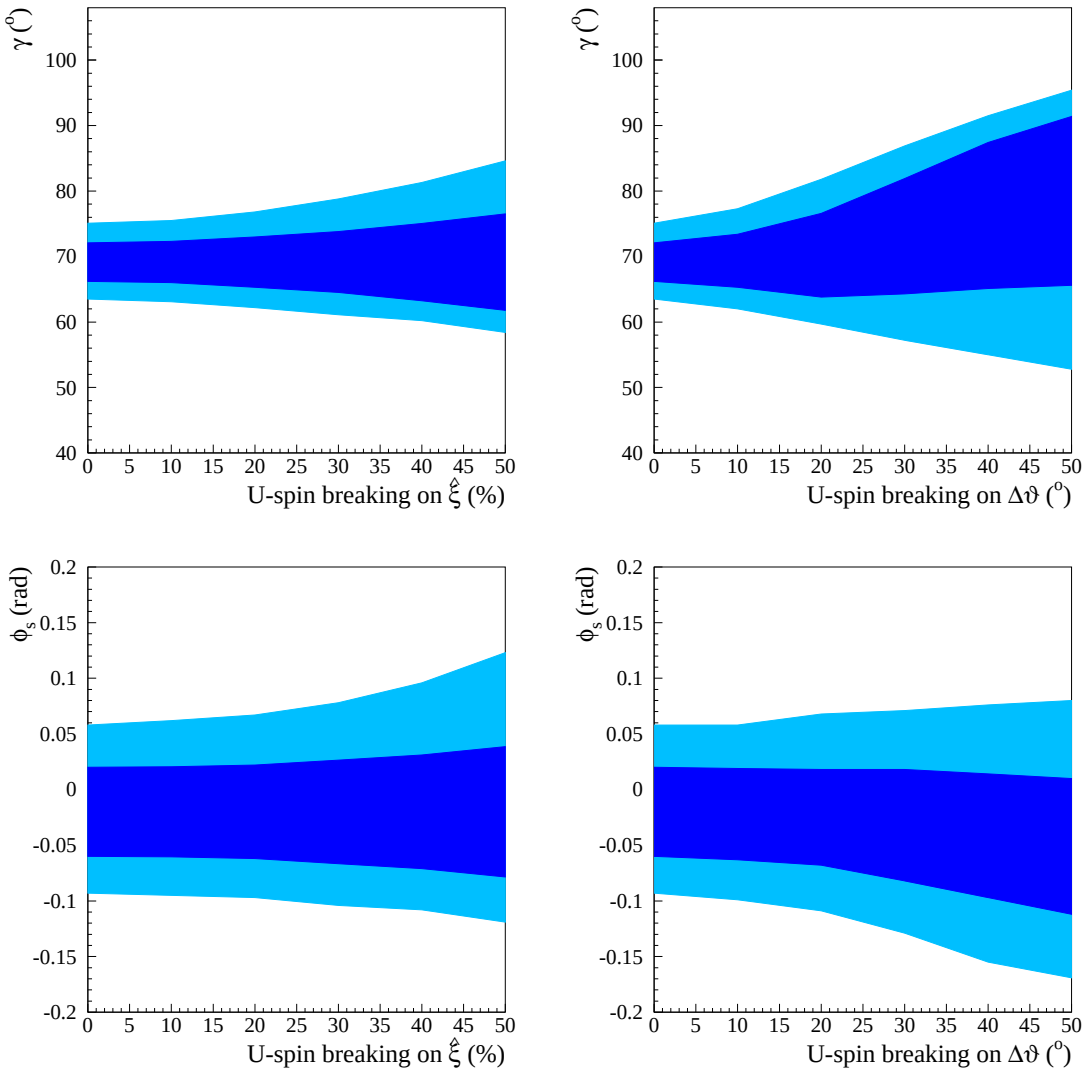

Figure 1.16: Variation of the 68% (dark) and 95% (light) probability intervals for γ (top) and for ϕ_s (bottom) as a function of the size of U-spin breaking, separately in $\hat{\xi}$ (left) and $\Delta\vartheta$ (right). The plots are obtained by using the hypothetical LHCb measurements shown in Tab. 1.7, with sensitivities corresponding to an integrated luminosity $L = 2\,\text{fb}^{-1}$. The condition $\vartheta > 90°$ was imposed in order to isolate the SM solution for γ.

1.8 $\Lambda_b \to ph'^-$ decays

Although Λ_b decays to a proton and a charged pion or kaon have not yet received significant attention from a theoretical point of view, $\mathcal{CP}$ violation with these decays will be studied with high precision at LHCb. The author of Ref. [65] claims that the measurement of the $\mathcal{CP}$ charge asymmetry in the $\Lambda_b \to p\pi^-$ decay can be sensitive to NP effects in the Minimal Supersymmetric Standard Model (MSSM) with R-parity violation. While the SM predicts a charge asymmetry

$\mathcal{A}^{\mathcal{CP}} \simeq 8\%$ and a branching fraction $\mathcal{BR} \simeq 10^{-6}$, in the R-parity violating model the charge asymmetry is predicted to be negligibly small, while the branching fraction as large as $1.6 \cdot 10^{-4}$. In other words, the presence of R-parity and lepton number violating couplings could significantly modify the SM predictions of the branching ratio and of the $\mathcal{CP}$ charge asymmetry, by enhancing the former and suppressing the latter. Although the recent measurements by CDF invalidate the possibility of a large branching ratio at the level of 10^{-4}, a precise measurement of the charge asymmetry has not yet been made.

Chapter 2

LHC collider and LHCb detector

LHCb [66] is one of the four major experiments operating at the Large Hadron Collider (LHC) at CERN, close to Geneva, in Switzerland. In this chapter we will provide a brief introduction to the LHC accelerator complex, followed by a detailed description of the LHCb detector and the related infrastructures necessary to fulfill its physics programme.

2.1 The Large Hadron Collider

The LHC[67] is a two-ring-hadron accelerator and collider installed inside a 27 km tunnel, already used for the LEP machine, placed 100 m underground across the Swiss and French borders, as shown in Fig 2.1. The machine design foresees to collide protons up to a centre-of-mass energy of 14 TeV and an instantaneous luminosity of 10^{34} cm^{-2}s^{-1}, and heavy ions (Pb-Pb) with an energy of 2.8 TeV per nucleon at a peak luminosity of 10^{27} cm^{-2}s^{-1}. Protons are obtained from ionized hydrogenum atoms deprived of their electrons. As it is not possible to inject protons and accelerate them from a quasi-rest condition up to 7 TeV, protons are injected into the LHC from the chain of preaccelerators Linac2 - Proton Synchrotron Booster (PSB) - Proton Synchrotron (PS) - Super Proton Synchrotron (SPS). Linac2 is a linear accelerator providing the PSB with proton bunches of 50 MeV energy. In the PSB protons are then accelerated up to 1 GeV before being injected into the PS. The PS raises their energy up to 26 GeV and passes them to the SPS. The SPS performs the last acceleration step, up to 450 GeV, before the injection of beams into the LHC via the two tunnels TI2 (placed near the ALICE experiment) and TI8 (placed near the LHCb experiment). The complex of CERN accelerators is schematically shown in Fig. 2.2.

The LHC synchrotron represents the status-of-the-art of particle accelerators and one of the most important technological challenges ever made. In order to achieve its design energy the magnetic field of a single dipole, used to bend protons and constrain their path inside the ring, must reach a magnitude of 8.34 T. Such goal is possible only using super-conducting dipole magnets working at a temperature of 1.9 K (-271.3°C). At its nominal regime the LHC rings will store 2808 proton bunches per ring, each of them containing 1.1^{11} protons and colliding with a frequency of 40 MHz.

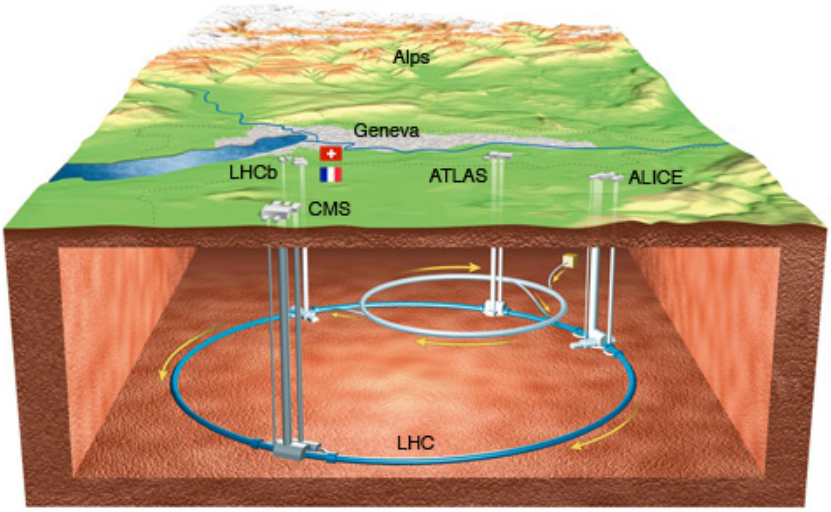

Figure 2.1: Graphical view of the LHC ring position. As reported in the text the ring is placed about 100 m underground. The ground-level positions of the access points of the four main experiments (ALICE, ATLAS, CMS and LHCb) is also shown.

2.1.1 2010 data taking

LHC started its physics operation on the 23$^{\text{rd}}$ November 2009, colliding two proton bunches with 450 GeV of energy per beam and increased to 1.18 GeV per beam within few operational days. The first proton-proton collision at 3.5 TeV per beam has been recorded on the 30$^{\text{th}}$ March 2010 and continued until the end of October. During this first year of high energy collisions, instantaneous luminosity achieved by the machine increased continously as shown in Fig. 2.3. The total integrated luminosity delivered by LHC to each of the four experiments has been about 42 pb^{-1}, out of which LHCb recorded about 38 pb^{-1} with an efficiency close to 90%. In Fig. 2.3 a pie chart representing the data taking efficiency and the various sources of inefficiencies is also shown. The LHCb detector and Data Acquisition (DAQ) system performed well during 2010, in particular considering that the system had to operate with an higher number of visible collisions μ with respect to the design value of 0.4. In Fig. 2.4 the values of μ as a function of the fill number during 2010.

2.1.2 2011 data taking

In 2011, the data taking operations started on the 12$^{\text{th}}$ April and ended at the end of October. During this period LHC operated again at an energy of 3.5 TeV per beam. The data taking conditions have been more stable with respect to 2010. In particular, LHCb, in order to cope with detector and trigger design limits, worked with a system allowing to continuously levelling the instantaneous luminosity to about 3.5×10^{32} cm^{-2}s^{-1}, as shown in Fig. 2.5. Such a value correspond to about 1.75 times the instantaneous design luminosity.
The total integrated luminosity delivered to LHCb has been 1.22 fb^{-1} and the experiment collected 1.11 fb^{-1} with an efficiency of about 90% as shown in Fig. 2.6.

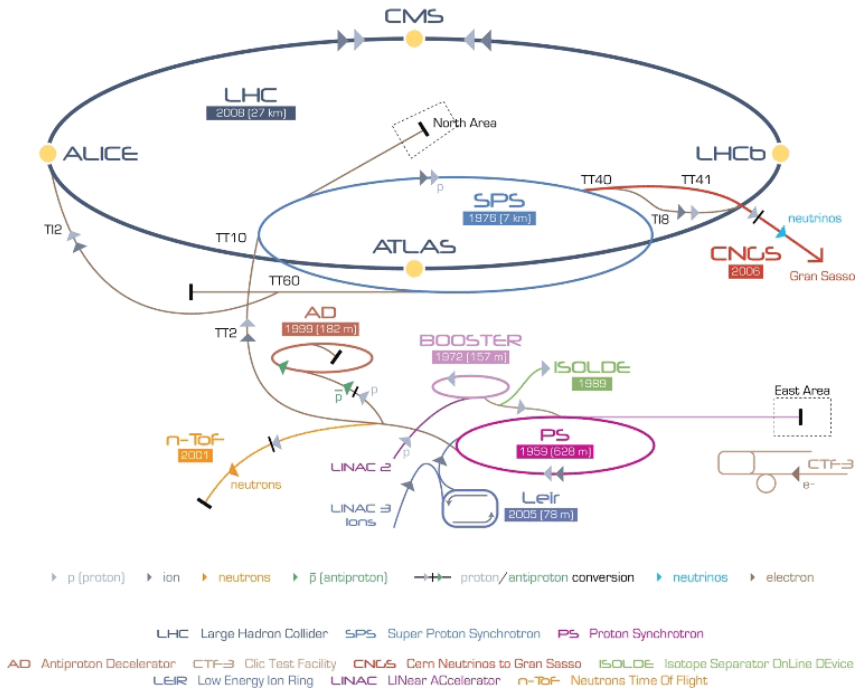

Figure 2.2: Schematic view of the complex of CERN accelerators. The Linac2, Proton Synchrotron Booster (PSB), Proton Synchrotron (PS), Super Proton Synchrotron (SPS) and LHC mentioned in the text are shown. The two tunnels for the injection of proton beams into the LHC, TI2 (near the ALICE experiment) and TI8 (near the LHCb experiment), are also shown.

2.2 The LHCb detector

When the two protons collide at the energy of 7 TeV the interaction between two partons leads to the creation of $b\bar{b}$ pairs. Due to the average imbalance in momentum of the two partons, the outcoming b quarks are strongly boosted along the beam-line. As a consequence, the B hadrons at the LHC are produced in the same forward of backward emisphere and with a small angle with respect to the beam direction. Fig. 2.7 shows the polar angle distribution of $b\bar{b}$ pairs as predicted by the PYTHIA event generator [68]. In order to exploit this feature of B hadron production, the LHCb detector, in contrast to other LHC detectors, has the structure of a forward spectrometer. Its geometrical acceptance lies between 10 and 300 mrad in the horizontal plane and between 10 and 250 mrad in the vertical plane. The difference between horizontal and vertical acceptances is justified by the fact that the horizontal plane is also the bending plane for charged particles deflected by the dipole magnetic field of LHCb. The pseudo-rapidity (η) range for tracks inside the LHCb geometrical acceptance is between about 1.8 and 4.9.

The LHCb physics program requires the detector to satisfy the following requirements:

- Most of the LHCb core analyses require time-dependent measurements of B-hadron decay rates. Thus the precision in the reconstruction of $p-p$ interaction vertices and B hadron decay vertices must be very high, in order to have a suitable proper-time resolution to follow the neutral B meson oscillations (in particular the fast B_s^0 one).

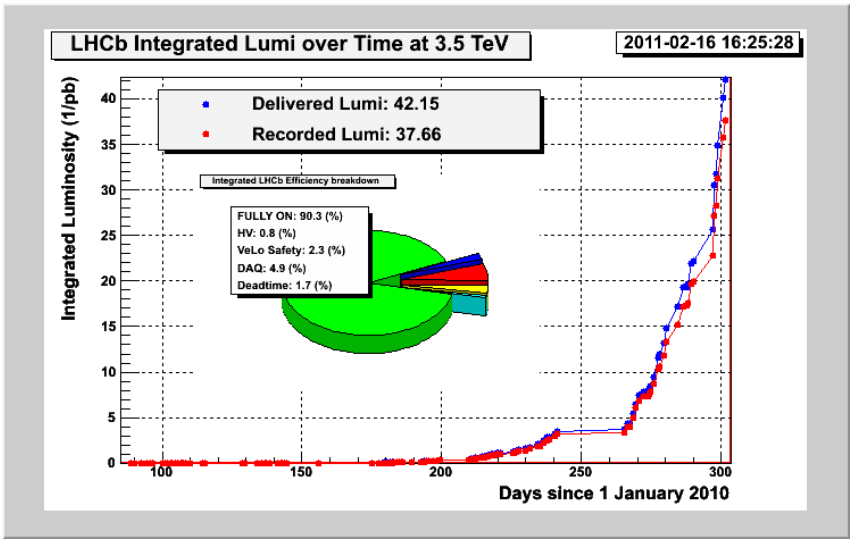

Figure 2.3: Integrated luminosity at $\sqrt{s} = 7$ TeV delivered by LHC to the LHCb experiment (blue points) and recorded luminosity by the LHCb experiment (red points) as a function of time during 2010. The pie chart shows the data taking efficiency (green) of the detector and the various sources of inefficiencies.

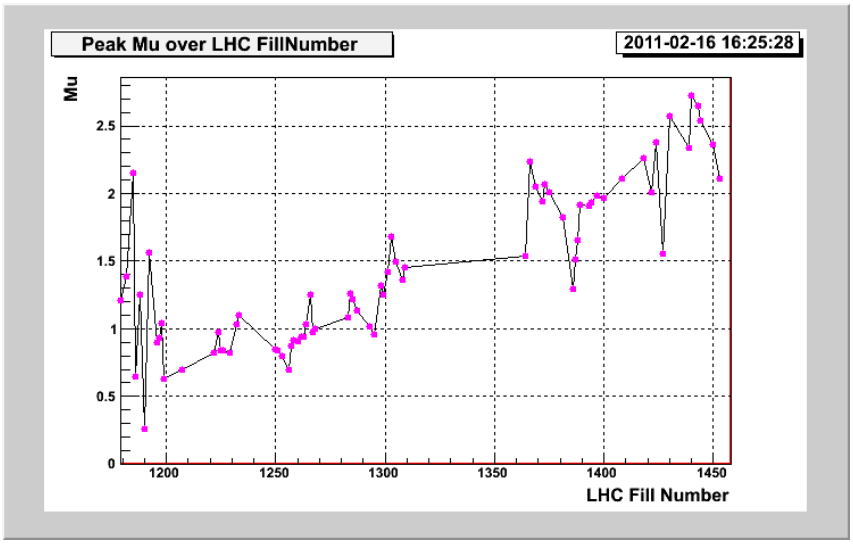

Figure 2.4: Peak number of visible collisions μ at the LHCb interaction point as a function of the fill number during 2010.

- The analysis of hadronic B decays requires an excellent discrimination between charged pions, charged kaons and protons in a very wide momentum range (betweem few GeV/c up to and above 100 GeV/c). In addition the analysis of B decays into final states containing leptons needs optimal identification of muons and electrons.

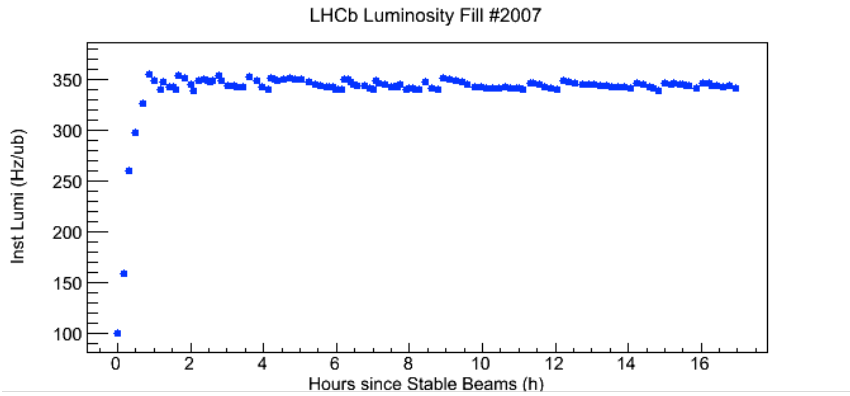

Figure 2.5: Instantaneous luminosity delivered by the LHC to the LHCb experiment as a function of time during the fill 2007 (7^{th} August 2011).

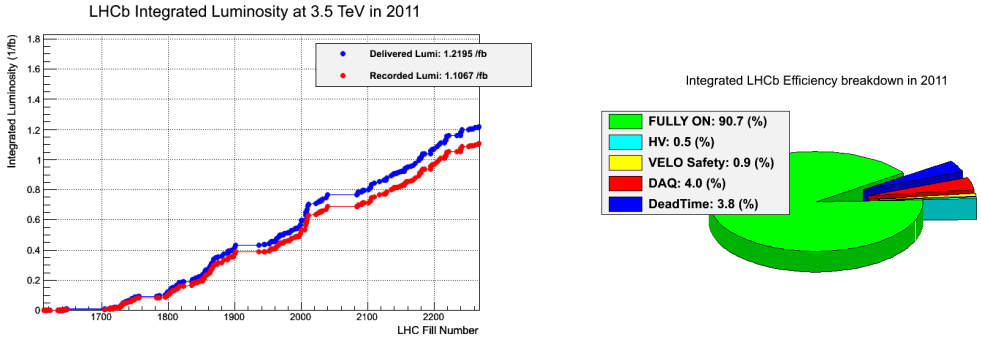

Figure 2.6: Left: integrated luminosity at $\sqrt{s} = 7$ TeV delivered by LHC to the LHCb experiment (blue points) and recorded luminosity by the LHCb experiment (red points) as a function of fill number 2011. Right: pie chart showing the data taking efficiency of the LHCb detector (green) and the various sources of inefficiencies.

- The invariant mass resolution must be as small as possible in order to discriminate the signals from the combinatorial background and in order to distinguish between B^0 and B_s^0 decays. In order to achive such a resolution the momentum of charged tracks must be measured with a relative precision of $\sim 10^{-3}$.

- Due to its geometrical acceptance the LHCb detector is designed to work in an high-occupancy region. In addition, at the LHC the measured cross-section of $b\bar{b}$ pair production at $\sqrt{s} = 7$ TeV is $(284 \pm 20 \pm 49)$ μb [69], between two and three order of magnitude smaller than the minimum bias cross-section. As a consequence the trigger system of LHCb must to have a very high background rejection to reduce the acquired data-sample to a manageable size. In order to match such requirements mantaining an high efficiency on signals the LHCb trigger is organized in multiple levels, each of them processing the output of the previous level.

- The amount of data delivered by LHC and thus collected by the experiment requires an

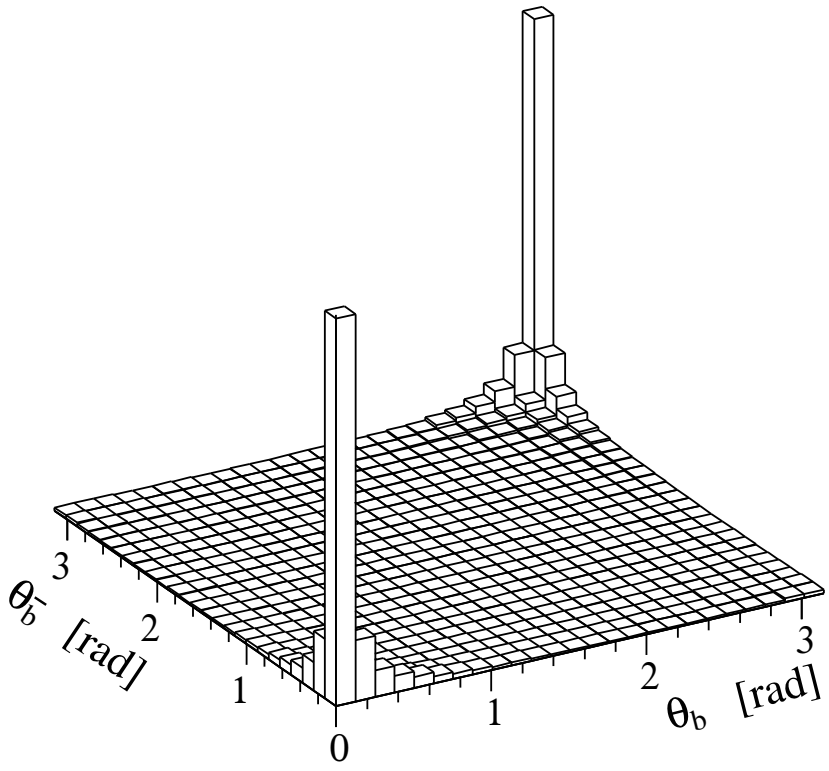

Figure 2.7: Polar angle distribution of $b\bar{b}$ pairs as predicted by the PYTHIA event generator [68].

efficient exploitation of large computing resources, needed both for the processing of data and for its storage.

An overview of the entire LHCb detector is shown in Fig. 2.8. From left to right the various sub-detectors are visible:

VELO: the Vertex Locator is placed around the interaction region, and provides the reconstruction of primary and secondary vertices;

RICH1: the first Ring Imaging Cherenkov detector is placed just after the VELO and it provides information for the identification of charged particles;

TT: the Trigger Tracker is the first tracking system;

Magnet: the magnetic field used to bend the particles in order to evaluate their charge and momentum;

Tracking Stations: three tracking stations (T1, T2 and T3) are placed behind the magnetic dipole;

RICH2: the second Ring Imaging Cherenkov detector is designed to provide efficient particle identification in a different momentum range with respect to RICH1;

Electromagnetic Calorimeter: the electromagnetic calorimeter system is necessary for an efficient trigger and the identification of electrons, photons;

Hadronic Calorimeter: the Hadronic Calorimeter (HCAL) is placed behind the ECAL and is used for the hadronic trigger;

Muon Stations: the Muon Stations are placed in the farest part of the detector from the interaction region where only muons can arrive without being stopped inside the calorimeter system and other absorbers. It is used both for efficient trigger of decays with muons in the final state and for muon identification.

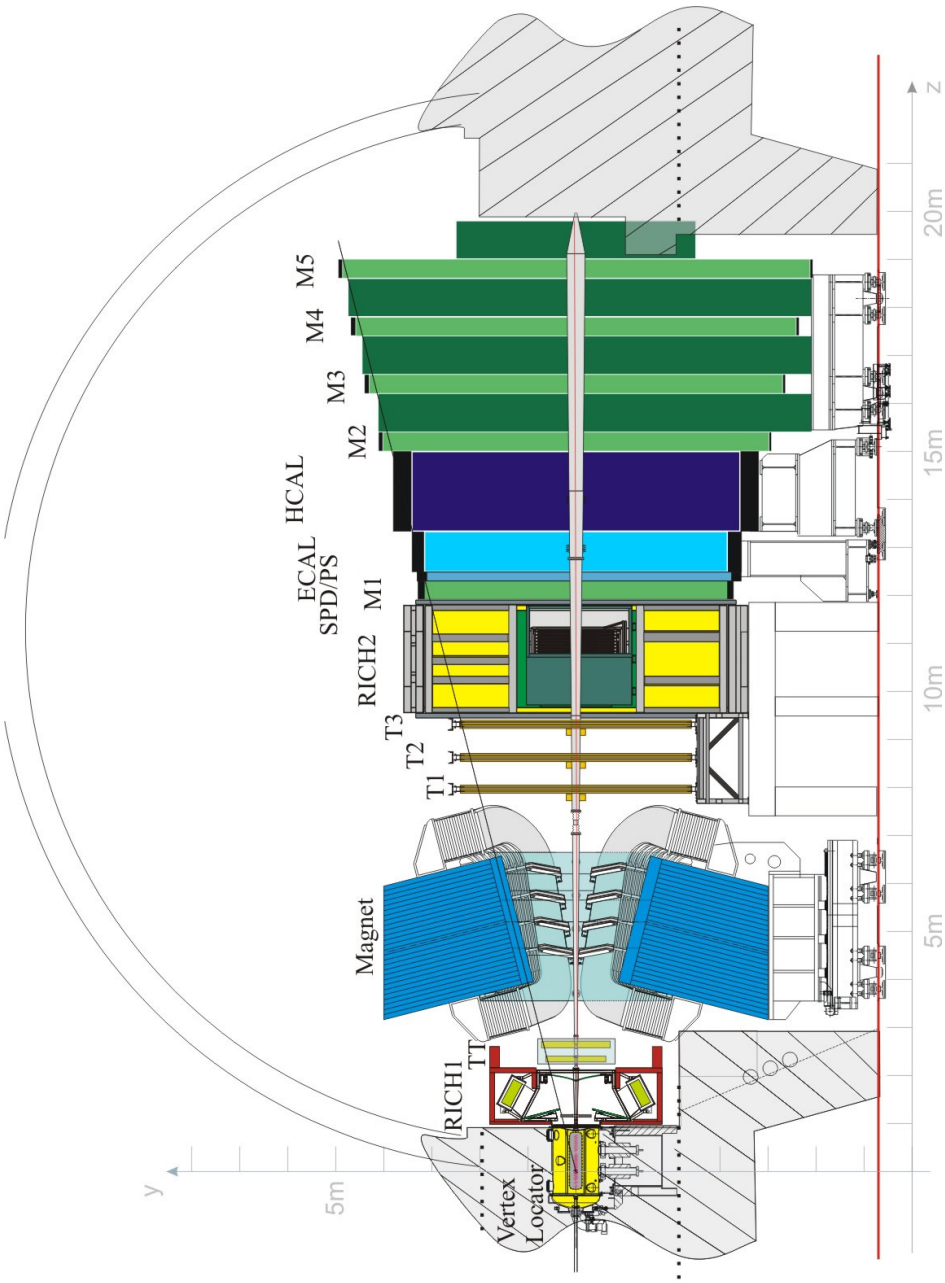

Figure 2.8: Overview of the entire LHCb detector. From left to right the various sub-detectors are visible: VELO, RICH1, TT, Magnet, Tracking Stations, RICH2, Electromagnetic Calorimeter (ECAL), Hadronic Calorimeter (HCAL) and Muon Stations.

2.3 The tracking system of LHCb

The reconstruction of charged particles is realized using the vertex detector (VELO), the Trigger Tracker (TT) and the three tracking stations (T1, T2 and T3). The magnetic dipole of LHCb is placed between the TT and T1.

2.3.1 The Vertex Locator

At the energy provided by the LHC, B hadrons produced by the proton-proton collisions have a mean distance of flight of about 1 cm. As a consequence the presence of a secondary vertex well spaced from the proton-proton primary interaction is an important signature for the presence of B hadrons. In order to exploit this feature to select in the most efficient way signals and reject most of the combinatorial background, having a vertex detector with micrometric precision is necessary. The VELO [70] sub-detector consists of a series of 21 circular silicon modules arranged perpendicularly along the beam line as shown in Fig. 2.9. Each module is subdivided into two halves allowing to move them far from or close to the beam depending on necessity. In fact during data-taking the VELO sensors are placed at a radial distance from the beam which is smaller than the aperture required by the LHC during injection and must therefore be retractable. Thus VELO modules are mounted on a moveable device inside a vessel that mantains vaccum and allows them to move between 3 cm (fully open) and 8 mm (data taking conditions) from the beam [70]. The polar angular acceptance of the halves is more than 180° allowing them to overlap during data taking. Module halves are composed of two planes of 220 μm thick silicon microstrip sensors allowing to measure radial (R sensors) and polar (ϕ sensors) coordinates of the hits generated by ionizing particles. A scheme of R and ϕ sensors is reported in Fig. 2.10. R sensors are subdivided into four sectors per halves of about 45° each. The microstrip are modelled in a semi-circular shape and their width varies from 40 μm (near the beam) to 92 μm (far from the beam) in order to take into account the higher particle occupancy near the interaction point. ϕ sensors are subdivided into two regions, inner and outer. The outer region starts at a radius of 17.25 mm and its pitch is set to be roughly half (39.3 μm) that of the inner region (78.3 μm), which ends at the same radius. Inner and outer regions have different skew to the radial direction in order to improve pattern recognition: 20° and 10° respectively. In addition for a better stereo view of track reconstruction longitudinally adiacent ϕ sensors have opposite skew to each other. Fig. 2.11 showns a 3-dimensional view of the entire VELO apparatus. Detection stations and radiation-hard read-out electronics are placed inside the vacuum tank (10^{-4} mbar), both mounted on the moveable device.

The performances of the VELO detector have been studied by means of the large amount of minimum bias events collected during the data taking periods of 2010 and 2011 and have been compared with full Monte Carlo simulated events. The resolutions achieved in the reconstruction of vertices are summarized in Fig. 2.12 (for only 1 primary vertex in the event) and in Fig. 2.13 (for events with many primary vertices). They depend on the number of tracks fitted into the vertex. The resolution on the X and Y coordinates goes from about 40 μm to about 10 μm, while the resolution on the Z position of vertices goes from about 250 μm to about 50 μm. The resolutions on the impact parameter of tracks with respect to the primary vertex in the X and Y coordinates are shown in Fig. 2.14 as a function of the inverse of transverse momentum of tracks ($1/p_T$).

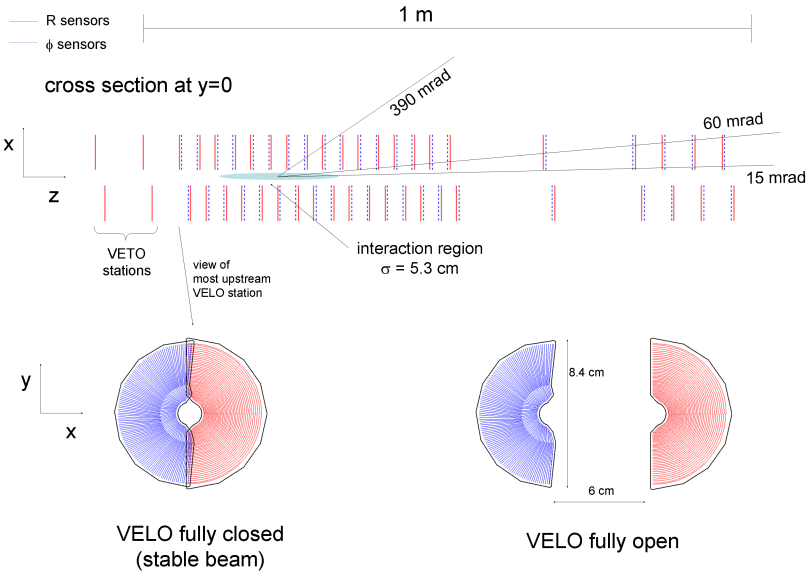

Figure 2.9: Top view of the VELO silicon sensors, with the detector in the fully closed position (top). Front view of the modules in both the closed (bottom left) and open positions (bottom right).

2.3.2 The Trigger Tracker sub-detector

The Trigger Tracker [71] is placed after the RICH1 sub-detector and before the magnetic dipole, in a region where a residual magnetic field is present . Its rôle is to provide reference segments to combine the tracks reconstructed in the tracking stations after the magnet and those reconstructed in the VELO in order to improve the resolution on their momentum and trajectory. The system comprises four stations, grouped two-by-two and called TTa and TTb, spaced by approximately 30cm (as shown in Fig. 2.15) and at a distance of approximatively 2.4 m from the interaction region. Each of the four stations cover a rectangular region about 120 cm in height and about 150 cm wide. In order to cope with the high spatial resolution required and the necessity to work in a region with high occupancy of charged tracks, a silicon microstrip technology has been adopted for the sensors of the TT sub-detector. The microstrips have a pitch of about 200 μm and are arranged into up to 38 cm long readout strips. In the first and fourth station the strips are disposed parallel to the vertical plane, while in the second and third station, in order to improve the precision in the reconstruction, they are tilted by +5° (u-layer) and -5° (v-layer) respectively.

2.3.3 The tracking stations T1-T2-T3

The tracking stations T1, T2 and T3 are placed behind the magnetic dipole, just before the second Cherenkov detector (RICH2). A schematical view is shown in Fig. 2.16. Two different technologies have been used for the tracking station: silicon microstrip sensor in the inner part of the detector (Inner Tracker or IT) and drift straw tube in the outer part (Outer Tracker or

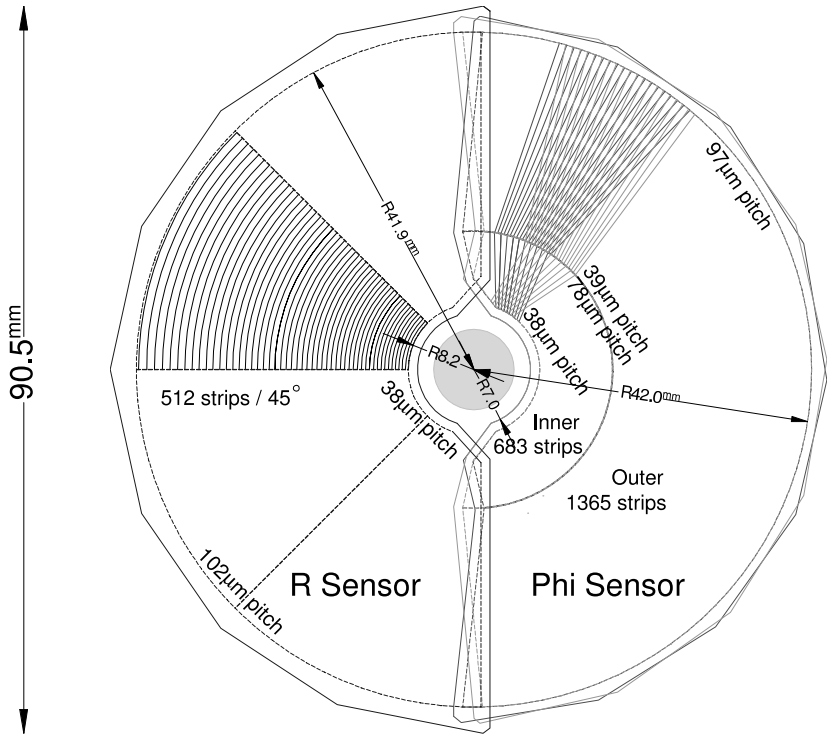

Figure 2.10: Illustration of the geometry of the R (left part) and ϕ (right part) sensors of the VELO. The strips of the ϕ sensors for two adjacent modules are drawn, in order to emphasize their different orientation.

OT). As shown in Fig. 2.16 the IT part of each station is placed in front the OT part. For the Inner Tracker [72] the choice of silicon microstrip sensors has been driven by the high charged track multiplicity close to the beam line. In Fig. 2.17 a scheme of the sub-detector is reported. Each IT station consists of four detection planes overlapped with two of them aligned with the Y axis (x planes) and two of them tilted by $\pm 5°$ (u- and v- plane respectively). The characteristics of silicon microstrip sensors are the same as those used for the TT: they have a pitch of about 200 μm and they are up to 22 cm long. The sizes of the total Inner Tracker sub-detector are about 1.2 m on the bending plane (X coordinate) and about 40 cm on the vertical plane (Y coordinate).

The Outer Tracker [73] is realized using drift straw tubes technology. For each station four planes of traw tubes are arranged in the same way as the microstrip of TT and IT: first and fourth planes have vertically aligned tubes, while the second and third planes have them tilted by $\pm 5°$ (usual u- and v- planes respectively). In addition each plane has two rows of tubes arranged with a honeycomb structure (see Fig. 2.18) in order to maximize the sensible area. The configuration defines a bidimensional lattice to measure both the X and Y coordinates of track hits, mantaining the occupancy low. The straw tubes have a radius of 5 mm and are filled with a mixture of $Ar/CF_4/CO_2$ that gives a drift time of the order of 50 ns.

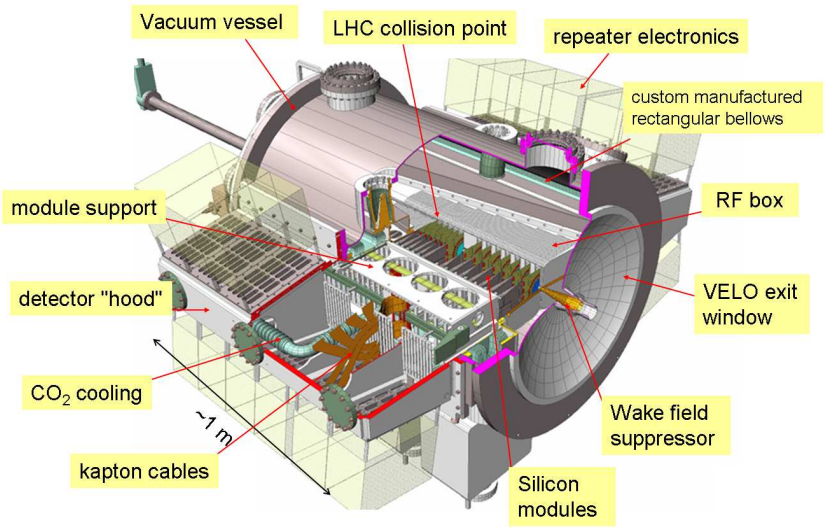

Figure 2.11: 3-dimensional view of the entire VELO apparatus.

2.3.4 The LHCb dipole magnet

The magnetic field of LHCb is provided by a warm dipole magnet placed between the TT and the first tracking station T1 (see Fig. 2.8) [74]. The magnet geometry is determined by the detector acceptance. It is formed by two coils inclined at a small angle with respect to the beam direction in order to become wider with the increase of the Z coordinate, following the profile of the detector acceptance. In Fig. 2.19 the two coils are shown and the inclined geometry is also visible.

The strength of generated magnetic field is mainly directed along the Y coordinate such that the bendind plane for charged tracks results to be almost parallel to the horizontal plane. In Fig. 2.20 the Y component of the magnetic field is reported as a function of the Z coordinate measured along the beam-pipe. The maximum intensity of the magnetic field is about 1 T, while the magnetic field integral is about 4 Tm. During the data taking the polarity of the dipole has been flipped several times in order to allow the evaluation of any left-right asymmetry introduced by the detector. In fact positively and negatively charged tracks are bent to different directions by the magnetic field, thus any variation of the detection efficiency between the left and right region of the detector could affect $\mathcal{CP}$ asymmetry measurements.

2.3.5 Tracking algorithm and performances

In Fig. 2.21 a schematic representation of the track types reconstructed by the tracking algorithm is shown. Particles generating hits in all the tracking sub-detectors are reconstructed as “Long tracks”; particles generating hits only inside the VELO are reconstructed as “VELO tracks” and they are usually particles produced with a wide angle with respect to the beam-line, which go out of the geometrical acceptance of the detector before traversing with the TT. For these tracks it is not possible to measure their momentum. “Upstream tracks” are reconstructed particles with a very low momentum that are swept by the magnetic field out of the detector acceptance

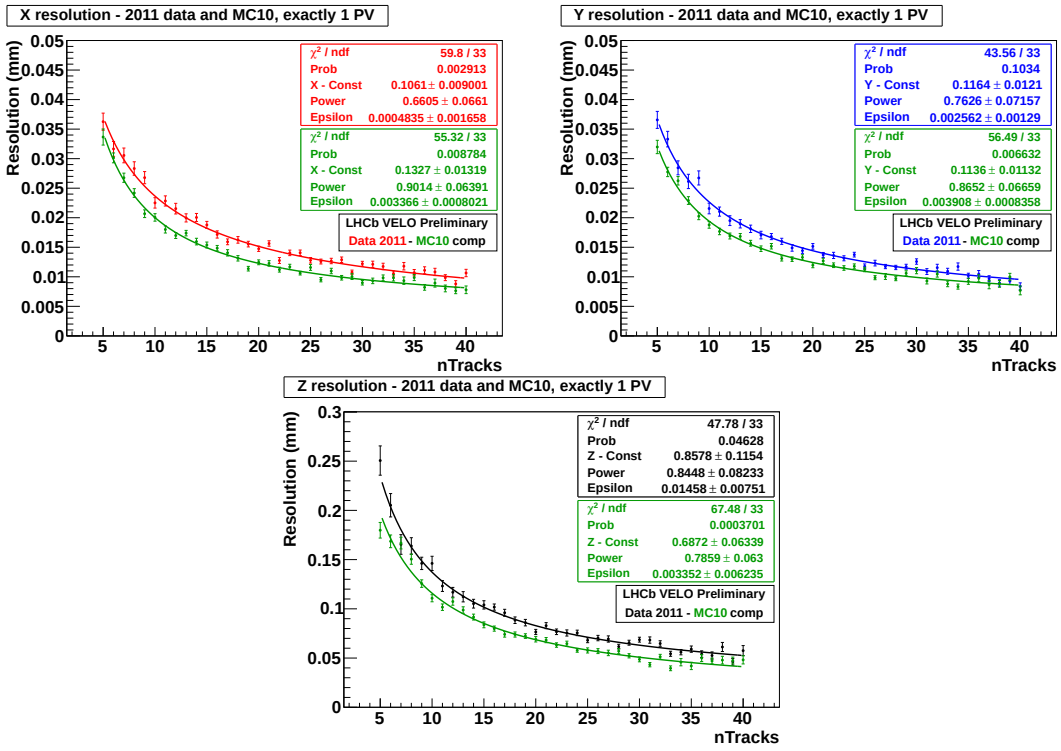

Figure 2.12: Resolutions achieved in the reconstruction of primary vertex coordinates as a function of the number of tracks in the event, as obtained from real data and Monte Carlo simulations. In the figures the resolutions for the X (top left), Y (top right) and Z (bottom) coordinates are reported. The performances shown refer to events where only one primary vertex has been reconstructed.

before they can reach T1. For these tracks it is possible to estimate their momentum, thanks to the residual magnetic field in the region between VELO and TT, but with a relative uncertainty of about 20%. Charged particles coming from long lived neutral particles decaying between the VELO and the TT (usually K^0_S, Λ or in minimal part K^0_L) are reconstructed as "Downstream tracks". In the end "T tracks" are reconstructed from track segments appearing only in the tracking stations after the magnetic dipole.

Track finding and reconstruction are performed in different steps starting from the reconstruction of the track segments in each sub-detector. Track finding starts with the definition of segments inside the VELO and the tracking stations T1-T3 (VELO seed and T station seed respectively). The reconstruction of VELO segments starts from the identification of VELO hits on the same straight trajectory in the $R-Z$ plane, thus reconstructing two-dimentional segments using only hits in the R-sensors of the VELO. In a second step ϕ-sensor hits are associated with compatible $R-Z$ segments, again assuming straight directions for the tracks. The reconstruction of T station seeds is done into two steps. The first step starts by dividing the $X-Y$ plane of the tracking stations into different regions and reconstruct segments that cross the three stations remaining in only one of these windows. The reconstruction starts from one hit in the x-plane of the first station and one hit in the x plane of the last station. Then, using

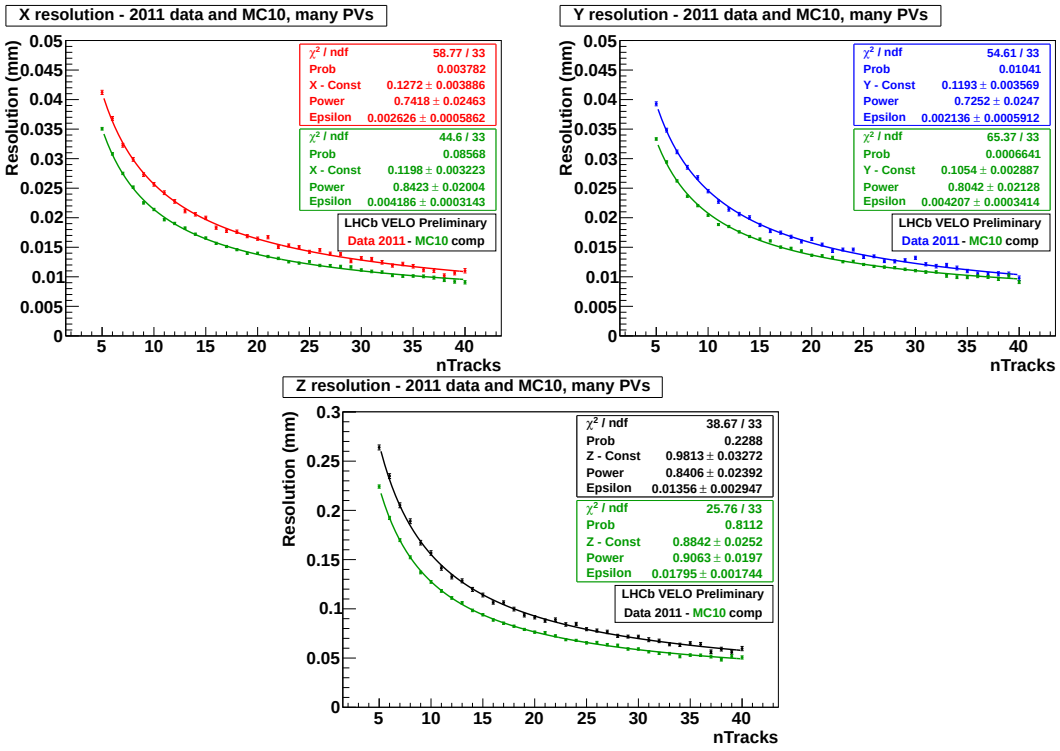

Figure 2.13: Resolutions achieved in the reconstruction of primary vertex coordinates as a function of the number of tracks in the event, as obtained from real data and Monte Carlo simulations. In the figures the resolutions for the X (top left), Y (top right) and Z (bottom) coordinates are reported. The performances shown refer to events where more than one primary vertex has been reconstructed.

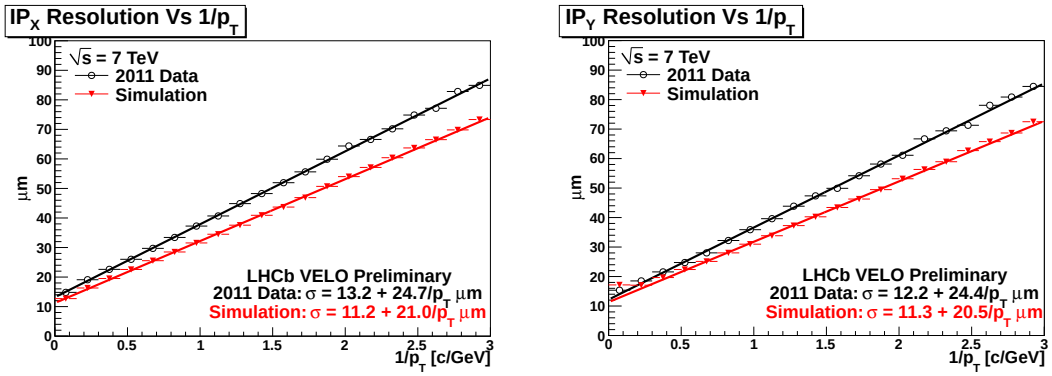

Figure 2.14: Resolution achieved for the X (left) and Y (right) components of the impact parameter (IP) of tracks with respect to the primary vertex as a function of the inverse of the transverse momentum of tracks $1/p_T$.

a parabola hypothesis for the trajectory, the algorithm predicts the position of the hit in the

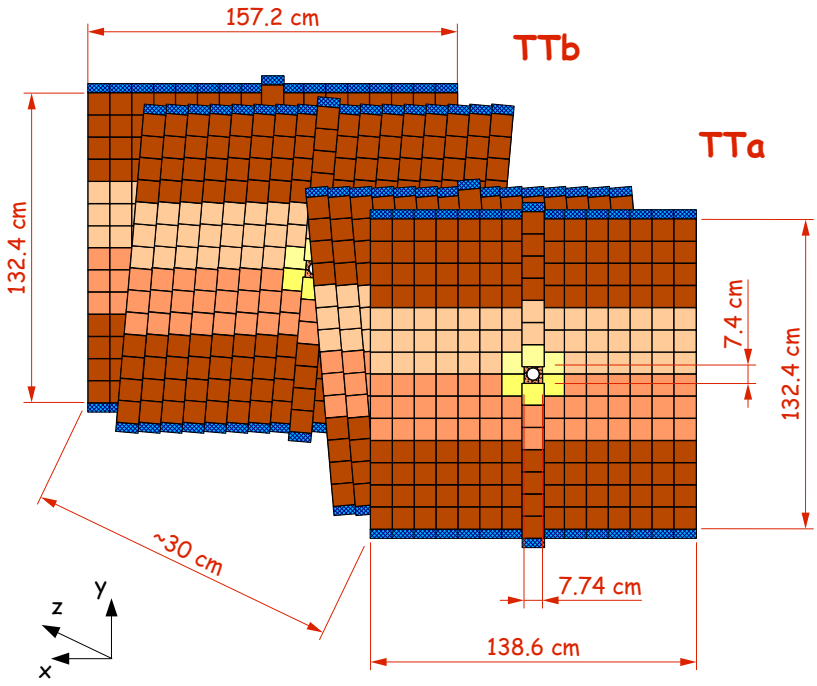

Figure 2.15: Layout of the four TT stations. The front and rear planes have sensors vertically arranged, while the two planes in the middle represent the u-plane and v-plane described in the text with sensors tilted by $\pm 5°$ respectively.

x-plane of the station in the middle. If the prediction matches a hit, it is added to the segment and it is used to determine more accurately the parameters of the parabola and all x hits in a window around the trajectory are collected to form the $X - Z$ projection of the segment candidate. After this step also the compatible hit from $u-$ and $v-$ planes of the tracking stations are added to the $X - Z$ projection in order to reconstruct the 3-dimentional segment. In a second step hits not associated with any reconstructed segment are matched with parabolic trajectories to find tracks crossing different $X - Y$ plane regions. Finally, reconstructed segments must satisfy quality requirements in order to be accepted.

Track finding is organized in a hyerarchical way: firstly the algorithm tries to reconstruct long tracks, then it picks up unused segments to reconstruct downstream and upstream tracks. In the end of each step a clone killer algorithm is applied. Long tracks are reconstructed using two algorithms. The first one extrapolates VELO segments to the tracking stations collecting together matching hits in the $X - Z$ plane and then adding also u and v plane hits. All the hits in the TT compatible with the trajectory are added to the track. The second algorithm matches reconstructed VELO and T stations segments one to each other, extrapolating VELO segments in the forward direction and T segments in the backward direction. TT hits close to the resulting track are added afterwards. Downstream tracks are reconstructed extrapolating T station segments to the TT and adding compatible hits. Upstream tracks are extracted from

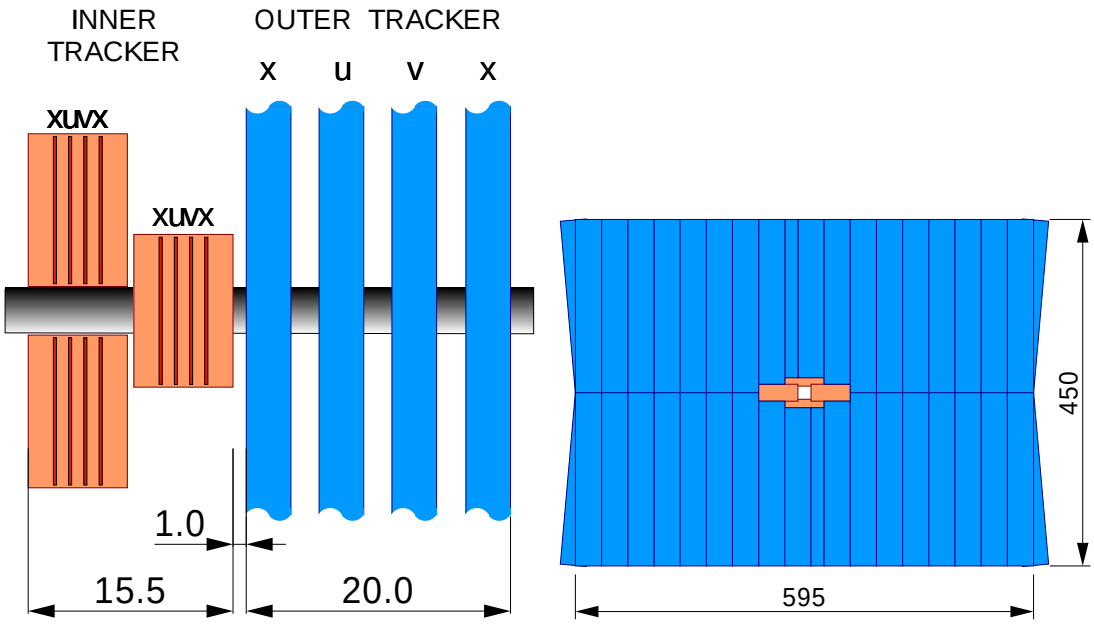

Figure 2.16: Left: layout of a T station from a side view. The IT sub-detector is placed in front of the OT sub-detector. The x- u- and v-planes described in the text are also drawn. Right: layout of a T station from a front view. The IT subdetector (in orange) is placed around the beam pipe, while the OT sub-detector covers the outer region of the station.

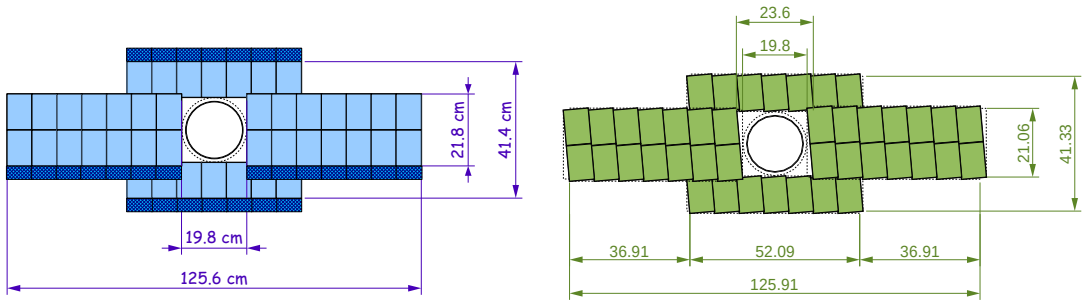

Figure 2.17: Layout of the x-plane (left) and u-plane (right) of the IT sub-detector. The alignment of sensor is vertical for the x-plane and tilted by $+5°$ for the u-plane.

the extrapolation of VELO seeds to the TT subdetector, requiring also a non-matching with any T station seed.

On all reconstructed tracks, before using the clone killer, a bi-directional Kalman filter is applied to better determine track parameters. The clone killer compares all tracks two by two. If two tracks share more than a certain percentage of hits they are considered clones. The track with more hits or, in case of the same number of hits, the one with best χ^2 is stored. Fig. 2.22 shows the track reconstruction efficiency as a function of track transverse momentum p_T obtained from $K^0_S \to \pi^+\pi^-$ decays reconstructed from 2010 long tracks sample and compared

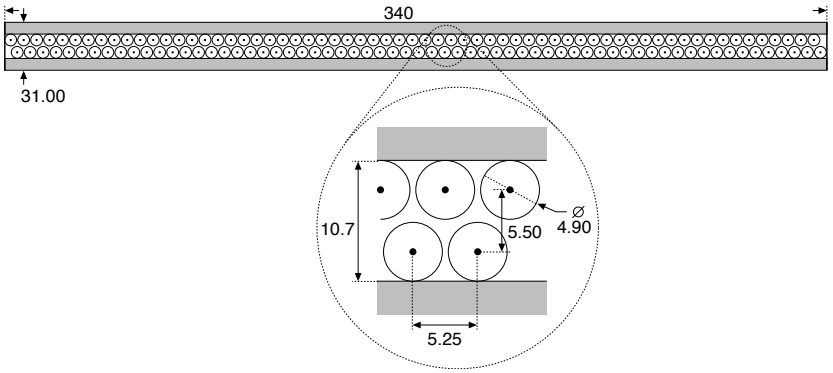

Figure 2.18: Cross section of a straw-tubes module. The zoom-in shows the honeycomb arrangement of the two layers of tubes.

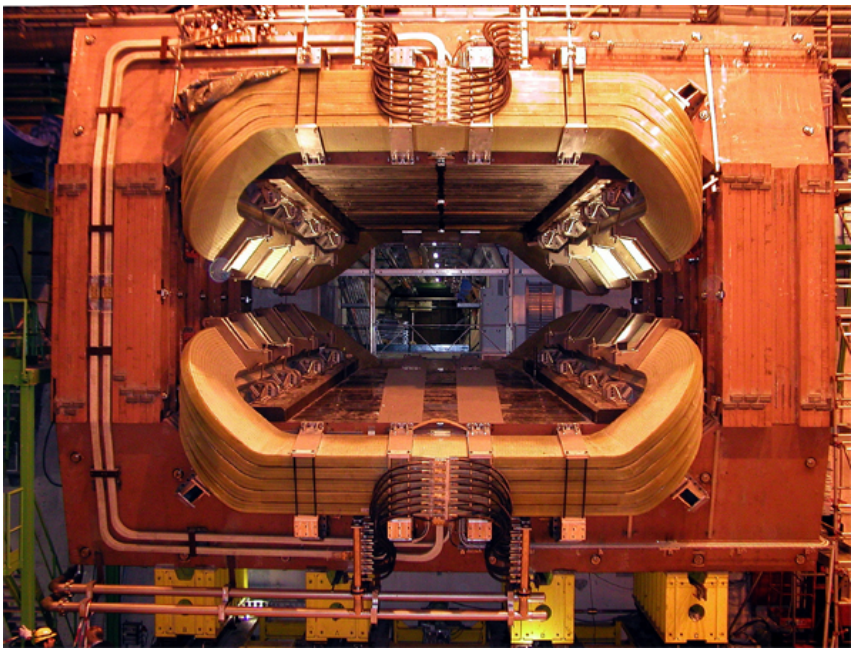

Figure 2.19: Front view of the LHCb dipole magnet after the installation in the detector cavern. The particular profile of the two coils, in order to follow the detector acceptance, is clearly visible.

with full Monte Carlo simulations. The momentum resolution achieved on long tracks results to be $\Delta p/p = (0.35 - 0.55)$ % as reported in Ref. [75].

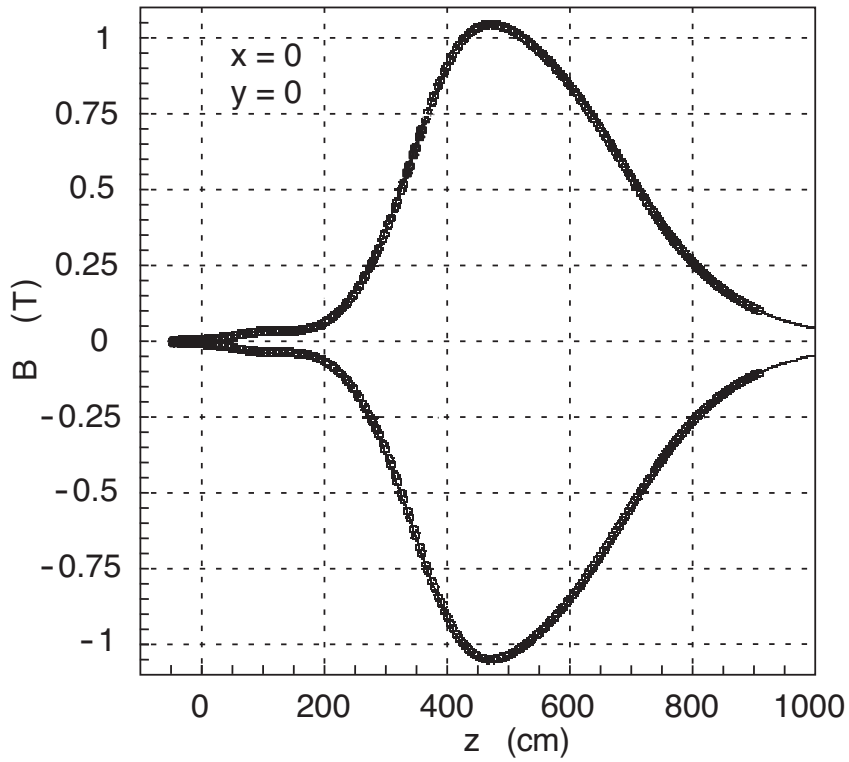

Figure 2.20: Y component of the magnetic field measured along the beam-pipe. Values of the measured field for both polarities (up and down) are represented by empty circles. The superimposed line represents the result of the model calculation.

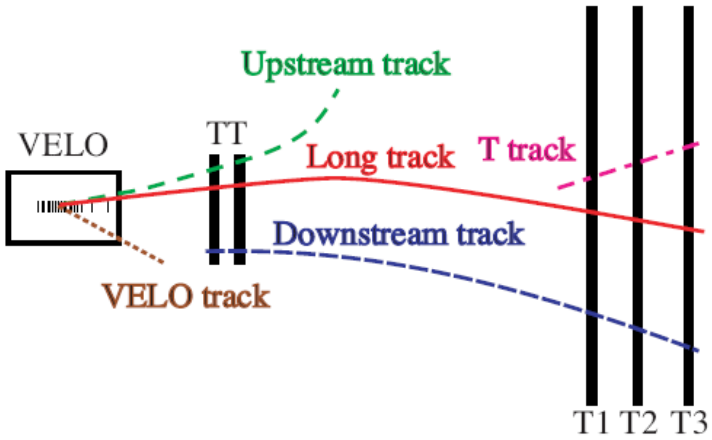

Figure 2.21: Schematic illustration of the various track types: long, upstream, downstream, VELO and T tracks. Tracking detector positions are reported as a reference.

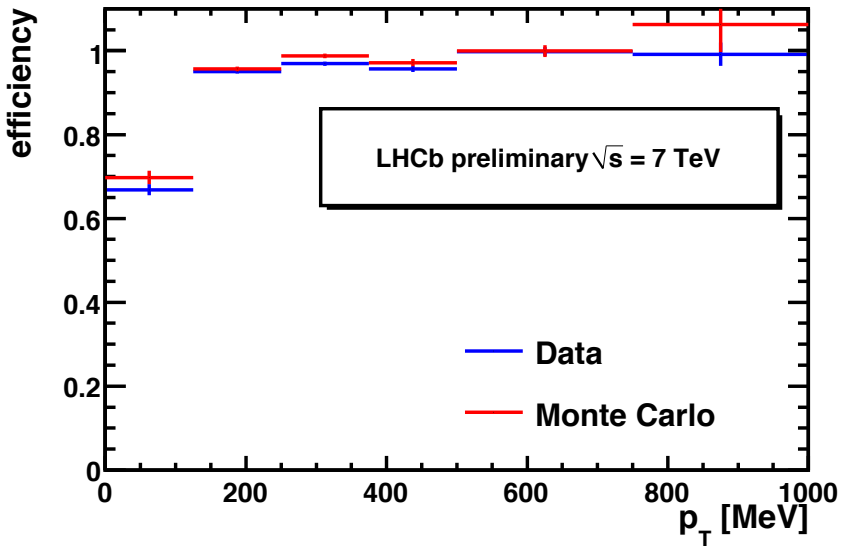

Figure 2.22: Efficiency of track reconstruction as a function of the transverse momentum p_T of the track. Efficiency as evaluated from real data (blue) and Monte Carlo simulations (red) are reported.

2.4 Identification of charged particles

Most of the $\mathcal{CP}$ violation measurements of the LHCb physics programme (and in particular those treated in this thesis) require the identification of charged leptons and hadrons. This task is accomplished by some dedicated sub-detectors that we are going to describe.

2.4.1 The RICH detectors

Cherenkov light detectors are used to discriminate charged pions, kaons and protons in a wide momentum range. Such a discrimination is crucial in the selection of B hadron decays with these particles in the final states. In addition the distinction between charged pions and kaons coming from the hadronization process of b quarks is crucial to determine the flavour state at the production of neutral B mesons. This procedure known as tagging and is used to determine if the neutral B meson at $t = 0$ has been produced as a B or $\overline{B}$. Cherenkov light detectors exploit the relation between the particle momentum and the emission angle of Cherenkov photons:

$$\cos(\theta_c) = \frac{1}{n \cdot v/c}, \tag{2.1}$$

where θ_c is the angle of Cherenkov photon emission with respect to the particle direction of flight, n is the refraction index of the radiator, v is the particle speed and c is the speed of light. Thus measuring also the momentum it is possible to determine the mass of the particle.

LHCb is provided by two Ring Imaging Cherenkov detectors (RICH1 and RICH2) [76] able to efficiently discriminate charged hadrons in the range between few GeV/c (typical of tracks used for tagging) up to about 150 GeV/c. This range of momentum comprises most of the particles

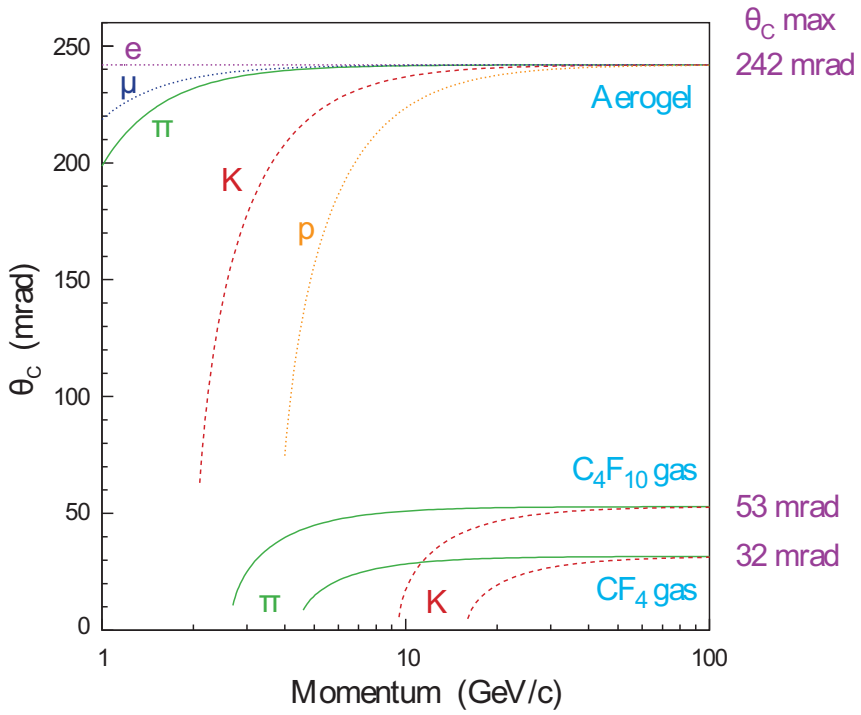

Figure 2.23: Cherenkov angle θ_c as a function of particle momentum p. The curves corresponding to the various radiators used in RICH1 and RICH2 and to the various particle types is reported.

coming from B hadron decays. RICH1 is optimized to identify tracks of lower momentum (between 1 and about 50 GeV/c), while RICH2 is optimized for the identification of tracks of higher momentum (up to 150 GeV/c). In fact, the only way to cover such a wide range of momentum is to use different radiators, with different refraction indices. This is because Cherenkov light is emitted only by particles with the parameter $\beta = v/c$ in the range $c/n < \beta < c$. For $\beta = 1/n$ the Cherenkov angle will be 0, while approaching the speed of light the Cherenkov angle will saturate at a value $\theta_c = \arccos(1/n)$. This behaviour is shown in Fig. 2.23. A schematical picture of RICH1 is shown in Fig. 2.24 (left). It is placed between the VELO and the TT detectors and is able to cover practically the entire geometrical acceptance of LHCb (between 25 mrad to 330 mrad). It uses two different radiators: a layer of 5 cm thick Aerogel, with a refraction index of about $n = 1.03$ (optimal for low momentum particles $1-10$ GeV/c) and a gap about 85 cm thick filled with C_4F_{10} with refraction index $n = 1.0015$ (optimal momenta up to 50 GeV/c). RICH2 (right picture in Fig. 2.24) is placed between the last tracking station and the first muon station (see Fig. 2.8). Its geometrical acceptance covers an angular region of about 120 mrad in the vertical plane and 100 mrad in the horizontal plane, the region with most of the high momentum particles. As radiator it uses CF_4 with refraction index $n = 1.00046$ inside a gap 170 cm thick.

In both the RICH detectors an optical system made of spherical and plane mirrors conveys the emitted Cherenkov photons on a lattice of photo-detectors (Hybrid Photon Detector, HPD). The HPD planes are placed out of the detector acceptance (where particle multiplicity is low) and properly shielded against the residual magnetic field (in particular the HPD's of RICH1).

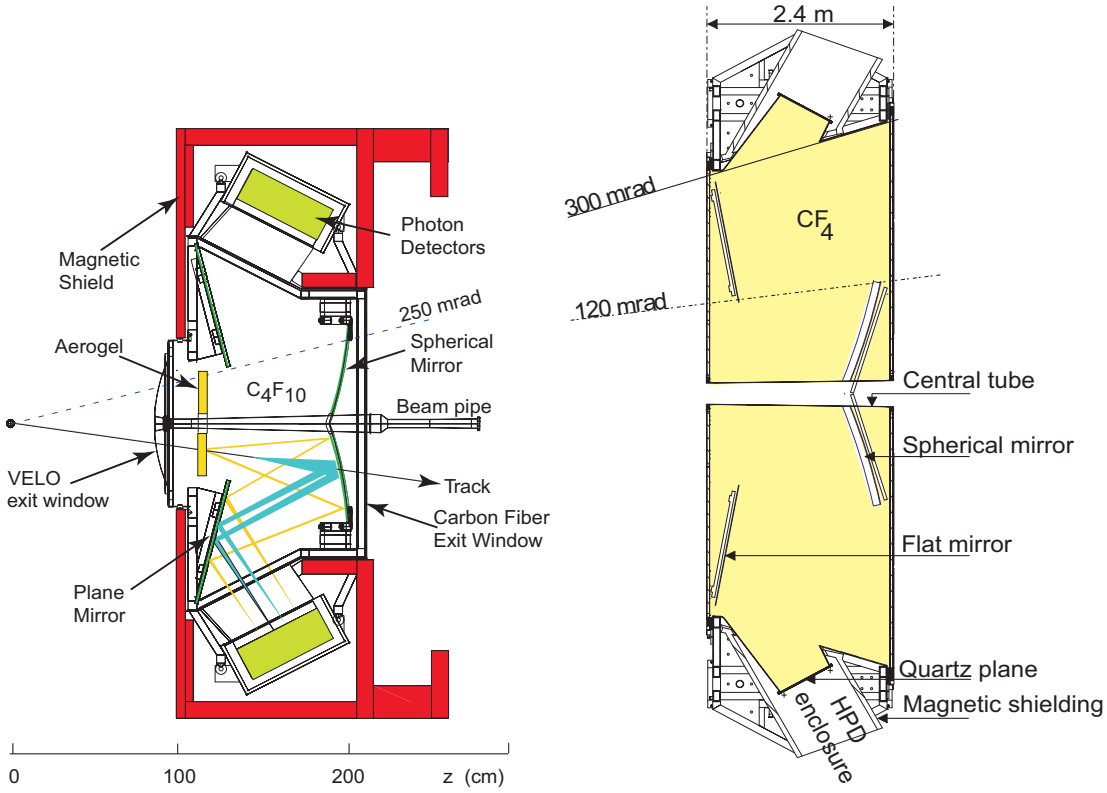

Figure 2.24: Left: schematic layout from a side view of the RICH 1 detector. The Cherenkov light as emitted by a charged track traversing the Aerogel tiles and the C_4F_{10} radiator is also drawn. Right: Schematic layout from a top view of the RICH2 detector.

2.4.2 Particle-identification performances

RICH detectors give the information to evaluate the mass-hypothesis likelihood for a given particle. As Cherenkov photons emitted by a particle are charachterized by the same emission angle θ_c, they are expected to form a ring on the HPD plane, with radius proportional to θ_c. Thus, given the direction of a particle, it is possible to extrapolate the position of the corresponding ring centre on the photo detector plane. The distribution of Cherenkov photon hits on the plane, as a function of the radial distance from the centre, is thus expected to be peaked around a value (related to θ_c) and smeared by resolution effects. In this way, fitting the photon hit positions, it is possible to measure in a simple and fast way θ_c for each particle. However, as the main background to the signal comes from photons emitted by other particles, in LHCb a "global" approach has been developed to measure the mass-hypothesis likelihood of tracks. Fig. 2.25 shows the Cherenkov angle as a function of track momentum (only for isolated tracks) with the theoretical expectation superimposed. The straightforward way to the "global" approach would be to perform a global fit of all Cherenkov photons emitted by all particles, resulting in a very complex and slow multi-parameter fit, without solving the problem of the other backgrounds, except that from cross-contamination between tracks.

Instead, for a given set of mass-hypotheses, the probability for a signal photon to be detected

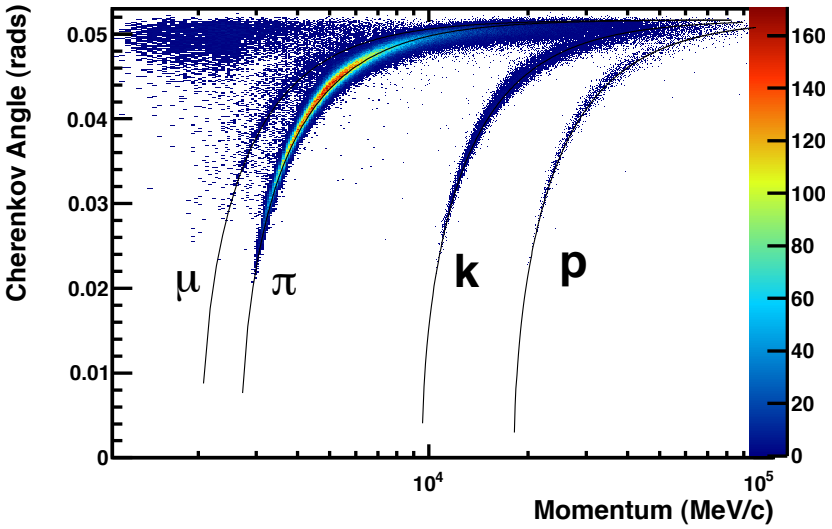

Figure 2.25: Cherenkov angle as a function of track momentum measured for isolated tracks. The theoretical expectations for the various particle hyptheses are superimposed.

on a specific pixel is computed. The probability computation is extended including background sources (such as scattered Cherenkov light and electronic noise) and detector effects (such as different efficiencies for different HPD's and edge effects). Then the expected contribution from all sources is compared with the observed number of photons and a likelihood is calculated.
It is important to note that within this method the change in the likelihood depends only on mass-hypothesis assigned to the tracks. Only 5 mass-hypotheses are considered for charged tracks: electron, muon, pion, kaon and proton. The computation of the likelihood for all possible hypotheses of all tracks results to be unfeasible. In order to reduce the number of likelihood evaluation a different strategy is used. An initial value of the likelihood is computed assigning to all tracks the pion mass-hypothesis. Then for each track in turn the mass-hypothesis is changed to e, μ, K and p, whilst leaving all the other track hypotheses unchanged. The mass-hypothesis change that returns the largest likelihood improvement is found and the mass-hypothesis for that track is set to its preferred value. The procedure is iterated changing again mass-hypoteses for all tracks until no improvements in the likelihood is found. Each computed value of the likelihood is stored in order to be used in the evaluation of the final particle-identification discriminator.

The particle-identification discriminating variable used in LHCb is the so called $\Delta \log \mathcal{L}$. The value of the likelihood is computed changing the mass-hypothesis of a single track, mantaining all the other hypotheses unchanged with respect to the maximum-likelihood solution. As the value of the global likelihood can be quite large its logarithm is used. In the end the pion mass-hypothesis is taken as reference, such that $\Delta \log \mathcal{L}$ for the pion hypothesis results to be always 0. Then the discrimination between mass-hypotheses is performed on the basis of the difference of the likelihood logarithm under a generic hypothesis and the pion hypothesis. For example $\Delta \log \mathcal{L}_{K\pi}(P)$ is the difference between the logarithm of the likelihood under the K hypothesis and under the π hypothesis for the particle P:

$$\Delta \log \mathcal{L}_{K\pi}(P) = \log \mathcal{L}_K(P) - \log \mathcal{L}_\pi(P), \tag{2.2}$$

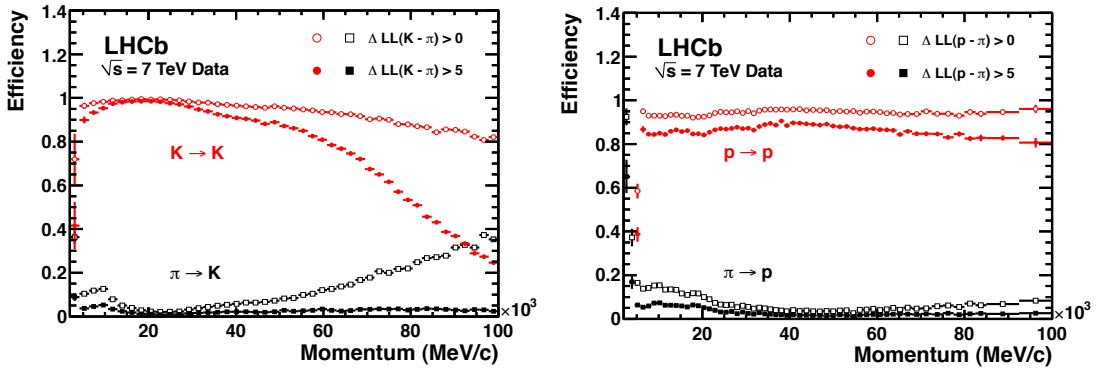

Figure 2.26: Left: Efficiency for the identification of kaons (red) and probability for the mis-identification of pions as kaons (black) as a function of particle momentum. Solid and empty points refers to different PID requirements. Right: Efficiency for the identification of protons (red) and probability for the mis-identification of pions as protons (black) as a function of particle momentum. Solid and empty points refers to different PID requirements.

thus a large positive value of $\Delta \log \mathcal{L}_{K\pi}(P)$ translates to a large confidence that the particle P is a kaon. Performances of RICH detectors in discriminating between mass-hypotheses have been studied by means of real data samples. Thanks to the high production rate and to their kinematic charachteristics, particle decays like $K^0_S \to \pi^+\pi^-$, $\Lambda \to p\pi^-$ and $D^{*+} \to D^0 (\to K^-\pi^+)\,\pi^+$ allow to select pure high statistics samples of pions, kaons and protons, without making any use of RICH detectors. Due to the dependence of θ_c on particle momentum, also $\Delta \log \mathcal{L}$ depends on particle momentum. Fig. 2.26 shows the efficiency (particle exactly identified) and misidentification (wrong mass-hypothesis assigned) fraction, as a function of momentum, for pions, kaons and protons achievable with two different PID requirements.

2.4.3 The calorimeter system

The calorimeter system [77] is used to identify neutral hadrons, electrons and photons, measuring their energy. In addition it provides important information for the Level-0 trigger (L0-trigger) evaluating transverse energy E_T of hadrons, photons and electrons[1]. It is divided into four sub-detector:

- Scintillator Pad Detector (SPD);
- Pre-Shower (PS);
- Electromagnetic Calorimeter (ECAL);
- Hadronic Calorimeter (HCAL).

Each sub-detector is divided into regions where differently sized sensors are used. ECAL, PS and SPD are divided into three regions (inner, middle and outer as shown in Fig. 2.27) while HCAL

[1]Transverse energy is defined as $E_T = E * sin\theta$ where E is the cluster energy in the calorimeter and θ is the polar angle of the cluster.

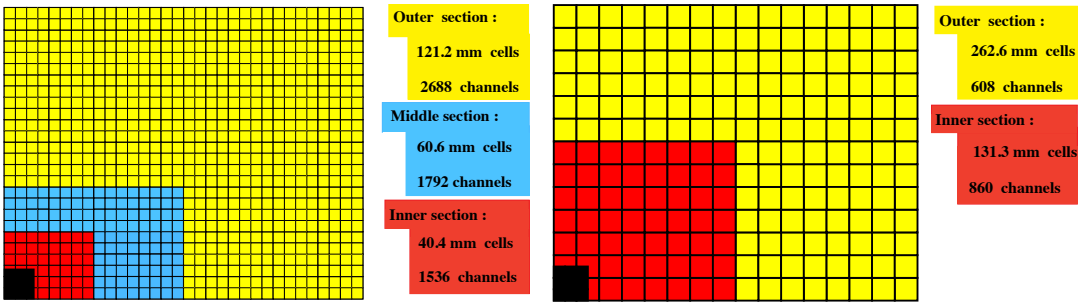

Figure 2.27: Lateral segmentation of the SPD/PS and ECAL (left) and the HCAL (right). One quarter of the detector front face is shown. In the left figure the cell dimensions are also given.

is subdivided only into two regions. The size of sensor elements increases going far from the beam-pipe and the high occupancy region. Such choice is motivated by a compromise between occupancy (in order to guarantee a good resolution in energy and position of clusters) and the necessity to mantain a reasonable number of read-out channels. SPD and PS are auxiliary sub-detectors of ECAL and are placed before it. SPD is used to discriminate between charged and neutral particles, as the former ones produce light inside the scintillator layers while the latter do not. The PS is used for a better discrimination between electrons and pions both at the trigger level and in the offline reconstruction. Both sub-detectors consist of a scintillator plane and they are separated by a lead converter layer about 15 mm thick. The total material budget of the two sub-detectors corresponds to about 2.5-3 radiation lengths. The light produced inside the scintillator is collected, by wave length shifter optical fibers, on multi-anode photo-multipliers.

The ECAL is a sampling calorimeter realized using Shashlik technology and separated into different independent modules (a schematic view of an ECAL module is shown in Fig. 2.28). It is composed of 66 lead converter layers (2 mm thick), each one sandwiched between plastic scintillator layers 4 mm thick. The total material budget for each module is about 25 radiation lengths and 1.1 nuclear interaction lengths. The optical fibers WLS (drawn in green in Fig. 2.28) cross longitudinally the entire module and bring light to the read-out photo-multipliers situated in the backward part of the module. Sizes and number of read-out channels of modules for different regions are different: the inner region has modules with a section of 4×4 cm^2 with 9 read-out channels per module; the middle region has modules of 6×6 cm^2 with 4 channels each; finally the outer region has 12×12 cm^2 modules with one channle each.

The hadronic calorimeter HCAL has as main purpose the measurement of energies of hadronic showers that is the main information needed by the Level-0 hadronic trigger. Its structure is similar to ECAL, but each module is built by layers of scintillators 4 mm thick separated by layers of steal 16 mm thick. The total material budget corresponds to 5.6 nuclear interaction lengths. Module sizes are bigger than for ECAL and only two regions are defined: inner and outer (see Fig. 2.27). In the inner region modules are 13×13 cm^2, while in the outer region they are 26×26 cm^2.

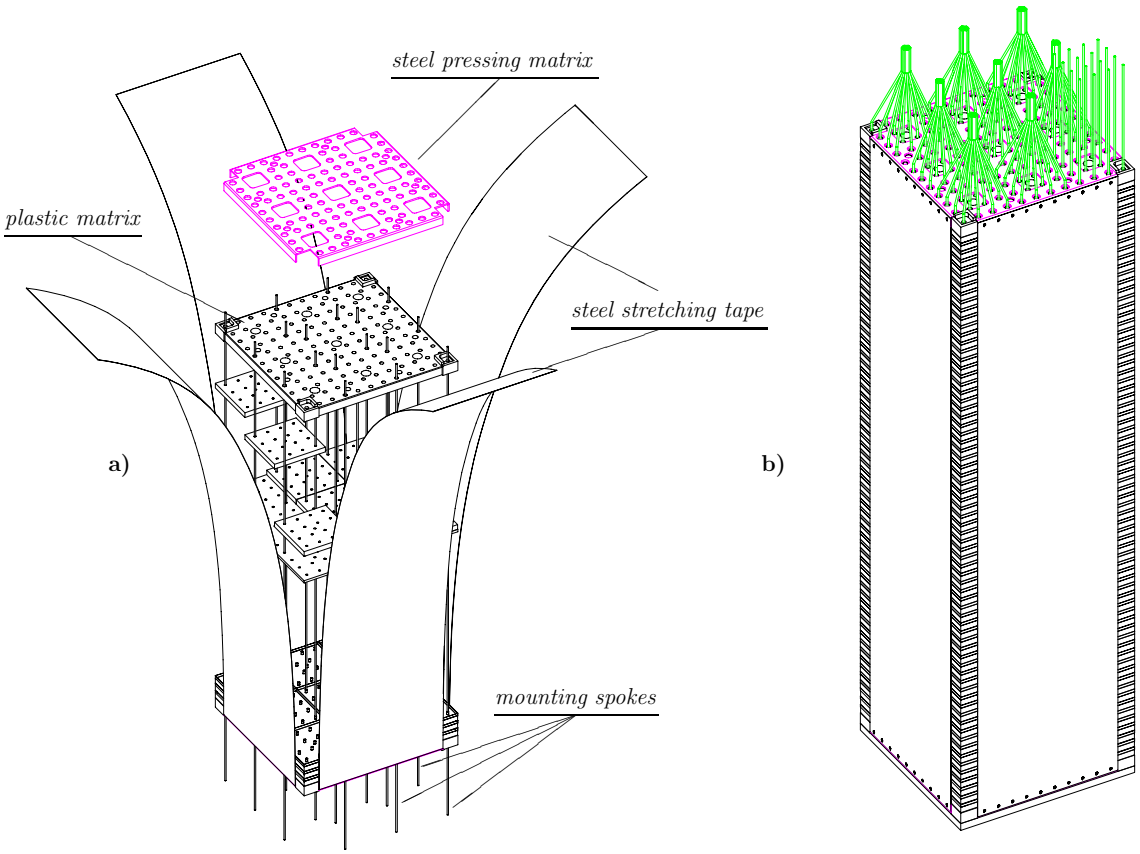

Figure 2.28: Left: Assembly of an ECAL module. The lead/scintillator layers are shown. Right: Assembled ECAL module. The green lines represent the optical fibers conveying the light to the photo-multipliers.

2.4.4 Performances of the calorimeters system

Performances have been evaluated from several test beam made before the start of the data taking [78]. Energy resolutions are given by $\sigma(E)/E = (8.5-9.5)\%/\sqrt{E} \oplus 0.8\%$ for ECAL and $\sigma(E)/E = (69 \pm 5)\%/\sqrt{E} \oplus (9 \pm 2)\%$ for HCAL. The calibration of ECAL is realized by reconstructing resonances decaying to two photons like $\pi^0 \to \gamma\gamma$ and $\eta \to \gamma\gamma$. Fig. 2.29 shows the $\gamma\gamma$ invariant mass spectrum where π^0 and η peaks are clearly visible. Any difference between photo multipliers response and deposited energy will result in a shift of the reconstructed invariant mass peak. The reconstruction of π^0's allows indeed to calibrate the ECAL response on the basis of the observed mass shift. Calibration of HCAL can be achieved by measuring the ratio E/p between the energy E as measured in the calorimeter for a hadron with momentum p, as measured from the tracking system. In Fig. 2.30 the distribution of E/p is shown, comparing full Monte Carlo simulations with real data. Differences between simulations and the real data do not exceed 3%.

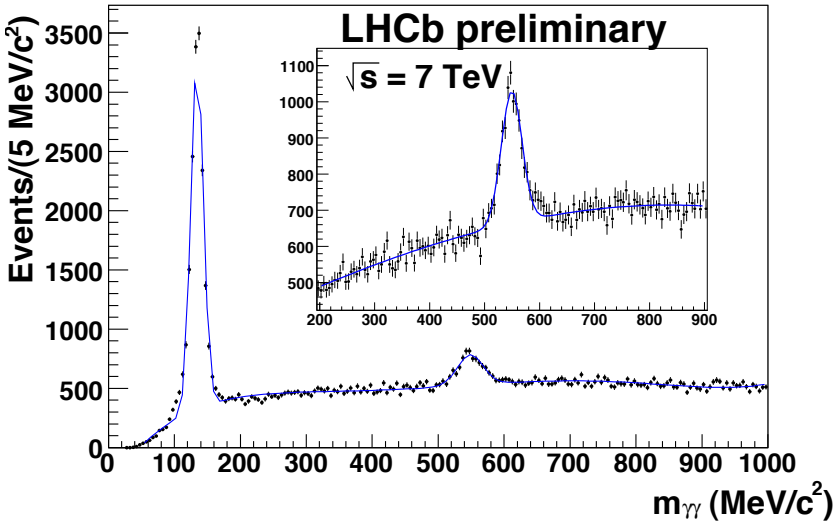

Figure 2.29: Reconstructed $\gamma\gamma$ invariant mass obtained from real data. The $\pi^0 \to \gamma\gamma$ and $\eta \to \gamma\gamma$ decay peaks are clearly visible. The superimposed line is the result of a best fit.

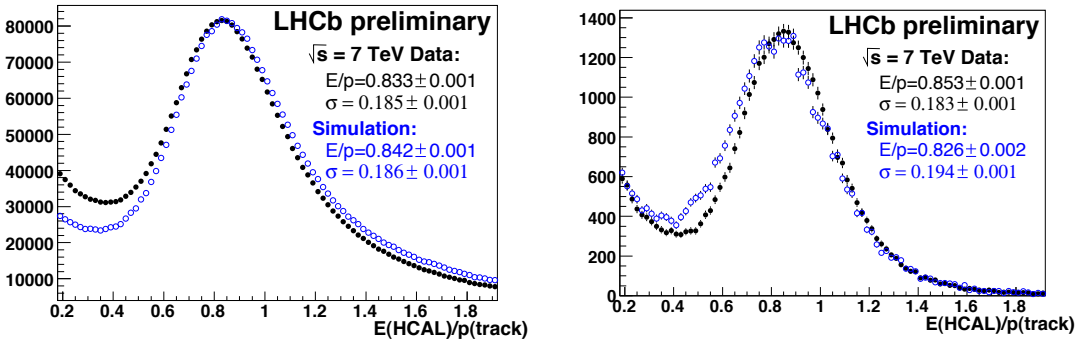

(a) (b)

Figure 2.30: Distribution of the ratio E/p as measured by the inner (a) and outer (b) of the HCAL detector. Both real data measurements (black points) and Monte Carlo simulations (blue points) are shown.

2.4.5 Muon detectors

Muons with high p_T and high impact parameter with respect to the primary vertex are a very clean signal for triggering events with B-hadrons. Such muons are also utilized in the tagging algorithm to identify the flavour of the spectator B-hadron produced associated to the signal B-hadron. Muons are even present as final products in various core analyses of LHCb, like $B_s^0 \to J/\psi\,(\mu^+\mu^-)\,\phi$, $B^0 \to K^{*0}\mu^+\mu^-$ and $B_{s,d} \to \mu^+\mu^-$.

The muon detector [79] is composed of five stations (M1,..., M5), covering an angular accep-

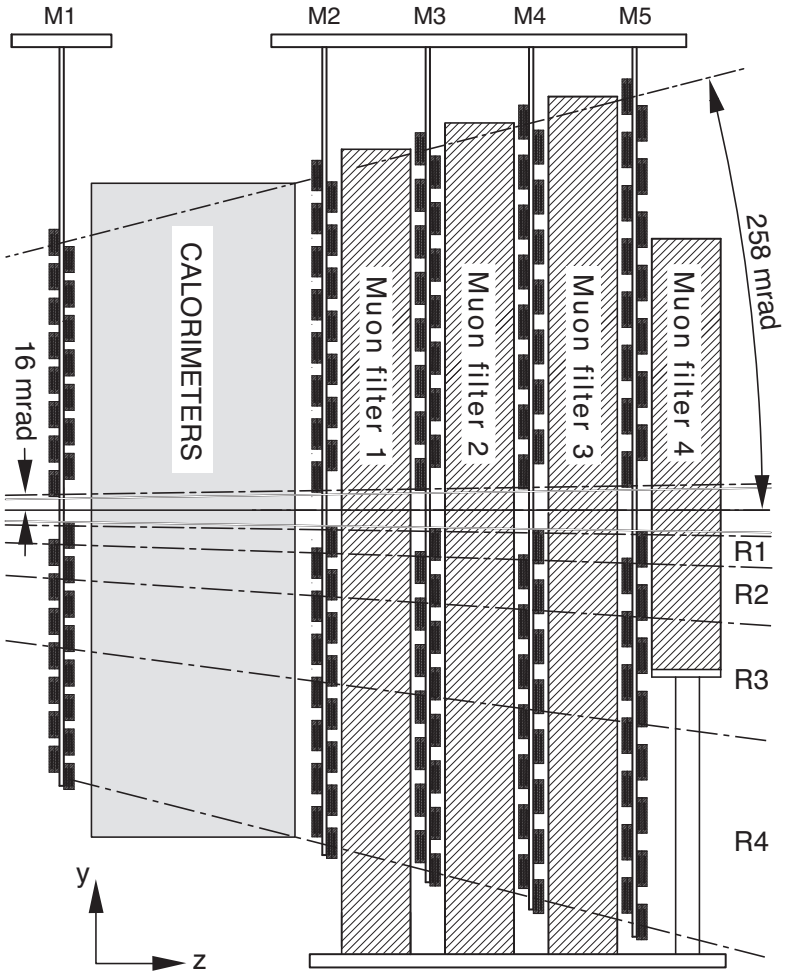

Figure 2.31: Scheme of the muon system from a side view.

tance of ±300 mrad in the horizontal plane and ±200 mrad in the vertical plane, corresponding to a geometrical efficiency of about 46% for the detection of muons coming from B-hadrons. The first muon station M1 is placed before the calorimeter system in order to avoid possible multiple scattering effects from the calorimeter material budget, that can modify the muon trajectory. M2-M5 are placed after the hadronic calorimeter and are separated by iron planes 80 cm thick as depicted in Fig. 2.31.

Each muon station is subdivided into four regions (R1-R4) with increasing distance and segmentation from the beam-pipe, in a ratio of $1 : 2 : 4 : 8$ (see Fig. 2.32). With this geometry the charged particle occupancy is expected to be more or less the same in each region. Multi-Wire Proportional Chambers (MWPC) are used for all regions except the inner region of station M1 where the expected particle rate exceeds safety limits for ageing. In this region triple-GEM detectors are used. Multi-wire chambers have a structure with four overlapped gaps, in order to increase the detection efficiency for the single hit, each one 5 mm thick and with a distance between wires of about 2 mm (see Fig. 2.33). The total number of chambers used to build the

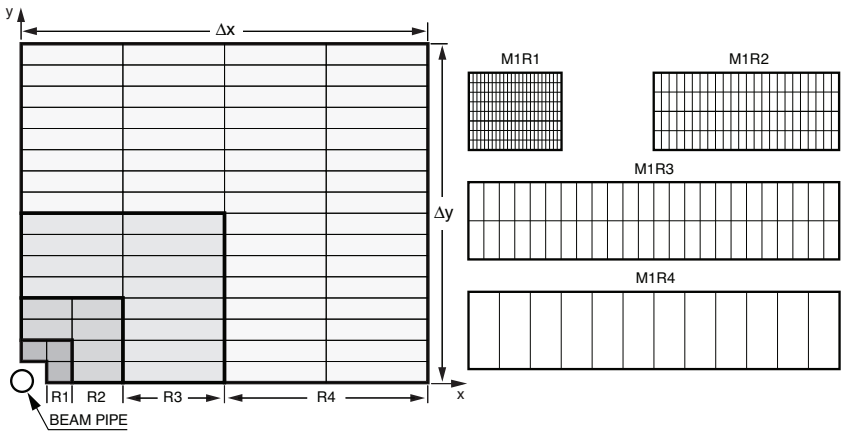

Figure 2.32: Left: front view of a quadrant of a muon station. Each rectangle represents one chamber. Right: segmentation of four chambers belonging to the four regions of station M1.

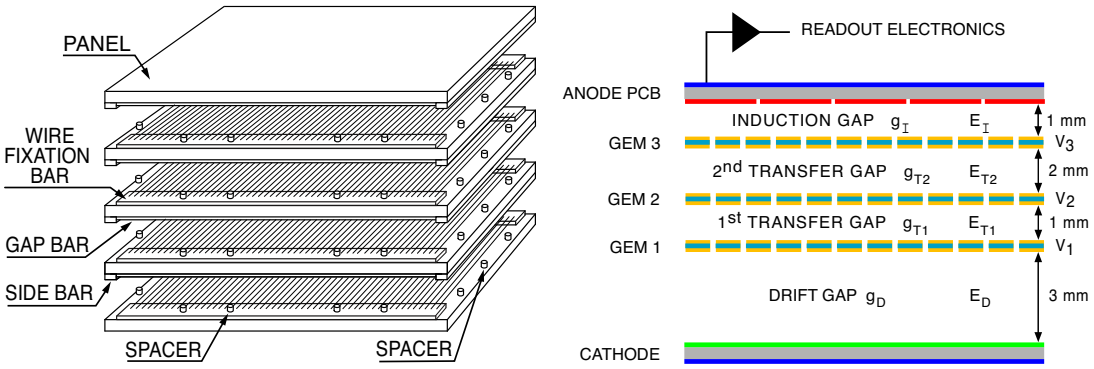

Figure 2.33: Left: schematic view of a MWPC showing the various elements. Right: schematic cross section of a triple-GEM detector showing the most relevant elements and dimensions.

muon detector is 1380. The triple-GEM detector consists of three gas electron multiplier (GEM) foils sandwiched between anode and cathode planes (see Fig. 2.33).

2.4.6 Performances of the muon-ID algorithm

The algorithm for muon-ID in the hardware trigger starts from hits in the M3 station. For each hits a straight line is extrapolated to the interaction region defining a "field of interest", that takes into account also the magnetic field kick, around such a trajectory. In order to identify a muon coincidence in all five muon stations and inside the field of interest are required. The muon identification algorithm for physics analysis starts from long and downstream tracks, extrapolated from the T stations to all the muon stations. Hits found inside a region of interest around the extrapolated trajectory are then fitted together to form a muon track. In order to flag the track as a muon it is required to have hits in M1-M3 if its momentum is between 3

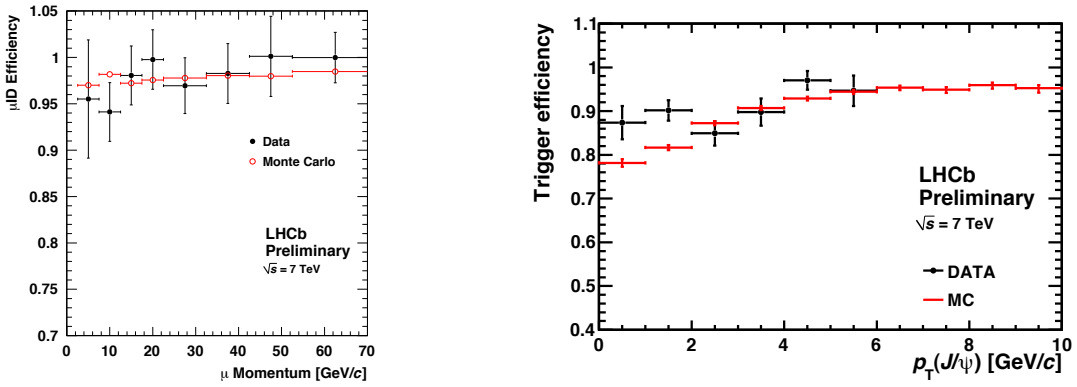

Figure 2.34: Left: muon identification efficiency as a function of the particle momentum, obtained from the study of $J/\psi \to \mu^+\mu^-$ decays. Performances obtained from real data (black) and Monte Carlo simulations (red) are shown. Right: muon trigger efficiency on the $J/\psi \to \mu^+\mu^-$ decau as a function of the transverse momentum of the J/ψ.

and 3.5 GeV/c, to have hits in M1-M4 if its momentum is between 3.5 and 4.5 GeV/c and to have hits in all the five station if its momentum is higher than 4.5 GeV/c. Complex algorithms are then used to assign a muon likelihood to each muon track that is then used as particle identification discriminator. Performances of muon-ID algorithm have been studied by means of $J/\psi \to \mu^+\mu^-$ decays in order to evaluate the efficiency and $K^0_S \to \pi^+\pi^-$ decays in order to evaluate mis-identification probability. Fig. 2.34 shows the muon identification efficiency from offline analysis and after the hardware and software trigger stages.

2.5 The LHCb trigger

As already said in previous chapters the production cross sections of $b\bar{b}$ [69] and $c\bar{c}$ [80] pairs are small with respect to the inelastic cross section. In addition, the capabilities to store data are limited by technological and cost constraints. Thus the LHCb trigger is required to be very efficient in accepting signals, rejecting most of the background events. The only way achieve the required efficiency and purity of the stored sample is to subdivide the trigger system into different levels. The LHCb trigger system is divided into three levels as shown in Fig. 2.35. The earliest trigger level (Level-0 or L0) is based on custom electronics and is designed to perform a first filtering, taking events with a maximum input rate of 40 MHz and sending them to the next trigger level at a maximum rate of about 1 MHz. Second (High Level Trigger 1 or HLT1) and third (High Level Trigger 2 or HLT2) trigger levels are software based and they perform a full reconstruction of the events on a dedicated computing farm. HLT1 filters heavy hadron events in an inclusive way and reduces the rate of accepted events to about 50 kHz. HLT2 is based on the same software used by HLT1 but it performs an exclusive selection of beauty and charm decays quite close to the final offline selections. The output of HLT2 is sent to mass storage at a rate of about 3 kHz.

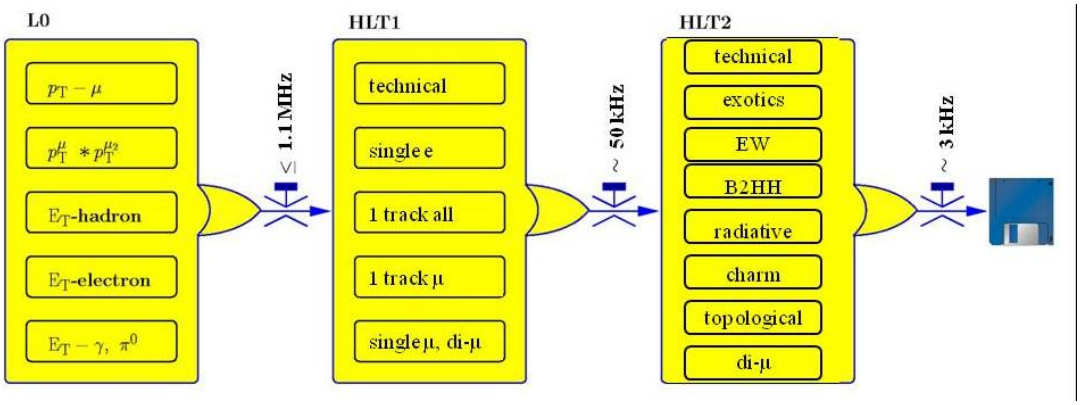

Figure 2.35: Structure of the LHCb trigger. The L0, HLT1 and HLT2 with their algorithms and output rates are reported.

2.5.1 The Level-0 Trigger

The L0 exploits fast detectors, able to provide valuable information without performing complicated reconstruction algorithms. The basic strategy is to measure transverse momentum of electrons, photons, hadrons and muons. The system utilizes three independent systems running in parallel.

Electron/photon trigger: it uses the electromagnetic calorimeter ECAL and the auxiliar PS and SPD detectors (to discriminate between charged and neutral particles). Custom electronic boards are programmed to measure energy of the electromagnetic showers, identifying those with highest transverse energy. An event is accepted if at least one cluster with transverse energy greater than a given threshold is present;

Hadronic trigger: it uses the information of HCAL. It works like the electron/photon trigger, accepting events with at least one hadronic cluster with transverse energy higher than a given threshold;

Muon trigger: it uses information coming from the hits in the five muon chambers. Muon segments are reconstructed dividing the muon chambers in fields of interest and connecting hits in the same field of interest from different chambers. The reconstructed tracks are then extrapolated to the proton-proton interaction region and a value for the transverse momentum of the muon is evaluated. Events are accepted if at least one muon candidate has a transverse momentum greater than a threshold; also a line allowing to select muon pairs is used, asking for muon pairs with the product of transverse momentum exceeding a given threshold.

Data taking conditions during 2010 and 2011 have been quite different from what planned during the design. In particular the mean number of interactions per bunch crossing has been approximatively four times the design level. This brought an increase in the number of primary vertices and tracks in each event. In addition the event size to be transfered to the second trigger level resulted to be higher. As a consequence both online and offline reconstruction and the data transfer timing for high occpuancy events overcame the capabilities of the DAQ and of the offline

reprocessing of LHCb. In order to cope with these difficulties a system to reject high occupancy events has been developed at the L0 trigger level. The very fast response of SPD detector allows to use it to roughly estimate the number of charged particles in the event satisfying the timing requirements of the Level-0 trigger. Events are accepted only if the number of hits in the SPD is less than 600. The final trigger decision is taken by an electronic module name *L0 Decision Unit*, that collects all the information and performs the OR of the three subsystem decisions. Events are accepted when at least one of the subsystems gives a positive decision.

2.5.2 The High Level Trigger

For events passing the Level-0 trigger, the full set of detector information is transferred to the Event Filter Farm (EFF), composed of about 1000 multi-core computing nodes, where the High Level Trigger (HLT) is run. The HLT is a software based C++ application performing a fast full reconstruction of events. Actually up to about 26000 copies of online reconstruction applications can run concurrently in the EFF. The HLT is divided in two steps: HLT1 and HLT2.

2.5.2.1 HLT1

Before the track reconstruction of the event is performed, the HLT1 algorithm makes a first selection of events based on the detector occupancy. Events with high occupancy (espectially in the OT sub-detector) could take much more than the average allowed processing time of ~ 25 ms to be reconstructed. Thus events with OT occupancy larger than 20% are rejected, allowing to avoid the throttling of the HLT process with a small loss in efficiency. For remaining events the reconstruction strategy is a consequence of the following considerations:

- High mass of B hadrons and their production processes imply that the particles coming from B hadron decays have a large momentum (p) and transverse momentum (p_T) compared with light-quark hadrons originating from the PV;
- The average decay length of B hadrons produced in the LHCb acceptance is ~ 1 cm so that their decay products will have a large impact parameter (IP) with respect to their PV.
- each B hadron decay has at least one final state particle characterized by large p, p_T and IP;
- the VELO reconstruction is fast enough to allow a full 3D pattern recognition and PV finding to be performed for all events entering the HLT;
- the full reconstruction can be performed only for a limited number of tracks due to limited time.

The last two points bring to the choice of subdividing the reconstruction into two steps. In the first step VELO tracks and PV are reconstructed. VELO tracks are selected asking for large impact parameters with respect to the closest PV and for a minimum number of hits in the VELO. In order to kill as much as possible ghost tracks the expected number of hits in the VELO for each track is performed considering the track direction and its first hit in the detector. If the difference between the expected number of hits and the number of hits used to reconstruct the tracks is greater than a certain threshold the track is rejected. Cut values changed several

times during 2010 but during 2011 they have been stable. As a reference the cut values used in the 2011 trigger are: $IP > 125$ μm, number of hits greater than 9 and difference between expected and observed hits less than 3. The number of VELO tracks selected by this first step allows to perform the full forward reconstruction without exceeding the timing limit. Forward reconstructed tracks are then selected asking for minimal p and p_T requirements further reducing their number. Remaining tracks are then fitted using a bi-directional Kalman filter with outlier removal, in order to obtain an offline-quality value for the track χ^2 as well as an offline-quality covariance matrix at the first state of the track, allowing a cut on the IP significance squared ($\chi^2(IP)$). Cut on $\chi^2(IP)$ is very efficient in rejecting background from the primary vertex and track χ^2 is very efficient in rejecting ghosts.

2.5.2.2 HLT2

The lower input rate to HLT2 allows to perform the bi-directional Kalman filter on all the tracks in the event passing a minimal requirement of $p > 5$ GeV/c and $p_T > 0.5$ GeV/c. In this way it is possible to proceed to the full reconstruction of beauty and charm hadron decays with an almost offline-like reconstruction quality. HLT2 filtering is mainly based on three inclusive selections, so-called topological lines. In addition few dedicated lines for the core analyses of LHCb are used.

The main strategy of topological line is to build multibody candidates in the following way: two input particles are combined to form a two-body object; another input particle is added to the two body object to form a three-body object, and so on; the kaon mass hypothesis is assigned to all particles. Thus an n-body candidate is formed combining a $(n-1)$-body candidate and a particle (saving CPU time with respect to combining directly n particles). Only a particle satisfying a cut on the distance of closest approach ($DOCA$) can be added to form a $(n+1)$-body candidate. When a 2-body object is built, a $DOCA < 0.15$ mm cut is imposed for the object to either become a 2-body candidate or to become the seed for a 3-body candidate. When a 3-body object is made by combining a 2-body object and another particle, another $DOCA < 0.15$ mm cut is imposed for the object to either become a 3-body candidate or input to a 4-body candidate. This DOCA is of the 2-body object and the additional particle, not the maximum DOCA of the three particles. This greatly enhances the efficiency of the HLT2 topological lines (in particular on $B \to DX$ decays) and saves CPU time. In addition to the topological lines, HLT2 contains a set of lines which exploit tracks which have been identified as muons. Dimuon candidates are formed and, depending on their mass, cuts are applied on the flight distance and p_T of the dimuon candidate. Single muon candidates are accepted either requiring large p_T, or a combination of $\chi^2(IP)$ and p_T cuts.

2.6 Computing

The availability of computing resources is a key factor in a modern High Energy Physics (HEP) experiment. In particular the amount of data delivered by LHC and thus collected by the experiment can not be processed inside one computing center alone. In addition the distribution of data to various storage centres guarantees the possibility to have various backup copies of data. The baseline LHCb computing model is based on a distributed multi-tier regional centre model denominated WLCG [81]. The LHCb computing model is centrally controlled by the DIRAC [82] framework (Distributed Infrastructure with Remote Agent Control) and in partic-

ular by a version of DIRAC specifically designed for the LHCb collaboration. The principal DIRAC functionality are the Workload Management System (WMS), the Data Management System (DMS) and the Transformation Management System (TMS). WMS exploit the now widely used concept of Pilot Agents, allowing an efficient allocation of computing resources. DMS manage in a versatile way the routine distribution tasks. TMS is built on top of the Workload and Data Management services, providing an automated data driven submission of processing jobs. A workload monitoring service allows an on-time monitoring of resource usage and of storage system status. The event filtered by the EFF are sent to the storage of the CERN Tier-0. At this level data contains only the information of the detector itself, like hits in the tracking system, response of the calorimeter read-out, the hits on the HPD plane of the RICH system and are denominated RAW data. From the Tier-0 storage RAW data are copied to different Tier-1's where they will be processed. Data are transferred dependently on the available storage at the various Tier-1's. The next stage consists in data reconstruction, where RAW files are processed downloading them directly to the worker node where the process will run. Reconstruction consists in providing physical quantities out of the detector information: track trajectories and momentum, primary vertex coordinates, energy of calorimeter clusters, mass-hypothesis likelihood for the tracks. The output of the reconstruction phase is a new data type, the so called SDST. SDST's do not contains all the detector information, but just the reconstructed physical quantities. The pattern recognition algorithms in the reconstruction program make use of calibration and alignment constants to correct for any temporal changes in the response of the detector, its electronics and in its movements. Such information are stored into distributed databases, continously updated by online monitoring of detector response. The computing model plan periodical reprocessings of collected data during the year, in order to utilize more precise calibration and alignment information obtained from off-line reprocessed data. The next stage of the computing system consists of a preselection of events named "Stripping". The output of this stage will be used for the physics analysis, thus is necessary to mantain it available on disk. The amount of disk space required by the full LHCb data sample would be too much expensive. In addition the fraction of events useful for each single analysis inside the total sample is very small. Thus the "Stripping" stage runs loose selections on the collected data sample, filtering the sample and creating the candidates that will be used in the final analysis. The events that pass the selection criteria will contain the candidates, the information of the reconstruction phase and also the RAW data relative to each event, in order to have as detailed event information as needed for the analysis. Because of this the output file are named (full) DST. "Stripping" selections are divided into physics macro areas of interest denominated "streams" (BHADRON, LEPTONIC,CHARM,...). As the stripping output from each SDST+RAW file could contain very few selected events, files are merged up to a dimension of about 5 GB for each final merged DST. In addition, in order to facilitate the access to interesting events, merged DST are separated according to "streams", *i.e.* they contain only events filtered by a sub-group of selections. A schematic explanation of the process is shown in Fig. 2.36. For what concerns simulated data, the processing phases are the same described above, but with small differences. Simulated RAW data (MC-RAW) are produced from a detailed description of the LHCb detector incorporating the current best understanding of detector reponse, trigger response and dead material. MC-RAW data contain simulated hit information and extra "truth" information. The truth information is used to record the simulated particles in the event and their relationship with hits in the detector. Such truth information are carried through all the processing step in order to use it during final analysis. The main difference with respect to real data is that

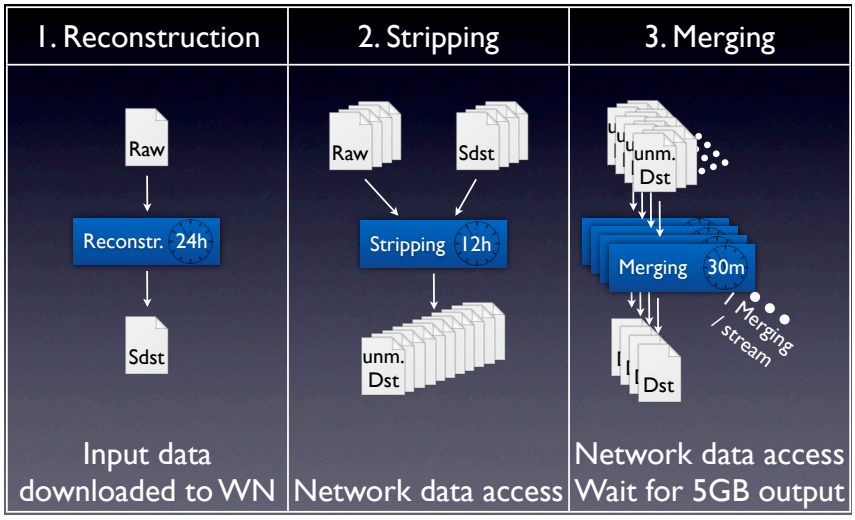

Figure 2.36: Schematic view of the "Reconstruction", "Stripping" and "Merging" steps of the data processing as described in the text.

Process	Data Type	CPU (HS06·s/evt)	Storage (kB/evt)
Data Taking	RAW	–	50
Reconstruction	SDST	25	40
Stripping	DST	1.75	130
Simulation	DST	1700	400

Table 2.1: Computing resources needed for the processing of a single event at each step as observed during the first half of 2011.

trigger and stripping responses are just used to flag events, without rejecting it in case of non affermative answer from selection algorithms. In order to save storage space also production with trigger and stripping in "rejection" mode are planned. Another difference with respect to real data processing is that all the steps except "merging" are executed one after the other on the same worker node, saving the output of intermediate steps temporarily on the local worker node disk. Because of the presence of "truth" information inside the data, simulated files are bigger than real data files. As for real data processing, simulated data are produced almost continuously during the year, using updated information on detector response and alignment, stored inside distributed database. Final DST's (both from real and simulated data) are meant for user analysis, thus they need to be stored on disk for a faster and more efficient access. RAW and SDST files, instead, are transferred to magnetic tape support after the creation of the corresponding DST in order to save disk space. In order to facilitate calibration, alignment and comparison of performance between different processings of data, at least the last two corresponding DST's are mantained on available on disk. In Tab. 2.1 are reported the computing resources needed to process and store a single event at each step, as observed during the first half of 2011 activity.

Chapter 3

$\mathcal{CP}$ violation in $B^0_{(s)} \to K\pi$ decays using 2010 data

In this chapter we present an analysis performed using the data collected by LHCb during 2010 at a center of mass energy of 7 TeV. The data sample is composed of the full Reco08-Stripping12 BHADRON stream for both magnet polarities, and corresponds to an integrated luminosity $\int \mathcal{L}dt \simeq 37$ pb^{-1}. We report measurements of the direct CP asymmetries in the $B^0 \to K\pi$ and $B^0_s \to \pi K$ decays, defined in terms of decay rates as

$$A_{CP}(B^0 \to K\pi) = \frac{\Gamma(\bar{B}^0 \to K^-\pi^+) - \Gamma(B^0 \to K^+\pi^-)}{\Gamma(\bar{B}^0 \to K^-\pi^+) + \Gamma(B^0 \to K^+\pi^-)} \tag{3.1}$$

and

$$A_{CP}(B^0_s \to \pi K) = \frac{\Gamma(\bar{B}^0_s \to \pi^-K^+) - \Gamma(B^0_s \to \pi^+K^-)}{\Gamma(\bar{B}^0_s \to \pi^-K^+) + \Gamma(B^0_s \to \pi^+K^-)}. \tag{3.2}$$

3.1 Event selection

3.1.1 Stripping

The events used for this analysis are those passing by the `Hb2ChargedBody` stripping line. This stripping line implements an inclusive pre-selection of $B \to h^+h'^-$ candidates, with no requirements on the identity of the daughter particles, i.e. without using information provided by the Particle Identification (PID) sub-detectors.

The first step of the stripping pre-selection consists of applying some filter criteria to each charged track in the event, in particular cutting on (the small roman numerals in parentheses indicate the corresponding entries in Tab. 3.1):

- the transverse momentum of the track (i);
- the smallest impact parameter of the track computed with respect to all the reconstructed primary vertices (ii);
- the reduced χ^2 of the track reconstruction (iii).

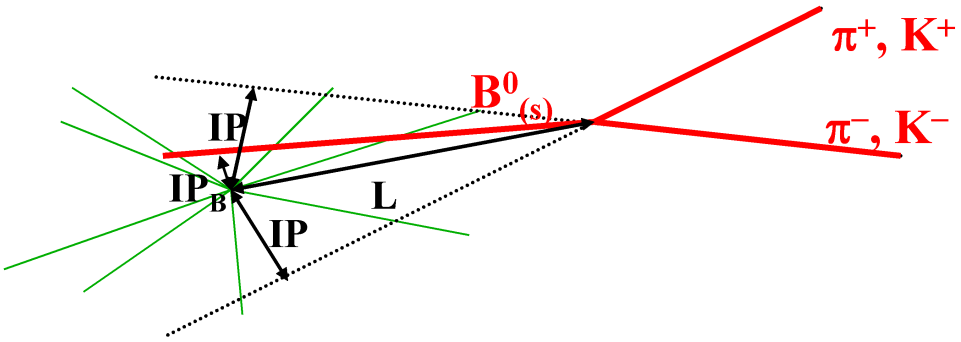

Figure 3.1: Sketch of the two-body B meson decay topology.

These three simple criteria provide a reduction of the number of track combinations to process in the subsequent steps.

Before fitting the two tracks to a common vertex, for each pair of oppositely charged tracks we perform a further reduction of the sample by cutting on:

- the invariant mass of the two tracks, assuming the pion-mass hypothesis for each track (iv);
- the distance of closest approach between the two tracks (v);
- the larger of the transverse momenta of the two tracks (vi);
- the larger of the smallest impact parameters of the two tracks computed with respect to all the reconstructed primary vertices (vii);

Finally, the surviving pairs are fitted to a common vertex and a B hadron candidate is defined. On this candidate we apply the last set of cuts on:

- the invariant mass, again calculated assuming the pion-mass hypothesis for each track, but using momenta adjusted by the common vertex fit (viii);
- the impact parameter of the B candidate, in order to constrain its direction of flight to point to the primary vertex (ix);
- the distance of flight, i.e. the distance between the primary and secondary vertices (x).

A graphical representation of the decay topology is shown in Fig. 3.1. The values of the stripping cuts are summarized in Tab. 3.1.

3.1.2 Offline selection

An offline selection is applied to the events that pass the stripping line to further refine the data. A set of kinematic selection cuts is imposed, and then particle identification cuts are applied to the two final state tracks, in order to disentangle the various $B \to h^+h'^-$ decay modes.

ID	Cut type	Accepted regions
i	Track p_T [GeV/c]	> 0.7
ii	Track IP [μm]	> 80
iii	Track χ^2/d.o.f.	< 5
iv	$m_{h^+h'^-}$ [GeV/c^2]	$[4.5,\ 6.5]$
v	Distance of closest approach [μm]	< 80
vi	$\max(p_T^{h^+},\ p_T^{h'^-})$ [GeV/c]	> 2.4
vii	$\max(IP^h,\ IP^{h'^-})$ [μm]	> 200
viii	m_B [GeV/c^2]	$[4.8,\ 5.8]$
ix	IP_B [μm]	< 60
x	L_B [mm]	> 1.8

Table 3.1: Summary of stripping cuts used in the `Hb2ChargedBody` line. The index in the first column refers to the steps of the pre-selection algorithm, as described in the text.

3.1.2.1 Kinematic selection

The values of the offline kinematic selection cuts have been determined with the aim of minimizing the expected uncertainty on $A_{CP}(B^0 \to K^+\pi^-)$ or $A_{CP}(B_s^0 \to \pi^+K^-)$. It is possible to estimate this uncertainty without explicitly performing the maximum likelihood fit, as explained in the following.

In presence of a signal and a background source, using the invariant mass as a discriminating variable, the relevant p.d.f. can be written as:

$$f(m \mid \vec{\alpha},\ \vec{\beta},\ p) = p \cdot s(m \mid \vec{\alpha}) + (1-p) \cdot b(m \mid \vec{\beta}), \tag{3.3}$$

where m is the invariant mass, $s(\cdot)$ and $b(\cdot)$ are p.d.f.'s which describe the signal and background components respectively, $\vec{\alpha}$ and $\vec{\beta}$ are vectors of parameters determining the shapes of $s(\cdot)$ and $b(\cdot)$, and p is the fraction of signal events. Given a sample of N events, the likelihood function is

$$\mathcal{L} = \prod_{i=1}^{N} f(m_i \mid \vec{\alpha},\ \vec{\beta},\ p). \tag{3.4}$$

Under some general regularity conditions, the likelihood function tends asymptotically to a multi-variate Normal distribution in the $\vec{\alpha}$, $\vec{\beta}$, and p parameters as the number of events increases. The covariance matrix is given by the inverse of the Fisher Information Matrix (FIM), calculated at the maximum $\hat{\vec{\theta}} \equiv (\hat{\vec{\alpha}},\ \hat{\vec{\beta}},\ \hat{p})$, divided by the square root of the number of events in the sample:

$$\mathcal{L} \to G\left(\hat{\vec{\theta}};\ I\left(\hat{\vec{\theta}}\right)^{-1}/\sqrt{N}\right), \tag{3.5}$$

where G denotes the multi-variate Gaussian and $I\left(\hat{\vec{\theta}}\right)$ is the FIM.

The ij-th element of the FIM can be calculated analytically as

$$\left[I\left(\hat{\vec{\theta}}\right)\right]_{ij} = -\int f\left(m \mid \hat{\vec{\theta}}\right) \frac{\partial^2}{\partial\theta_i \partial\theta_j} \log f\left(m \mid \hat{\vec{\theta}}\right) dm. \tag{3.6}$$

By calculating the FIM it is then possible to estimate the statistical error that a fit would return on a given parameter, without the need of carrying out the fit itself. This is given by

$$\sigma(\theta_i)\sqrt{N} = \left[I\left(\hat{\vec{\theta}}\right)^{-1} \right]_{ii}, \tag{3.7}$$

i.e. the sensitivity on the parameter of interest θ_i times the square root of the total number of events is given by a calculable function of the parameters at the likelihood maximum, and in particular of the fraction of signal events $\hat{p}$. Once this function is determined, it can be used as a score function to identify a set of cut values which minimizes the statistical error $\sigma(\theta_i)$.

For many practical purposes, it is difficult to calculate the FIM, but this is not strictly necessary. The most relevant effect of the event selection is to modify the value of the fraction of signal events $\hat{p}$ at the likelihood maximum, without affecting in a significant way the other parameters $\hat{\vec{\alpha}}$ and $\hat{\vec{\beta}}$. This is particularly true for physical parameters like $\mathcal{CP}$ asymmetries, while it is a valid approximation for other nuisance parameters, like mass mean values and resolutions, background mass exponential slopes, etc.. For this reason, the FIM calculated at the maximum of the likelihood function can be well approximated as a function of the fraction of signal events $\hat{p}$ only. This dependence can be determined by means of toy Monte Carlo studies, where the value of $\hat{p}$ is varied in steps and maximum likelihood fits to toy samples with a fixed total number of events N are made in order to determine the expected sensitivity $\sigma(\theta_i)$.

The predicted sensitivities for $A_{CP}(B^0 \to K^+\pi^-)$ and $A_{CP}(B^0_s \to \pi^+K^-)$ determined by using this technique, as a function of the fraction of signal events $\hat{p}$, are shown in Fig. 3.2. Note that the interesting range for $\hat{p}$ in the bottom plot of Fig. 3.2 is restricted to low values. This is because here the background includes also the $B^0 \to K^+\pi^-$ decay, which is irreducible irrespective of any set of selection cuts, having the same final state signature of the $B^0_s \to \pi^+K^-$ decay.

In order to avoid biases in the choice of optimal selection cuts with this procedure, we have used full Monte Carlo samples of $B^0 \to K^+\pi^-$ and $B^0_s \to \pi^+K^-$ signal events[1] passing the pre-selection, while combinatorial background events were extracted from the right sideband of the pre-selected real data mass spectrum, where no other background source is expected to contribute. In this way the optimization has been performed without using any information on signal events from data.

We have determined two sets of cuts, optimized to reject combinatorial background events, with the aim of achieving the best sensitivity on $A_{CP}(B^0 \to K^+\pi^-)$ or on $A_{CP}(B^0_s \to \pi^+K^-)$. For this purpose, we have first defined a suitable set of variables to use in the selection, and then we have defined a lattice of cut values with fixed spacing. We have varied the cut values over all the points of the lattice, at each step counting the number of signal and background events passing the selection and calculating the fraction of signal events. By using the functions depicted in Fig. 3.2 we were then able to estimate at each step the statistical error either on $A_{CP}(B^0 \to K^+\pi^-)$ or on $A_{CP}(B^0_s \to \pi^+K^-)$.

We chose the two sets of cuts providing the best sensitivity on the two parameters of interest. Note that the custom approach of employing $\sqrt{S+B}/S \equiv 1/(p\sqrt{N})$, as a score function to be minimized, is equivalent to approximating the functions of Fig. 3.2 with a simple hyperbolic

[1]The simulated samples for all the studies in this thesis were produced with Gauss v39r0, Boole v21r9, Moore v10r2 and Brunel v37r8p5. The simulation was made with an average number of proton-proton interactions per crossing $\nu = 2.5$. The trigger configuration was TCK 0x2e002a.

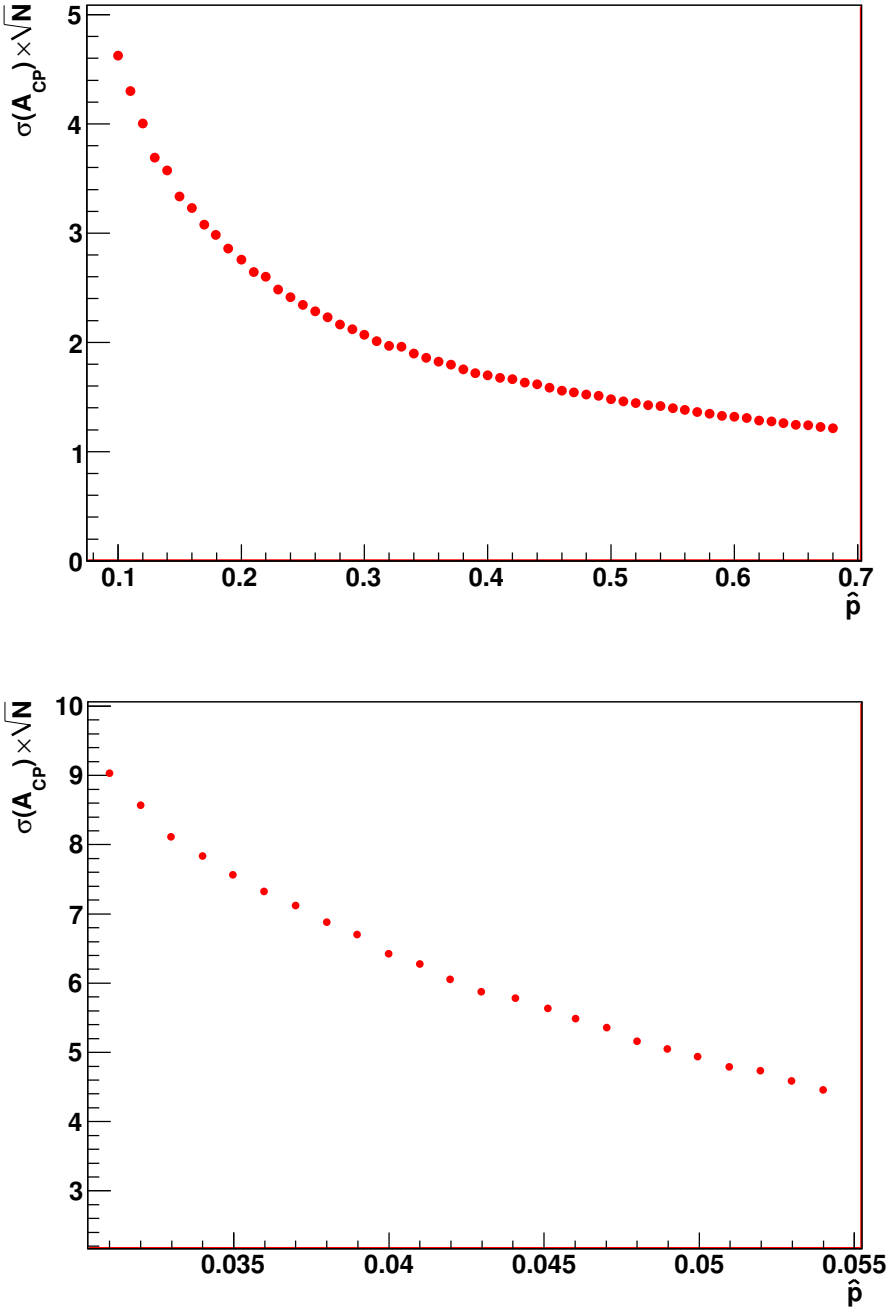

Figure 3.2: Predicted statistical errors times the square root of the sample statistics for $A_{CP}(B^0 \to K^+\pi^-)$ (top) and $A_{CP}(B_s^0 \to \pi^+K^-)$ (bottom), as a function of the fraction of signal events $\hat{p}$.

behaviour $1/p$. Although this is not dramatically far from the correct behaviour, it can be shown

that the approach here described leads to better sensitivities with respect to adopting the usual $\sqrt{S+B}/S$, but this is beyond the scope of this thesis.

There are two relevant aspects to be addressed:

- the relative normalization between signal and combinatorial background events must be determined, and this involves the estimation of the number of signal and combinatorial background events which are present in the real data pre-selected sample;
- in order to employ Monte Carlo signal events in the procedure, the validity of the Monte Carlo description of the distributions of selection variables and their correlations must be checked on data.

To determine the number of $B^0 \to K^+\pi^-$ signal events in the pre-selected sample, we applied on that sample a pair of simple PID cuts: $\Delta \log \mathcal{L}_{K\pi} > 5$ to select kaons and $\Delta \log \mathcal{L}_{K\pi} < -5$ to select pions (see Sec. 3.2 for the definition of these variables). Then we performed an unbinned maximum likelihood fit, modeling the mass lineshape as in the following:

- one Gaussian has been used for the $B^0 \to K^+\pi^-$ decay, and one Gaussian for the $B^0_s \to \pi^+K^-$ decay;
- the combinatorial background has been modeled with an exponential function;
- the contribution of partially reconstructed 3-body B decays has been described by means of the p.d.f.

$$f(m) = A \cdot \left[m' \sqrt{1 - \frac{m'^2}{m_0^2}} \Theta(m_0 - m')\, e^{c \cdot m'} \right] \otimes G(m - m';\, \sigma), \tag{3.8}$$

  where A is a normalization factor, $\Theta(\cdot)$ is a step function, m_0 and c are two parameters governing the shape of the distribution, $\otimes$ stands for convolution product and $G(\cdot)$ is a Gaussian resolution function of width σ, whose value is in common with that of the width of the signal model.

The result of the fit is shown in Fig. 3.3. The number of $B^0 \to K^+\pi^-$ events determined by the fit is $\nu_{K\pi} = 1527 \pm 105$. The total number of such events present in the pre-selected sample before the PID cuts were applied can be obtained once the efficiency of the PID cuts is known. This efficiency has been determined with the technique described in Sec. 3.2, yielding in this case $\epsilon_{K\pi} \simeq 0.45$. Hence, we estimate the total number of $B^0 \to K^+\pi^-$ events present in the pre-selected sample to be about 3400. We did not determine an error to associate to this number, as this is irrelevant for our purposes. The number of $B^0_s \to \pi^+K^-$ events was estimated by assuming the ratio $\frac{f_s\, \mathcal{BR}(B^0_s \to \pi^+K^-)}{f_d\, \mathcal{BR}(B^0 \to K^+\pi^-)}$ measured by CDF [48], yielding about $3400 \cdot 0.071 \simeq 240$ events. Finally, to estimate the number of combinatorial background events present in the pre-selected sample, we performed a simple exponential fit to the right sideband mass spectrum, within the range 5.6 GeV/c^2 $< m_{K\pi} <$ 5.8 GeV/c^2. The $K\pi$ or πK mass hypotheses were chosen by using the simple requirement that the value of $\Delta \log \mathcal{L}_{K\pi}$ of one track must be greater than that of the other track, to decide which of the two is the kaon candidate. Extrapolating the number of events in such a sideband to the mass window between 4.9 GeV/c^2 and 5.8 GeV/c^2 we got about 267000 events. With these estimates of the total number of $B^0 \to K^+\pi^-$, $B^0_s \to \pi^+K^-$ and

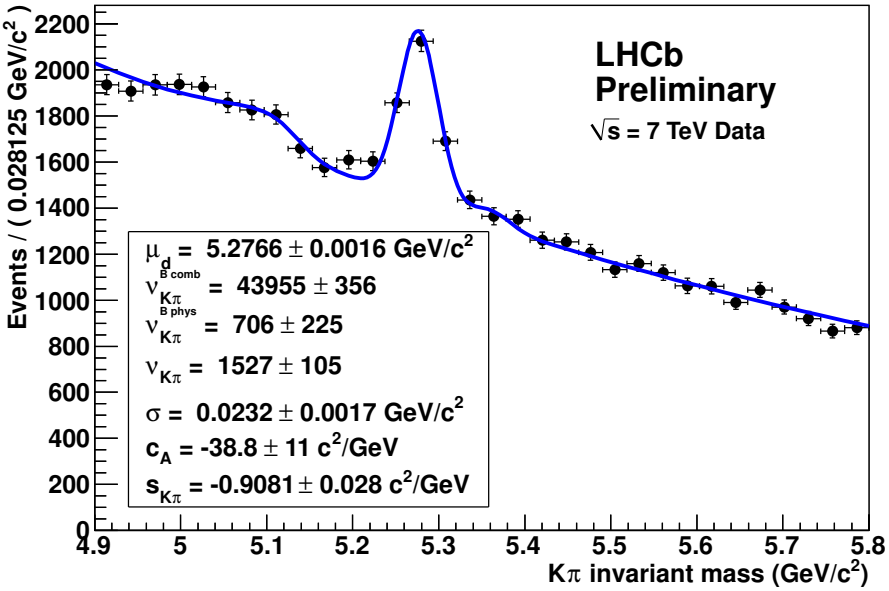

Figure 3.3: Mass spectrum under the $K\pi$ mass hypothesis, from pre-selected events where the PID requirements $\Delta \log \mathcal{L}_{K\pi} > 5$ and $\Delta \log \mathcal{L}_{K\pi} < -5$ have been used to identify kaon and pion candidates, respectively. The curve represents the result of an unbinned maximum likelihood fit to the data set.

Cut type	Accepted regions
Track p_T [GeV/c]	> 1.1
Track IP [μm]	> 150
Track χ^2/d.o.f.	< 3
$\max(p_T^{h^+}, p_T^{h'^-})$ [GeV/c]	> 2.8
$\max(IP^h, IP^{h'^-})$ [μm]	> 300
p_T^B [GeV/c]	> 2.2
$t_{\pi\pi}$ [ps]	> 0.9

Table 3.2: Summary of offline selection cuts optimized for the best sensitivity on $A_{CP}(B^0 \to K^+\pi^-)$.

combinatorial background events present in the pre-selected sample, the relative normalizations are determined.

The two optimal sets of kinematic cuts for the offline selection are summarized in Tabs. 3.2 and 3.3. The offline selection algorithm follows a similar path as the one used in the pre-selection, but some of the cuts have been tightened while other new cuts have been added, i.e. a cut on the transverse momentum of the B candidate p_T^B and on the lifetime of the B candidate, calculated under the $\pi\pi$ hypothesis $t_{\pi\pi}$.

In order to check that the Monte Carlo reproduces well the distributions of selection variables

Cut type	Accepted regions
Track p_T [GeV/c]	> 1.2
Track IP [μm]	> 200
Track χ^2/d.o.f.	< 3
$\max(p_T^{h^+}, p_T^{h'^-})$ [GeV/c]	> 3
$\max(IP^h, IP^{h'^-})$ [μm]	> 400
p_T^B [GeV/c]	> 2.4
$t_{\pi\pi}$ [ps]	> 1.2

Table 3.3: Summary of offline selection cuts optimized for the best sensitivity on $A_{CP}(B^0_s \to \pi^+K^-)$.

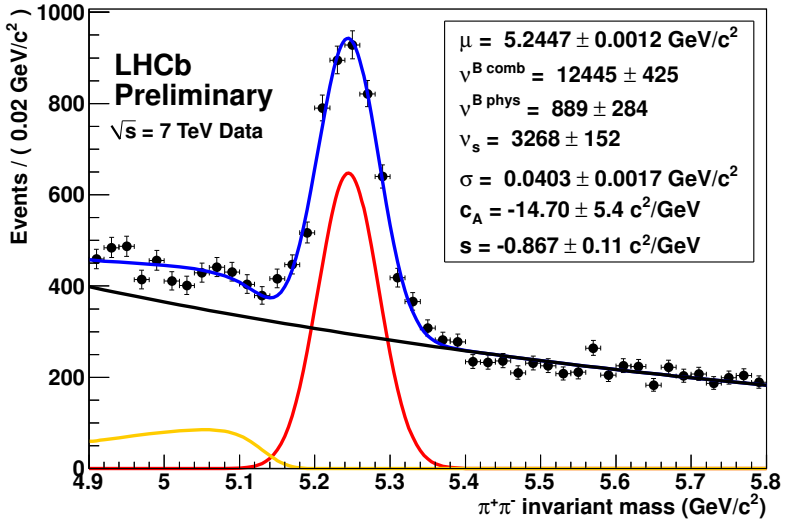

Figure 3.4: Mass spectrum under the $\pi\pi$ hypothesis for real data events which survived the set of cuts of Tab. 3.2, with the result of a maximum likelihood fit superimposed. The three individual components (signal, combinatorial background and 3-body bockground) are also shown.

and their correlations, we performed a fit of the mass spectrum assuming the $\pi\pi$ hypothesis for real data events which survived the set of cuts of Tab. 3.2. The p.d.f.'s of the signal and of the combinatorial background components have been modeled by a single Gaussian and an exponential function respectively. The 3-body background at the left of the mass peak has been parameterized with the function given in Eq. (3.8). The mass spectrum with the result of the unbinned maximum likelihood fit superimposed is shown in Fig. 3.4. Such a fit selects inclusively different decay modes. The dominating ones are $B^0 \to K^+\pi^-$, $B^0 \to \pi^+\pi^-$ and $B^0_s \to K^+K^-$. Then, by using the ${}_s\mathcal{P}lot$ technique [85], we determined from data the distributions of kinematic variables of signal events. Fig. 3.5 shows the comparison of Monte Carlo and data distributions of the kinematic variables used in the event selection. At the same time we determined from data also the correlations amongst the kinematic variables of signal events. Fig. 3.6 shows the

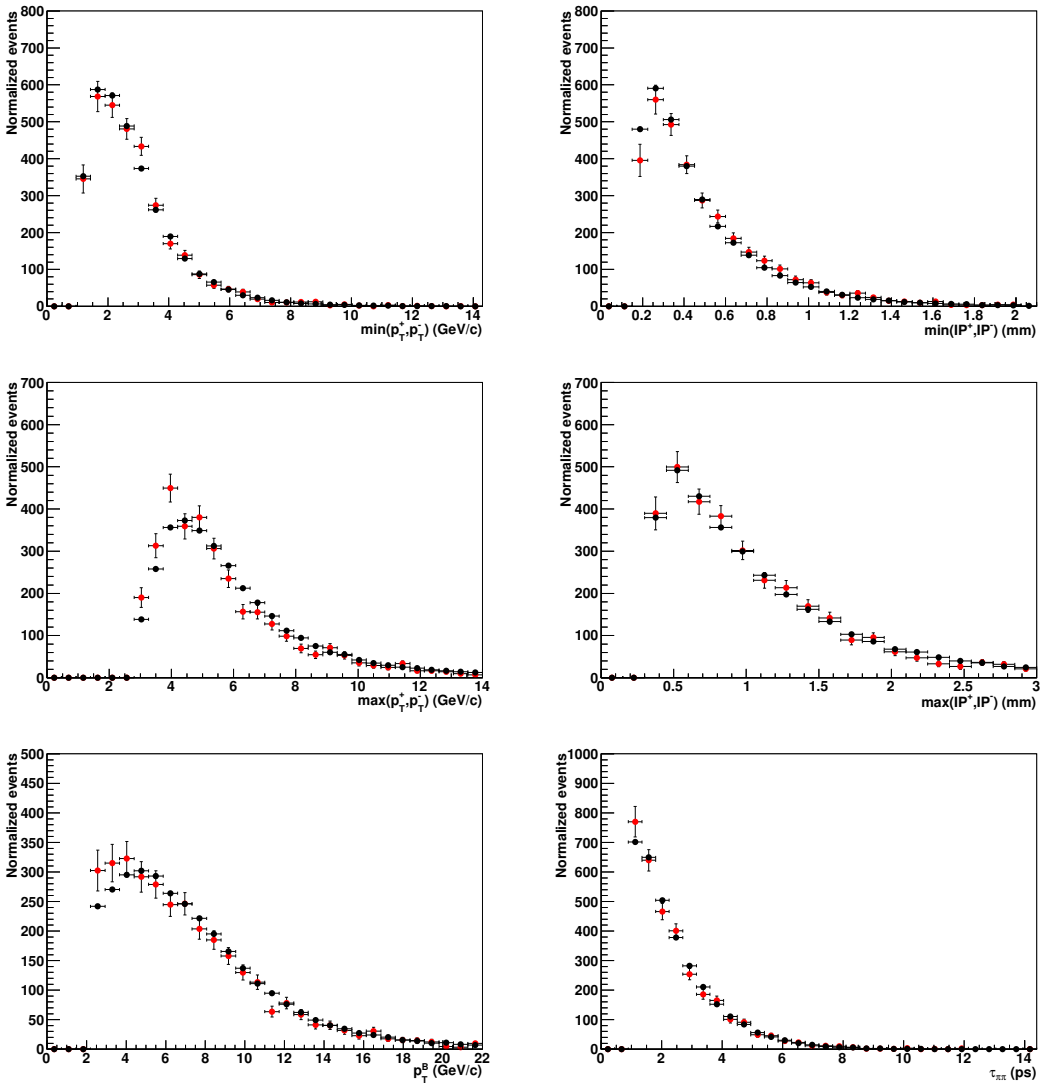

Figure 3.5: Comparison of Monte Carlo ($B^0 \to K^+\pi^-$ decays, black dots) and data (inclusive sample of various modes as explained in the text, red dots) distributions of the kinematic variables used in the event selection: minimum p_T (top left), minimum IP (top right), maximum p_T (middle left), maximum IP (middle right), B candidate p_T^B (bottom left), B candidate lifetime under the $\pi\pi$ hypothesis $t_{\pi\pi}^B$ (bottom right).

corresponding Monte Carlo and data linear correlation matrices. Despite the fact that in the Monte Carlo only one of the various trigger configurations of the 2010 run was simulated, a good agreement between Monte Carlo and data is observed within the current statistical errors.

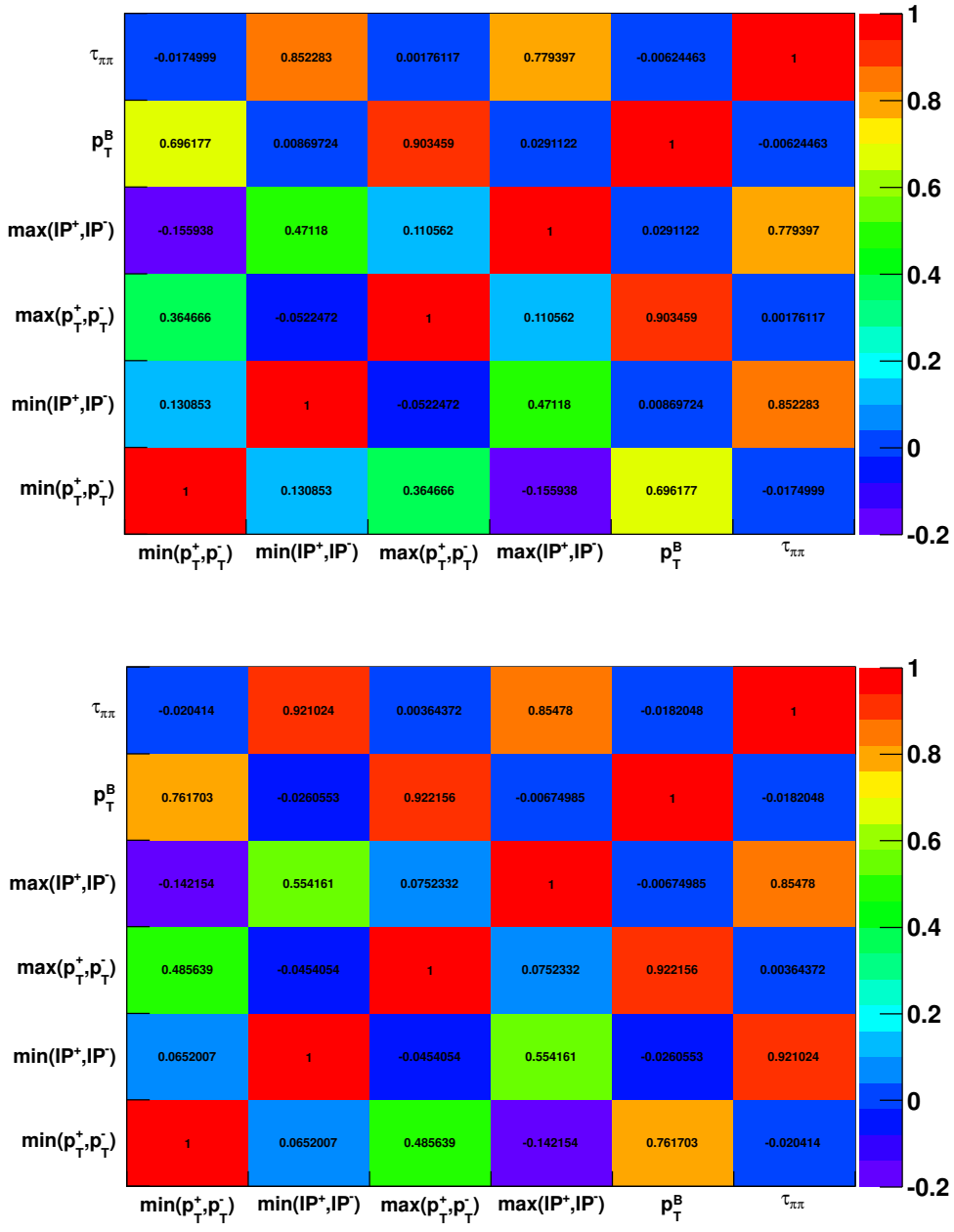

Figure 3.6: Linear correlation matrices amongst the kinematic variables used in the event selection, as determined from Monte Carlo simulations ($B^0 \to K^+\pi^-$ decays, top) and real data (inclusive sample of various modes as explained in the text, bottom).

$K^+\pi^-$ PID cuts for $A_{CP}(B^0 \to K^+\pi^-)$	π^+K^- PID cuts for $A_{CP}(B^0_s \to \pi^+K^-)$
$\Delta\log\mathcal{L}_{K\pi}(h^+) > 0$	$\Delta\log\mathcal{L}_{K\pi}(h^+) < -7$
$\Delta\log\mathcal{L}_{K\pi}(h^-) < 0$	$\Delta\log\mathcal{L}_{K\pi}(h^-) > 7$
$\Delta\log\mathcal{L}_{pK}(h^+) < 5$	$\Delta\log\mathcal{L}_{pK}(h^+) < 5$
$\Delta\log\mathcal{L}_{p\pi}(h^-) < 5$	$\Delta\log\mathcal{L}_{p\pi}(h^-) < 5$

Table 3.4: PID cuts applied for the identification of the $K^+\pi^-$ mass hypothesis for the measurement of $A_{CP}(B^0 \to K^+\pi^-)$ and of the π^+K^- mass hypothesis for the measurement of $A_{CP}(B^0_s \to \pi^+K^-)$. The charge conjugated hypotheses require h^+ and h^- to be exchanged.

3.1.2.2 Final state selection

The $B \to h^+h'^-$ sample passing the kinematic event selection is then subdivided into different final states using the PID capabilities of the two RICH sub-detectors. In particular we employed the quantities $\Delta\log\mathcal{L}_{K\pi}$ and $\Delta\log\mathcal{L}_{p\pi}$, or their difference $\Delta\log\mathcal{L}_{K\pi}$ when appropriate. A discussion on these quantities can be found in Sec. 3.2.

While to determine the best set of kinematic cut values we employed the technique described in the previous section, the choice of optimal cuts for the PID observables was guided by different considerations. In constrast to the combinatorial and 3-body backgrounds, whose amounts can be determined by maximum likelihood fits using only the invariant mass as discriminating variable, it is very difficult to do the same with the cross-feed backgrounds for a given $B \to h^+h'^-$ channel. Such backgrounds are due to all the other charmless two-body decays where one or both the final state particles have been mis-identified. This is because their mass lineshapes are typically peaked around the nominal masses of the decaying B's, with appropriate shifts due to the usage of incorrect masses of the daughter particles, and in general such peaks are buried under the signal peaks of the decays of interest. The sizes of such peaking backgrounds can be fixed by determining the yields of all the $B \to h^+h'^-$ decays by means of maximum likelihood fits made with the correct mass hypotheses, and then multiplying such yields by the appropriate ratios of PID efficiencies. For example, in order to determine how many $B^0 \to \pi^+\pi^-$ are present in the $K^+\pi^-$ mass spectrum, we can first perform a fit to the $\pi^+\pi^-$ mass spectrum using PID cuts which identify the $\pi^+\pi^-$ final state, so determining the $B^0 \to \pi^+\pi^-$ signal yield, and then we can multiply this yield by the ratio of PID efficiencies $\varepsilon_{K\pi}/\varepsilon_{\pi\pi}$. But in order to extract such yield from the $\pi^+\pi^-$ spectrum, we have to include the $B^0 \to K^+\pi^-$ decay as a cross-feed background in the fit. In other words, we need to perform a simultaneous fit of all the mass spectra under the various mass hypotheses, and determine signal yields and cross-feed backgrounds of any decay mode to all the other modes.

The guiding principle to identify the two appropriate sets of PID cut values for the $K\pi$ mass hypotheses, individually for the measurements of $A_{CP}(B^0 \to K^+\pi^-)$ and $A_{CP}(B^0_s \to \pi^+K^-)$, has been to limit the total amount of cross-feed backgrounds present under the $B^0 \to K^+\pi^-$ and $B^0_s \to \pi^+K^-$ mass peaks to the same level of the corresponding combinatorial background. For all the other modes, namely $B^0 \to \pi^+\pi^-$, $B^0_s \to K^+K^-$, $\Lambda_b \to p\pi^-$ and $\Lambda_b \to pK^-$, we adopted instead a unique set of exclusive PID cuts. The two sets of cuts for the $K\pi$ mass hypothesis are reported in Tab. 3.4, while the adopted cuts for the other mass hypotheses are given in Tab. 3.5. It can be noted that the adopted cuts identify mutually exclusive samples for each mass hypothesis.

$\pi^+\pi^-$	K^+K^-	pK^-	$p\pi^-$
$\Delta\log\mathcal{L}_{K\pi}(h^+) < -3$	$\Delta\log\mathcal{L}_{K\pi}(h^+) > 3$	$\Delta\log\mathcal{L}_{pK}(h^+) > 5$	$\Delta\log\mathcal{L}_{pK}(h^+) > 10$
$\Delta\log\mathcal{L}_{K\pi}(h^-) < -3$	$\Delta\log\mathcal{L}_{K\pi}(h^-) > 3$	$\Delta\log\mathcal{L}_{K\pi}(h^-) > 3$	$\Delta\log\mathcal{L}_{K\pi}(h^-) < -3$
$\Delta\log\mathcal{L}_{p\pi}(h^+) < 5$	$\Delta\log\mathcal{L}_{pK}(h^+) < 5$	$\Delta\log\mathcal{L}_{p\pi}(h^+) > 5$	$\Delta\log\mathcal{L}_{p\pi}(h^+) > 10$
$\Delta\log\mathcal{L}_{p\pi}(h^-) < 5$	$\Delta\log\mathcal{L}_{pK}(h^-) < 5$	$\Delta\log\mathcal{L}_{pK}(h^-) < 5$	$\Delta\log\mathcal{L}_{p\pi}(h^-) < 5$

Table 3.5: PID cuts applied for the identification of the $\pi^+\pi^-$, K^+K^-, pK^- and $p\pi^-$ mass hypotheses (for the $\bar{p}K^+$ and $\bar{p}\pi^+$, h^+ and h^- must be exchanged in the last two columns).

3.2 Calibration of particle identification

The calibration of PID observables is one of the crucial aspects of this analysis. As we use the same set of kinematic cuts to select all the various $B \to h^+h'^-$ channels, the only difference in selecting each decay mode is due to cuts on PID variables. Hence, in order to determine the amount of background for a given channel, due to all the other channels where at least one particle has been mis-identified, the relative efficiencies of the PID selection cuts employed to identify the specific final state of interest play a key role.

3.2.1 Method

The discrimination of charged pions, kaons and protons is essentially based on the information provided by the two RICH sub-detectors. The variable that is commonly employed to discriminate between different particle hypotheses in LHCb is denoted as $\Delta\log\mathcal{L}_{ij}$, that for a given track is defined as:

$$\Delta\log\mathcal{L}_{ij} = \log\mathcal{L}_i - \log\mathcal{L}_j, \tag{3.9}$$

where $\mathcal{L}_i$ and $\mathcal{L}_j$ are the likelihoods for particle hypotheses i and j respectively, and i and j, in our case, stand for charged π, K or p. Note that for three types of final state particles, a complete set of independent PID variables is composed of only two elements, e.g. $\Delta\log\mathcal{L}_{K\pi}$ and $\Delta\log\mathcal{L}_{Kp}$, since the third possibility $\Delta\log\mathcal{L}_{p\pi}$ can be calculated as the difference between the two.

The high production rate of charged D^* mesons at the LHC and the kinematic characteristics of the $D^{*+} \to D^0(K^-\pi^+)\pi^+$ decay chain (and its charge conjugate) make such events an ideal calibration sample for particle identification studies of kaons and pions. In addition, for calibrating the RICH response for protons, a sample of $\Lambda \to p\pi^-$ decays can be used. In both cases, no use of PID information needs to be made in selecting the samples, as the selection of highly pure final states can be realized by means of kinematic cuts alone. In this analysis we used D^* calibration samples selected by the `StripDstarNoPIDsWithD02RSKPiLine` stripping line (about 770.000 events), and Λ calibration samples selected by the `Lam0Line_1`, `Lam0Line_2` and `Lam0Line_3` stripping lines (about 400.000 events).

However, there are some issues which need to be addressed:

- The response of the RICH sub-detectors is obviously dependent on the momentum p of the particles, and it can be shown that also other kinematic variables play a role, due to acceptance effects of the RICH system, such as the transverse momentum p_T. Since production and decay kinematics of the $D^0 \to K^-\pi^+$ and $\Lambda \to p\pi^-$ channels differ from

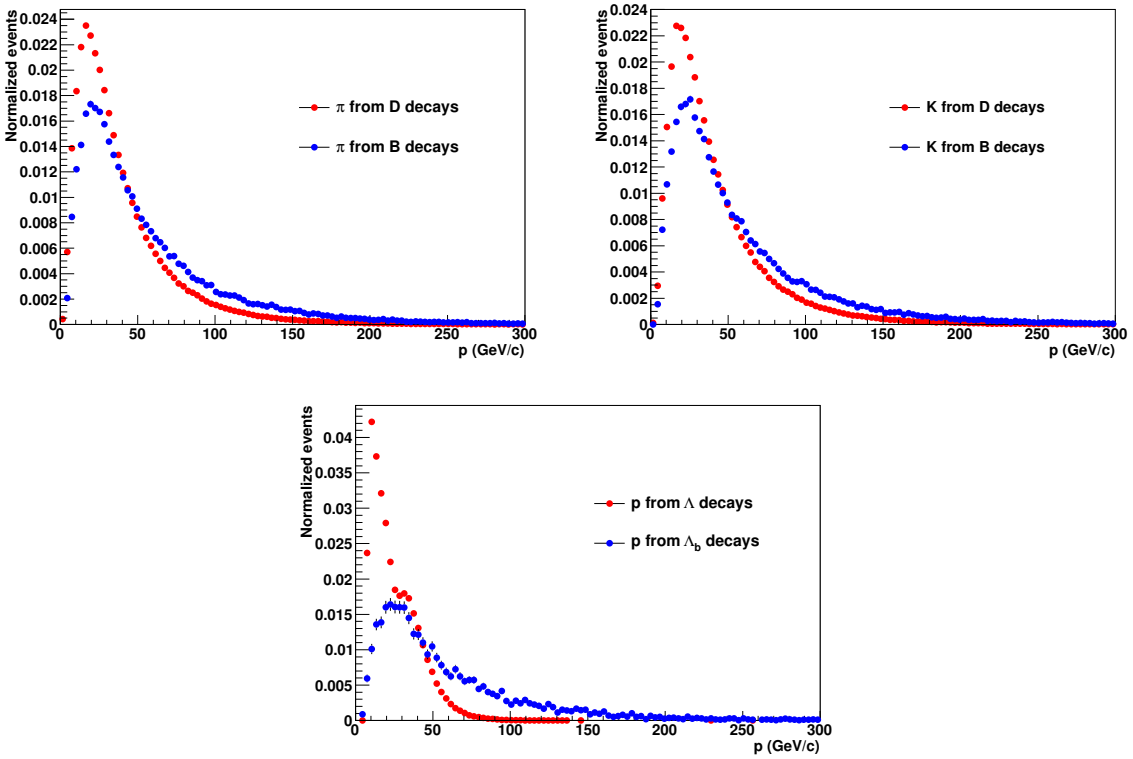

Figure 3.7: Comparison of momentum distributions for pions (top left), kaons (top right) and protons (bottom) between real data calibration samples and offline selected $B^0 \to K^+\pi^-$ and $\Lambda_b \to p\pi^-$ Monte Carlo samples. The distributions are normalized to the same area.

that of $B \to h^+h'^-$ decays (see Figs. 3.7 and 3.8), the distributions of $\Delta \log \mathcal{L}_{ij}$ variables are different as well, as shown in Fig. 3.9. For this reason an appropriate reweighting procedure must be put in place.

- An additional complication comes from the fact that the momenta and transverse momenta of the positive and negative particles in $B \to h^+h'^-$ decays exhibit non negligible correlations (see Fig. 3.10). For this reason, in the most accurate approach which aims to take such correlations into account, the reweighting procedure should be applied using simultaneously the momenta and transverse momenta of both the final state particles, thus enlarging the dimensionality of the problem.

- Two PID variables like $\Delta \log \mathcal{L}_{K\pi}$ and $\Delta \log \mathcal{L}_{p\pi}$, as well as their difference $\Delta \log \mathcal{L}_{Kp}$, are themselves correlated (see Fig. 3.11), hence their simultaneous calibration is also required, if one aims to identify a given particle by employing simultaneous cuts on both variables.

All these considerations translate into the following equation, where we have chosen as an example the pair of PID variables suitable for discriminating the $\pi\pi$ final state from final states

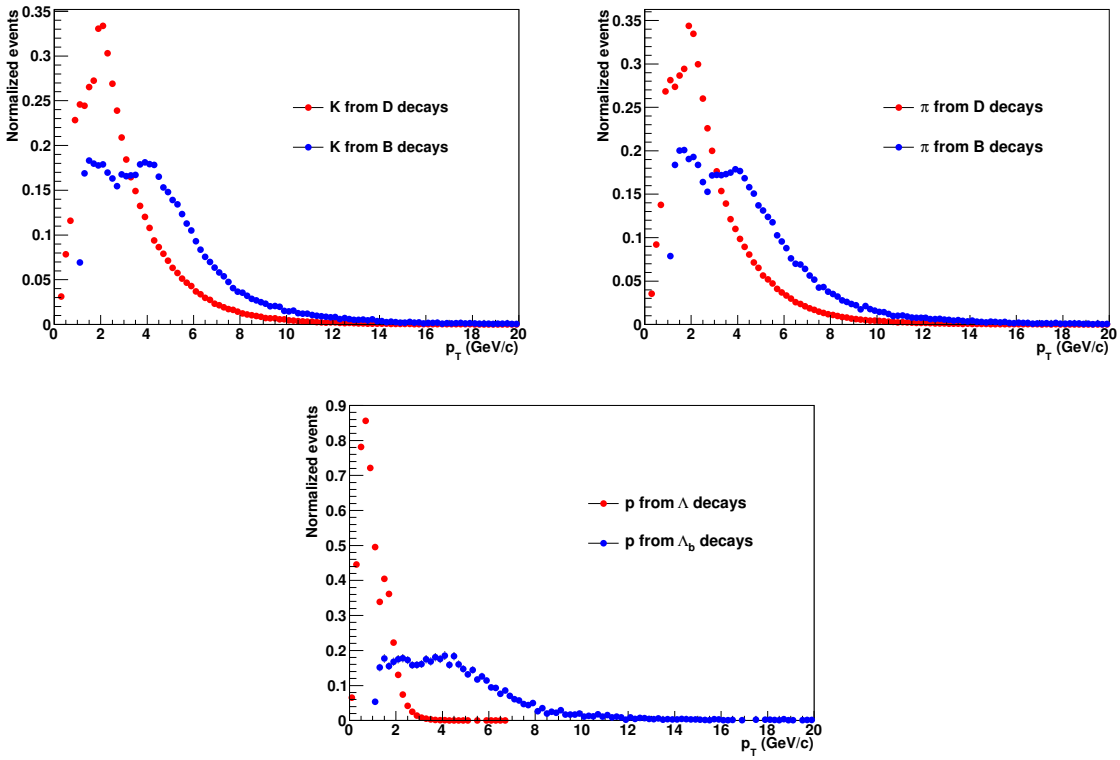

Figure 3.8: Comparison of transverse momentum distributions for pions (top left), kaons (top right) and protons (bottom) between real data calibration samples and offline selected $B^0 \to K^+\pi^-$ and $\Lambda_b \to p\pi^-$ Monte Carlo samples. The distributions are normalized to the same area.

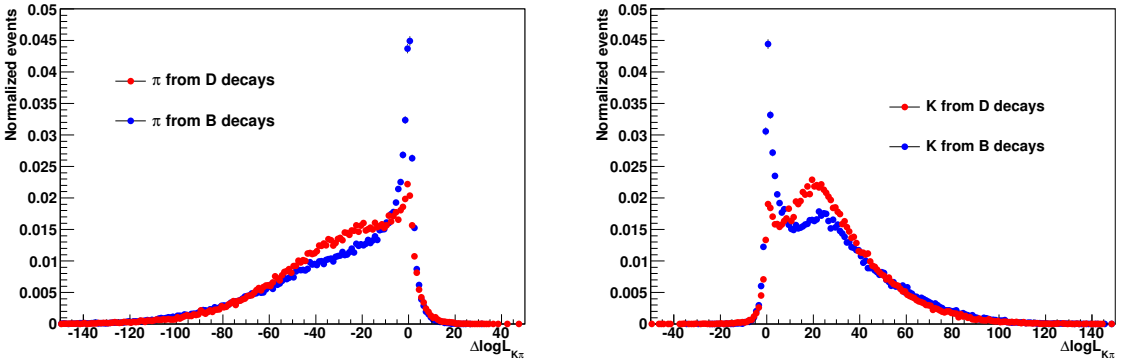

Figure 3.9: Comparison of Monte Carlo $\Delta \log \mathcal{L}_{K\pi}$ distributions for true pions (left) and kaons (right) from calibration $D^0 \to K^-\pi^+$ decays and offline selected $B^0 \to K^+\pi^-$ decays. The distributions are normalized to the same area.

with kaons and protons:

$$f\left(\Delta \log \mathcal{L}^+_{K\pi},\ \Delta \log \mathcal{L}^+_{p\pi},\ \Delta \log \mathcal{L}^-_{K\pi},\ \Delta \log \mathcal{L}^-_{p\pi},\ p^+,\ p^-,\ p^+_T,\ p^-_T\right) = \tag{3.10}$$
$$= g^+\left(\Delta \log \mathcal{L}^+_{K\pi},\ \Delta \log \mathcal{L}^+_{p\pi} \mid p^+,\ p^+_T\right) \cdot g^-\left(\Delta \log \mathcal{L}^-_{K\pi},\ \Delta \log \mathcal{L}^-_{p\pi} \mid p^-,\ p^-_T\right) \cdot$$
$$\cdot\ h\left(p^+,\ p^-,\ p^+_T,\ p^-_T\right).$$

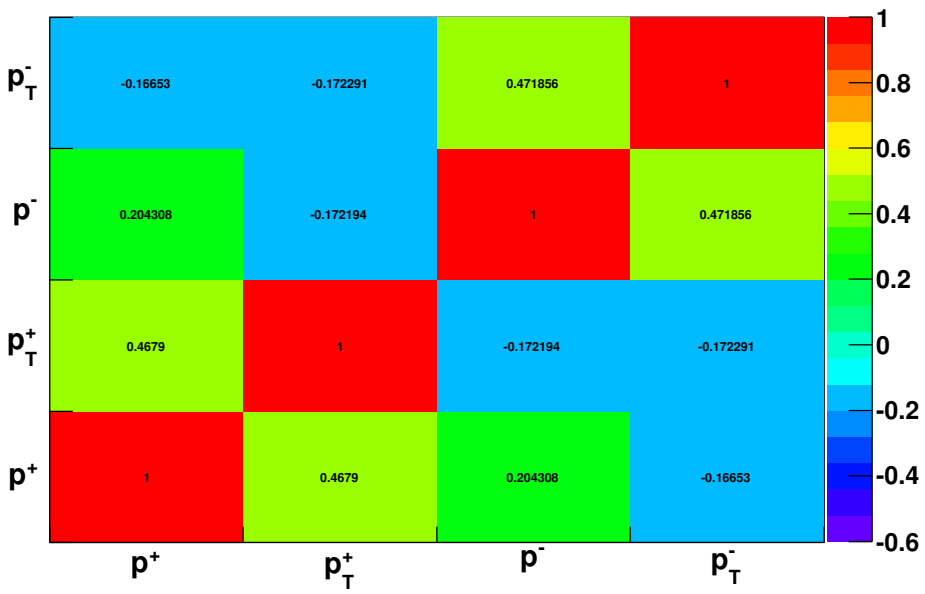

Figure 3.10: Linear correlation matrix for momenta and transverse momenta of positive and negative particles from offline selected $B^0 \to K^+\pi^-$ Monte Carlo events.

which expresses the joint p.d.f. $f(\cdot)$ of PID observables, momenta and transverse momenta of the daughter particles in terms of two conditional p.d.f.'s $g^+(\cdot)$ and $g^-(\cdot)$, determined from the calibration samples, and a joint p.d.f. $h(\cdot)$ of the momenta and transverse momenta themselves. Note that $g^+(\cdot)$ and $g^-(\cdot)$ are in general different functions, which coincide only when the positive and negative daughters have the same identity.

Then it is clear that, in order to determine $f(\cdot)$, one needs to know the p.d.f. of momenta and transverse momenta of the $B \to h^+h'^-$ final state particles surviving the kinematic offline selection, denoted as $h(\cdot)$, which is *a priori* unknown. We can employ full Monte Carlo simulations to obtain such p.d.f., but this can be done only after having verified that the Monte Carlo simulation reproduces reasonably well the momentum and transverse momentum distributions observed in real data, albeit within the limited statistical sensitivity achievable with the few thousand signal events currently available.

Using the same procedure as described in Sec. 3.1, we have determined the distribution of momenta and tranverse momenta for offline selected events, inclusively for all the $B \to h^+h'^-$ signal events under the Gaussian mass peak (see Fig. 3.4). Fig. 3.12 shows the comparison of such distributions obtained from Monte Carlo simulations and real data, while Fig. 3.13 shows the linear correlation matrix amongst the momenta and transverse momenta of the daughters obtained from real data (this plot is the real data analogue of the one shown in Fig. 3.10, and should be compared with that). Within the current statistics, these results demonstrate a substantial agreement between Monte Carlo simulations and real data, in particular for the most sensitive variable concerning the PID calibration, i.e. the momentum p.

Albeit the agreement between kinematic distributions of Monte Carlo simulation and real

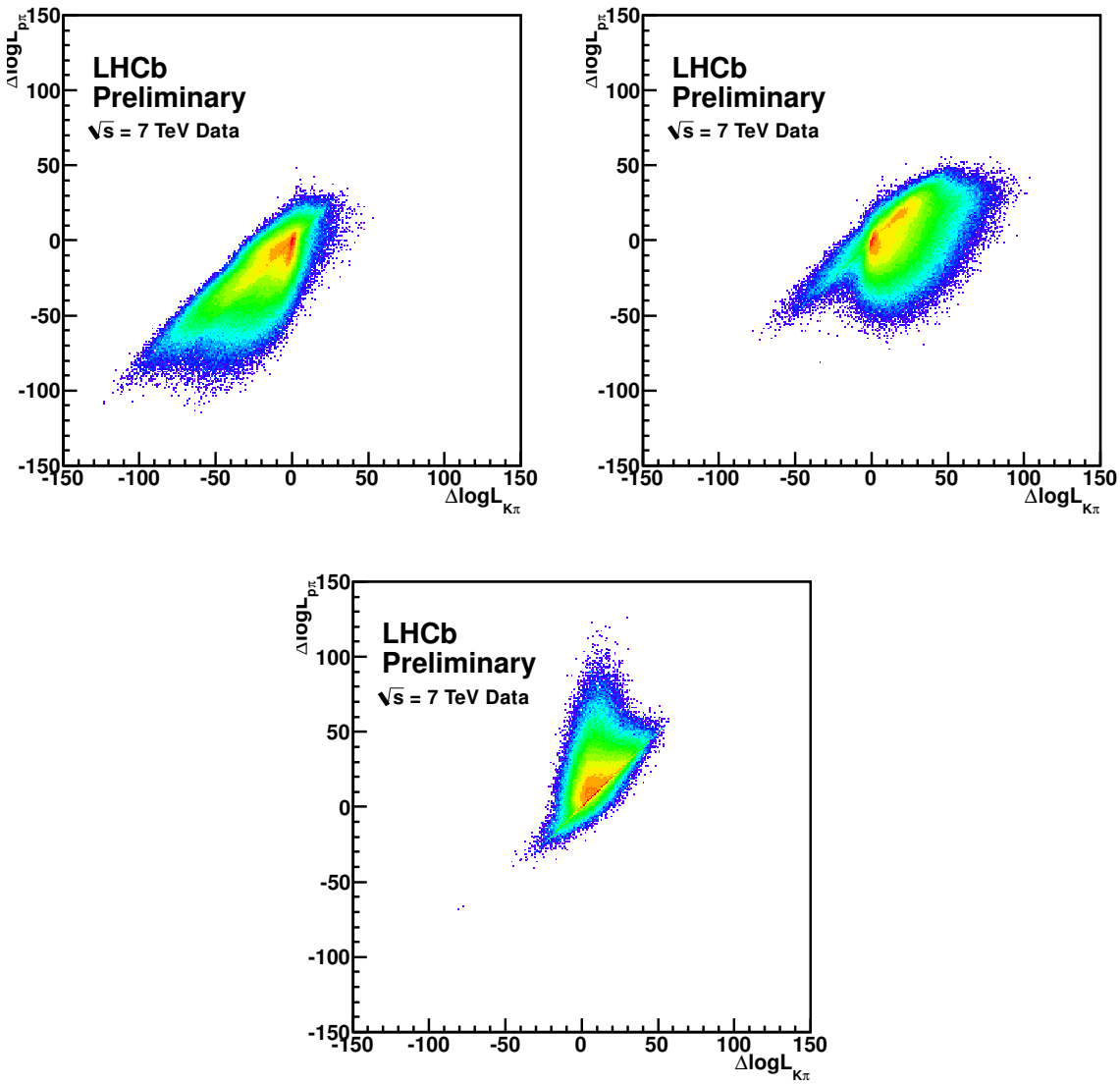

Figure 3.11: $\Delta \log \mathcal{L}_{p\pi}$ versus $\Delta \log \mathcal{L}_{K\pi}$ for pions (top left), kaons (top right) and protons (bottom) from real data calibration samples.

data samples is quite satisfactory (see also Figs. 3.5 and 3.6), it is worth mentioning that the same consideration does not hold for $\Delta \log \mathcal{L}$ distributions of calibration channels, as can be seen in Fig. 3.14.

Efficiencies for a given set of PID cuts can be calculated by integrating the joint p.d.f. given in Eq. (3.10), or its analogues depending on the particle hypotheses under considerations, over the whole momentum and transverse momentum ranges, and over the desired ranges of $\Delta \log \mathcal{L}$ variables. In order to perform such integration, we have used a simple Monte Carlo technique, by generating events according to the joint p.d.f. and then counting the number of events with the appropriate $\Delta \log \mathcal{L}$ values exceeding or not the desired thresholds. The number of generated

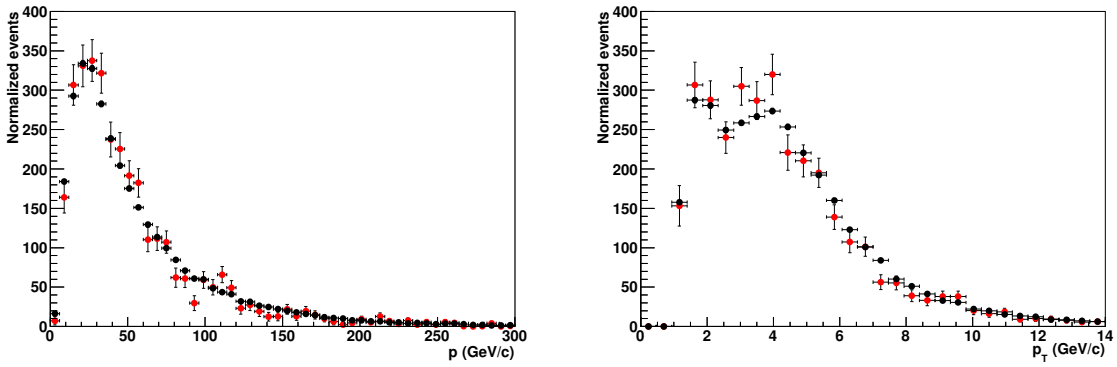

Figure 3.12: Comparison of momentum (left) and transverse momentum (right) distributions for offline selected events from full Monte Carlo simulations ($B^0 \to K^+\pi^-$ events, black dots) and from real data (inclusive sample of $B \to h^+h'^-$ decays, red dots).

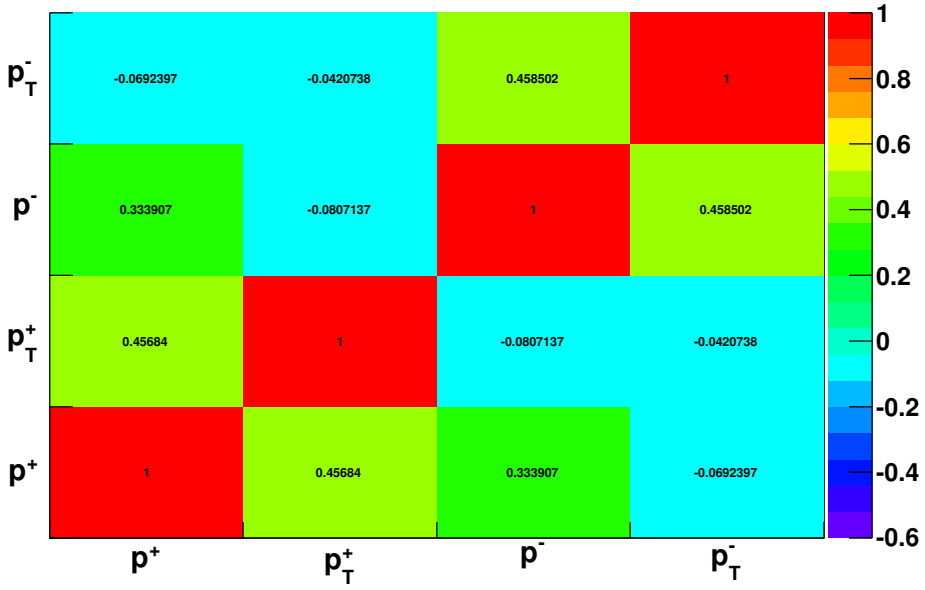

Figure 3.13: Linear correlation matrix for momenta and transverse momenta of positive and negative particles from offline selected $B^0 \to K^+\pi^-$ events.

events was always equal to the number of events used to define the p and p_T distributions employed in the reweighting procedure. The results are presented in the following sub-section.

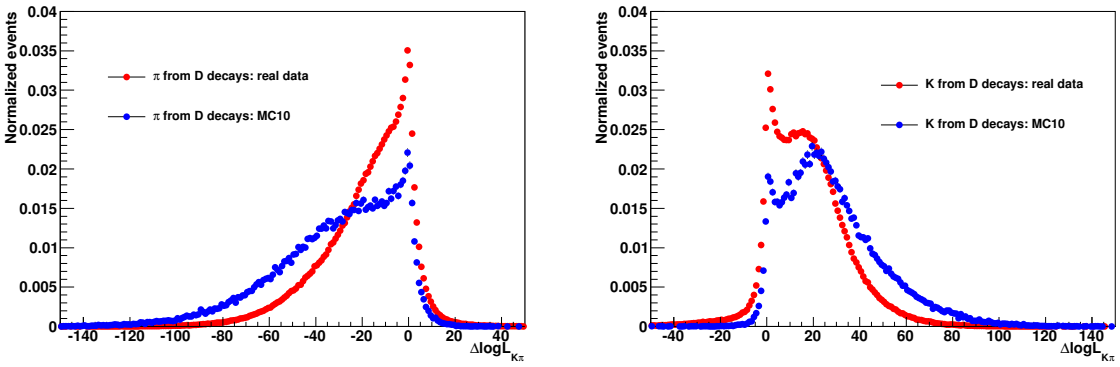

Figure 3.14: Comparison of $\Delta \log \mathcal{L}_{K\pi}$ distributions for pions (left) and kaons (right) from Monte Carlo and real data D^0 decays.

3.2.2 Validation and results

The PID calibration procedure has been first validated using D^* and Λ Monte Carlo calibration samples. We used such samples to calculate the efficiencies of the cuts, reported in Tabs. 3.6 and 3.7, for the various $B \to h^+h'^-$ surviving the offline selection. In this way we can compare the calculated efficiencies with the ones determined directly using the corresponding $B \to h^+h'^-$ Monte Carlo $\Delta \log \mathcal{L}$ values. As an illustrative example, in Fig. 3.15 we also show a comparison of the $\Delta \log \mathcal{L}_{K\pi}$ and $\Delta \log \mathcal{L}_{p\pi}$ distributions for pions from $B^0 \to K^+\pi^-$ decays, obtained using the reweighting procedure or determined from full Monte Carlo simulations.

The agreement is generally good when only kaons and pions are involved, i.e. when the calibration sample in use is the D^* one, while the agreement is significantly worse for final states with protons. This is because protons from the Λ calibration sample have a limited coverage of the phase space in p and in particular p_T, as is apparent in Figs. 3.7 and 3.8, hence the reweighting is unable to correctly match the p and p_T distributions of protons from Λ_b decays.

The predicted efficiencies for events passing the offline selections optimized for $A_{CP}(B^0 \to K^+\pi^-)$ and $A_{CP}(B^0_s \to \pi^+K^-)$, now using real data D^* and Λ calibration samples, can be found in Tabs. 3.8 and 3.9 respectively. These will be the reference efficiencies that we will use in the remainder of this chapter. By comparing these efficiencies with those given in Tabs. 3.6 and 3.7, we can see that the PID efficiencies determined by means of full Monte Carlo simulations are quite different from those measured in data, as was already shown in Fig. 3.14.

To conclude this section, we also checked the stability of the efficiencies by replacing the Monte Carlo momentum and transverse momentum distributions used in the reweighting procedure with distributions extracted from real data with the ${}_s\mathcal{P}lot$ techique already described. The results are reported in Tabs. 3.10 and 3.11. For comparison, in the same tables we reported also the corresponding efficiencies from Tabs. 3.8 and 3.9.

3.3 Instrumental and production asymmetries

The possible presence of asymmetries arising from the different production rate of B and $\bar{B}$ mesons in proton-proton collisions, or asymmetries induced by detector topology and event

	$\pi^+\pi^-$		K^+K^-		$K\pi$		$p\pi^-$		pK^-	
	MC	MC_R	MC	MC_R	MC	MC_R	MC	MC_R	MC	MC_R
$B^0 \to \pi^+\pi^-$	57.1(4)	54.5(4)	0.10(2)	0.07(1)	20.9(4)	22.2(4)	0.37(5)	0.36(5)	0.04(1)	0.04(1)
$B_s^0 \to K^+K^-$	0.01(1)	0.01(1)	65.5(5)	63.8(5)	12.7(3)	12.3(3)	0.003(2)	0.002(1)	1.7(1)	2.2(1)
$B_{(s)}^0 \to K^+\pi^-$	0.67(3)	0.69(3)	2.33(6)	2.26(5)	79.8(3)	78.7(3)	0.15(1)	0.21(2)	0.31(6)	0.41(7)
$\bar{B}_{(s)}^0 \to \pi^+K^-$	0.67(3)	0.69(3)	2.33(6)	2.26(5)	1.15(4)	1.13(4)	0.004(2)	0.003(2)	0.66(3)	0.87(3)
$\Lambda_b \to p\pi^-$	0.09(4)	0.9(1)	0.17(5)	0.43(8)	11.5(4)	14.0(5)	57.8(9)	46.0(8)	2.3(2)	2.4(2)
$\Lambda_b \to \pi^+\bar{p}$	0.09(4)	0.9(1)	0.9(1)	0.43(8)	0.32(7)	0.38(8)	0.01(1)	0.01(1)	0.02(1)	0.12(4)
$\Lambda_b \to pK^-$	0.01(1)	0.02(1)	6.2(3)	12.0(4)	1.2(1)	1.0(1)	0.57(9)	0.58(9)	70(1)	63(1)
$\bar{\Lambda}_b \to K^+\bar{p}$	0.01(1)	0.02(1)	6.2(3)	12.0(4)	1.8(2)	2.1(2)	0.02(1)	0.02(1)	0.03(1)	0.14(5)

Table 3.6: Efficiencies (in %) of PID cuts, for the various mass hypotheses, for events passing the offline selection optimized for $A_{CP}(B^0 \to K^+\pi^-)$. The values in the MC columns are the efficiencies determined from $B \to h^+h'^-$ Monte Carlo simulations, while those in the MC_R columns are the efficiencies predicted from reweighting the D^* and Λ Monte Carlo calibration samples. The values in parentheses represent the statistical errors on the last digit due to the statistics of Monte Carlo simulations (MC columns) or to the statistics used in the Monte Carlo integration (MC_R columns).

	$\pi^+\pi^-$		K^+K^-		$K\pi$		$p\pi^-$		pK^-	
	MC	MC_R	MC	MC_R	MC	MC_R	MC	MC_R	MC	MC_R
$B^0 \to \pi^+\pi^-$	57.7(5)	55.4(5)	0.08(2)	0.10(2)	0.91(9)	0.77(8)	0.43(6)	0.43(6)	0.04(1)	0.02(1)
$B_s^0 \to K^+K^-$	0.01(1)	0.01(1)	65.5(5)	63.8(5)	0.17(4)	0.14(4)	0.004(3)	0.004(3)	1.8(1)	2.1(1)
$B_{(s)}^0 \to K^+\pi^-$	0.67(3)	0.74(4)	2.31(6)	2.20(6)	48.2(3)	50.2(3)	0.15(2)	0.23(2)	0.031(7)	0.05(1)
$\bar{B}_{(s)}^0 \to \pi^+K^-$	0.67(3)	0.74(4)	2.31(6)	2.20(6)	0.002(1)	0.002(1)	0.005(3)	0.003(2)	0.63(3)	0.80(3)
$\Lambda_b \to p\pi^-$	0.08(4)	0.6(1)	0.14(5)	0.30(8)	3.8(3)	9.6(4)	58(1)	45(1)	2.2(2)	2.5(2)
$\Lambda_b \to \pi^+\bar{p}$	0.08(4)	0.6(1)	0.14(5)	0.30(8)	0.02(1)	0.02(1)	0.02(1)	0.02(1)	0.02(1)	0.08(4)
$\Lambda_b \to pK^-$	0.02(1)	0.03(1)	6.0(4)	11.5(5)	0.02(1)	0.02(1)	0.6(1)	0.7(1)	70(1)	64(1)
$\bar{\Lambda}_b \to K^+\bar{p}$	0.02(1)	0.03(1)	6.0(4)	11.5(5)	0.15(6)	0.5(1)	0.02(1)	0.03(1)	0.02(1)	0.36(9)

Table 3.7: Efficiencies (in %) of PID cuts, for the various mass hypotheses, for events passing the offline selection optimized for $A_{CP}(B_s^0 \to \pi^+K^-)$. The values in the MC columns are the efficiencies determined from $B \to h^+h'^-$ Monte Carlo simulations, while those in the MC_R columns are the efficiencies predicted from reweighting the D^* and Λ Monte Carlo calibration samples. The values in parentheses represent the statistical errors on the last digit due to the statistics of Monte Carlo simulations (MC columns) or to the statistics used in the Monte Carlo integration (MC_R columns).

reconstruction, as well as due to strong interactions of final state particles with the detector material, need to be taken into account when passing from the observed asymmetries to the physical $\mathcal{CP}$ asymmetries.

Instrumental charge asymmetries

Here we describe method and results of a study aimed to measure such effects on real data, using high statistics samples of $D^{*+} \to D^0(K^-\pi^+)\pi^+$, $D^{*+} \to D^0(K^+K^-)\pi^+$ and $D^{*+} \to D^0(\pi^+\pi^-)\pi^+$, and $D^0 \to K^-\pi^+$ decays (plus their charge conjugate modes). The combination of the integrated $\mathcal{CP}$ raw asymmetries of all these decay modes is necessary to disentangle the various contributions to the raw asymmetries of each mode. The presence of open charm

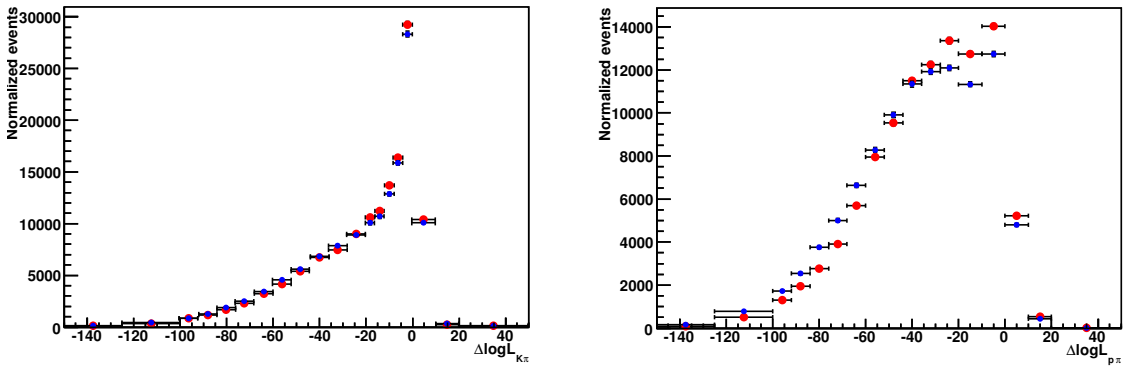

Figure 3.15: Comparison of $\Delta \log \mathcal{L}_{K\pi}$ (left) and $\Delta \log \mathcal{L}_{p\pi}$ (right) distributions for pions from $B^0 \to K^+\pi^-$ decays: determined using the reweighting procedure (red dots) or from full Monte Carlo simulations (blue dots).

	$\pi^+\pi^-$	K^+K^-	$K^+\pi^-$	$p\pi^-$	pK^-
$B^0 \to \pi^+\pi^-$	45.2(4)	0.29(3)	27.0(4)	1.03(8)	0.34(5)
$B^0_s \to K^+K^-$	0.17(2)	50.7(4)	21.2(4)	0.04(1)	3.9(2)
$B^0_{(s)} \to K^+\pi^-$	2.70(6)	4.02(7)	68.2(3)	0.42(2)	0.17(1)
$\bar{B}^0_{(s)} \to \pi^+K^-$	2.70(6)	4.02(7)	2.30(5)	0.026(6)	1.92(5)
$\Lambda_b \to p\pi^-$	2.9(2)	0.49(9)	14.0(5)	44.1(8)	4.8(3)
$\bar{\Lambda}_b \to \pi^+\bar{p}$	2.9(2)	0.49(9)	0.9(1)	0.03(2)	0.27(6)
$\Lambda_b \to pK^-$	0.08(4)	8.1(4)	1.9(2)	2.9(2)	55.4(9)
$\bar{\Lambda}_b \to K^+\bar{p}$	0.08(40	8.1(4)	4.0(3)	0.06(3)	0.20(5)

Table 3.8: Efficiencies (in %) of PID cuts, for the various mass hypotheses, predicted for real data events passing the offline selection optimized for $A_{CP}(B^0 \to K^+\pi^-)$. The values in parentheses represent the statistical errors on the last digit due to the statistics used in the Monte Carlo integration.

production asymmetries arising from the primary proton-proton interaction and the subsequent hadronization phase constitutes an additional complication which needs to be considered. The technique we are going to describe has been succesfully used in Ref. [88], although in that case there was no need to include production asymmetry effects.

For each of the decay modes mentioned before, we can write the following set of equations relating the observed raw asymmetries to the physical $\mathcal{CP}$ asymmetries:

$$A_{CP}^{RAW}(K\pi)^* = A_{CP}(K\pi) + A_D(\pi_s) + A_D(K\pi) + A_P(D^*), \tag{3.11}$$

$$A_{CP}^{RAW}(KK)^* = A_{CP}(KK) + A_D(\pi_s) + A_P(D^*), \tag{3.12}$$

$$A_{CP}^{RAW}(\pi\pi)^* = A_{CP}(\pi\pi) + A_D(\pi_s) + A_P(D^*), \tag{3.13}$$

	$\pi^+\pi^-$	K^+K^-	$K^+\pi^-$	$p\pi^-$	pK^-
$B^0 \to \pi^+\pi^-$	45.3(4)	0.29(3)	2.5(1)	1.08(9)	0.36(5)
$B_s^0 \to K^+K^-$	0.18(3)	50.9(5)	2.2(1)	0.03(1)	3.9(2)
$B_{(s)}^0 \to K^+\pi^-$	2.73(7)	4.02(8)	38.1(3)	0.38(3)	0.17(2)
$\bar{B}_{(s)}^0 \to \pi^+K^-$	2.73(7)	4.02(8)	0.021(6)	0.019(6)	1.82(6)
$\Lambda_b \to p\pi^-$	2.8(2)	0.5(1)	6.1(4)	43.3(9)	3.6(3)
$\bar{\Lambda}_b \to \pi^+\bar{p}$	2.8(2)	0.5(1)	0.06(4)	0.08(4)	0.30(8)
$\Lambda_b \to pK^-$	0.13(5)	7.6(4)	0.06(4)	3.2(3)	54(1)
$\bar{\Lambda}_b \to K^+\bar{p}$	0.13(5)	7.6(4)	1.7(2)	0.02(1)	0.15(6)

Table 3.9: Efficiencies (in %) of PID cuts, for the various mass hypotheses, predicted for real data events passing the offline selection optimized for $A_{CP}(B_s^0 \to \pi^+K^-)$. The values in parentheses represent the statistical errors on the last digit due to the statistics used in the Monte Carlo integration.

	$\pi^+\pi^-$		K^+K^-		$K^+\pi^-$	
	MC	${}_s\mathcal{P}lot$	MC	${}_s\mathcal{P}lot$	MC	${}_s\mathcal{P}lot$
$B^0 \to \pi^+\pi^-$	45.2(4)	41(1)	0.29(3)	0.4(1)	27.0(4)	29(1)
$B_s^0 \to K^+K^-$	0.17(2)	0.15(7)	50.7(4)	48(1)	21.2(4)	21(1)
$B_{(s)}^0 \to K^+\pi^-$	2.70(2)	3.3(3)	4.02(7)	4.0(3)	68.2(3)	62(1)
$\bar{B}_{(s)}^0 \to \pi^+K^-$	2.70(2)	3.3(3)	4.02(7)	4.0(3)	2.30(5)	2.9(3)

Table 3.10: Efficiencies (in %) of PID cuts, for some of the relevant mass hypotheses, predicted for real data events passing the offline selection optimized for $A_{CP}(B^0 \to K^+\pi^-)$. The MC and ${}_s\mathcal{P}lot$ columns contain the efficiencies calculated by reweighting in p and p_T with distributions from Monte Carlo simulations and real data, respectively. The values in parentheses represent the statistical errors on the last digit due to the statistics used in the Monte Carlo integration.

and

$$A_{CP}^{RAW}(K\pi) = A_{CP}(K\pi) + A_D(K\pi) + A_P(D^0), \tag{3.14}$$

	$\pi^+\pi^-$		K^+K^-		$K^+\pi^-$	
	MC	${}_s\mathcal{P}lot$	MC	${}_s\mathcal{P}lot$	MC	${}_s\mathcal{P}lot$
$B^0 \to \pi^+\pi^-$	45.3(4)	44(2)	0.29(3)	0.3(1)	2.5(1)	3.2(5)
$B_s^0 \to K^+K^-$	0.18(3)	0.13(7)	50.9(5)	50(1)	2.2(1)	2.8(5)
$B_{(s)}^0 \to K^+\pi^-$	2.73(7)	2.9(4)	4.02(8)	4.3(4)	38.1(3)	36(1)
$\bar{B}_{(s)}^0 \to \pi^+K^-$	2.73(7)	2.9(8)	4.02(8)	4.3(4)	0.021(6)	0.04(3)

Table 3.11: Efficiencies (in %) of PID cuts, for some of the relevant mass hypotheses, predicted for real data events passing the offline selection optimized for $A_{CP}(B_s^0 \to \pi^+K^-)$. The values in parentheses represent the statistical errors on the last digit due to the statistics used in the Monte Carlo integration.

where

- $A_{CP}^{RAW}(K\pi)^*$, $A_{CP}^{RAW}(KK)^*$, $A_{CP}^{RAW}(\pi\pi)^*$ and $A_{CP}^{RAW}(K\pi)$ are the respective $D^0 \to h^+h'^-$ integrated raw asymmetries (the "*" denotes the D^* tagged decays);
- $A_{CP}(K\pi)$, $A_{CP}(\pi\pi)$, $A_{CP}(KK)$ are the physical $\mathcal{CP}$ asymmetries;
- $A_D(K\pi)$ is the instrumental charge asymmetry in reconstructing $K^+\pi^-$ and $K^-\pi^+$ final states, which is mainly due to the different strong interaction cross-sections between positive and negative kaons, as strong interactions may take place while the final state particles traverse the detector material, as well as to the left-right asymmetry of the detector;
- $A_D(\pi_s)$ is the analogue of $A_D(K\pi)$, but for the pion originated from the D^* decays (also referred to as "slow pion" due to its lower momentum, with respect to the D^0 daughter particles);
- $A_P(D^0)$ and $A_P(D^*)$ are the production asymmetries for prompt D^0 and D^* mesons, respectively.

It is useful to express the instrumental charge asymmetry in terms of two distinct contributions:

$$A_D(K\pi) = A_I(K\pi) + A_R(K\pi) \tag{3.15}$$

and

$$A_D(\pi_s) = A_I(\pi_s) + A_R(\pi_s), \tag{3.16}$$

where $A_I(K\pi)$ and $A_I(\pi_s)$ are the asymmetries due to the different strong interaction cross-sections with the detector material of $K^+\pi^-/K^-\pi^+$ and π_s^-/π_s^+ final state particles, while $A_R(K\pi)$ and $A_R(\pi_s)$ are asymmetries arising from the presence of a left-right detector and possibly reconstruction asymmetry.

The distinction between A_I and A_R turns out to be useful because they exhibit different behaviors under the inversion of the magnetic field polarity. There is no reason to expect that A_I changes its value inverting the magnetic field, as the difference in the interaction lenghts seen by the positive and negative particles for opposite polarities can be safely considered negligible. Instead, the nature of A_R leads to the expectation that this quantity inverts its sign when the magnetic field is inverted, if one neglects a small effect due to the different beam crossing angles in the two field configurations, i.e.:

$$A_R(K\pi)^{\uparrow} = -A_R(K\pi)^{\downarrow} \tag{3.17}$$

and

$$A_R(\pi_s)^{\uparrow} = -A_R(\pi_s)^{\downarrow}. \tag{3.18}$$

In order to verify that this is an effective assumption, Fig. 3.16 shows the dependence of $A_{CP}^{RAW}(K\pi)$ as a function of the azimuthal angle φ of the decaying D^0, separately for data samples acquired for the two magnet polarities. As is apparent, each of the two distributions is incompatible with a flat dependence on φ, exhibiting a clear modulation. Nevertheless, as shown in Fig. 3.17, if one takes the average of the two distributions, the dependence on φ becomes flat with great accuracy over the whole φ range.

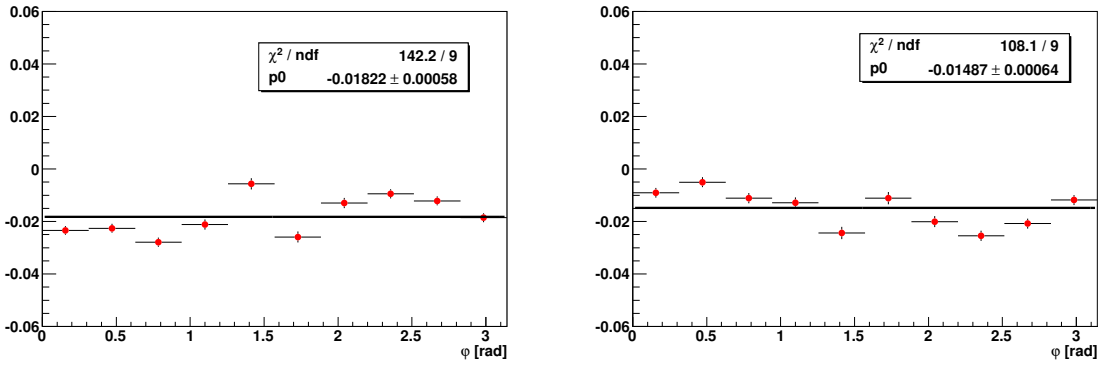

Figure 3.16: $A_{CP}^{RAW}(K\pi)$ as a function of the azimuthal angle φ of the decaying D^0, for up (left) and down (right) polarities of the magnetic field. The azimuthal angle φ is limited from 0 to π because the two bottom quadrants of the detector have been integrated together with the two upper quadrants. The straight line is the result of a χ^2 fit with a constant term.

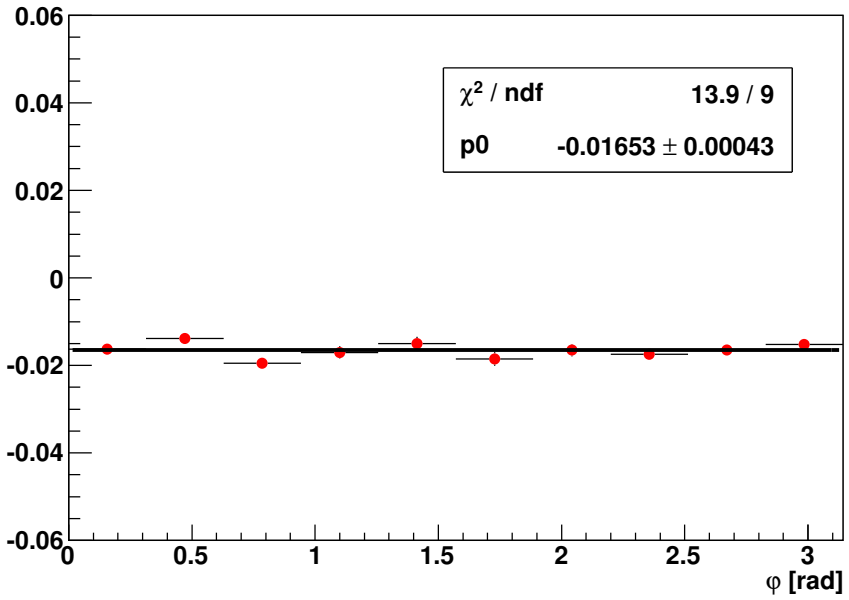

Figure 3.17: Bin-by-bin average of the two plots shown in Fig. 3.16. The straight line is the result of a χ^2 fit with a constant term.

This confirms the validity of Eq. (3.17), since specializing Eq. (3.14) for the two magnet polarities as in the following:

$$A_{CP}^{RAW}(K\pi)^{\uparrow} = A_{CP}(K\pi) + A_I(K\pi) + A_R(K\pi)^{\uparrow} + A_P(D^0), \tag{3.19}$$

$$A_{CP}^{RAW}(K\pi)^{\downarrow} = A_{CP}(K\pi) + A_I(K\pi) - A_R(K\pi)^{\uparrow} + A_P(D^0), \tag{3.20}$$

and then summing these two equations, only quantities that do not have any dependence on φ remain, i.e.:

$$\left(A_{CP}^{RAW}(K\pi)^{\uparrow} + A_{CP}^{RAW}(K\pi)^{\downarrow}\right)/2 = A_{CP}(K\pi) + A_I(K\pi) + A_P(D^0). \tag{3.21}$$

In conclusion, the final set of relevant equations kept distinct for the two up and down magnet polarities, where for convenience we write again Eqs. (3.19) and (3.20), is:

$$A_{CP}^{RAW}(K\pi)^{\uparrow *} = A_{CP}(K\pi) + A_I(\pi_s) + A_R(\pi_s)^{\uparrow} + A_I(K\pi) + A_R(K\pi)^{\uparrow} + A_P(D^*), \tag{3.22}$$

$$A_{CP}^{RAW}(KK)^{\uparrow *} = A_{CP}(KK) + A_I(\pi_s) + A_R(\pi_s)^{\uparrow} + A_P(D^*), \tag{3.23}$$

$$A_{CP}^{RAW}(\pi\pi)^{\uparrow *} = A_{CP}(\pi\pi) + A_I(\pi_s) + A_R(\pi_s)^{\uparrow} + A_P(D^*), \tag{3.24}$$

$$A_{CP}^{RAW}(K\pi)^{\uparrow} = A_{CP}(K\pi) + A_I(K\pi) + A_R(K\pi)^{\uparrow} + A_P(D^0), \tag{3.25}$$

$$A_{CP}^{RAW}(K\pi)^{\downarrow *} = A_{CP}(K\pi) + A_I(\pi_s) - A_R(\pi_s)^{\uparrow} + A_I(K\pi) - A_R(K\pi)^{\uparrow} + A_P(D^*), \tag{3.26}$$

$$A_{CP}^{RAW}(KK)^{\downarrow *} = A_{CP}(KK) + A_I(\pi_s) - A_R(\pi_s)^{\uparrow} + A_P(D^*), \tag{3.27}$$

$$A_{CP}^{RAW}(\pi\pi)^{\downarrow *} = A_{CP}(\pi\pi) + A_I(\pi_s) - A_R(\pi_s)^{\uparrow} + A_P(D^*) \tag{3.28}$$

and

$$A_{CP}^{RAW}(K\pi)^{\downarrow} = A_{CP}(K\pi) + A_I(K\pi) - A_R(K\pi)^{\uparrow} + A_P(D^0). \tag{3.29}$$

Once the raw asymmetries are measured, employing external measurements of the $\mathcal{CP}$ physical asymmetries, this system of equations allows to extract unambiguously a set of quantities, notably including the D^0 production asymmetry and the various instrumental asymmetries A_I and A_R described above.

Data sample and extraction of raw $\mathcal{CP}$ asymmetries

The data sample was composed of the full Reco08-Stripping12 CHARM stream for both magnet polarities. The data were selected using the stripping line `DstarForPromptCharm` for the $D^{*+} \to D^0(h^+h'^-)\pi^+$ modes and the line `D02HHForPromptCharm` for the $D^0 \to K^-\pi^+$ mode. For the latter, to avoid double counting, all events which were used to reconstruct $D^{*+} \to D^0(K^-\pi^+)\pi^+$ decays were discarded while reconstructing $D^0 \to K^-\pi^+$ decays.

In order to extract the raw $\mathcal{CP}$ asymmetry of the $D^0 \to K^-\pi^+$ decay, we performed a binned likelihood fit of the $K^-\pi^+$ and $K^+\pi^-$ mass spectra. The fit was complicated by the fact that the data sample had to be subdivided into four subsamples acquired using different triggers. The

largest part of the available data has been acquired using triggers which tightly cut off the events present in the mass peak sidebands (`Hlt2CharmTF2BodySignal` and `Hlt2CharmOSTF2Body`). As the sidebands were not available, the data acquired with these triggers alone did not allow to estimate the amount of combinatorial background under the mass peak. However, other trigger lines had been foreseen without such requirement (`Hlt2CharmTF2BodyWideMass` and `Hlt2CharmOSTF2BodyWideMass`), albeit they are heavily prescaled. The amount of combinatorial background could be extracted from the events which fired these triggers. Schematically, four exclusive categories can be identified. They are composed of:

- events which fired the `Hlt2CharmTF2BodyWideMass` trigger (TFWM);
- events which fired the `Hlt2CharmOSTF2BodyWideMass` trigger (OSTFWM);
- events which fired the `Hlt2CharmTF2BodySignal` trigger, but not the `Hlt2CharmTF2BodyWideMass` trigger (TF);
- events which fired the `Hlt2CharmOSTF2Body` trigger, but not the `Hlt2CharmOSTF2BodyWideMass` trigger (OSTF).

Only TOS (triggered on signal) events were used. For the TF category, we accepted events which had a reconstructed D^0 mass within the window $1.855\ \mathrm{GeV/c^2} < M_{D^0} < 1.880\ \mathrm{GeV/c^2}$, that is a region with flat HLT2 acceptance, i.e. far enough from the HLT2 cuts in order to avoid smearing effects due to the HLT2 mass resolution. For the same reason, in the case of the OSTF category we accepted only events which had a reconstructed D^0 mass within the window $1.844\ \mathrm{GeV/c^2} < M_{D^0} < 1.880\ \mathrm{GeV/c^2}$.

The signal mass peaks were modeled as the sum of two Gaussians convolved with a component accounting for final state QED radiation processes [90, 91]. The resulting signal component of the p.d.f. was given by

$$g(m) = A\left[\Theta(\mu - m')\ \left(\mu - m'\right)^s\right] \otimes G_2(m - m';\, f_1,\, \sigma_1,\, \sigma_2), \tag{3.30}$$

where A is a normalization factor, $\Theta(\cdot)$ is a *step* function, μ is the mean mass, $G_2(\cdot)$ is the sum of two Gaussians, and the symbol $\otimes$ stands for convolution product. The combinatorial background was instead modeled by a simple exponential p.d.f..

We made a joint fit of the TFWM and the TF categories, where the average mass μ, the fraction of the first Gaussian f_1 and the two widths σ_1 and σ_2 and the raw $\mathcal{CP}$ asymmetry $A_{CP}^{RAW}(K\pi)$ were common parameters. Similarly, a separate joint fit was made for the OSTFWM and OSTF categories. The mass plots for each of the four categories, with the result of the fits superimposed, are shown in Figs. 3.18 and 3.19.

For the three decays $D^{*+} \to D^0(K^-\pi^+)\pi^+$, $D^{*+} \to D^0(K^+K^-)\pi^+$ and $D^{*+} \to D^0(\pi^+\pi^-)\pi^+$ (plus charge conjugates), we performed maximum likelihood fits using as discriminating observable the variable $M_{D^*} - M_{D^0} + M_{D^0}^{PDG}$, where M_{D^*} and M_{D^0} are the reconstructed D^* and D^0 invariant masses respectively, and $M_{D^0}^{PDG}$ is the central value of the current D^0 mass world average. The latter term gives simply a constant shift not bringing any additional information, but we find it useful for plotting purposes.

In this case, the restricted D^0 mass window imposed by the `Hlt2CharmTF2BodySignal` and `Hlt2CharmOSTF2Body` triggers does not pose particular problems, as the distribution of $M_{D^*} - M_{D^0} + M_{D^0}^{PDG}$ is practically unaffected by the D^0 mass cut. Here, for each final state hypothesis, we subdivided the data sample into two categories:

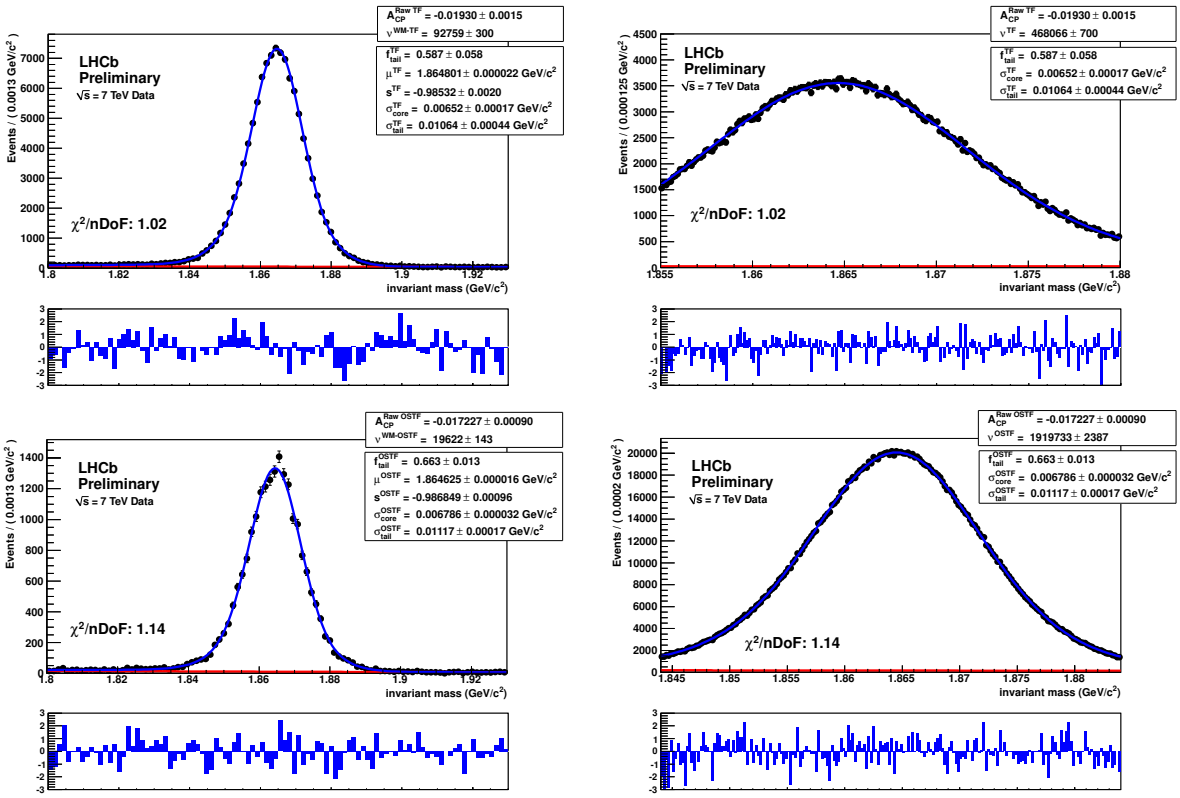

Figure 3.18: $D^0 \to K^-\pi^+$ (plus charge conjugate) mass spectra with the results of the maximum likelihood fit superimposed, for data acquired with up polarity of the magnetic field. The four plots are for the TFWM category (top left), the TF category (top right) and the OSTFWM category (bottom left) and the OSTF category (bottom right), see text for their definition.

- events which fired the `Hlt2CharmTF2BodySignal` trigger, where in addition we requested the M_{D^0} mass to be within the range 1.855 GeV/c^2 $< M_{D^0} <$ 1.880 GeV/c^2, or which fired the `Hlt2CharmTF2BodyWideMass` trigger (TF*);
- events which fired the `Hlt2CharmOSTF2Body` trigger, where in addition we requested the M_{D^0} mass to be within the range 1.844 GeV/c^2 $< M_{D^0} <$ 1.880 GeV/c^2, or which fired the `Hlt2CharmOSTF2BodyWideMass` trigger (OSTF*).

Only TOS events were used.

The signal mass peaks were modeled as the sum of three Gaussians for the $D^{*+} \to D^0(K^-\pi^+)\pi^+$ decay and two Gaussians for the $D^{*+} \to D^0(K^+K^-)\pi^+$ and $D^{*+} \to D^0(\pi^+\pi^-)\pi^+$ decays, where the lower statistics did not allow to appreciate the relevance of a third Gaussian, convolved with a component accounting for a long tail in the right part of the spectrum. Inspired by the parameterization used to describe the effect of QED radiation in the $D^0 \to K^-\pi^+$ fit described previously, we used here the same analytical formula, with the only difference that the radiative component had an inverted parity, i.e.:

$$g(m) = A\left[\Theta(m'-\mu)\ (m'-\mu)^s\right] \otimes G_3(m-m';\ f_1,\ f_3,\ \sigma_1,\ \sigma_2,\ \sigma_3) \tag{3.31}$$

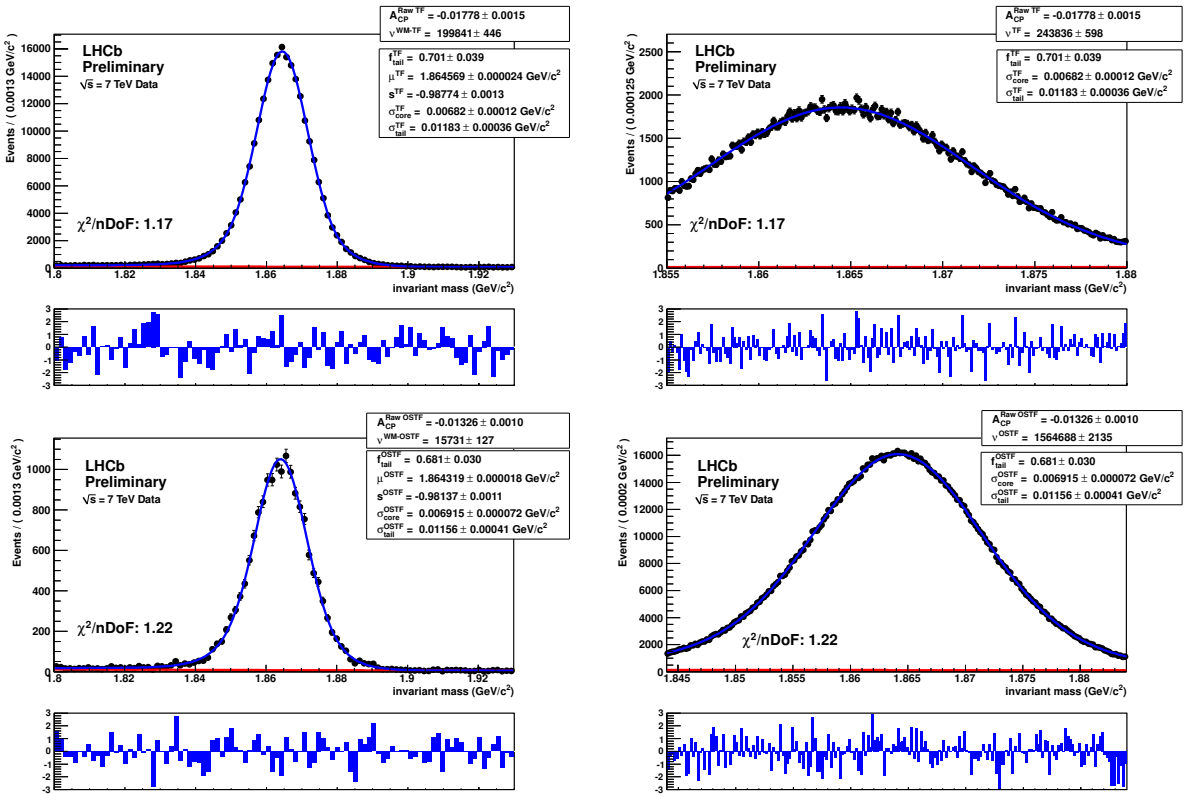

Figure 3.19: $D^0 \to K^-\pi^+$ (plus charge conjugate) mass spectra with the results of the maximum likelihood fit superimposed, for data acquired with down polarity of the magnetic field. The four plots are for the TFWM category (top left), the TF category (top right) and the OSTFWM category (bottom left) and the OSTF category (bottom right), see text for their definition.

and the analogue equation with G_2 instead of G_3 for the two lower statistics modes, where m represents the variable $M_{D^*} - M_{D^0} + M^{PDG}_{D^0}$. The background was instead modeled with the following p.d.f.:

$$h(m) = B\left[1 - \exp\left(-\frac{m - m_0}{c}\right)\right], \tag{3.32}$$

where B is a normalization factor, m_0 and c are two parameters governing the shape of the distribution.

We made separate fits for the TF* and OSTF* categories. The mass plots for each of the two categories, with the result of the fits superimposed, are shown in Figs. 3.20, 3.21, 3.22, 3.23, 3.24 and 3.25.

Yields and raw $\mathcal{CP}$ asymmetries determined by the fits are summarized in Tabs. 3.12 and 3.13. The raw asymmetries are also illustrated in Fig. 3.26.

Employing the current world averages of the integrated $\mathcal{CP}$ physical asymmetries for the two modes $D^0 \to K^+K^-$ and $D^0 \to \pi^+\pi^-$ (the $\mathcal{CP}$ asymmetry for the Cabibbo-favoured $D^0 \to K^-\pi^+$ decay is assumed negligible), which are summarized in Tab. 3.14, the system of Eqs. (3.22)-(3.29) can be solved in order to determine unambiguously some of the relevant instrumental and production asymmetries. The results are summarized in Tab. 3.15.

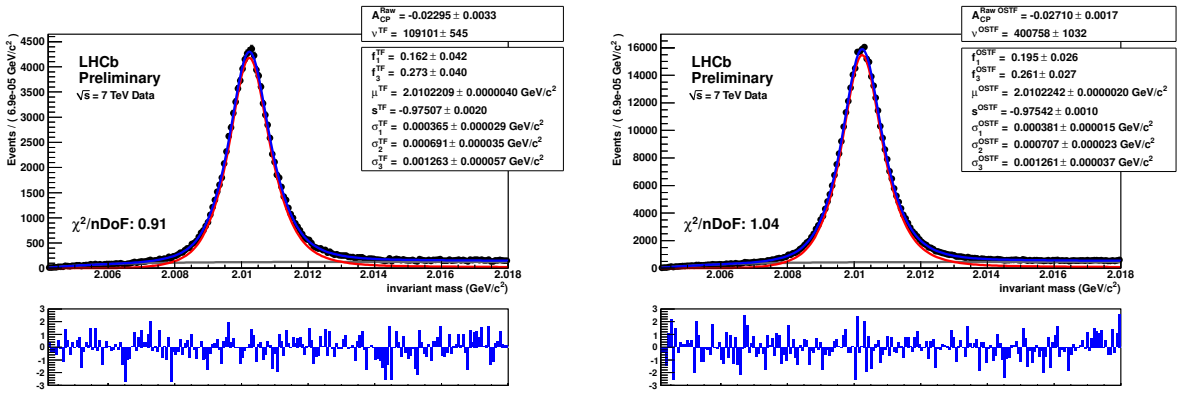

Figure 3.20: $D^{*+} \to D^0(K^-\pi^+)\pi^+$ (plus charge conjugate) mass spectra with the results of the maximum likelihood fit superimposed, for data acquired with the up polarity of the magnetic field. The two plots are for the TF* category (left) and the OSTF* category (right), see text for their definition.

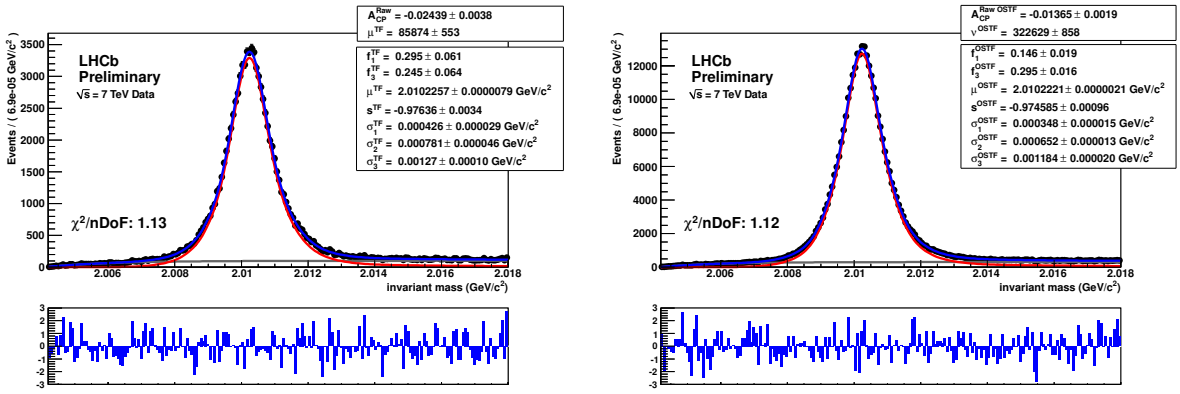

Figure 3.21: $D^{*+} \to D^0(K^-\pi^+)\pi^+$ (plus charge conjugate) mass spectra with the results of the maximum likelihood fit superimposed, for data acquired with the down polarity of the magnetic field. The two plots are for the TF* category (left) and the OSTF* category (right), see text for their definition.

The most relevant quantities for the analysis in this thesis are the asymmetries $A_D(K\pi)^{\uparrow}$ and $A_D(K\pi)^{\downarrow}$, since the same asymmetries are also present when measuring the direct $\mathcal{CP}$ asymmetry in the $B^0 \to K^+\pi^-$ and $B^0_s \to \pi^+K^-$ decay modes, and can be used to correct the raw $\mathcal{CP}$ asymmetries in order to isolate the physical ones. $A_D(K\pi)^{\uparrow}$ and $A_D(K\pi)^{\downarrow}$ are determined to be quite small, well compatible with zero, both with an absolute error of 0.38%, dominated by the uncertainty on $A_I(K\pi)$. Note that $A_D(K\pi)^{\uparrow}$ and $A_D(K\pi)^{\downarrow}$ are almost 100% correlated, and their average is equal to $A_I(K\pi)$. We are also able to measure the presence of a production asymmetry for D^0 mesons with a significance of $3\,\sigma$: $A_P(D^0) = -0.0115 \pm 0.0038$.

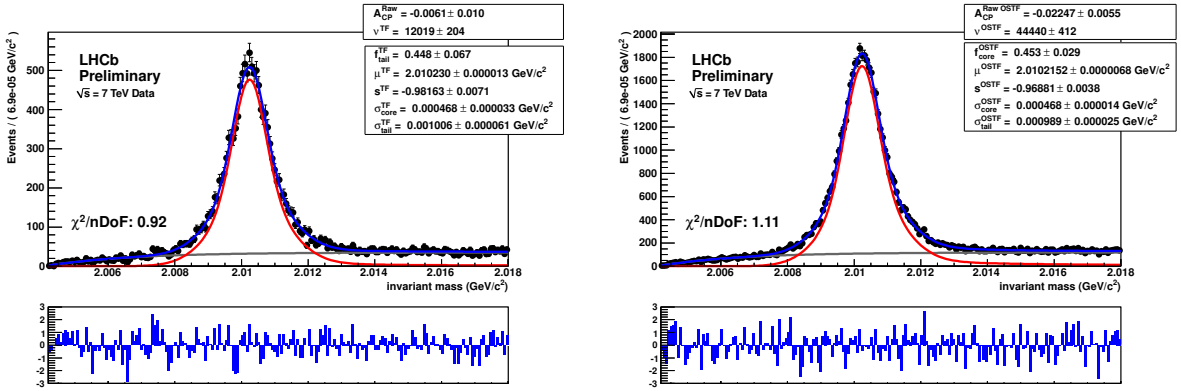

Figure 3.22: $D^{*+} \to D^0(K^+K^-)\pi^+$ (plus charge conjugate) mass spectra with the results of the maximum likelihood fit superimposed, for data acquired with the up polarity of the magnetic field. The two plots are for the TF* category (left) and the OSTF* category (right), see text for their definition.

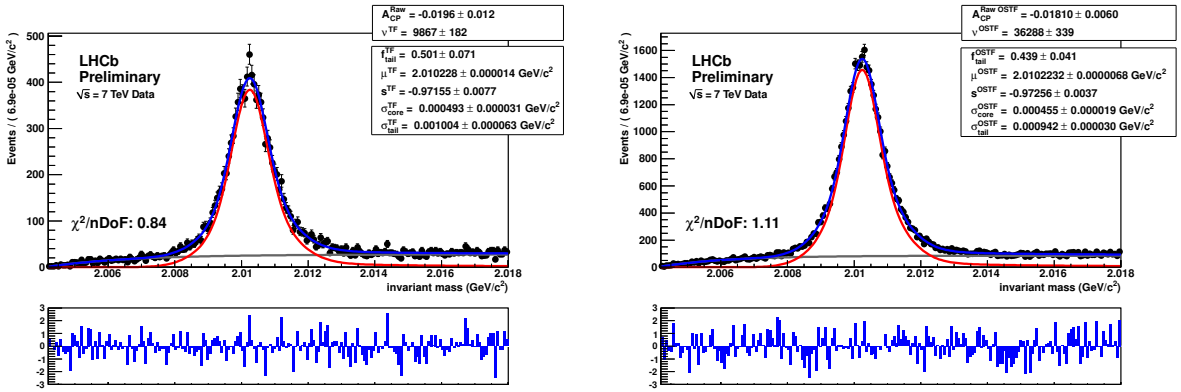

Figure 3.23: $D^{*+} \to D^0(K^+K^-)\pi^+$ (plus charge conjugate) mass spectra with the results of the maximum likelihood fit superimposed, for data acquired with the down polarity of the magnetic field. The two plots are for the TF* category (left) and the OSTF* category (right), see text for their definition.

3.3.1 B meson production asymmetry

In order to measure direct $\mathcal{CP}$ asymmetries using proton-proton collisions at the LHC with a single-arm spectrometer, one needs to cope with an additional complication, which is not present (or less relevant) with flavour-symmetric machines and detectors. Since B^+ and B^0 mesons share valence quarks with the initial protons, while B^- and $\bar{B}^0$ do not, it is expected that B^+'s and B^0's are produced at a higher rate, especially when produced at large pseudo-rapidities.

In this section we present a study aiming to estimate the size of such a production asymmetry, realized by reconstructing a sample of $B^\pm \to J/\psi(\mu^+\mu^-)K^\pm$ decays, where the flavour of the decaying B is tagged via the sign of the K meson. The physical $\mathcal{CP}$ asymmetry for this decay is expected to be $\mathcal{O}(10^{-3})$ in the SM [92], and the current world average is $A_{CP}(B^+ \to J/\psi K^+) = 0.009 \pm 0.008$ [21]. Hence from the measured asymmetry one can extract the production asymmetry, provided that instrumental effects are taken into account.

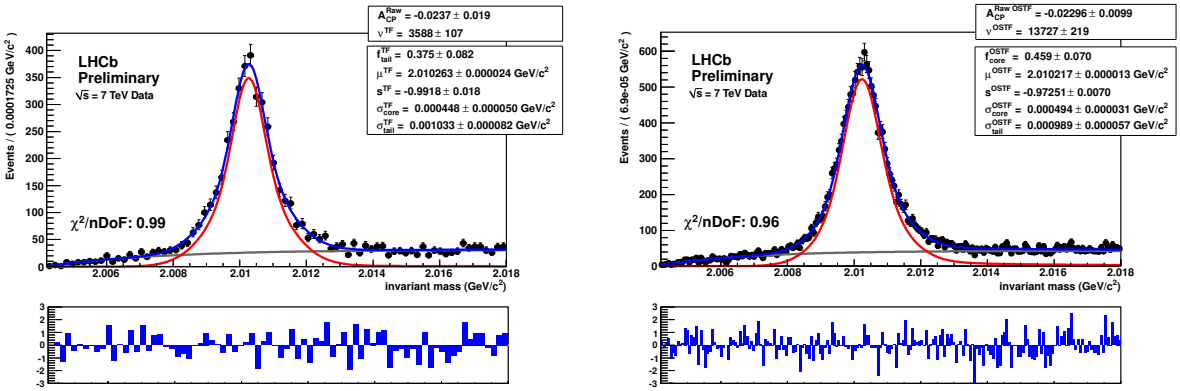

Figure 3.24: $D^{*+} \to D^0(\pi^+\pi^-)\pi^+$ (plus charge conjugate) mass spectra with the results of the maximum likelihood fit superimposed, for data acquired with the up polarity of the magnetic field. The two plots are for the TF* category (left) and the OSTF* category (right), see text for their definition.

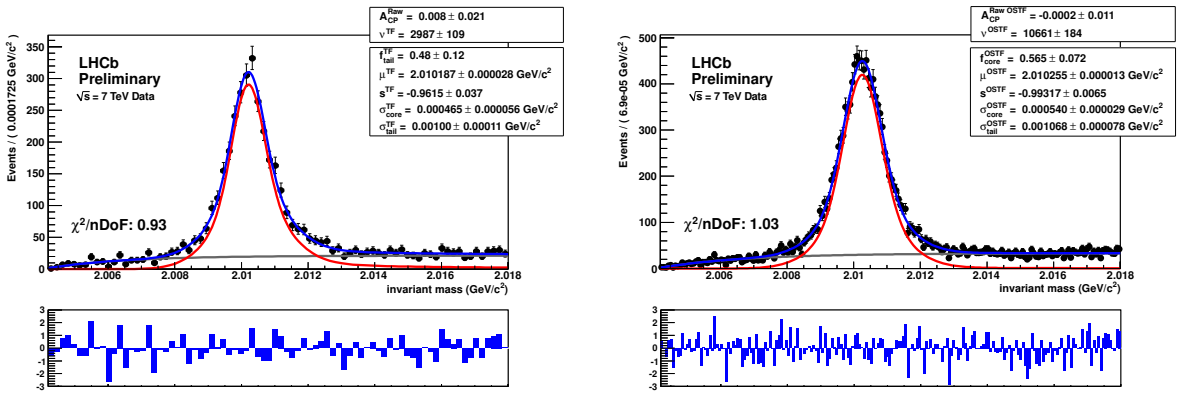

Figure 3.25: $D^{*+} \to D^0(\pi^+\pi^-)\pi^+$ (plus charge conjugate) mass spectra with the results of the maximum likelihood fit superimposed, for data acquired with the down polarity of the magnetic field. The two plots are for the TF* category (left) and the OSTF* category (right), see text for their definition.

3.3.1.1 Method

The observed raw asymmetry, in the two cases of up and down polarities of the magnetic field respectively, can be written as

$$A_{CP}^{RAW}(B^+ \to J/\psi K^+)^{\uparrow} = A_{CP}(B^+ \to J/\psi K^+) + A_I(K) + A_R(K)^{\uparrow} + A_P(B^+) \tag{3.33}$$

and

$$A_{CP}^{RAW}(B^+ \to J/\psi K^+)^{\downarrow} = A_{CP}(B^+ \to J/\psi K^+) + A_I(K) - A_R(K)^{\uparrow} + A_P(B^+), \tag{3.34}$$

where we have used the relation

$$A_R(K)^{\uparrow} = -A_R(K)^{\downarrow}. \tag{3.35}$$

Channel	Yield	
	Magnet up	Magnet down
$D^* \to D^0(K\pi)\pi$	509859 ± 1167	408503 ± 1021
$D^* \to D^0(KK)\pi$	56459 ± 460	46155 ± 385
$D^* \to D^0(\pi\pi)\pi$	17315 ± 244	13648 ± 214
$D^0 \to \pi K$	2500180 ± 2510	2024096 ± 2265

Table 3.12: Summary of the signal yields determined by the maximum likelihood fits, summing together the various trigger categories, separately for the up and down polarities of the magnetic field.

Channel	A_{CP}^{RAW}	
	Magnet up	Magnet down
$D^* \to D^0(K\pi)\pi$	-0.0262 ± 0.0015	-0.0159 ± 0.0017
$D^* \to D^0(KK)\pi$	-0.0190 ± 0.0048	-0.0184 ± 0.0053
$D^* \to D^0(\pi\pi)\pi$	-0.0231 ± 0.0087	0.0015 ± 0.0097
$D^0 \to K\pi$	-0.01776 ± 0.00078	-0.01470 ± 0.00083

Table 3.13: Summary of the raw asymmetries determined by the maximum likelihood fits, averaged between the various trigger categories, for the up and down polarities of the magnetic field.

The term $A_I(K)$ represents the asymmetry due to the different strong interaction probabilities of positive and negative kaons with the detector material, $A_R(K)^{\uparrow}$ and $A_R(K)^{\downarrow}$ account for a possible reconstruction asymmetry (e.g. arising from a left-right asymmetry of the detector) in magnet up and magnet down data respectively, and $A_P(B^+)$ is the production asymmetry. By averaging these two equations we get

$$\begin{aligned} \frac{A_{CP}^{RAW}(B^+ \to J/\psi K^+)^{\uparrow} + A_{CP}^{RAW}(B^+ \to J/\psi K^+)^{\downarrow}}{2} = \\ = A_{CP}(B^+ \to J/\psi K^+) + A_I(K) + A_P(B^+), \end{aligned} \tag{3.36}$$

i.e. using the world average of $A_{CP}(B^+ \to J/\psi K^+)$, we can extract $A_P(B^+)$ once we measure $A_I(K)$ and the raw $\mathcal{CP}$ asymmetries for both the magnet polarities.

Channel	A_{CP}
$D^0 \to K^+K^-$	-0.0016 ± 0.0023
$D^0 \to \pi^+\pi^-$	0.0022 ± 0.0021

Table 3.14: Current world averages of the integrated $\mathcal{CP}$ physical asymmetries for the two modes $D^0 \to K^+K^-$ and $D^0 \to \pi^+\pi^-$ [86]. The $D^0 \to \pi^+\pi^-$ asymmetry also includes the latest CDF result [88].

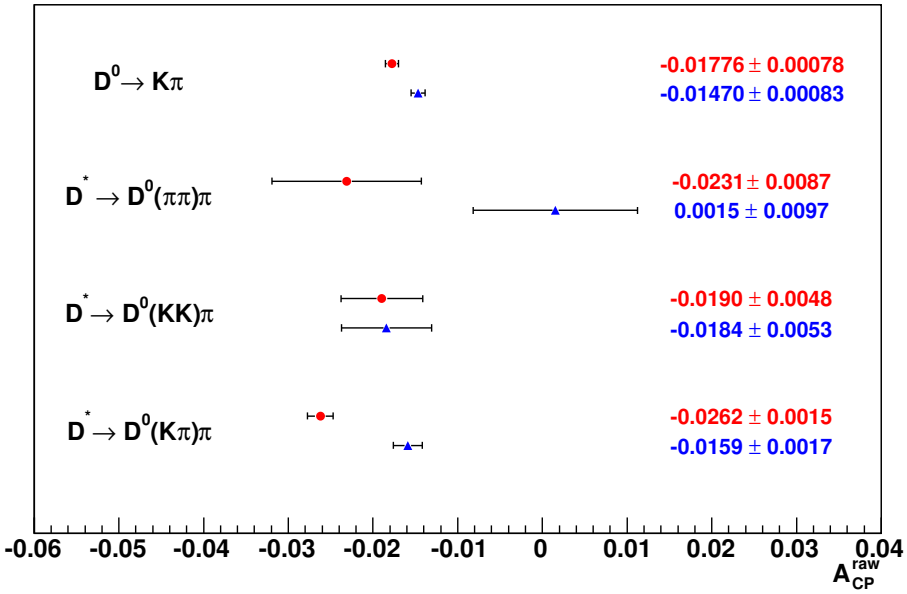

Figure 3.26: Graphical view of the A_{CP}^{RAW} measurements. Each pair of measurements corresponds to the up (red) and down (blue) polarities of the magnetic field.

Asymmetries	
$A_P(D^0)$	-0.0115 ± 0.0038
$A_I(K\pi)$	-0.0044 ± 0.0038
$A_R(K\pi)^{\uparrow}$	-0.0015 ± 0.0006
$A_I(\pi_s) + A_P(D^*)$	-0.0160 ± 0.0036
$A_R(\pi_s)^{\uparrow}$	-0.0035 ± 0.0012
$A_D(K\pi)^{\uparrow}$	-0.0059 ± 0.0038
$A_D(K\pi)^{\downarrow}$	-0.0030 ± 0.0038

Table 3.15: Summary of relevant instrumental and production asymmetries. See text for their definition.

3.3.2 Data sample and extraction of the production asymmetry

The data sample was composed of the full Reco08-Stripping12 DIMUON stream for both magnet polarities. The data were selected using the stripping line `Bu2JpsiKUnbiasedLine`. In addition to the pre-selection, in order to further suppress the combinatorial background, an offline selection was applied using the following simple set of cuts:

- the minimum impact parameter χ^2 values of the two muons and the kaon, calculated with respect to all primary vertices, were requested to exceed 9;
- the proper decay time of the B candidate had to be larger than 0.1 ps.

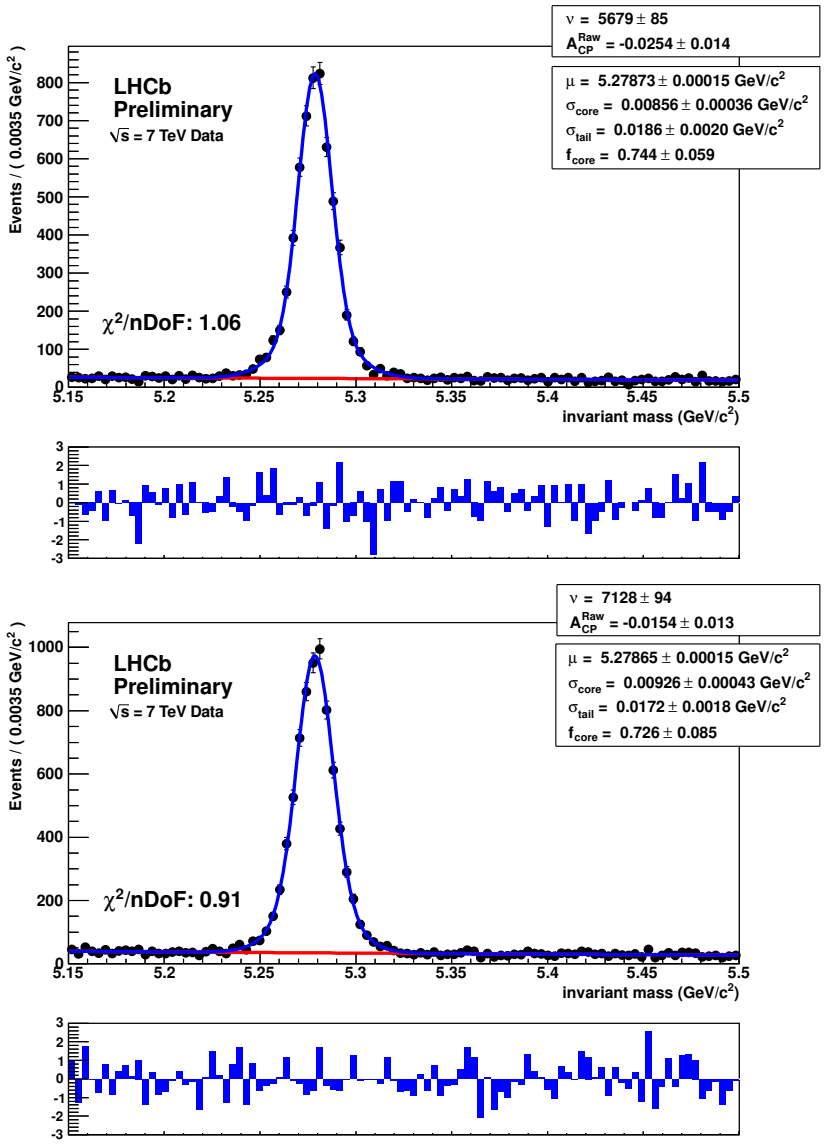

Figure 3.27: $B^{\pm} \to J/\psi(\mu^+\mu^-)K^{\pm}$ invariant mass plots, for up (top) and down (bottom) polarities of the magnetic field.

In order to extract the raw $\mathcal{CP}$ asymmetry we performed an unbinned maximum likelihood fit of the $J/\psi K^+$ and $J/\psi K^-$ mass spectra. The signal mass peak was modeled as the sum of two Gaussians with common mean, while the combinatorial background was modeled by means of an exponential p.d.f.. The mass plots with the result of the fit superimposed are shown in Fig. 3.27. Signal yields and raw $\mathcal{CP}$ asymmetries returned by the fit are reported in Tab. 3.16.

To determine $A_I(K)$, which is the last ingredient needed to extract $A_P(B^+)$, we can again make use of two-body charm control samples, by noting that $A_I(K)$ can be approximated with the corresponding quantity $A_I(K\pi)$, i.e. the asymmetry due to the different absorption probabilities of the $K^+\pi^-$ and $K^-\pi^+$ final states from $\bar{D}^0$ and D^0 Cabibbo-favoured decays

	Magnet up	Magnet down
$B^\pm \to J/\psi(\mu^+\mu^-)K^\pm$ event yield	5679 ± 85	7128 ± 94
$A_{CP}^{RAW}(B^+ \to J/\psi(\mu^+\mu^-)K^+)$	-0.025 ± 0.014	-0.015 ± 0.013

Table 3.16: Signal yields and raw $\mathcal{CP}$ asymmetries determined by unbinned maximum likelihood fits to the $B^\pm \to J/\psi(\mu^+\mu^-)K^\pm$ reconstructed invariant mass spectra.

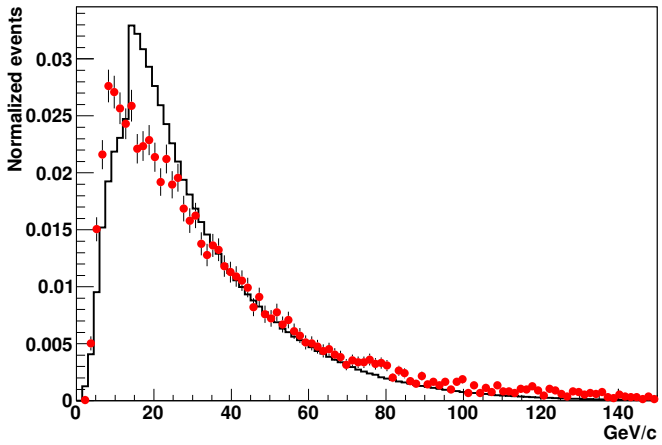

Figure 3.28: Comparison of momentum distributions for charged kaons from $D^0 \to K^-\pi^+$ (histogram) and $B^+ \to J/\psi(\mu^+\mu^-)K^+$ (dots with error bars) decays.

respectively. This is a valid approximation as we can neglect the difference in strong interaction cross-sections of positive and negative pions in the high momentum region under consideration, provided that the momenta of charged kaons from $D^0 \to K^-\pi^+$ and $B^+ \to J/\psi(\mu^+\mu^-)K^-$ decays cover the same range. A comparison of the momentum distributions of these charged kaons determined from real data is shown in Fig. 3.28.

3.3.2.1 Impact on A_{CP} measurements

B meson production asymmetries affect the extraction of physical A_{CP} asymmetries, such as $A_{CP}(B^0 \to K^+\pi^-)$. If we denote as $\Gamma_f(t)$ and $\Gamma_{\bar{f}}(t)$ the decay rates of neutral reconstructed B or $\bar{B}$ mesons to f and $\bar{f}$ specific-flavour final states, regardless of the initial flavour of the decaying mesons, we have:

$$\Gamma_f(t) \propto \mathcal{BR}(B \to f)\left[e^{-\Gamma t'}\left(\cosh\frac{\Delta\Gamma}{2}t' - A_P\cos\Delta m t'\right)\right]\varepsilon(t) \tag{3.37}$$

and

$$\Gamma_{\bar{f}}(t) \propto \mathcal{BR}(\bar{B} \to \bar{f})\left[e^{-\Gamma t'}\left(\cosh\frac{\Delta\Gamma}{2}t' + A_P\cos\Delta m t'\right)\right]\varepsilon(t) \tag{3.38}$$

Channel	κ
$B^0 \to K^+\pi^-$	0.33
$B_s^0 \to \pi^+K^-$	0.015

Table 3.17: κ factors calculated for the $B^0 \to K^+\pi^-$ and $B_s^0 \to \pi^+K^-$ selections.

where $\varepsilon(t)$ is the acceptance as a function of the proper decay time, and the production asymmetry A_P is defined as

$$A_P = \frac{N_{\bar{B}} - N_B}{N_{\bar{B}} + N_B}. \tag{3.39}$$

The raw $\mathcal{CP}$ asymmetry in then given by

$$A_{CP}^{RAW} = \frac{\int \Gamma_{\bar{f}}(t)dt - \int \Gamma_f(t)dt}{\int \Gamma_{\bar{f}}(t)dt + \int \Gamma_f(t)dt} = \frac{A_{CP} + \kappa A_P}{1 + \kappa A_P A_{CP}} \simeq A_{CP} + \kappa A_P, \tag{3.40}$$

where the factor κ can be calculated as

$$\kappa = \frac{\int \left(e^{-\Gamma t'} \cos \Delta m t'\right) \varepsilon(t)dt}{\int \left(e^{-\Gamma t'} \cosh \frac{\Delta\Gamma}{2} t'\right) \varepsilon(t)dt}. \tag{3.41}$$

In other words, as $\varepsilon(t)$ is a function which depends on the event selection in use, the production asymmetry enters the expression of A_{CP}^{RAW} in a selection dependent way via the κ factor. The κ factors for $A_{CP}(B^0 \to K^+\pi^-)$ and $A_{CP}(B_s^0 \to \pi^+K^-)$ are reported in Tab. 3.17. They have been calculated by determining the acceptance function from Monte Carlo simulations, using the event selections optimized for the respective A_{CP} measurements.

It can be noted that, due to the fast B_s^0 oscillations, the κ factor for the case of the $B_s^0 \to \pi^+K^-$ decay is very small, i.e. the possible presence of a B_s^0 production asymmetry would not affect the measurement of $A_{CP}(B_s^0 \to \pi^+K^-)$ in a sizeable way. In contrast, the κ factor for the case of the $B^0 \to K^+\pi^-$ decay is 33%, hence the presence of a B^0 production asymmetry has a non negligible effect while extracting $A_{CP}(B^0 \to K^+\pi^-)$ from the respective raw asymmetry.

3.4 Fits to the $B \to h^+h'^-$ mass spectra

We performed unbinned maximum likelihood fits to the mass spectra of offline selected events, passing the kinematic selection with the PID cuts optimized for the measurements of $A_{CP}(B^0 \to K^+\pi^-)$ or of $A_{CP}(B_s^0 \to \pi^+K^-)$, summarized in Tabs. 3.2, 3.3, 3.4 and 3.5. The selection cuts were applied on the full Reco08-Stripping12 BHADRON stream passing the `Hb2ChargedBody` stripping line.

The extraction of the two signal decays $B^0 \to K^+\pi^-$ and $B_s^0 \to \pi^+K^-$ from the $K^\pm\pi^\mp$ mass spectra is plagued by three distinct sources of background:

- combinatorial background, that is a non-peaking component present over the whole mass window;
- 3-body B-decay background, e.g. composed of $B \to \rho\pi$ decays where one of the pions from the ρ decay is missed, which occurs at the left of the signal mass peaks due to the missing mass;

- cross-feed background, i.e. the background determined by all the other charmless B decay modes, where one or both the decay products have been mis-identified.

This last component is the most dangerous amongst the three, because, differently from the other two, is characterized by a peaking behaviour below the mass peaks we want to measure.

Each of the two sets of PID cuts given in Tabs. 3.4 and 3.5 allows to subdivide the events passing the kinematic selection into eight mutually exclusive categories corresponding to distinct final state hypotheses, namely $K^+\pi^-$, $K^-\pi^+$, $\pi^+\pi^-$, K^+K^-, $p\pi^-$, $\bar{p}\pi^+$, pK^- and $\bar{p}K^+$.

3.4.1 Fit model

The signal component for each of the eight categories has been parameterized as a single Gaussian convolved with a component accounting for the final state QED radiation [90, 91]. The p.d.f. was given by

$$g(m) = A\left[\Theta(\mu - m')\ \left(\mu - m'\right)^s\right] \otimes G(m - m'; \sigma), \tag{3.42}$$

where A is a normalization factor, $\Theta(\cdot)$ is a *step* function, μ and σ are the mean mass and the mass resolution, $G(\cdot)$ is a Gaussian, and the symbol $\otimes$ stands for convolution product. Within the current statistics it was not possible to appreciate the need of a second Gaussian in the signal model. The parameter s, governing the final state QED radiation, was fixed for each signal component by using the respective theoretical QED prediction, calculated as shown in Ref. [91].

The combinatorial background was modeled by an exponential p.d.f., while the background from 3-body partially reconstructed decays was modeled with the p.d.f. defined in Eq. (3.8). While it was possible to appreciate the presence of a 3-body background in the $K^+\pi^-$, $K^-\pi^+$ and $\pi^+\pi^-$ categories, in all the other categories there was not any significant evidence. Thus we have foreseen such a component only for these three categories.

Finally, the modelling of the cross-feed background has been made by means of Monte Carlo simulations. PID cuts for each of the eight categories have been applied to $B^0 \to \pi^+\pi^-$, $B^0 \to K^+\pi^-$, $B^0_s \to K^+K^-$, $B^0_s \to \pi^+K^-$, $\Lambda_b \to pK^-$ and $\Lambda_b \to p\pi^-$ Monte Carlo events surviving the kinematic event selection. We determined in this way, for each final state hypothesis, a set of mass distributions from events where one or both tracks were mis-identified, and we parameterized each of them by means of a kernel estimation technique [93]. To this end we used the *RooKeysPdf* class embedded in the *RooFit* framework [94], i.e. the statistical software toolkit that we employed for performing all the maximum likelihood fits described in this thesis. The normalization of each cross-feed background component was determined as the product of the yield of the respective background channel with the ratio of the PID efficiencies of the signal and background final state hypotheses.

As an example, the $K^+\pi^-$ mass spectrum receives cross-feed contributions from $\bar{B}^0 \to K^-\pi^+$ events (where the identities of both particles has been swapped), from $B^0 \to \pi^+\pi^-$ events (where the the positive particle has been misidentified) and so on. The number of $B^0 \to \pi^+\pi^-$ events giving a cross-feed background contribution to the $K^+\pi^-$ mass spectrum is given by:

$$N(\pi^+\pi^- \to K^+\pi^-) = Y(B^0 \to \pi^+\pi^-)\frac{\varepsilon_{K\pi}}{\varepsilon_{\pi\pi}}, \tag{3.43}$$

where $Y(B^0 \to \pi^+\pi^-)$ is the yield of reconstructed $B^0 \to \pi^+\pi^-$ decays, $\varepsilon_{K\pi}$ is the PID cut efficiency using the $K^+\pi^-$ hypothesis on $B^0 \to \pi^+\pi^-$ decays, and $\varepsilon_{K\pi}$ is its analogue using the

$\pi^+\pi^-$ hypothesis, as given in Tabs. 3.8 and 3.9. Conversely, the $\pi^+\pi^-$ mass spectrum receives cross-feed background contributions from $B^0 \to K^+\pi^-$ decays, where the positive particle has been mis-identified. Hence, in order to determine the $B^0 \to \pi^+\pi^-$ yield, symmetrically one needs to know the $B^0 \to K^+\pi^-$ signal yield and use the analogue of Eq. (3.43) to fix the cross-feed background normalization.

In order to properly take into account the presence of such many-to-many cross-feed backgrounds, we performed a joint fit of all the eight categories at once. In this way we determined simultaneously all the signal yields and all the normalizations of the cross-feed backgrounds.

The unbinned maximum likelihood fit featured 34 free parameters. The complete list of free parameters is:

- three mean masses of B^0, B_s^0 and Λ_b hadrons and the width of the single Gaussian modeling the mass resolution, which was in common between all the decay modes;
- five yields of the $B^0 \to \pi^+\pi^-$, $B^0 \to K^+\pi^-$, $B_s^0 \to K^+K^-$, $\Lambda_b \to pK^-$ and $\Lambda_b \to p\pi^-$ decays, and the ratio of the $B_s^0 \to \pi^+K^-$ and $B^0 \to K^+\pi^-$ yields;
- four raw $\mathcal{CP}$ asymmetries $A_{CP}^{RAW}(B^0 \to K^+\pi^-)$, $A_{CP}^{RAW}(B_s^0 \to \pi^+K^-)$, $A_{CP}^{RAW}(\Lambda_b \to pK^-)$ and $A_{CP}^{RAW}(\Lambda_b \to p\pi^-)$;
- five exponential slopes for the combinatorial background of the $K^+\pi^-$+c.c., $\pi^+\pi^-$, K^+K^-, pK^-+c.c. and $p\pi^-$+c.c. categories;
- two yields of 3-body background events in the $\pi^+\pi^-$ and $K^+\pi^-$+c.c. categories;
- five yields of combinatorial background events of the $K^+\pi^-$+c.c., $\pi^+\pi^-$, K^+K^-, pK^-+c.c. and $p\pi^-$+c.c. categories;
- three charge asymmetries for combinatorial background events in the $K^+\pi^-$+c.c., pK^-+c.c. and $p\pi^-$+c.c. categories;
- one charge asymmetry for 3-body background events in the $K^+\pi^-$+c.c. categories;
- two parameters governing the shape of the function modeling the 3-body background for the $K^+\pi^-$+c.c. categories, and other two for the $\pi^+\pi^-$ category.

3.4.2 Fit results

The fits were realized by using the MIGRAD minimization engine of the MINUIT software library [95], configured with the so-called *Strategy 2*, followed upon convergence by the HESSE algorithm of the same library, in order to calculate with better precision the covariance matrix. Two fits were done, either using the selection optimized for the best sensitivity on $A_{CP}(B^0 \to K^+\pi^-)$ or on $A_{CP}(B_s^0 \to \pi^+K^-)$ (see Tabs. 3.2, 3.3, 3.4 and 3.5).

3.4.2.1 Selection optimized for $A_{CP}(B^0 \to K^+\pi^-)$

The $K^+\pi^-$ (plus charge conjugate) mass spectrum is shown in Fig. 3.29. The dominant signal visible in the mass spectrum is due to the $B^0 \to K^+\pi^-$ decay. The peaked distributions below the $B^0 \to K^+\pi^-$ peak are due to the cross-feed background. Three of them give a non negligible contribution that is clearly visible in the plot:

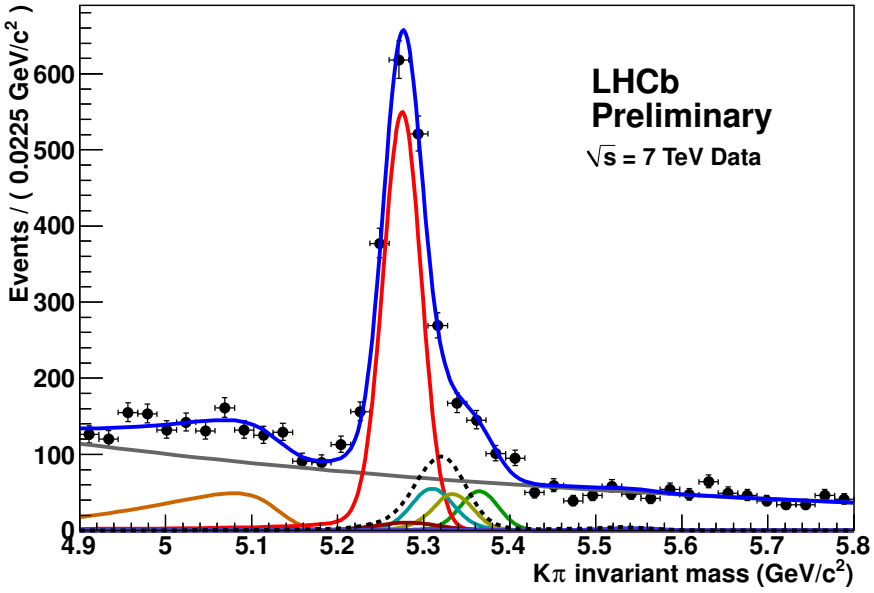

Figure 3.29: $K^+\pi^-$ (plus charge conjugate) invariant mass spectrum for events surviving the event selection optimized for the best sensitivity on $A_{CP}(B^0 \to K^+\pi^-)$. The result of the unbinned maximum likelihood fit is superimposed to the histogram. The various signal and background components contributing to the fit model are also shown. The dashed curve represents the sum of all the cross-feed background components.

- wrong sign $B^0 \to K\pi$ combination, i.e. when the identities of the two particles have been swapped (dark red);
- $B^0 \to \pi^+\pi^-$ decays, where one of the two pions has been mis-identified as a kaon (light blue);
- $B^0_s \to K^+K^-$ decays, where one of the two kaons has been mis-identified as a pion (dark yellow).

The plot also shows as a dashed curve the sum of these three components. A fourth component (green), due to the $B^0_s \to \pi^+K^-$ signal decay and not accounted by the dashed curve as a cross-feed background, is also visible.

A visual indication of $\mathcal{CP}$ violation is given in Fig. 3.30, showing the $K^+\pi^-$ and $K^-\pi^+$ invariant mass spectra separately: the difference in the heights of the $B^0 \to K^+\pi^-$ and $\bar{B}^0 \to K^-\pi^+$ mass peaks is apparent.

Fig. 3.31 shows the $\pi^+\pi^-$ and K^+K^- invariant mass spectra. In both the cases, the dominant cross-feed background comes from the $B^0 \to K^+\pi^-$ decay, where one of the two final state particles is mis-identified as a pion or a kaon. Finally, Fig. 3.32 shows the pK^- and $p\pi^-$ invariant mass spectra.

The relevant parameters determined by the maximum likelihood fit are summarized in Tab. 3.18. It can be noted that the statistical uncertainty on $A^{RAW}_{CP}(B^0 \to K^+\pi^-)$ is about two times

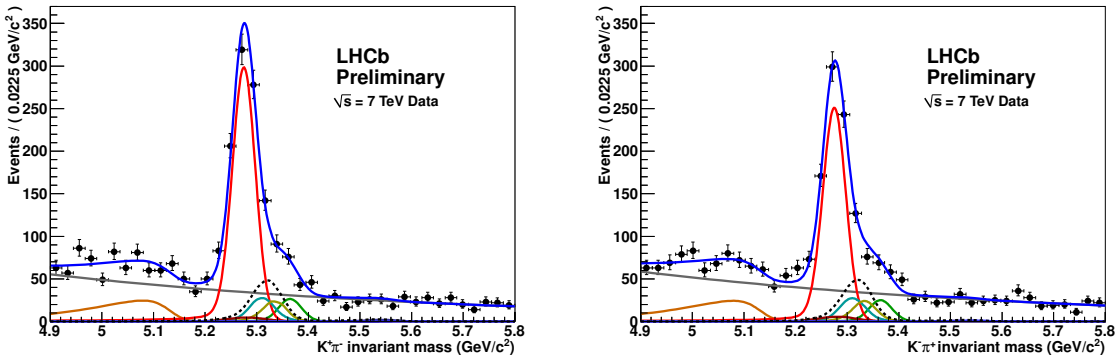

Figure 3.30: $K^+\pi^-$ (left) and $K^-\pi^+$ (right) invariant mass spectra for events surviving the selection optimized for the best sensitivity on $A_{CP}(B^0 \to K^+\pi^-)$. The result of the unbinned maximum likelihood fit is superimposed to the histograms. The various signal and background components contributing to the fit model are also shown. The dashed curve represents the sum of all the cross-feed background components.

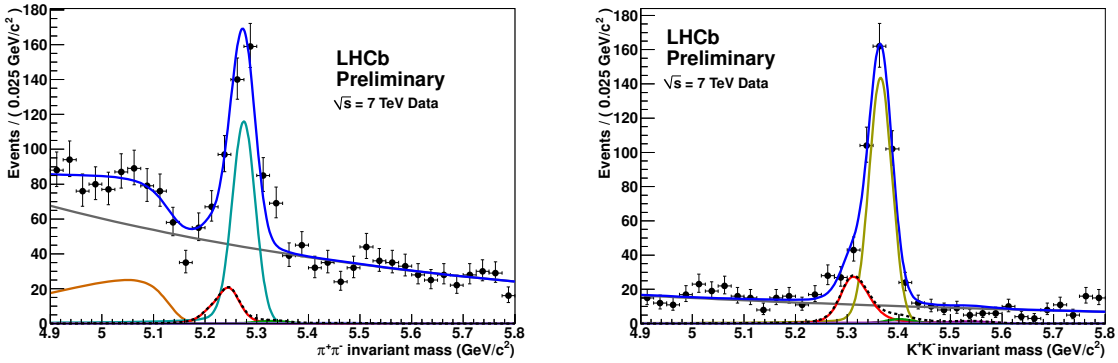

Figure 3.31: $\pi^+\pi^-$ (left) and K^+K^- (right) invariant mass spectra for events surviving the event selection optimized for the best sensitivity on $A_{CP}(B^0 \to K^+\pi^-)$. The result of the unbinned maximum likelihood fit is superimposed to the histogram. The various signal and background components contributing to the fit model are also shown. The dashed curves represent the sums of all the cross-feed background components, and are dominated by the $B^0 \to K^+\pi^-$ decay.

larger than that of the corresponding physical $\mathcal{CP}$ asymmetry measured by BaBar and Belle, and about a factor 1.4 larger than measured by CDF with an integrated luminosity $\int \mathcal{L}dt = 1$ fb^{-1} (see Tab. 1.5).

3.4.2.2 Selection optimized for $A_{CP}(B_s^0 \to \pi^+K^-)$

The π^+K^- (plus charge conjugate) mass spectrum is shown in Fig. 3.33. The dominant signal visible in the mass spectrum is again due to the $B^0 \to K^+\pi^-$ decay, as it shares the same

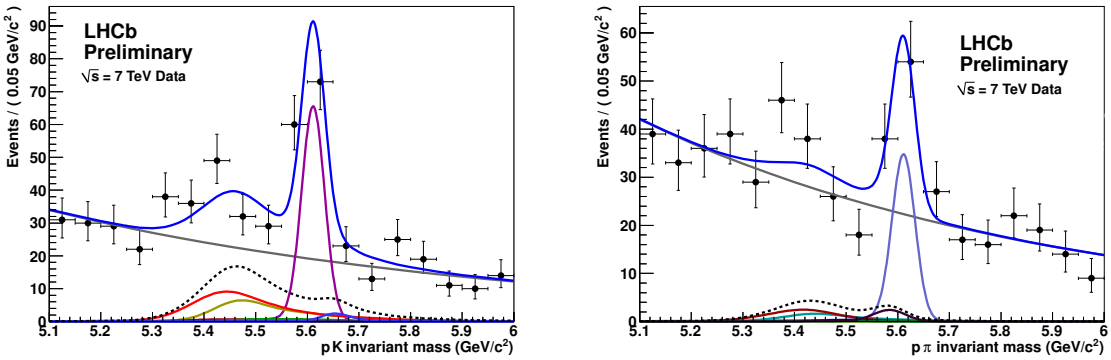

Figure 3.32: pK^- (plus charge conjugate, left) and $p\pi^-$ (plus charge conjugate, right) invariant mass spectra for events surviving the event selection optimized for the best sensitivity on $A_{CP}(B^0 \to K^+\pi^-)$. The result of the unbinned maximum likelihood fit is superimposed to the histogram. The various signal and background components contributing to the fit model are also shown. The dashed curve represents the sum of all the cross-feed background components.

Parameter	Fit result
$B^0 \to K^+\pi^-$ yield	1447 ± 50
$B^0_s \to \pi^+K^-$yield	140 ± 25
$B^0 \to \pi^+\pi^-$ yield	275 ± 24
$B^0_s \to K^+K^-$ yield	333 ± 21
$\Lambda_b \to pK^-$ yield	76 ± 12
$\Lambda_b \to p\pi^-$ yield	41 ± 10
B^0 mass [GeV/c^2]	5.2757 ± 0.0008
B^0_s mass [GeV/c^2]	5.3651 ± 0.0015
Λ_b mass [GeV/c^2]	5.612 ± 0.004
Mass resolution [MeV/c^2]	22.1 ± 0.6
$A_{CP}^{RAW}(B^0 \to K^+\pi^-)$	-0.086 ± 0.033
A_{CP}^{RAW}(combinatorial background)	0.032 ± 0.032

Table 3.18: Relevant parameters determined by the unbinned maximum likelihood fit to the data sample surviving the event selection optimized for the best sensitivity on $A_{CP}(B^0 \to K^+\pi^-)$. Only statistical errors are shown.

final state signature of the $\bar{B}^0_s \to \pi^-K^+$ decay and constitutes for the latter an irreducible background. As is apparent, the tighter selection optimized for $A_{CP}(B^0_s \to \pi^+K^-)$ causes a stronger suppression of the combinatorial background, with respect to the selection optimized for $A_{CP}(B^0 \to K^+\pi^-)$. Apart for the already mentioned $B^0 \to K^+\pi^-$ decay, the other two main cross-feed backgrounds to the $B^0_s \to \pi^+K^-$ signal (green), visibile in the right plot of Fig. 3.33, are again from the $B^0 \to \pi^+\pi^-$ (light blue) and the $B^0_s \to K^+K^-$ (dark yellow) decays.

Also in this case, to have a visual glance at $\mathcal{CP}$ violation, Fig. 3.34 shows the π^+K^- and

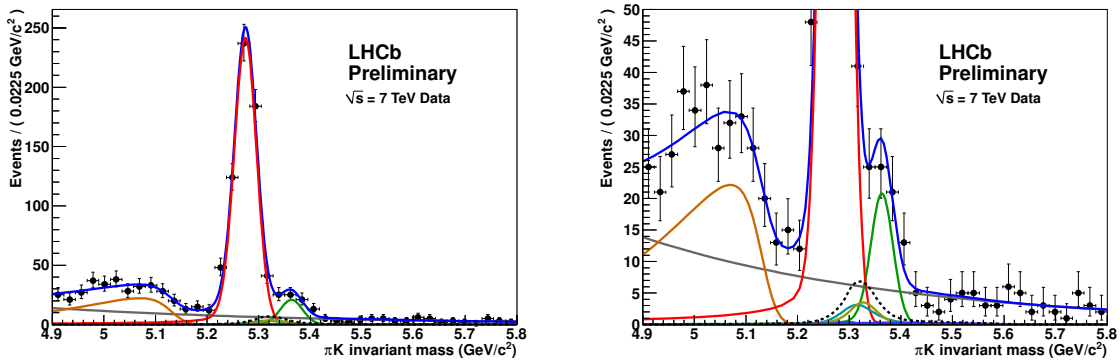

Figure 3.33: Left: π^+K^- (plus charge conjugate) invariant mass spectrum for events surviving the event selection optimized for the best sensitivity on $A_{CP}(B_s^0 \to \pi^+K^-)$. Right: magnification of the plot on the left. The result of an unbinned maximum likelihood fit is superimposed to the histograms. The various signal and background components contributing to the fit model are also shown. The dashed curves represent the sum of all the cross-feed background components.

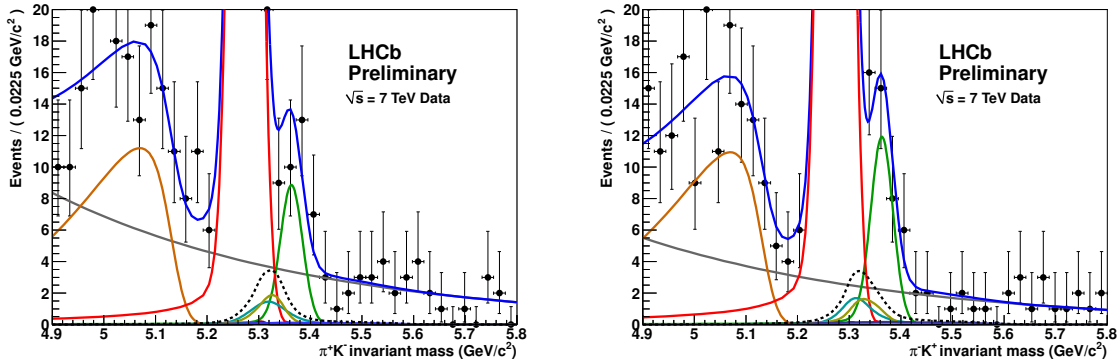

Figure 3.34: π^+K^- (left) and π^-K^+ (right) invariant mass spectra, magnified to put in evidence the two signal mass peaks, for events surviving the event selection optimized for the best sensitivity on $A_{CP}(B_s^0 \to \pi^+K^-)$. The result of an unbinned maximum likelihood fit is superimposed to the histograms. The various signal and background components contributing to the fit model are also shown. The dashed curves represent the sum of all the cross-feed background components.

π^-K^+ invariant mass spectra separately. The difference in the heights of the $B_s^0 \to \pi^+K^-$ and $\bar{B}^0 \to \pi^-K^+$ mass peaks is apparent, albeit statistically compatible with zero, as opposed to the $B^0 \to K^+\pi^-$ case of Fig. 3.30.

The relevant parameters determined by the maximum likelihood fit are summarized in Tab. 3.19. The statistical uncertainty on $A_{CP}^{RAW}(B_s^0 \to \pi^+K^-)$ is only a factor 1.27 larger than that of the corresponding physical $\mathcal{CP}$ asymmetry measured by CDF with an integrated luminosity $\int \mathcal{L}dt = 1$ fb^{-1}, i.e. $A_{CP}(B_s^0 \to \pi^+K^-) = 0.39 \pm 0.15 \pm 0.08$ [48].

Parameter	Fit result
$B^0 \to K^+\pi^-$ yield	610 ± 27
$B^0_s \to \pi^+K^-$yield	52 ± 10
$B^0 \to \pi^+\pi^-$ yield	224 ± 19
$B^0_s \to K^+K^-$ yield	256 ± 18
$\Lambda_b \to pK^-$ yield	51 ± 9
$\Lambda_b \to p\pi^-$ yield	29 ± 7
B^0 mass [GeV/c^2]	5.2749 ± 0.0009
B^0_s mass [GeV/c^2]	5.3639 ± 0.0016
Λ_b mass [GeV/c^2]	5.619 ± 0.004
Mass resolution [MeV/c^2]	21.3 ± 0.7
$A_{CP}^{RAW}(B^0_s \to \pi^+K^-)$	0.15 ± 0.19
A_{CP}^{RAW}(combinatorial background)	0.21 ± 0.11

Table 3.19: Relevant parameters determined by the unbinned maximum likelihood fit to the data sample surviving the event selection optimized for the best sensitivity on $A_{CP}(B^0_s \to \pi^+K^-)$. Only statistical errors are shown.

3.5 Systematic errors and final results

The systematic errors on $A_{CP}(B^0 \to K^+\pi^-)$ and $A_{CP}(B^0_s \to \pi^+K^-)$ that we identified fall into three main categories, related to:

- PID calibration;
- modelling of the signal and background components in the maximum likelihood fits;
- instrumental and production asymmetries.

3.5.1 PID calibration

PID cut efficiencies are necessary, in this analysis, to compute the number of cross-feed background events affecting the mass fit of a given B channel. An imperfect PID calibration can lead to an incorrect estimate of the number of such background events, thus altering the values of the direct $\mathcal{CP}$ asymmetries returned by the maximum likelihood fits.

There are various sources of systematic errors entering the determination of PID cut efficiencies using the technique described in Sec. 3.2. The technique relies on the employment of calibration samples from $D^* \to D^0(K\pi)\pi$ and $\Lambda \to p\pi$ decays, reweighting the relevant $\Delta\log\mathcal{L}$ distributions according to the p and p_T distributions of the B hadron daughters, which are determined from Monte Carlo simulations.

On the one hand, due to limited statistics, the conditional distributions of $\Delta\log\mathcal{L}$ variables might not cover the full phase space in terms of momentum and transverse momentum of the B hadron daughters. For this reason there might be difficulties in reproducing the desired p and p_T spectra by applying the reweighting procedure. Furthermore, p and p_T do not necessarily constitute a complete set of observables to reweight in, hence a potential systematic uncertainty intrinsic to the method should be taken into account. On the other hand, the usage of Monte

Carlo simulations to determine the distributions of p and p_T of the B hadron daughters is an approximation which introduces itself a systematic error.

To estimate the size of such uncertainties we have first compared the efficiencies determined by applying the PID cuts on $B \to h^+h'^-$ Monte Carlo events with those predicted from the reweighting procedure using Monte Carlo calibration samples, as shown in Tabs. 3.6 and 3.7. From such a comparison we could study the intrinsic limitations of the calibration technique. Then, in order to estimate the impact of an imprecise knowledge of the p and p_T distributions of B meson daughters, we have compared the efficiencies determined by reweighting in p and p_T with distributions obtained from Monte Carlo simulations and real data, as shown in Tabs. 3.10 and 3.11.

We have summarized the relevant information, extracted from Tabs. 3.6, 3.7, 3.10 and 3.11, in Tabs. 3.20 and 3.21. We have only reported the efficiencies which are needed to calculate the yields of cross-feed background events affecting the $B^0 \to K^+\pi^-$ and $B_s^0 \to \pi^+K^-$ signals. As we have seen in Sec. 5.3, the dominant cross-feed backgrounds are from wrong sign $B^0 \to K\pi$ (i.e. where the identities of both final state particles have been swapped), $B^0 \to \pi^+\pi^-$ and $B_s^0 \to K^+K^-$ decays. In the case of the selection optimized for $A_{CP}(B_s^0 \to \pi^+K^-)$, the cross-feed background from wrong sign $B^0 \to K\pi$ decays is indeed negligible. The last column in each of the two Tabs. 3.20 and 3.21 reports the estimated relative systematic error on the efficiencies. The values in the "Absolute systematics" column are calculated as:

$$\text{Absolute systematics} = \left[\left(2 \cdot \frac{\text{MC} - \text{MC}_R}{\text{MC} + \text{MC}_R} \cdot \text{Data}\right)^2 + (\text{Data} -_s \mathcal{P}lot)^2\right]^{\frac{1}{2}}, \tag{3.44}$$

i.e. we took the relative difference between the efficiencies in the MC and MC_R columns, rescaled to the efficiencies in the Data column, and then we summed the result in quadrature with the absolute difference between the efficiencies in the ${}_s\mathcal{P}lot$ and Data columns. Finally, the values in the "Relative systematics" column are given by the ratio of the values in the "Absolute systematic" and Data columns. We have then averaged the relative systematic errors of each row, determining an average relative systematic error $\sigma_\varepsilon/\varepsilon = (8 \pm 1)\%$ using the values in Tab. 3.20 and $\sigma_\varepsilon/\varepsilon = (5 \pm 2)\%$ using those in Tab. 3.21. Conservatively we decided to use in the following the largest of the two numbers, i.e. 8%.

According to Eq. (3.43), in order to determine the yield of cross-feed background events, we need the ratios of PID cut efficiencies. We estimated the systematic errors on such ratios as $\sigma_R = \sqrt{2 \cdot (\sigma_\varepsilon/\varepsilon)^2} \simeq 11\%$, i.e. summing in quadrature $\sigma_\varepsilon/\varepsilon$ with itself. In conclusion, we estimate the relative systematic error on the cross-feed background yields we used in the fits of Sec. 3.4 to be 11%.

Albeit such an error might look very conservative, the corresponding systematic errors induced on $A_{CP}(B^0 \to K^+\pi^-)$ and $A_{CP}(B_s^0 \to \pi^+K^-)$, as we shall see, are quite small. We performed unbinned maximum likelihood fits increasing and decreasing by 11%, with respect to the central fit shown in Sec. 3.4, the number of cross-feed background events present in the relevant mass spectra. We found systematic shifts by 0.002 and 0.001 on $A_{CP}(B^0 \to K^+\pi^-)$ and $A_{CP}(B_s^0 \to \pi^+K^-)$, respectively.

3.5.2 Signal and background modelling

The signal p.d.f. used to build the likelihood function for each B decay mode was given by a single Gaussian convolved with an additional component taking into account QED final state

	MC	MC_R	${}_s\mathcal{P}lot$	Data	Absolute systematics	Relative systematics
$(B^0 \to \pi^+\pi^-) \to \pi^+\pi^-$	57.1(4)	54.5(4)	41(1)	45.2(4)	4.7 ± 1.2	10 ± 3
$(B^0 \to \pi^+\pi^-) \to K^+\pi^-$	20.9(4)	22.2(4)	29(1)	27.0(4)	2.6 ± 1.3	10 ± 5
$(B^0_s \to K^+K^-) \to K^+K^-$	65.5(5)	63.8(5)	48(1)	50.7(4)	3.0 ± 1.2	6 ± 2
$(B^0_s \to K^+K^-) \to K^+\pi^-$	12.7(3)	12.3(3)	21(1)	21.2(4)	0.7 ± 1.3	3 ± 6
$(B^0_{(s)} \to K^+\pi^-) \to K^+\pi^-$	79.8(3)	78.7(3)	62(1)	68.2(3)	6.3 ± 1.1	9 ± 2
$(B^0_{(s)} \to K^+\pi^-) \to \pi^+\pi^-$	0.67(3)	0.69(3)	3.3(3)	2.70(6)	0.6 ± 0.3	22 ± 11
$(B^0_{(s)} \to K^+\pi^-) \to K^+K^-$	2.33(6)	2.26(5)	4.0(3)	4.02(7)	0.1 ± 0.3	3 ± 8
$(B^0_{(s)} \to \pi^+K^-) \to K^+\pi^-$	1.15(4)	1.13(4)	2.9(3)	2.30(5)	0.6 ± 0.3	26 ± 13

Table 3.20: Summary of the quantities used to estimate the systematic errors on the PID cut efficiencies, for events passing the offline selection optimized for $A_{CP}(B^0 \to K^+\pi^-)$. The first column indicates the decay channel which contributes to a given final state category. The MC column contains the efficiencies calculated by applying PID cuts on full Monte Carlo events (see Tab. 3.6). The MC_R column contains the efficiencies obtained by using the reweighting procedure of Sec. 3.2 with Monte Carlo calibration samples (see Tab. 3.6). The ${}_s\mathcal{P}lot$ columns contains the efficiencies determined using the reweighting procedure of Sec. 3.2 with real data calibration samples and real data p and p_T distributions (see Tab. 3.10). The Data column contains the efficiencies determined using the reweighting procedure of Sec. 3.2 with real data calibration samples and Monte Carlo p and p_T distributions (see Tab. 3.10). Finally the last two columns contain the values of the absolute and relative systematic errors referred to the efficiencies in the Data column. The values in parentheses represent the statistical errors on the last digit. All the values are given in percent.

	MC	MC_R	${}_s\mathcal{P}lot$	Data	Absolute systematics	Relative systematics
$(B^0 \to \pi^+\pi^-) \to \pi^+\pi^-$	57.7(5)	55.4(5)	44(2)	45.3(4)	2.3 ± 2.1	5 ± 5
$(B^0 \to \pi^+\pi^-) \to K^+\pi^-$	0.91(9)	0.77(8)	3.2(5)	2.5(1)	0.8 ± 0.6	32 ± 24
$(B^0_s \to K^+K^-) \to K^+K^-$	65.5(5)	63.8(5)	50(1)	50.9(4)	1.6 ± 1.2	3 ± 2
$(B^0_s \to K^+K^-) \to K^+\pi^-$	0.17(4)	0.14(4)	2.8(5)	2.2(1)	0.7 ± 1.0	31 ± 45
$(B^0_{(s)} \to K^+\pi^-) \to K^+\pi^-$	48.2(3)	50.2(3)	36(1)	38.1(3)	2.6 ± 1.1	7 ± 3
$(B^0_{(s)} \to K^+\pi^-) \to \pi^+\pi^-$	0.67(3)	0.74(4)	2.9(4)	2.73(7)	2.3 ± 2.1	11 ± 5
$(B^0_{(s)} \to K^+\pi^-) \to K^+K^-$	2.31(6)	2.20(6)	4.3(4)	4.02(8)	0.3 ± 0.4	7 ± 10

Table 3.21: Summary of the quantities used to estimate the systematic errors on the PID cut efficiencies, for events passing the offline selection optimized for $A_{CP}(B^0_s \to \pi^+K^-)$. The first column indicates the decay channel which contributes to a given final state category. The MC column contains the efficiencies calculated by applying PID cuts on full Monte Carlo events (see Tab. 3.7). The MC_R column contains the efficiencies obtained by using the reweighting procedure of Sec. 3.2 with Monte Carlo calibration samples (see Tab. 3.7). The ${}_s\mathcal{P}lot$ columns contains the efficiencies determined using the reweighting procedure of Sec. 3.2 with real data calibration samples and real data p and p_T distributions (see Tab. 3.11). The Data column contains the efficiencies determined using the reweighting procedure of Sec. 3.2 with real data calibration samples and Monte Carlo p and p_T distributions (see Tab. 3.11). Finally the last two columns contain the values of the absolute and relative systematic errors referred to the efficiencies in the Data column. The values in parentheses represent the statistical errors on the last digit. All the values are given in percent.

radiation processes, see Eq. (3.42). We estimated systematic errors either due to an incorrect description of the final state radiation or to the employment of a single Gaussian function.

In the former case, we removed completely the radiative component and performed unbinned maximum likelihood fits using a simple Gaussian as signal model. Although such approximation might look very rough, we found that the systematic shifts of the central values of $A_{CP}(B^0 \to K^+\pi^-)$ and $A_{CP}(B_s^0 \to \pi^+K^-)$, returned by the fits, were very small if compared with the statistical errors of the respective measurements. We estimated a systematic error of 0.003 on $A_{CP}(B^0 \to K^+\pi^-)$ and of 0.01 on $A_{CP}(B_s^0 \to \pi^+K^-)$.

Then we substituted the single Gaussian with a double Gaussian, where we fixed the width and fraction of the second Gaussian to 30 MeV/c^2 and 30% respectively. By performing unbinned maximum likelihood fits with this new parameterization, we found a shift of the central values by 0.002 for $A_{CP}(B^0 \to K^+\pi^-)$ and 0.01 for $A_{CP}(B_s^0 \to \pi^+K^-)$.

To estimate systematic errors due to an incorrect modelling of background components, we proceeded as in the following. In the case of the combinatorial background, we replaced the exponential p.d.f. with a first degree polinomial. This parameterization led to unbinned maximum likelihood fits where the central values were shifted by 0.0001 for $A_{CP}(B^0 \to K^+\pi^-)$ and again 0.01 for $A_{CP}(B_s^0 \to \pi^+K^-)$. For the case of the cross-feed backgrounds, since we took from Monte Carlo the corresponding distributions, in order to estimate a systematic uncertainty arising from their imperfect description, we made new distributions where the event-by-event mass values were shifted by a fixed amount or were calculated by smearing with Gaussian-distributed random numbers the value of the true mass, i.e. the mass calculated using momenta from Monte Carlo truth. We made different unbinned maximum likelihood fits with the altered cross-feed background distributions, where in each trial a shift of ± 3 MeV/c^2 on the mass values was applied, or where the width of the Gaussian smearing ranged from 19 MeV/c^2 to 25 MeV/c^2, i.e. a window of ± 3 MeV/c^2 around the mass resolution determined from signal events. In the case of the mass shift, we estimated the corresponding systematic error to be 0.0009 on $A_{CP}(B^0 \to K^+\pi^-)$ and 0.005 on $A_{CP}(B_s^0 \to \pi^+K^-)$, while with the Gaussian smearing we estimated a systematic error of 0.0006 on $A_{CP}(B^0 \to K^+\pi^-)$ and 0.006 on $A_{CP}(B_s^0 \to \pi^+K^-)$.

3.5.3 Instrumental and production asymmetries

The third main category of systematic uncertainties involves the presence of asymmetries induced by detector and reconstruction, as well as of B meson production asymmetries arising from primary proton-proton collisions, as discussed in Sec. 3.3. The physical $\mathcal{CP}$ asymmetries we want to measure are related to the raw asymmetries measured in data by

$$A_{CP} = A_{CP}^{RAW} - A_D(K\pi) - \kappa A_P, \tag{3.45}$$

where $A_D(K\pi)$ is the instrumental asymmetry, κ is the factor given in Tab. 3.17, and A_P is the production asymmetry.

We have determined from charm control samples the value of $A_D(K\pi)$, averaged between the data samples with opposite magnet polarities, and it is $A_D(K\pi) = -0.004 \pm 0.004$. The usage of such an average value is justified by the fact that the two magnet up and down samples that we analyzed contain the same number of B decays. We performed separate unbinned maximum likelihood fits of magnet up and down data sets, where the events passed the selection optimized for the measurement of $A_{CP}(B^0 \to K^+\pi^-)$, and we found $\nu_{K\pi} = 739 \pm 35$ $B^0 \to K^+\pi^-$ (plus charge conjugate) events in the magnet up sample and $\nu_{K\pi} = 707 \pm 35$ events in the magnet

Reason	$A_{CP}(B^0 \to K^+\pi^-)$	$A_{CP}(B^0_s \to \pi^+K^-)$
PID calibration	0.002	0.001
Final state radiation	0.003	0.01
Signal model	0.002	0.01
Combinatorial background model	0.0001	0.01
Cross-feed background model (shift)	0.0009	0.005
Cross-feed background model (smearing)	0.0006	0.006
Instrumental asymmetry	0.004	0.004
Production asymmetry	0.005	0.0002
Total	0.008	0.02

Table 3.22: Summary of systematic uncertainties on $A_{CP}(B^0 \to K^+\pi^-)$ and $A_{CP}(B^0_s \to \pi^+K^-)$. The values in the last row are obtained by summing in quadrature all the systematic uncertainties.

down sample. The value $A_P(B^+)$ was estimated by using $B^\pm \to J/\psi(\mu^+\mu^-)K^\pm$ decays. The raw $\mathcal{CP}$ asymmetries measured using magnet up and magnet down data sets were shown in Tab. 3.16. Averaging the two values and taking into account the instrumental asymmetry and the current world average for $A_{CP}(B^+ \to J/\psi(\mu^+\mu^-)K^+)$, we get $A_P(B^+) = -0.024 \pm 0.013$.

As we need the production asymmetry for neutral B mesons, we assumed that $A_P(B^0)$ is equal to $A_P(B^+)$, introducing a systematic error of 0.01 to account for possible differences, i.e.

$$A_P(B^0) = -0.024 \pm 0.013 \pm 0.010. \tag{3.46}$$

By using the value $\kappa = 0.33$ and the central value of $A_{CP}^{RAW}(B^0 \to K^+\pi^-)$ given in Tab. 3.18, we get the central value of the physical asymmetry:

$$A_{CP}(B^0 \to K^+\pi^-) = -0.074. \tag{3.47}$$

The systematic errors associated to this physical asymmetry, due to instrumental and production asymmetries, are 0.004 and 0.005 respectively.

For the case of the $B^0_s \to \pi^+K^-$ decay, even assuming very conservatively that the B^0_s production asymmetry is as large as the one used above, one gets a negligible systematic shift $\kappa A_P = -0.0004 \pm 0.0002$, due to the very small value $\kappa = 0.015$, also given in Tab. 3.17. The central value of $A_{CP}^{RAW}(B^0_s \to \pi^+K^-)$ given in Tab. 3.19 is practically unaffected by any correction.

3.5.4 Summary

The systematic uncertainties for $A_{CP}(B^0 \to K^+\pi^-)$ and $A_{CP}(B^0_s \to \pi^+K^-)$ are summarized in Tab. 3.22.

3.6 Conclusions

Using data collected by the LHCb detector during the 2010 run we provide measurements of the direct $\mathcal{CP}$ asymmetries:

$$A_{CP}(B^0 \to K^+\pi^-) = -0.074 \pm 0.033 \pm 0.008$$

and

$$A_{CP}(B_s^0 \to \pi^+K^-) = 0.15 \pm 0.19 \pm 0.02.$$

These results have to be compared with the current world average $A_{CP}(B^0 \to K^+\pi^-) = -0.098^{+0.012}_{-0.011}$ [60] and with the CDF measurement $A_{CP}(B_s^0 \to \pi^+K^-) = 0.39 \pm 0.15 \pm 0.08$ [48].

Chapter 4

2011 $\mathcal{CP}$ violation analysis update and rare decays

In this chapter we present an update of the studies already performed on 2010 data, discussed in the previous chapter, using part of the statistics which became available in the first part of 2011. In addition we also present the measurements of the relative branching fractions $\mathcal{B}\left(B^0 \to K^+K^-\right)$ and $\mathcal{B}\left(B_s^0 \to \pi^+\pi^-\right)$.

4.1 Data set and event selection

The data sample is composed of the full Reco10-Stripping13b BHADRON stream for both magnet polarities, and corresponds to an integrated luminosity of about 200 pb^{-1} for magnet down and 120 pb^{-1} for magnet up.

4.1.1 HLT2 trigger

An exclusive HLT selection for the family of $B \to h^+h'^-$ decays, so-called `Hlt2B2HH` trigger line, has been used in the data taking. To discriminate signal events from the background, it uses kinematic variables like transverse momentum (p_T) and impact parameter (IP) of the daughter tracks, as well as the transverse momentum (P_T^B), the impact parameter (IP_B) and the proper decay time $t_{\pi\pi}$ of the B-hadron candidate, calculated under the $\pi\pi$ mass hypothesis. Tab. 4.1 reports a summary of the selection criteria used by this trigger line. The `Hlt2B2HH` line has a very high efficiency in triggering signal events which are then selected offline, but in our analysis we do not require explicitly that the events need to have been triggered by this specific line.

4.1.2 Stripping

The events used for this analysis are those passing the `Hb2ChargedBody` stripping line. This stripping line has been slightly changed since the 2010 analysis. The present stripping algorithm employs a lifetime cut $t_{\pi\pi}$ on the B candidate, calculated under the $\pi\pi$ hypothesis, in place of the distance of flight cut. We also use a cut on the B transverse momentum, which was not present before. Finally we retuned the values of other cuts in order to match the stripping requirements for 2011 data. The summary of the stripping cuts are reported in Tab. 4.2.

Cut type	Accepted regions
Track p_T [GeV/c]	> 1.0
Track IP [μm]	> 120
Track χ^2/d.o.f.	< 5
$m_{h^+h'^-}$ [GeV/c^2]	[4.7, 5.9]
Distance of closest approach [μm]	< 100
IP_B [μm]	< 120
$t_{\pi\pi}$[ps]	> 0.6
p_T^B[GeV/c]	> 1.2

Table 4.1: Summary of the HLT2 selection cuts used in the `Hlt2B2HH` trigger line.

Cut type	Accepted regions
Track p_T [GeV/c]	> 1.1
Track IP [μm]	> 150
Track χ^2/d.o.f.	< 5
$m_{h^+h'^-}$ [GeV/c^2]	[4.8, 5.8]
Distance of closest approach [μm]	< 80
$\max(p_T^{h^+}, p_T^{h'^-})$ [GeV/c]	> 2.7
$\max(IP^{h^+}, IP^{h'^-})$ [μm]	> 300
m_B [GeV/c^2]	[4.8, 5.8]
IP_B [μm]	< 60
$t_{\pi\pi}$[ps]	> 0.9
p_T^B[GeV/c]	> 1.2

Table 4.2: Summary of the stripping cuts used in the `Hb2ChargedBody` line.

4.1.3 Final offline selection

As for the 2010 analysis, a further offline selection is applied to the events which pass the stripping line, in order to further refine the data. A set of kinematic selection cuts is imposed, and then particle identification cuts are applied to the two final state tracks, in order to disentangle the various $B \to h^+h'^-$ decay modes.

4.1.3.1 Kinematic selection

The values of the offline kinematic selection cuts have been chosen with the aim of minimizing the expected uncertainty on $A_{CP}(B^0 \to K\pi)$, $A_{CP}(B_s^0 \to \pi K)$, and for observing the rare decays $B^0 \to K^+K^-$ and $B_s^0 \to \pi^+\pi^-$. Hence we determined three sets of kinematic cuts for the offline selection, as summarized in Tabs. 4.3, 4.4 and 4.5. The offline selection algorithm follows a similar path as the one used in the stripping.

4.1.3.2 Final state selection

The three $B \to h^+h'^-$ samples passing the kinematic event selections are then subdivided into different final states using the PID capabilities of the two RICH sub-detectors. In particular we

Cut type	Accepted regions
Track p_T [GeV/c]	> 1.1
Track IP [μm]	> 150
Track χ^2/d.o.f.	< 3
$\max(p_T^{h^+}, p_T^{h'^-})$ [GeV/c]	> 2.8
$\max(IP^{h^+}, IP^{h'^-})$ [μm]	> 300
p_T^B [GeV/c]	> 2.2
$t_{\pi\pi}$ [ps]	> 0.9

Table 4.3: Summary of the offline selection cuts adopted for the best sensitivity on $A_{CP}(B^0 \to K\pi)$.

Cut type	Accepted regions
Track p_T [GeV/c]	> 1.2
Track IP [μm]	> 200
Track χ^2/d.o.f.	< 3
$\max(p_T^{h^+}, p_T^{h'^-})$ [GeV/c]	> 3.0
$\max(IP^{h^+}, IP^{h'^-})$ [μm]	> 400
p_T^B [GeV/c]	> 2.4
$t_{\pi\pi}$ [ps]	> 1.5

Table 4.4: Summary of the offline selection cuts adopted for the best sensitivity on $A_{CP}(B_s^0 \to \pi K)$.

employ the quantities $\Delta \log \mathcal{L}_{K\pi}$ and $\Delta \log \mathcal{L}_{p\pi}$, or their difference $\Delta \log \mathcal{L}_{Kp}$ when appropriate. The respective three sets of PID cuts are reported in Tabs. 4.6, 4.7 and 4.8.

Cut type	Accepted regions
Track p_T [GeV/c]	> 1.2
Track IP [μm]	> 200
Track χ^2/d.o.f.	< 3
$\max(p_T^{h^+}, p_T^{h'^-})$ [GeV/c]	> 3.0
$\max(IP^{h^+}, IP^{h'^-})$ [μm]	> 400
p_T^B [GeV/c]	> 2.8
$t_{\pi\pi}$ [ps]	> 2.0

Table 4.5: Summary of the offline selection cuts adopted for observing the rare decays $B^0 \to K^+K^-$ and $B_s^0 \to \pi^+\pi^-$.

$K^+\pi^-$	$\pi^+\pi^-$	K^+K^-	pK^-	$p\pi^-$
$\Delta\log\mathcal{L}_{K\pi}(h^+) > 0$	$\Delta\log\mathcal{L}_{K\pi}(h^+) < -3$	$\Delta\log\mathcal{L}_{K\pi}(h^+) > 3$	$\Delta\log\mathcal{L}_{pK}(h^+) > 10$	$\Delta\log\mathcal{L}_{pK}(h^+) > 10$
$\Delta\log\mathcal{L}_{K\pi}(h^-) < 0$	$\Delta\log\mathcal{L}_{K\pi}(h^-) < -3$	$\Delta\log\mathcal{L}_{K\pi}(h^-) > 3$	$\Delta\log\mathcal{L}_{K\pi}(h^-) > 3$	$\Delta\log\mathcal{L}_{K\pi}(h^-) < -3$
$\Delta\log\mathcal{L}_{pK}(h^+) < 5$	$\Delta\log\mathcal{L}_{p\pi}(h^+) < 5$	$\Delta\log\mathcal{L}_{pK}(h^+) < 5$	$\Delta\log\mathcal{L}_{p\pi}(h^+) > 10$	$\Delta\log\mathcal{L}_{p\pi}(h^+) > 10$
$\Delta\log\mathcal{L}_{p\pi}(h^-) < 5$	$\Delta\log\mathcal{L}_{p\pi}(h^-) < 5$	$\Delta\log\mathcal{L}_{pK}(h^-) < 5$	$\Delta\log\mathcal{L}_{pK}(h^-) < 5$	$\Delta\log\mathcal{L}_{p\pi}(h^-) < 5$

Table 4.6: PID cuts applied after the offline kinematic selection for the best sensitivity on $A_{CP}(B^0 \to K\pi)$.

$K^+\pi^-$	$\pi^+\pi^-$	K^+K^-	pK^-	$p\pi^-$
$\Delta\log\mathcal{L}_{K\pi}(h^+) > 7$	$\Delta\log\mathcal{L}_{K\pi}(h^+) < -3$	$\Delta\log\mathcal{L}_{K\pi}(h^+) > 3$	$\Delta\log\mathcal{L}_{pK}(h^+) > 10$	$\Delta\log\mathcal{L}_{pK}(h^+) > 10$
$\Delta\log\mathcal{L}_{K\pi}(h^-) < -7$	$\Delta\log\mathcal{L}_{K\pi}(h^-) < -3$	$\Delta\log\mathcal{L}_{K\pi}(h^-) > 3$	$\Delta\log\mathcal{L}_{K\pi}(h^-) > 3$	$\Delta\log\mathcal{L}_{K\pi}(h^-) < -3$
$\Delta\log\mathcal{L}_{pK}(h^+) < 5$	$\Delta\log\mathcal{L}_{p\pi}(h^+) < 5$	$\Delta\log\mathcal{L}_{pK}(h^+) < 5$	$\Delta\log\mathcal{L}_{p\pi}(h^+) > 10$	$\Delta\log\mathcal{L}_{p\pi}(h^+) > 10$
$\Delta\log\mathcal{L}_{p\pi}(h^-) < 5$	$\Delta\log\mathcal{L}_{p\pi}(h^-) < 5$	$\Delta\log\mathcal{L}_{pK}(h^-) < 5$	$\Delta\log\mathcal{L}_{pK}(h^-) < 5$	$\Delta\log\mathcal{L}_{p\pi}(h^-) < 5$

Table 4.7: PID cuts applied after the offline kinematic selection for the best sensitivity on $A_{CP}(B_s^0 \to \pi K)$.

$K^+\pi^-$	$\pi^+\pi^-$	K^+K^-	pK^-	$p\pi^-$
$\Delta\log\mathcal{L}_{K\pi}(h^+) > 7$	$\Delta\log\mathcal{L}_{K\pi}(h^+) < -3$	$\Delta\log\mathcal{L}_{K\pi}(h^+) > 15$	$\Delta\log\mathcal{L}_{pK}(h^+) > 10$	$\Delta\log\mathcal{L}_{pK}(h^+) > 10$
$\Delta\log\mathcal{L}_{K\pi}(h^-) < -7$	$\Delta\log\mathcal{L}_{K\pi}(h^-) < -3$	$\Delta\log\mathcal{L}_{K\pi}(h^-) > 15$	$\Delta\log\mathcal{L}_{K\pi}(h^-) > 15$	$\Delta\log\mathcal{L}_{K\pi}(h^-) < -3$
$\Delta\log\mathcal{L}_{pK}(h^+) < 0$	$\Delta\log\mathcal{L}_{p\pi}(h^+) < 0$	$\Delta\log\mathcal{L}_{pK}(h^+) < 0$	$\Delta\log\mathcal{L}_{p\pi}(h^+) > 10$	$\Delta\log\mathcal{L}_{p\pi}(h^+) > 10$
$\Delta\log\mathcal{L}_{p\pi}(h^-) < 0$	$\Delta\log\mathcal{L}_{p\pi}(h^-) < 0$	$\Delta\log\mathcal{L}_{pK}(h^-) < 0$	$\Delta\log\mathcal{L}_{pK}(h^-) < 0$	$\Delta\log\mathcal{L}_{p\pi}(h^-) < 0$

Table 4.8: PID cuts applied after the offline kinematic selection for observing the rare decays $B^0 \to K^+K^-$ and $B_s^0 \to \pi^+\pi^-$.

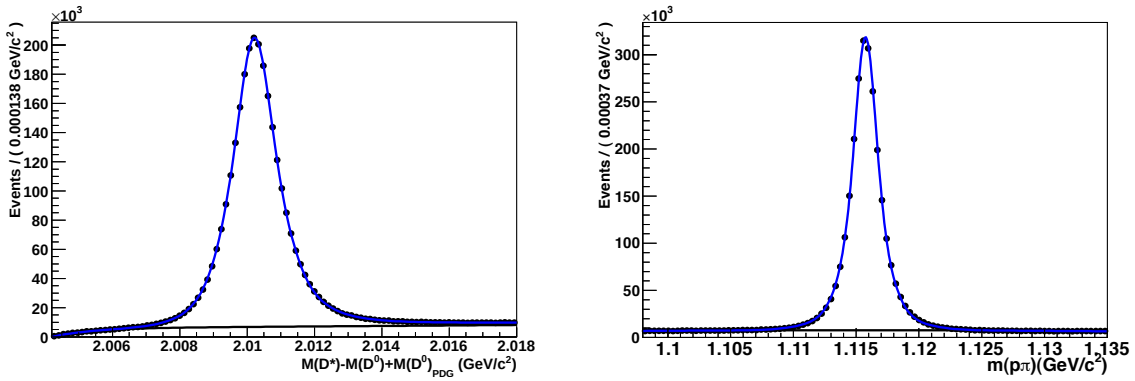

Figure 4.1: Distributions of $M = M(D^*) - M(D^0) + M(D^0)_{PDG}$ for $D^* \to D^0(K\pi)\pi$ events (left) and invariant mass of $\Lambda \to p\pi$ events (right) used for the PID calibration. The curves are the results of maximum likelihood fits. As an example, these plots are only shown for the down polarity of the magnetic field.

4.2 Calibration of particle identification

4.2.1 Calibration data sample

As in the 2010 analysis, in order to calibrate the RICH response for pions, kaons and protons we use a sample of $D^{*+} \to D^0(K^-\pi^+)\pi^+$ and $\Lambda \to p\pi^-$ decays. We use D^* calibration samples selected by the `StripDstarNoPIDsWithD02RSKPiLine` stripping line (about 6.7 million events), and Λ calibration samples selected by the `Lam0LLLine1V0ForPID` and `Lam0LLLine2V0ForPID` stripping lines (about 4.2 million events).

4.2.2 Method and validation

The calibration procedure consists of reweighting the $\Delta \log \mathcal{L}$ distributions extracted using the ${}_s\mathcal{P}lot$ [85] technique from the calibration samples of pions, kaons and protons, with the momentum distributions of daughter tracks coming from $B \to h^+h'^-$ decays. The technique is similar to that used in the 2010 analysis, but with the difference that in the present analysis we do not reweight also in transverse momentum, as owing to a detailed study using Monte Carlo simulations we find that, in the $\Delta \log \mathcal{L}$ regions of our interest, the reweight in momentum alone provides an excellent calibration, with an agreement between the predicted and observed efficiencies at a sub-percent level.

Fig. 4.1 shows the distribution of the variable $M = M(D^*) - M(D^0) + M(D^0)_{PDG}$ for $D^* \to D^0(K\pi)\pi$ events, as well as the invariant mass of $\Lambda \to p\pi$ events. The curves are the results of maximum likelihood fits to the spectra. We modeled the $D^* \to D^0(K\pi)\pi$ signal as the sum of three Gaussians with a common mean, convolved with a function which describes the asymmetric tail on the right-hand side of the spectrum:

$$g(M) = \left[\Theta(M' - \mu) \cdot A\left(M' - \mu\right)^s\right] \otimes G_3(M - M';\, f_1,\, f_3,\, \sigma_1,\, \sigma_2,\, \sigma_3) \tag{4.1}$$

Since we are close to the threshold, the background shape cannot be described by a simple

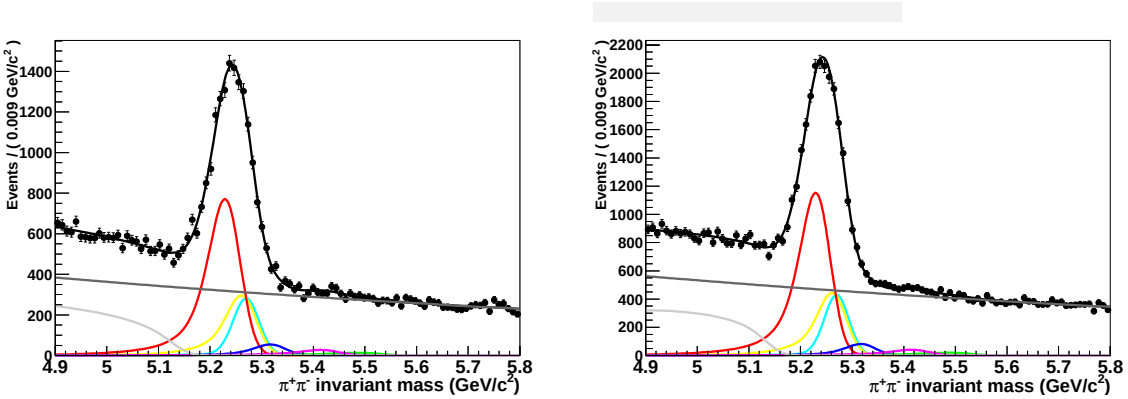

Figure 4.2: $\pi^+\pi^-$ invariant mass for events passing the offline selection of Tab. 4.3, with the result of a maximum likelihood fit superimposed, in magnet up (left) and magnet down (right) data sets. The various components are: $B^0 \to K\pi$ (red), $B^0 \to \pi^+\pi^-$ (cyan), $B_s^0 \to K^+K^-$ (yellow), $B_s^0 \to \pi K$ (blue), $\Lambda_b \to pK^-$ (purple), $\Lambda_b \to p\pi^-$ (green), 3-body partially reconstructed decays (light grey), combinatorial background (dark grey).

polynomial or exponential function. Instead, we use the following p.d.f.

$$h(M) = A\left[1 - \exp\left(-\frac{M - m_0}{c}\right)\right], \tag{4.2}$$

where A is a normalization factor, and the parameters m_0 and c govern the shape of the distribution. The fit to the $\Lambda \to p\pi$ spectrum is made using a sum of three Gaussians for the signal and a second order polynomial for the background. From this fit, by means of the ${}_s\mathcal{P}lot$ technique we can extract $\Delta \log \mathcal{L}$ and momentum distributions of pions, kaons and protons.

Another difference with the 2010 analysis consists in the fact that now we determine the distributions of the momenta of B daughter tracks to be used in the reweighting procedure directly from data, again by means of the ${}_s\mathcal{P}lot$ technique (due to the lack of statistics, in the 2010 analysis we determined such distributions from Monte Carlo). Fig. 4.2 shows the invariant mass plot under the $\pi^+\pi^-$ hypothesis for offline selected events in magnet up and magnet down data sets, using the kinematic cuts of Tab. 4.3 and without using any PID cut. The shapes of the various signal components have been fixed by parameterizing Monte Carlo truth invariant masses convolved with a Gaussian resolution function with variable mean and width. The 3-body and combinatorial backgrounds are modelled using an Argus function and an exponential, respectively. The relative yields between the signal components have been fixed according to the known values of branching fractions and hadronization probabilities of B^0, B_s^0 and Λ_b hadrons. From this fit we determine the total amount of $B \to h^+h'^-$ decays in the offline selected sample with no PID cuts to be about 34000. Similar fits, but for offline selected events using the kinematic cuts of Tabs. 4.4 and 4.5 have also been made, in order to take into account possible differences in the momentum distributions arising from different selection cuts. From these fits, by means of the ${}_s\mathcal{P}lot$ technique, we extract the inclusive momentum distributions of B daughter tracks. Fig. 4.3 shows the momentum distributions of calibration pions, kaons and protons (red circles) together with those of B daughter tracks (blue squares).

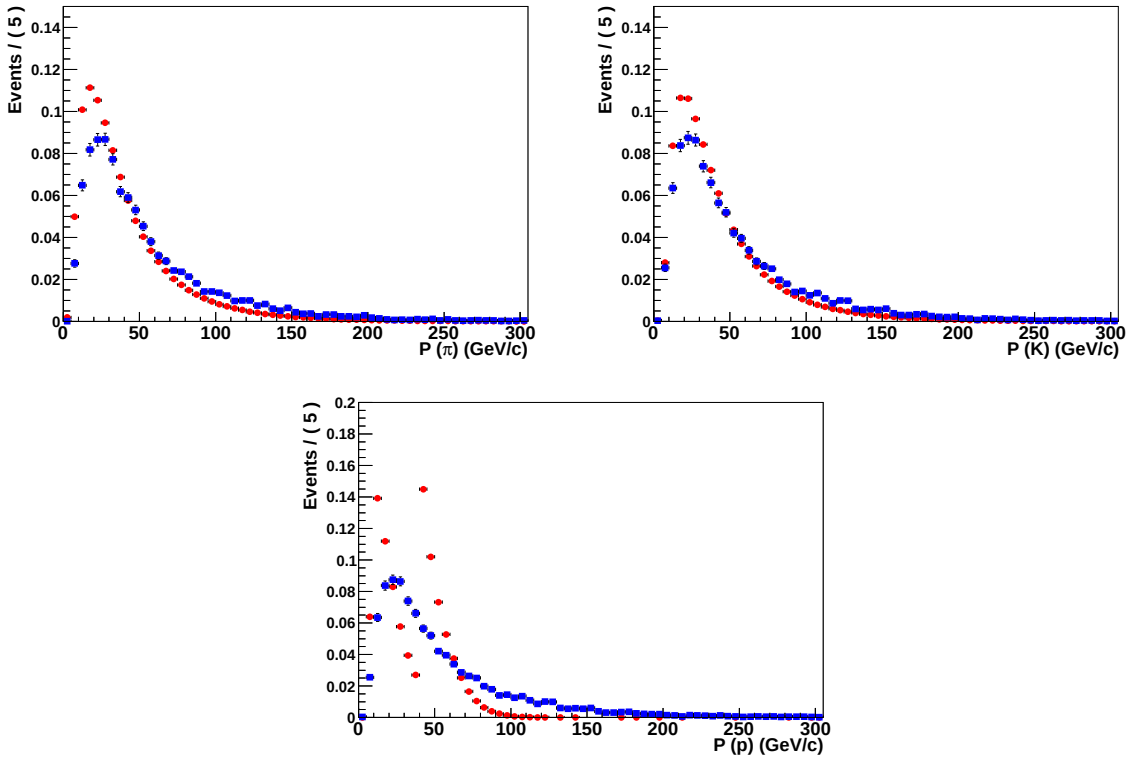

Figure 4.3: Comparison of momentum distributions of calibration pions, kaons and protons (red circles) and B daughter tracks (blue squares). The two peaks in the distribution of the calibration protons is due to the usage of the distinct calibration lines, selecting different regions of the phase space.

4.2.3 PID efficiencies

The PID efficiencies determined by the reweighting procedure, for events passing the offline selections adopted for the measurements of $A_{CP}(B^0 \to K\pi)$, $A_{CP}(B^0_s \to \pi K)$ and for observing the rare decays $B^0 \to K^+K^-$ and $B^0_s \to \pi^+\pi^-$, are reported in in Tabs. 4.9, 4.10 and 4.11 respectively. Note that for the selection of the rare decays, we do not distinguish between magnet up and magnet down data sets. We made such a distinction only for the measurement of direct CP asymmetries, which might be affected by different instrumental corrections, depending on the field polarity.

4.2.4 PID systematics

We consider three sources of possible systematics to be associated with the PID calibration:

- We evaluate the impact of using inclusive momentum distributions of B daughters, ignoring the flavour of the decaying hadron and the final state. The study was made by means of Monte Carlo simulations, determining the momentum distributions from a mixture of the various $B \to h^+h'^-$ decays, with the same relative fractions of yields as in data,

	$\pi^+\pi^-$	K^+K^-	$K^+\pi^-$	$p\pi^-$	pK^-
$B^0 \to \pi^+\pi^-$	44.5	0.36	27.3	1.73	0.15
$B_s^0 \to K^+K^-$	0.05	57.3	14.0	0.05	1.85
$B_{(s)}^0 \to K^+\pi^-$	1.40	4.44	68.4	0.81	0.07
$\bar{B}_{(s)}^0 \to \pi^+K^-$	1.40	4.44	1.96	0.03	0.96
$\Lambda_b \to p\pi^-$	2.17	1.01	17.7	34.7	3.24
$\bar{\Lambda}_b \to \pi^+\bar{p}$	2.17	1.01	0.95	0.04	0.22
$\Lambda_b \to pK^-$	0.07	13.4	1.79	1.13	39.7
$\bar{\Lambda}_b \to K^+\bar{p}$	0.07	13.4	4.97	0.04	0.21

	$\pi^+\pi^-$	K^+K^-	$K^+\pi^-$	$p\pi^-$	pK^-
$B^0 \to \pi^+\pi^-$	46.7	0.30	25.4	1.64	0.12
$B_s^0 \to K^+K^-$	0.05	58.5	14.3	0.04	1.63
$B_{(s)}^0 \to K^+\pi^-$	1.41	4.12	69.9	0.73	0.06
$\bar{B}_{(s)}^0 \to \pi^+K^-$	1.41	4.12	1.81	0.02	0.90
$\Lambda_b \to p\pi^-$	2.21	0.90	18.0	35.6	2.98
$\bar{\Lambda}_b \to \pi^+\bar{p}$	2.21	0.90	0.90	0.04	0.21
$\Lambda_b \to pK^-$	0.07	13.7	1.84	1.13	40.2
$\bar{\Lambda}_b \to K^+\bar{p}$	0.07	13.7	4.92	0.03	0.19

Table 4.9: Efficiencies (in %) of PID cuts, for the various mass hypotheses, predicted for events passing the offline selection used for measuring $A_{CP}(B^0 \to K\pi)$. The efficiencies are calculated using the calibration data sample acquired with the up (top table) and down (bottom table) polarities of the magnetic field.

and comparing the efficiencies obtained using the mixture with those obtained using the correct momentum distributions. We find this source of systematic errors to be completely negligible.

- In order to evaluate the effect of the limited statistics in the real data sample used to determine the momentum distributions, we subdivided a Monte Carlo sample in several subsamples of 20000 events each, and then we apply the reweighting procedure for each subsample, studying the variation of the PID efficiency for the $B^0 \to K\pi$ decay. We observe a small absolute variation of the efficiency, of up to 0.5%.

- As a final check, we perform several fits to the offline selected $K\pi$ spectrum, using the model described in Sec. 4.3, where the cuts on $\Delta \log \mathcal{L}_{K\pi}$ and $\Delta \log \mathcal{L}_{\pi K}$ are tightened from 0 to 10. Then we determine the relative PID efficiencies as a function of the cut, by taking the ratio of the $B^0 \to K\pi$ yields determined from the fits with a reference point, corresponding to the $\Delta \log \mathcal{L}_{\pi K}$ cut at 0. By comparing the dependence on the cut with the predicted efficiencies from the calibration procedure, as shown in Fig. 4.4, we observe a systematic difference of up to 2%.

In conclusion, we estimate a total systematic error on the PID efficiencies of about 2%.

	$\pi^+\pi^-$	K^+K^-	$K^+\pi^-$	$p\pi^-$	pK^-
$B^0 \to \pi^+\pi^-$	43.6	0.36	2.33	1.68	0.12
$B_s^0 \to K^+K^-$	0.05	56.2	1.16	0.05	1.88
$B_{(s)}^0 \to K^+\pi^-$	1.40	4.36	37.0	0.80	0.06
$\bar{B}_{(s)}^0 \to \pi^+K^-$	1.40	4.36	0.02	0.03	0.91
$\Lambda_b \to p\pi^-$	2.08	0.98	6.75	34.9	3.31
$\bar{\Lambda}_b \to \pi^+\bar{p}$	2.08	0.98	0.03	0.04	0.24
$\Lambda_b \to pK^-$	0.06	12.8	0.10	1.14	39.8
$\bar{\Lambda}_b \to K^+\bar{p}$	0.06	12.8	0.99	0.04	0.19

	$\pi^+\pi^-$	K^+K^-	$K^+\pi^-$	$p\pi^-$	pK^-
$B^0 \to \pi^+\pi^-$	46.2	0.30	2.10	1.60	0.13
$B_s^0 \to K^+K^-$	0.05	57.8	1.17	0.04	1.59
$B_{(s)}^0 \to K^+\pi^-$	1.41	4.08	39.1	0.72	0.04
$\bar{B}_{(s)}^0 \to \pi^+K^-$	1.41	4.08	0.02	0.02	0.88
$\Lambda_b \to p\pi^-$	2.17	0.91	7.05	35.8	2.89
$\bar{\Lambda}_b \to \pi^+\bar{p}$	2.17	0.91	0.03	0.04	0.20
$\Lambda_b \to pK^-$	0.07	13.2	0.10	1.16	40.4
$\bar{\Lambda}_b \to K^+\bar{p}$	0.07	13.2	1.02	0.03	0.17

Table 4.10: Efficiencies (in %) of PID cuts, for the various mass hypotheses, predicted for events passing the offline selection used for measuring $A_{CP}(B_s^0 \to \pi K)$. The efficiencies are calculated using the calibration data sample acquired with the up (top table) and down (bottom table) polarities of the magnetic field.

	$\pi^+\pi^-$	K^+K^-	$K^+\pi^-$	$p\pi^-$	pK^-
$B^0 \to \pi^+\pi^-$	40.5	0.00	1.64	1.51	0.00
$B_s^0 \to K^+K^-$	0.04	21.4	0.98	0.04	1.01
$B_{(s)}^0 \to K^+\pi^-$	1.27	0.11	32.4	0.70	0.00
$\bar{B}_{(s)}^0 \to \pi^+K^-$	1.27	0.11	0.01	0.02	0.54
$\Lambda_b \to p\pi^-$	1.26	0.00	3.16	33.5	0.13
$\bar{\Lambda}_b \to \pi^+\bar{p}$	1.26	0.00	0.02	0.02	0.03
$\Lambda_b \to pK^-$	0.04	1.35	0.05	1.08	23.9
$\bar{\Lambda}_b \to K^+\bar{p}$	0.04	1.35	0.65	0.02	0.03

Table 4.11: Efficiencies (in %) of PID cuts, for the various mass hypotheses, predicted for events passing the offline selection used for observing the rare decays $B^0 \to K^+K^-$ and $B_s^0 \to \pi^+\pi^-$. The efficiencies are calculated using the calibration data sample acquired with both the magnet polarities.

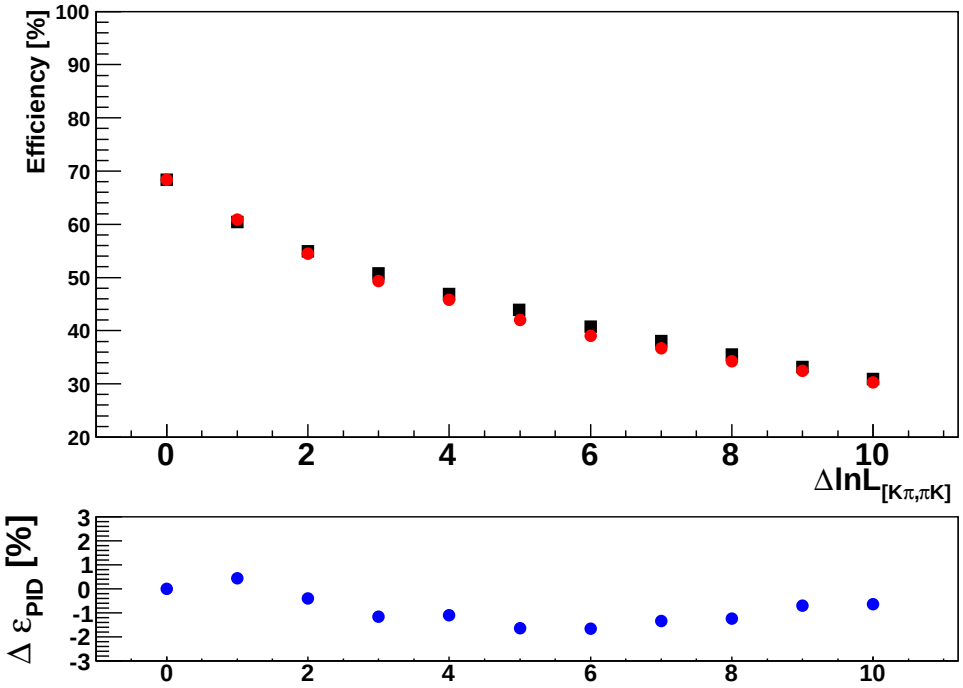

Figure 4.4: Comparison between PID efficiencies obtained from the ratio of $B^0 \to K^+\pi^-$ yields from fits to the $K\pi$ mass spectrum (red circles) and from the calibration procedure (black squares). The bottom frame reports the difference between the two efficiencies.

4.3 Fits to the $B \to h^+h'^-$ mass spectra

We perform unbinned maximum likelihood fits to the mass spectra of offline selected events, passing the kinematic selection with the PID cuts adopted either for the measurements of $A_{CP}(B^0 \to K\pi)$, $A_{CP}(B_s^0 \to \pi K)$ or for the observation of the rare modes $B^0 \to K^+K^-$ and $B_s^0 \to \pi^+\pi^-$, summarized in Tabs. 4.3, 4.4, 4.5, 4.6, 4.7 and 4.8. For the CP measurements we perform separate fits for magnet up and magnet down data sets: on the one hand it allows us to have an idea of the stability of results in different periods of data taking, and on the other hand we can accomodate for possible discrepancies due to different instrumental effects connected to the inversion of the magnetic field. The modeling of signal and background components is the same as in the 2010 analysis, with the only difference that with increased statistics it is necessary to introduce the description of a 3-body background component also in the K^+K^- mass spectrum.

4.3.1 Selection for the measurement of $A_{CP}(B^0 \to K\pi)$

The $K^+\pi^-$ (plus charge-conjugate) mass spectrum in the magnet up data set is shown in Fig. 4.5. The dominant signal visible in the plot is due to the $B^0 \to K\pi$ decay. The peaked distributions below the $B^0 \to K\pi$ peak are due to the cross-feed background. Three of them give a non-negligible contribution:

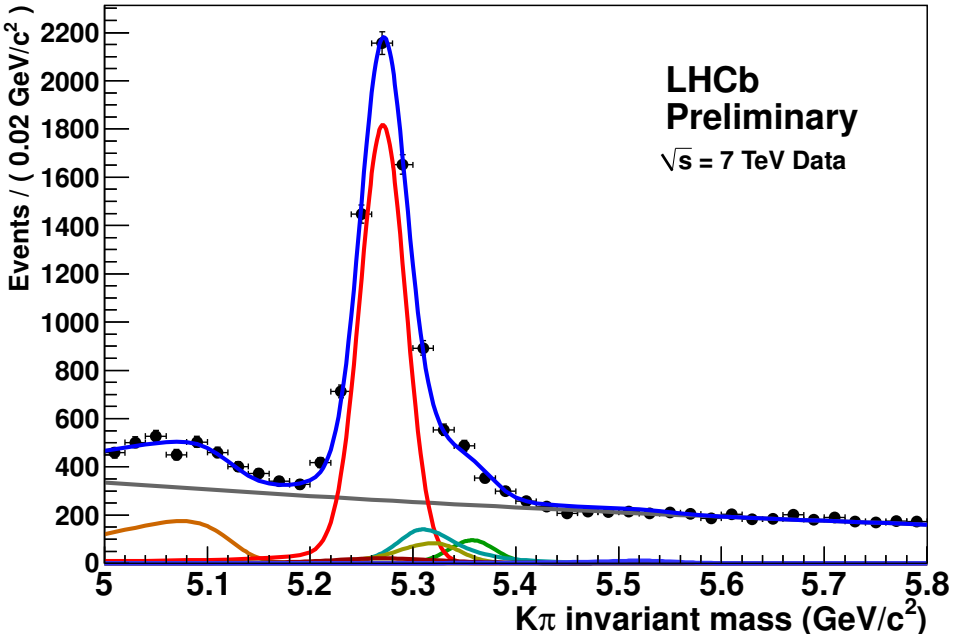

Figure 4.5: $K^+\pi^-$ (plus charge-conjugate) invariant mass spectrum, event selection adopted for the best sensitivity on $A_{CP}(B^0 \to K\pi)$ in the magnet up data set. The result of the unbinned maximum likelihood fit is superimposed. The main components contributing to the fit model are also visible: $B^0 \to K\pi$ (red), wrong sign $B^0 \to K\pi$ combination (dark red), $B^0 \to \pi^+\pi^-$ (light blue), $B_s^0 \to K^+K^-$ (dark yellow), $B_s^0 \to \pi K$ (green), combinatorial background (grey), 3-body partially reconstructed decays (orange).

- wrong sign $B^0 \to K\pi$ combination, i.e. when the identities of the two particles have been swapped;
- $B^0 \to \pi^+\pi^-$ decays, where one of the two pions has been mis-identified as a kaon;
- $B_s^0 \to K^+K^-$ decays, where one of the two kaons has been mis-identified as a pion.

A fourth component (green), due to the $B_s^0 \to \pi K$ signal decay, is also visible. Fig. 4.6 shows the $\pi^+\pi^-$ and K^+K^- invariant mass spectra in the magnet up data set. In both cases, the dominant cross-feed background comes from the $B^0 \to K\pi$ decay, where one of the two final state particles is mis-identified as a pion or a kaon. Fig. 4.7 shows the pK^- and $p\pi^-$ (plus charge conjugate) invariant mass spectra in the magnet up data set. Finally, Fig. 4.8 gives a visual indication of CP violation in the $B^0 \to K\pi$ decay, showing the $K^+\pi^-$ and $K^-\pi^+$ invariant mass spectra separately, in the magnet up data set: the difference in the heights of the $B^0 \to K^+\pi^-$ and $\bar{B}^0 \to K^-\pi^+$ mass peaks is apparent.

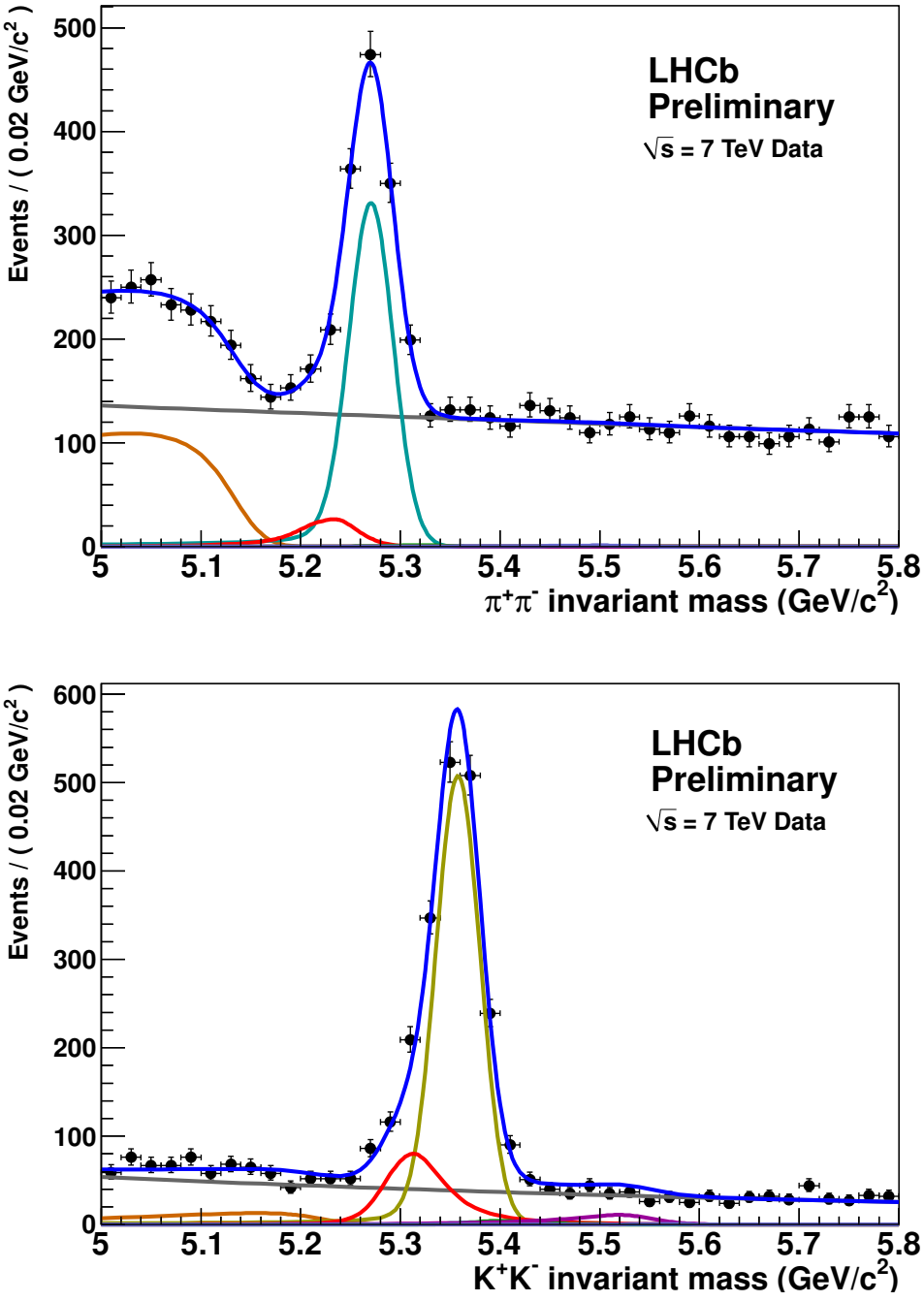

Figure 4.6: $\pi^+\pi^-$ (top) and K^+K^- (bottom) invariant mass spectra, event selection adopted for the best sensitivity on $A_{CP}(B^0 \to K^+\pi^-)$ in the magnet up data set. The result of the unbinned maximum likelihood fit is superimposed. The main components contributing to the fit model are also visible: $B^0 \to \pi^+\pi^-$ (light blue), $B_s^0 \to K^+K^-$ (dark yellow), $B^0 \to K\pi$ (red), combinatorial background (grey), 3-body partially reconstructed decays (orange). Also a small contribution from $\Lambda_b \to pK$ decays (purple) is visible in the bottom plot.

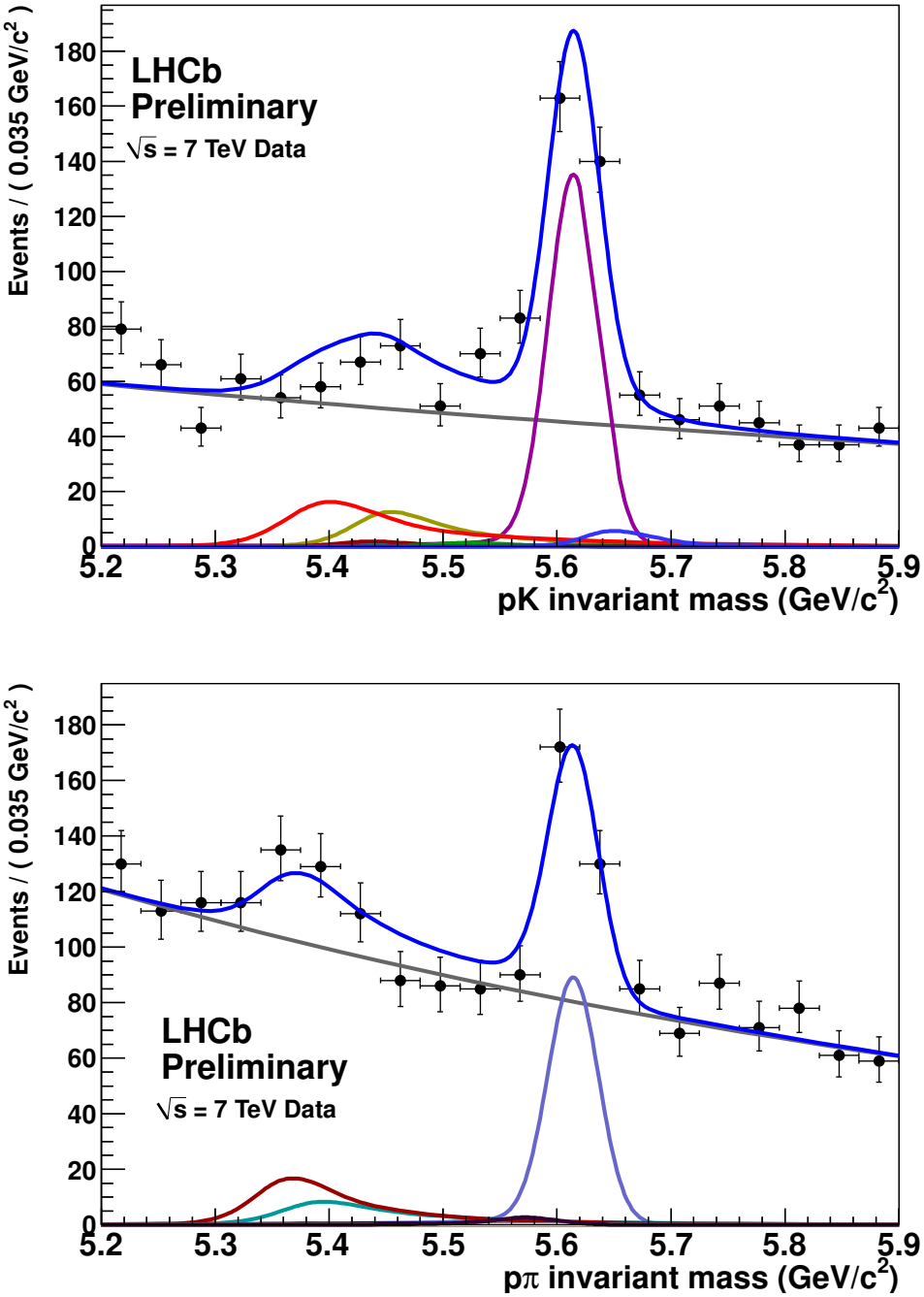

Figure 4.7: pK^- (plus charge conjugate, top) and $p\pi^-$ (plus charge conjugate, bottom) invariant mass spectra, event selection adopted for the best sensitivity on $A_{CP}(B^0 \to K\pi)$ in the magnet up data set. The result of the unbinned maximum likelihood fit is superimposed. Clear signals of $\Lambda_b \to pK^-$ and $\Lambda_b \to p\pi^-$ decays are visible, together with $B^0 \to K\pi$ (red), $B_s^0 \to K^+K^-$ (dark yellow), $B^0 \to \pi^+\pi^-$ (light blue) and combinatorial background (grey). The tiny background component peaked at about 5.65 GeV/c^2, visible in the bottom plot, is due to misidentified $\Lambda_b \to p\pi^-$ decays.

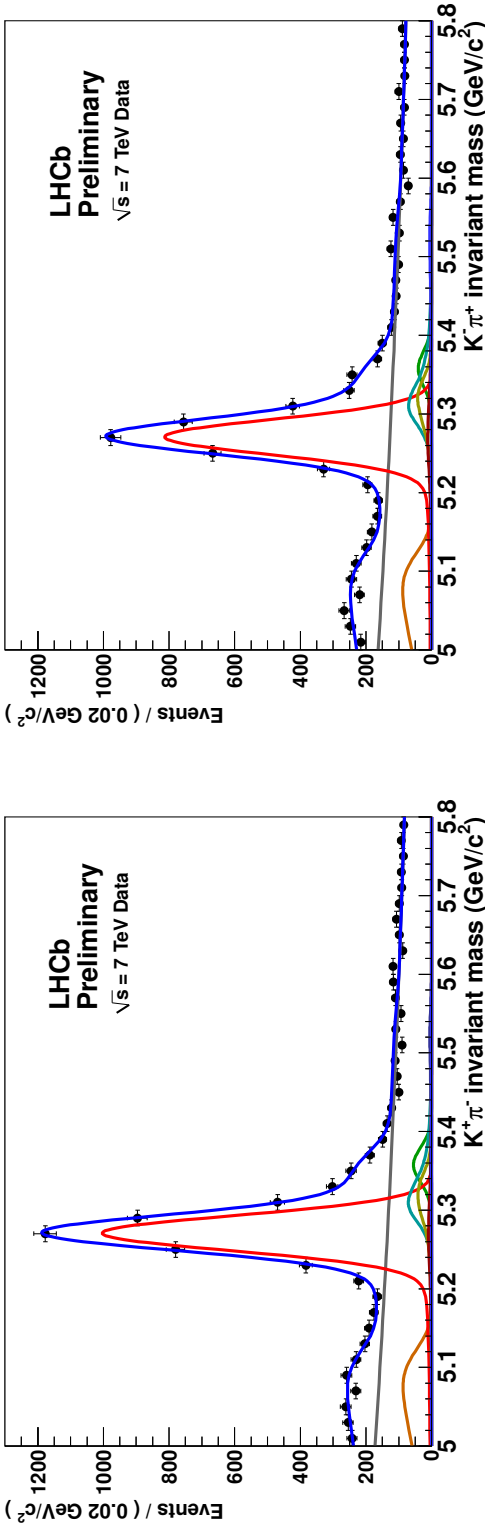

Figure 4.8: $K^+\pi^-$ (left) and $K^-\pi^+$ (right) invariant mass spectra, event selection adopted for the best sensitivity on $A_{CP}(B^0 \to K\pi)$ in the magnet up data set. The result of the unbinned maximum likelihood fit is superimposed. The main components contributing to the fit model are also visible: $B^0 \to K\pi$ (red), wrong sign $B^0 \to K\pi$ combination (dark red), $B^0 \to \pi^+\pi^-$ (light blue), $B_s^0 \to K^+K^-$ (dark yellow), $B_s^0 \to \pi K$ (green), combinatorial background (grey), 3-body partially reconstructed decays (orange).

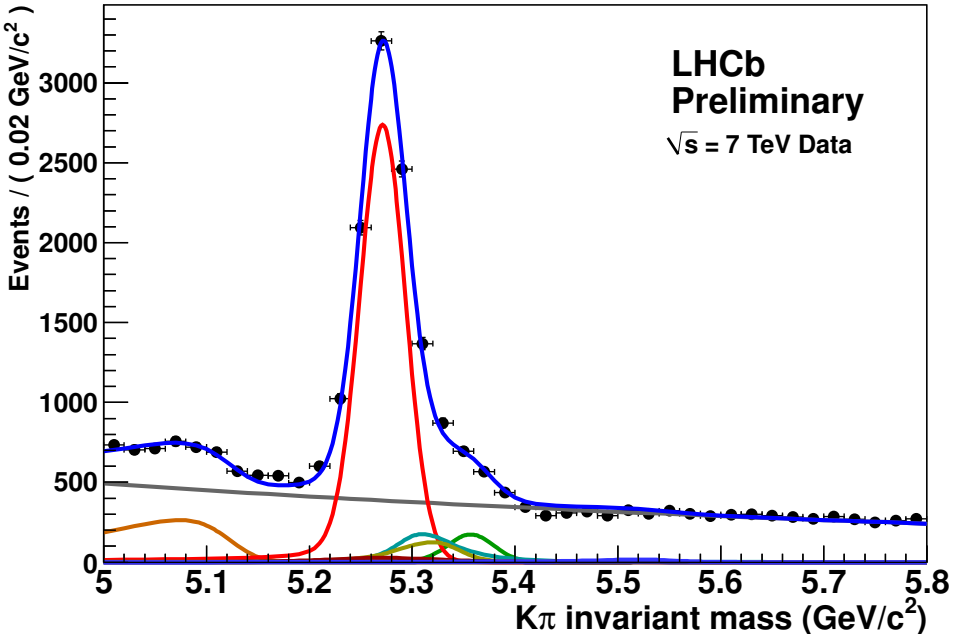

Figure 4.9: $K^+\pi^-$ (plus charge-conjugate) invariant mass spectrum, event selection adopted for the best sensitivity on $A_{CP}(B^0 \to K\pi)$ in the magnet down data set. The result of the unbinned maximum likelihood fit is superimposed. The main components contributing to the fit model are also visible: $B^0 \to K\pi$ (red), wrong sign $B^0 \to K\pi$ combination (dark red), $B^0 \to \pi^+\pi^-$ (light blue), $B_s^0 \to K^+K^-$ (dark yellow), $B_s^0 \to \pi K$ (green), combinatorial background (grey), 3-body partially reconstructed decays (orange).

The analogue plots corresponding to the magnet down data sets are shown in Figs. 4.9, 4.10, 4.11 and 4.12. The relevant parameters determined by the maximum likelihood fits are summarized in Tab. 4.12.

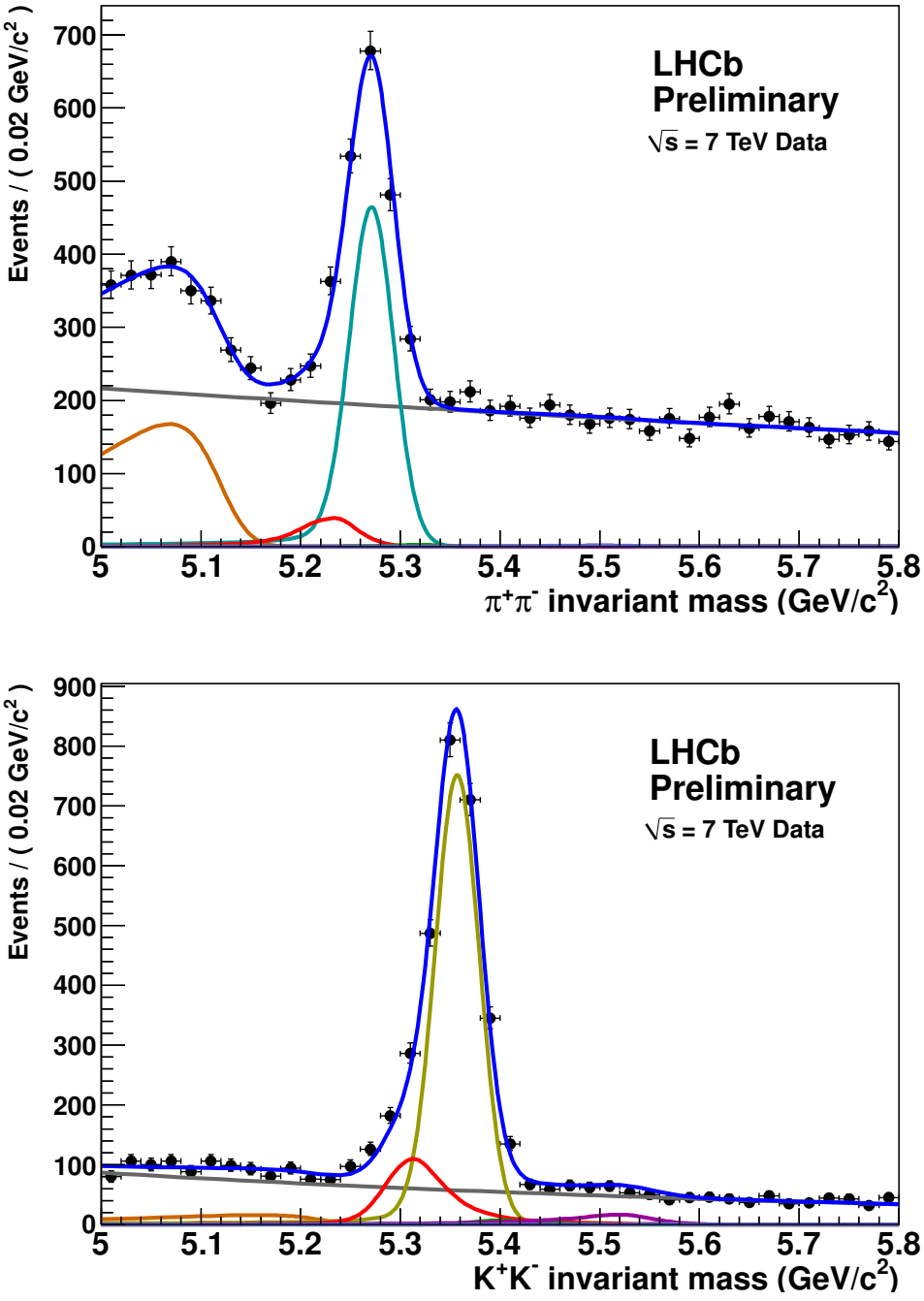

Figure 4.10: $\pi^+\pi^-$ (top) and K^+K^- (bottom) invariant mass spectra, event selection adopted for the best sensitivity on $A_{CP}(B^0 \to K^+\pi^-)$ in the magnet down data set. The result of the unbinned maximum likelihood fit is superimposed. The main components contributing to the fit model are also visible: $B^0 \to \pi^+\pi^-$ (light blue), $B_s^0 \to K^+K^-$ (dark yellow), $B^0 \to K\pi$ (red), combinatorial background (grey), 3-body partially reconstructed decays (orange). Also a small contribution from $\Lambda_b \to pK$ decays (purple) is visible in the bottom plot.

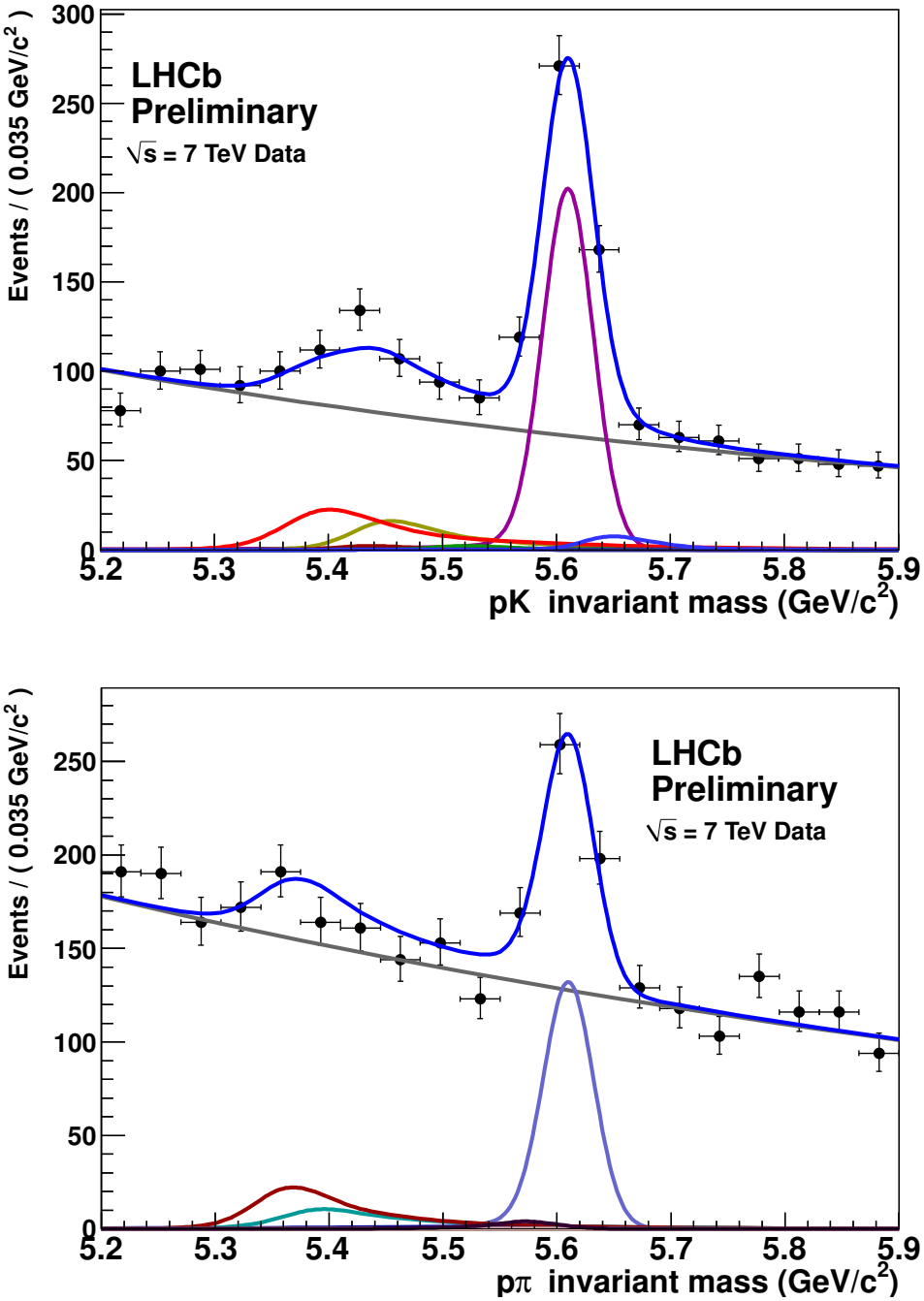

Figure 4.11: pK^- (plus charge conjugate, top) and $p\pi^-$ (plus charge conjugate, bottom) invariant mass spectra, event selection adopted for the best sensitivity on $A_{CP}(B^0 \to K\pi)$ in the magnet down data set. The result of the unbinned maximum likelihood fit is superimposed. Clear signals of $\Lambda_b \to pK^-$ and $\Lambda_b \to p\pi^-$ decays are visible, together with $B^0 \to K\pi$ (red), $B_s^0 \to K^+K^-$ (dark yellow), $B^0 \to \pi^+\pi^-$ (light blue) and combinatorial background (grey). The tiny background component peaked at about 5.65 GeV/c^2, visible in the bottom plot, is due to misidentified $\Lambda_b \to p\pi^-$ decays.

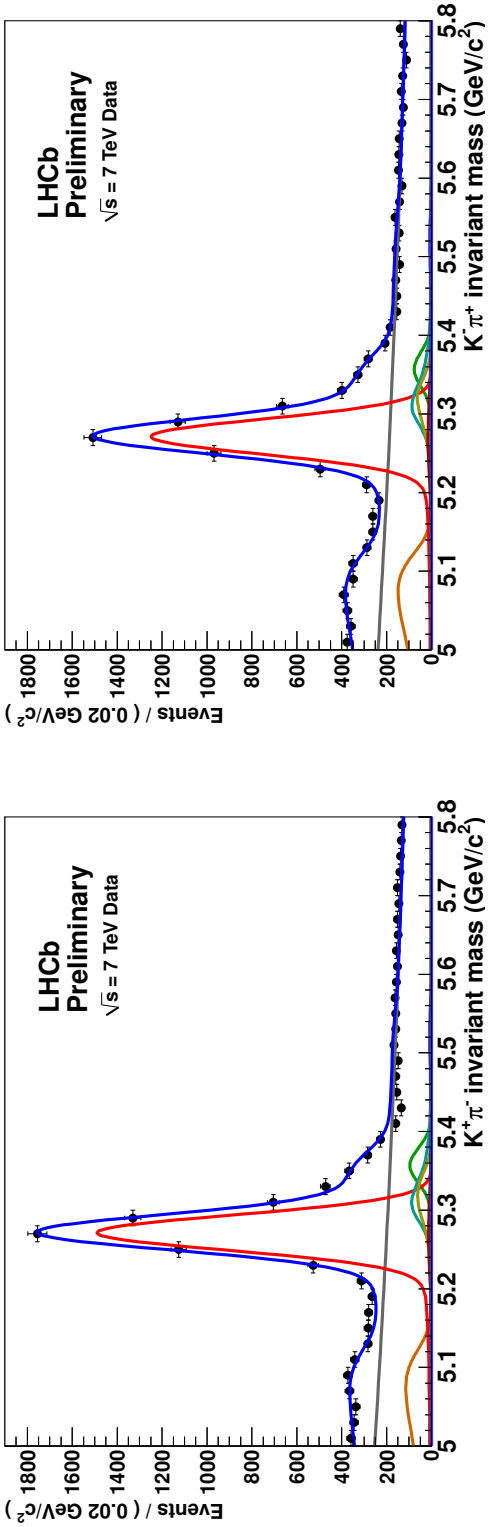

Figure 4.12: $K^+\pi^-$ (left) and $K^-\pi^+$ (right) invariant mass spectra, event selection adopted for the best sensitivity on $A_{CP}(B^0 \to K\pi)$ in the magnet down data set. The result of the unbinned maximum likelihood fit is superimposed. The main components contributing to the fit model are also visible: $B^0 \to K\pi$ (red), wrong sign $B^0 \to K\pi$ combination (dark red), $B^0 \to \pi^+\pi^-$ (light blue), $B_s^0 \to K^+K^-$ (dark yellow), $B_s^0 \to \pi K$ (green), combinatorial background (grey), 3-body partially reconstructed decays (orange).

Parameter	Fit result (magnet up)	Fit result (magnet down)
$B^0 \to K\pi$ yield	5282 ± 96	7963 ± 117
$B_s^0 \to \pi K$ yield	280 ± 46	507 ± 58
$B^0 \to \pi^+\pi^-$ yield	977 ± 45	1371 ± 55
$B_s^0 \to K^+K^-$ yield	1461 ± 46	2166 ± 56
$\Lambda_b \to pK$ yield	222 ± 19	332 ± 23
$\Lambda_b \to p\pi$ yield	149 ± 20	220 ± 25
B^0 mass [GeV/c^2]	5.2714 ± 0.0004	5.2719 ± 0.0003
B_s^0 mass [GeV/c^2]	5.3583 ± 0.0008	5.3575 ± 0.0006
Λ_b mass [GeV/c^2]	5.615 ± 0.002	5.611 ± 0.002
Mass resolution [MeV/c^2]	21.9 ± 0.4	22.0 ± 0.3
$A_{CP}^{RAW}(B^0 \to K\pi)$	-0.105 ± 0.017	-0.088 ± 0.014

Table 4.12: Relevant parameters determined by the unbinned maximum likelihood fit to the data sample surviving the event selection adopted for the best sensitivity on $A_{CP}(B^0 \to K\pi)$. Only statistical errors are shown.

4.3.2 Selection for the measurement of $A_{CP}(B_s^0 \to \pi K)$

The π^+K^- (plus charge-conjugate) mass spectrum in the magnet up data set is shown in Fig. 4.13. The dominant signal visible in the mass spectrum is again due to the $B^0 \to K\pi$ decay, as it shares the same final state signature as the $B_s^0 \to \pi K$ decay and constitutes an irreducible background for the latter. As is apparent, the tighter selection adopted for $A_{CP}(B_s^0 \to \pi K)$ causes a stronger suppression of the combinatorial background, with respect to the selection adopted for $A_{CP}(B^0 \to K\pi)$. A visual indication of CP violation is illustrated in Fig. 4.14, which shows the π^+K^- and π^-K^+ invariant mass spectra separately, in the magnet up data set. The difference in the heights of the $B_s^0 \to \pi^+K^-$ and $\bar{B}_s^0 \to \pi^-K^+$ mass peaks is apparent. Apart from the $B^0 \to K\pi$ decay, the other two main cross-feed backgrounds to the $B_s^0 \to \pi K$ signal, visible in the plots of Fig. 4.14, are again from the $B^0 \to \pi^+\pi^-$ and the $B_s^0 \to K^+K^-$ decays.

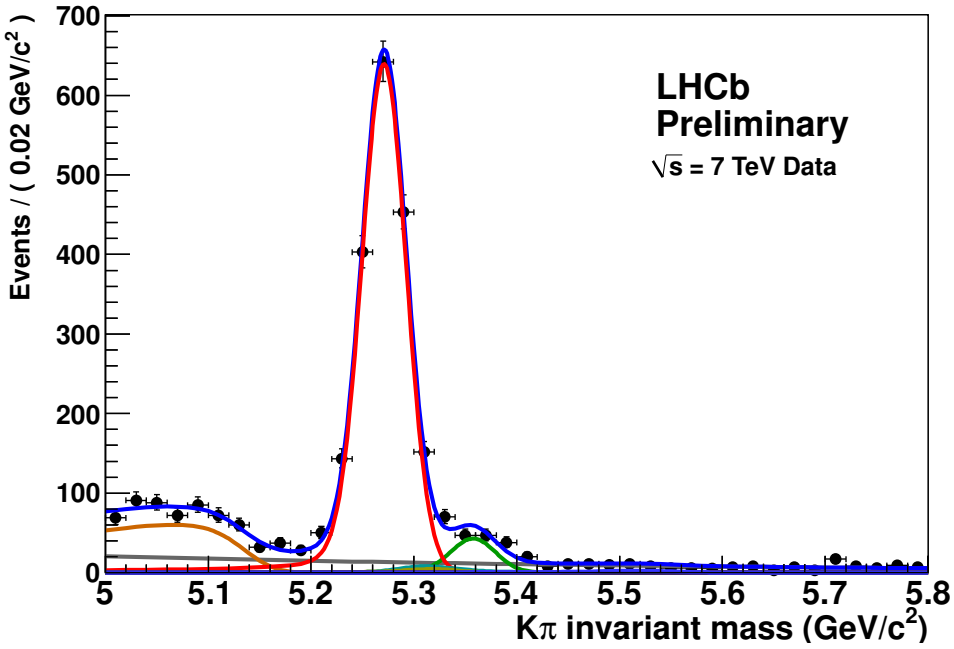

Figure 4.13: π^+K^- (plus charge-conjugate) invariant mass spectrum, event selection adopted for the best sensitivity on $A_{CP}(B_s^0 \to \pi^+K^-)$ in the magnet up data set. The result of an unbinned maximum likelihood fit is superimposed. The main components contributing to the fit model which are visible in the plots are: $B^0 \to K\pi$ (red), $B_s^0 \to \pi K$ (green), combinatorial background (grey), 3-body partially reconstructed decays (orange).

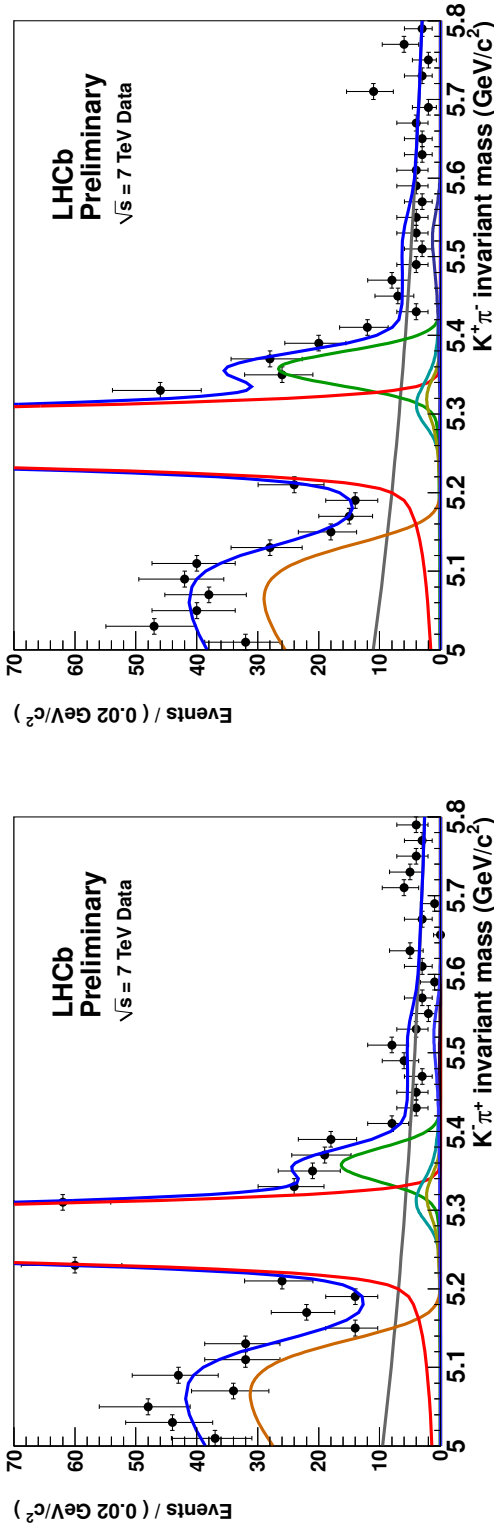

Figure 4.14: π^+K^- (left) and π^-K^+ (right) invariant mass spectra, magnified to focus on the two B_s^0 signal peaks, obtained using the event selection adopted for the best sensitivity on $A_{CP}(B_s^0 \to \pi K)$ in the magnet up data set. The result of an unbinned maximum likelihood fit is superimposed. The main components contributing to the fit model are also visible: $B^0 \to K\pi$ (red), $B^0 \to \pi^+\pi^-$ (light blue), $B_s^0 \to K^+K^-$ (dark yellow), $B_s^0 \to \pi K$ (green), combinatorial background (grey), 3-body partially reconstructed decays (orange).

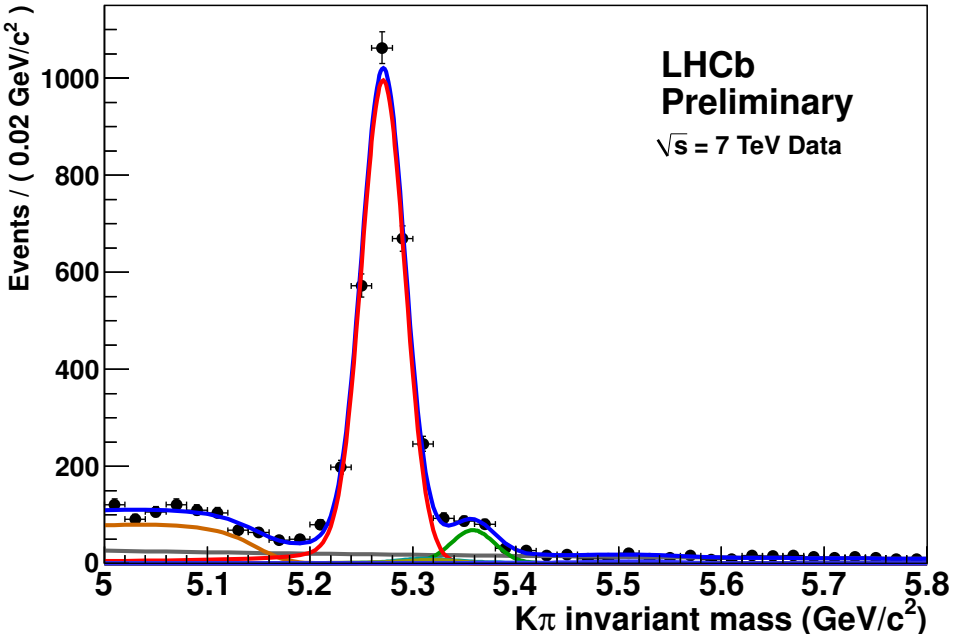

Figure 4.15: π^+K^- (plus charge-conjugate) invariant mass spectrum, event selection adopted for the best sensitivity on $A_{CP}(B_s^0 \to \pi^+K^-)$ in the magnet down data set. The result of an unbinned maximum likelihood fit is superimposed. The main components contributing to the fit model which are visible in the plots are: $B^0 \to K\pi$ (red), $B_s^0 \to \pi K$ (green), combinatorial background (grey), 3-body partially reconstructed decays (orange).

The analogue plots corresponding to the magnet down data sets are shown in Figs. 4.15 and 4.16. The relevant parameters determined by the maximum likelihood fits are summarized in Tab. 4.13.

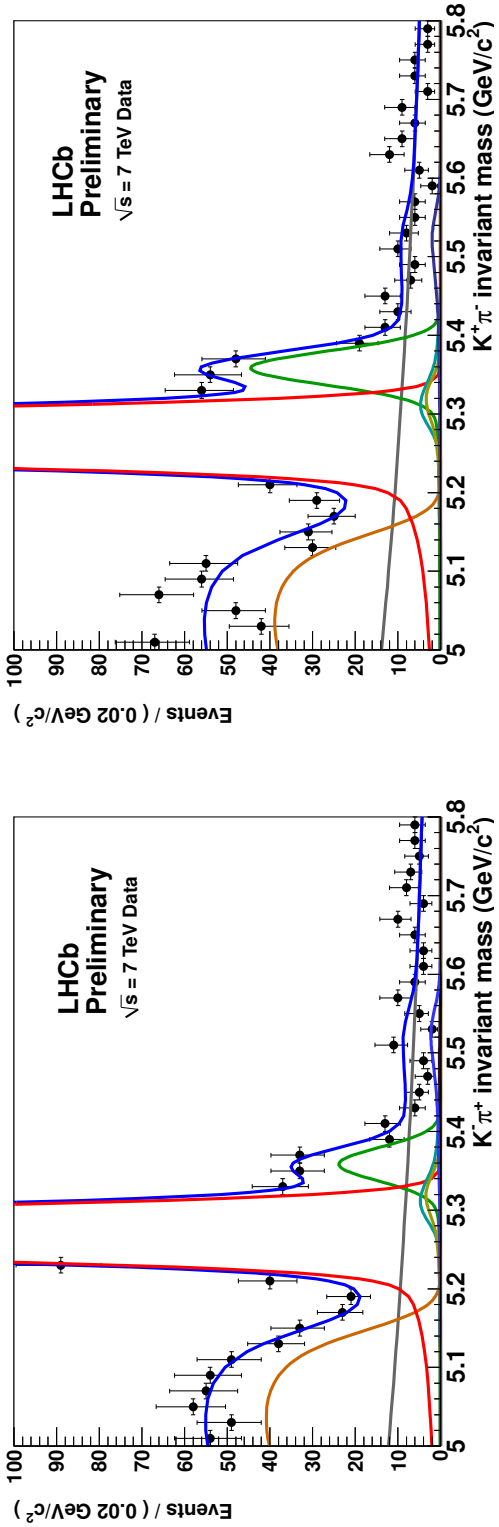

Figure 4.16: π^+K^- (left) and π^-K^+ (right) invariant mass spectra, magnified to focus on the two B_s^0 signal peaks, obtained using the event selection adopted for the best sensitivity on $A_{CP}(B_s^0 \to \pi K)$ in the magnet down data set. The result of an unbinned maximum likelihood fit is superimposed. The main components contributing to the fit model are also visible: $B^0 \to K\pi$ (red), $B^0 \to \pi^+\pi^-$ (light blue), $B_s^0 \to K^+K^-$ (dark yellow), $B_s^0 \to \pi K$ (green), combinatorial background (grey), 3-body partially reconstructed decays (orange).

Parameter	Fit result (magnet up)	Fit result (magnet down)
$B^0 \to K\pi$ yield	1809 ± 46	2773 ± 58
$B_s^0 \to \pi K$ yield	122 ± 17	192 ± 21
$B^0 \to \pi^+\pi^-$ yield	635 ± 29	886 ± 36
$B_s^0 \to K^+K^-$ yield	895 ± 34	1354 ± 41
$\Lambda_b \to pK$ yield	176 ± 15	228 ± 17
$\Lambda_b \to p\pi$ yield	88 ± 12	151 ± 15
B^0 mass [GeV/c^2]	5.2716 ± 0.0005	5.2717 ± 0.0004
B_s^0 mass [GeV/c^2]	5.3582 ± 0.0009	5.3590 ± 0.0007
Λ_b mass [GeV/c^2]	5.615 ± 0.002	5.611 ± 0.002
Mass resolution [MeV/c^2]	21.4 ± 0.4	21.0 ± 0.3
$A_{CP}^{RAW}(B_s^0 \to \pi K)$	0.24 ± 0.13	0.30 ± 0.10

Table 4.13: Relevant parameters determined by the unbinned maximum likelihood fit to the data sample surviving the event selection adopted for the best sensitivity on $A_{CP}(B_s^0 \to \pi K)$. Only statistical errors are shown.

4.3.3 Selection for observing $B^0 \to K^+K^-$ and $B_s^0 \to \pi^+\pi^-$ decays

The K^+K^- and $\pi^+\pi^-$ mass spectra are shown in Figs. 4.17 and 4.18 respectively. While a $B_s^0 \to \pi^+\pi^-$ mass peak is clearly emerging above the combinatorial background, there is not yet sufficient statistics to observe a clean $B^0 \to K^+K^-$ signal. As an additional complication, the mass peak of the $B^0 \to K^+K^-$ decay is expected to be placed in a region where various components give non negligible contributions, in particular the radiative tail of the $B_s^0 \to K^+K^-$ decay and the $B^0 \to K\pi$ cross-feed background. In order to suppress such a cross-feed background, in this case much tighter PID selection criteria have been employed. The relevant parameters determined by the maximum likelihood fit are summarized in Tab. 4.14.

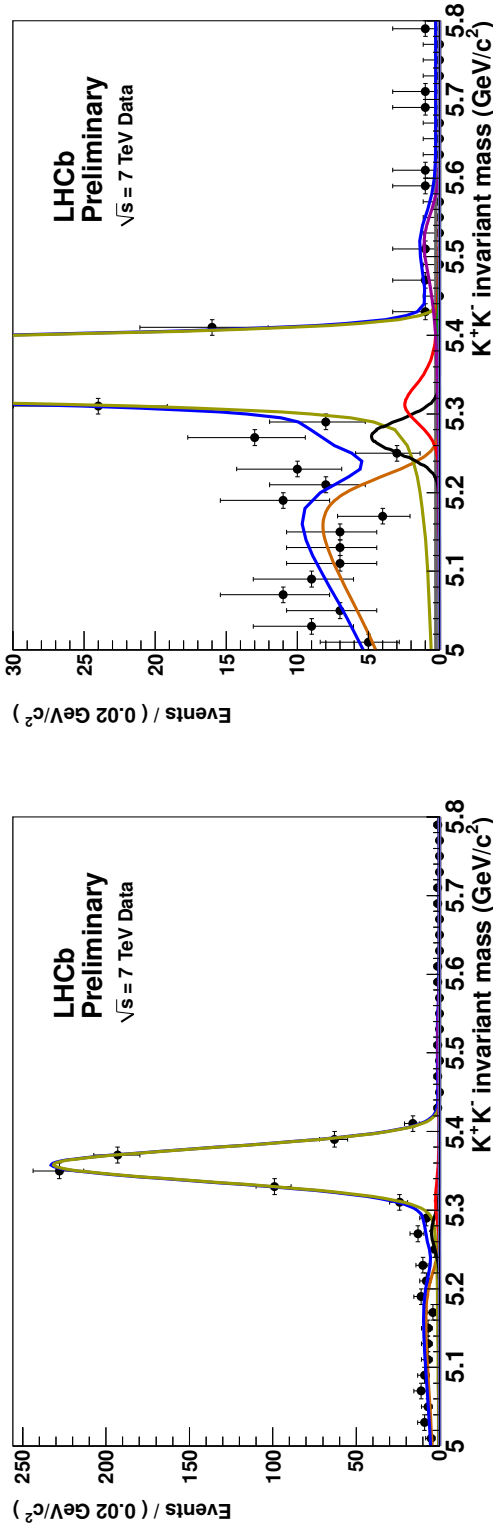

Figure 4.17: K^+K^- invariant mass spectrum, event selection adopted for the observation of the $B^0 \to K^+K^-$ and $B_s^0 \to \pi^+\pi^-$ rare decays. The right plot is the same as in the left, but magnified to focus on the rare $B^0 \to K^+K^-$ signal. The result of the unbinned maximum likelihood fit is superimposed. The main components contributing to the fit model are also visible: $B^0 \to K^+K^-$ (black), $B_s^0 \to K^+K^-$ (dark yellow), $B^0 \to K\pi$ (red), $\Lambda_b \to pK$ (purple), 3-body partially reconstructed decays (orange). The combinatorial background component (grey) is also present, but its contribution is very small.

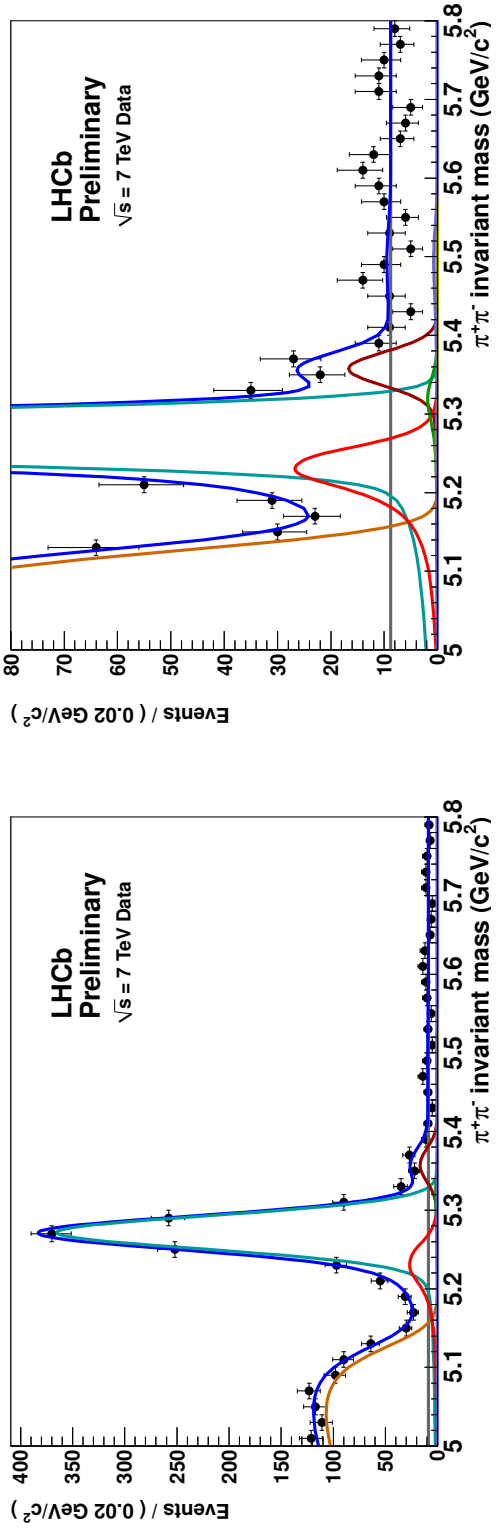

Figure 4.18: $\pi^+\pi^-$ invariant mass spectrum, event selection adopted for the observation of the $B^0 \to K^+K^-$ and $B_s^0 \to \pi^+\pi^-$ rare decays. The right plot is the same as in the left, but magnified to focus on the rare $B_s^0 \to \pi^+\pi^-$ signal. The result of the unbinned maximum likelihood fit is superimposed. The main components contributing to the fit model are also visible: $B_s^0 \to \pi^+\pi^-$ (brown), $B^0 \to \pi^+\pi^-$ (light blue), $B^0 \to K\pi$ (red), $B_s^0 \to \pi K$ (green), combinatorial background (grey), 3-body partially reconstructed decays (orange).

Parameter	Fit result
$B^0 \to K\pi$ yield	2803 ± 59
$B_s^0 \to \pi K$ yield	201 ± 20
$B^0 \to \pi^+\pi^-$ yield	1029 ± 35
$B_s^0 \to K^+K^-$ yield	636 ± 26
$\Lambda_b \to pK$ yield	141 ± 13
$\Lambda_b \to p\pi$ yield	160 ± 15
B^0 mass [GeV/c^2]	5.2724 ± 0.0004
B_s^0 mass [GeV/c^2]	5.3582 ± 0.0008
Λ_b mass [GeV/c^2]	5.611 ± 0.002
Mass resolution [MeV/c^2]	20.9 ± 0.3
$B^0 \to K^+K^-$ yield	13^{+6}_{-5}
$B_s^0 \to \pi^+\pi^-$ yield	47^{+11}_{-9}

Table 4.14: Relevant parameters determined by the unbinned maximum likelihood fit to the data sample surviving the event selection adopted for the observation of the $B^0 \to K^+K^-$ and $B_s^0 \to \pi^+\pi^-$ rare decays. Only statistical errors are shown.

4.4 Instrumental and production asymmetries

As we have seen in the previous chapter, the physical CP asymmetries are related to the raw asymmetries as in the following:

$$A_{CP}(B^0 \to K\pi) = A_{CP}^{RAW}(B^0 \to K\pi) - A_D(K\pi) - \kappa_d A_P(B^0) \tag{4.3}$$

and

$$A_{CP}(B_s^0 \to \pi K) = A_{CP}^{RAW}(B_s^0 \to \pi K) + A_D(K\pi) - \kappa_s A_P(B_s^0), \tag{4.4}$$

where the instrumental asymmetry is given in terms of the detection efficiencies of the charge-conjugate final states by

$$A_D(K\pi) = \frac{\varepsilon(K^-\pi^+) - \varepsilon(K^+\pi^-)}{\varepsilon(K^-\pi^+) + \varepsilon(K^+\pi^-)}, \tag{4.5}$$

the production asymmetry $A_P(B_{(s)}^0)$ is defined in terms of $\bar{B}_{(s)}^0$ and $B_{(s)}^0$ production rates as

$$A_P(B_{(s)}^0) = \frac{R(\bar{B}_{(s)}^0) - R(B_{(s)}^0)}{R(\bar{B}_{(s)}^0) + R(B_{(s)}^0)}, \tag{4.6}$$

and the factor $\kappa_{d,\,s}$ is defined as

$$\kappa_{d,\,s} = \frac{\int \left(e^{-\Gamma_{d,\,s}t}\cos\Delta m_{d,\,s}t\right)\varepsilon_{d,\,s}(t)dt}{\int \left(e^{-\Gamma_{d,\,s}t}\cosh\frac{\Delta\Gamma_{d,\,s}}{2}t\right)\varepsilon_{d,\,s}(t)dt}, \tag{4.7}$$

where $\varepsilon_{d,\,s}(t)$ is the acceptance as a function of the proper decay time.

Fig. 4.19 shows the reconstructed proper time distributions of $B^0 \to K\pi$ decays in magnet up and magnet down data sets, extracted by means of the ${}_s\mathcal{P}lot$ technique. The curves superimposed

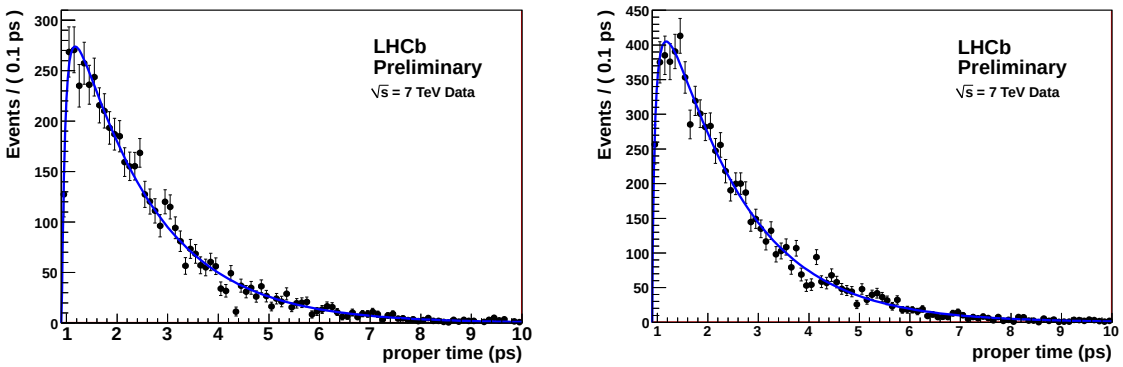

Figure 4.19: Proper time distributions of $B^0 \to K\pi$ decays, for up (left) and down (right) polarities of the magnetic field.

Parameter	Magnet up	Magnet down
a	14.8 ± 1.8	16.0 ± 2.9
b	1.38 ± 0.20	0.90 ± 0.13
κ_d	0.31	0.30

Table 4.15: Parameters governing the proper time acceptance function for reconstructed $B^0 \to K\pi$ decays. The corresponding factors κ_s are also shown.

to the histograms are the results of maximum likelihood fits made using the following p.d.f.:

$$f(t) = A\exp(-\Gamma t') \otimes G(t-t';\sigma_\tau)\frac{[a(t-t_0)]^b}{1+[a(t-t_0)]^b}, \tag{4.8}$$

where A is a normalization factor, Γ is the B^0 decay width, G is a Gaussian resolution function of width $\sigma_\tau = 40$ fs (the precise value of the resolution width is irrelevant), $t_0 = 0.9$ ps is a fixed threshold reflecting the offline selection cut in the $t_{\pi\pi}$ variable, and finally a and b are two free parameters describing the acceptance as a function of the proper time, i.e. the acceptance function is given by:

$$\varepsilon(t) = \frac{[a(t-t_0)]^b}{1+[a(t-t_0)]^b}. \tag{4.9}$$

The a and b acceptance parameters returned by the fits are reported in Tab. 4.15, together with the corresponding κ_d factors calculated using Eq. (4.7). In the calculation of κ_d we assume $\Delta\Gamma_d = 0$ and we use the central values of the current world averages for Γ_d and Δm_d [21].

Fig. 4.20 shows the reconstructed proper time distributions of $B_s^0 \to \pi K$ decays in magnet up and magnet down data sets, again extracted by means of the ${}_s\mathcal{P}lot$ technique. The a and b acceptance parameters for $B_s^0 \to \pi K$ decays returned by the fits, using the same proper time acceptance function with $t_0 = 1.5\ ps$, are reported in Tab. 4.16, together with the corresponding κ_s factors calculated using Eq. (4.7). In the calculation of κ_s we use the central values of the current world averages for Γ_s, Δm_s and $\Delta\Gamma_s$ [21]. Due to the fast B_s^0 oscillation, the κ_s in this

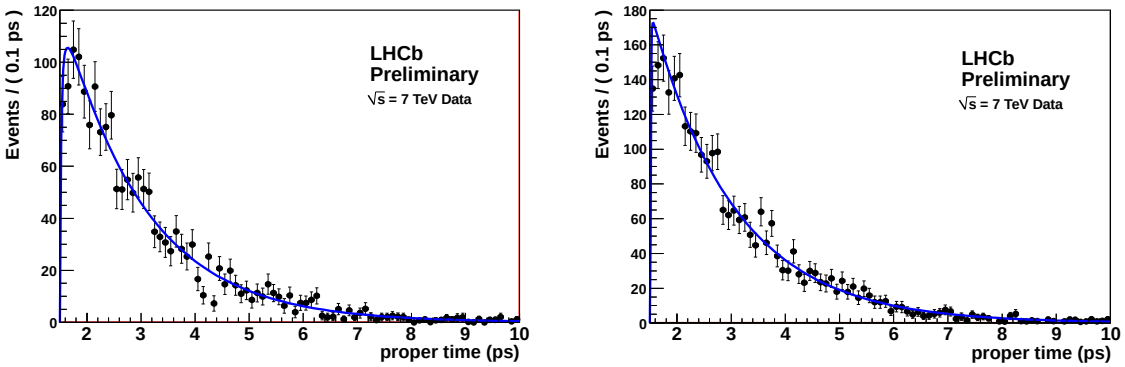

Figure 4.20: Proper time distributions of $B_s^0 \to \pi K$ decays, for up (left) and down (right) polarities of the magnetic field.

Parameter	Magnet up	Magnet down
a	47 ± 15	61 ± 10
b	1.3 ± 0.5	3.7 ± 1.9
κ_s	-0.028	-0.036

Table 4.16: Parameters governing the proper time acceptance function for reconstructed $B_s^0 \to \pi K$ decays. The corresponding factors κ_s are also shown.

case is very small, thus leading to a negligible impact of a possible production asymmetry of B_s^0 mesons.

4.4.1 Instrumental asymmetries from charm control samples

Similarly to the 2010 analysis, the instrumental asymmetry of the final state $K\pi$ has been studied on data using high statistics samples of $D^{*+} \to D^0(K^-\pi^+)\pi^+$ and $D^{*+} \to D^0(K^+K^-)\pi^+$, and $D^0 \to K^-\pi^+$ decays (plus their charge-conjugate modes).

The data sample is composed of about 120 pb^{-1} (magnet up) and 200 pb^{-1} (magnet down) of integrated luminosity in the Reco10-Stripping13b CHARM stream. The data is selected using the stripping line `DstarForPromptCharm` for the $D^{*+} \to D^0(h^+h'^-)\pi^+$ modes and the line `D02HHForPromptCharm` for the $D^0 \to K^-\pi^+$ mode.

In order to extract the raw CP asymmetry of the $D^0 \to K^-\pi^+$ decay, we perform a binned likelihood fit to the $K^-\pi^+$ and $K^+\pi^-$ mass spectra. The fit model is the same as that used in Ref. [83]. The mass plots with the result of the fit superimposed are shown in Figs. 4.21. For the decays $D^{*+} \to D^0(K^-\pi^+)\pi^+$ and $D^{*+} \to D^0(K^+K^-)\pi^+$ (plus charge-conjugates), we perform maximum likelihood fits using as discriminating observable the variable $M_{D^*} - M_{D^0}$, where M_{D^*} and M_{D^0} are the reconstructed D^* and D^0 invariant masses respectively. Again, the fit model is the same as in the 2010 analysis. The mass plots with the result of the fit superimposed are shown in Figs. 4.22 and 4.23. Yields and raw CP asymmetries are summarized in Tabs. 4.17 and 4.18.

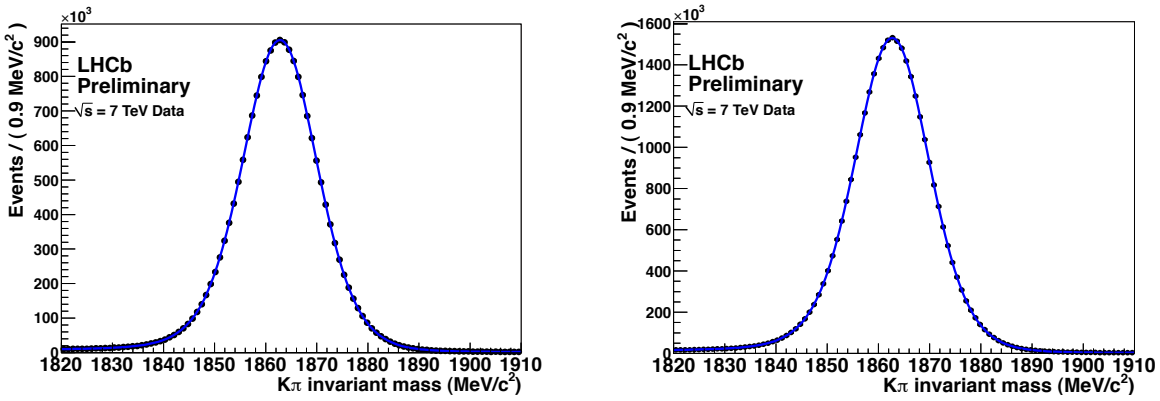

Figure 4.21: $D^0 \to K^-\pi^+$ (plus charge-conjugate) mass spectra with the results of the maximum likelihood fit superimposed, for data acquired with up (left) and down (right) polarities of the magnetic field.

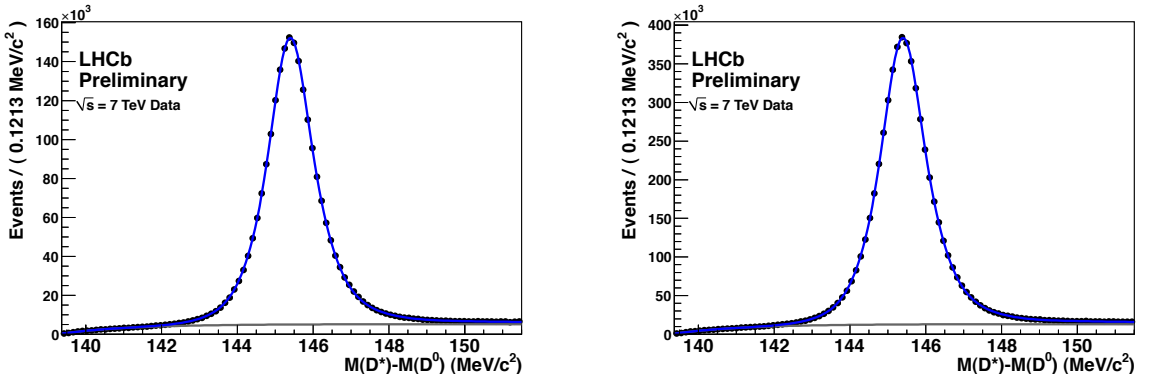

Figure 4.22: $D^{*+} \to D^0(K^-\pi^+)\pi^+$ (plus charge-conjugate) mass spectra with the results of the maximum likelihood fit superimposed, for data acquired with the up (left) and down (right) polarities of the magnetic field.

Employing the current world average of the integrated CP asymmetry for the $D^0 \to K^+K^-$ decay [86, 87] (the CP asymmetry for the Cabibbo-favoured $D^0 \to K^-\pi^+$ decay is assumed negligible), the system of Eqs. (3.19), (3.20), (3.22), (3.23), (3.25), (3.26), (3.27) and (3.29) can be solved in order to determine some of the relevant instrumental asymmetries. The results are summarized in Tab. 4.19.

4.4.2 Production asymmetry from $B^0 \to J/\psi K^{*0}$

Differently from the 2010 analysis, where the production asymmetry was studied using $B^+ \to J/\psi K^+$ decays, for the 2011 analysis the study has been made using $B^0 \to J/\psi K^{*0}$ decays. Averaging together magnet up and magnet down data, Eqs. (4.3) and (4.4) can be rewritten as

$$A_{CP}(B^0 \to K\pi) = A_{CP}^{RAW}(B^0 \to K\pi)^{\uparrow\downarrow} - A_I(K\pi) - \alpha A_R(K\pi)^{\uparrow} - \kappa_d A_P(B^0) \qquad (4.10)$$

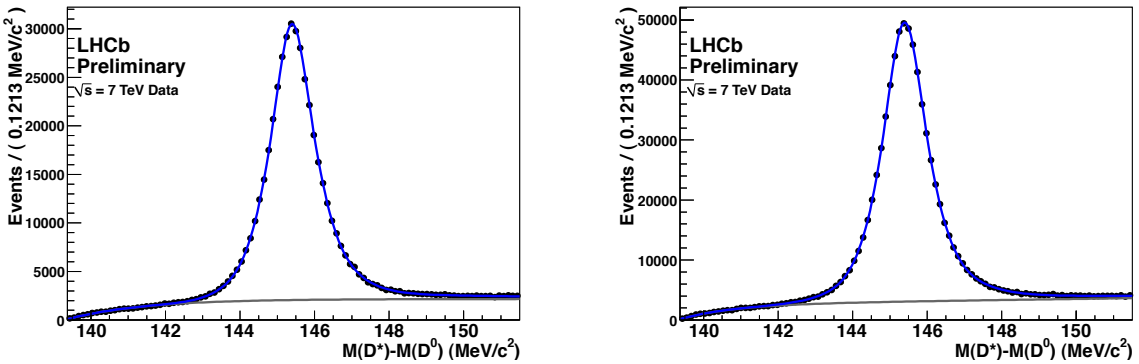

Figure 4.23: $D^{*+} \to D^0(K^+K^-)\pi^+$ (plus charge-conjugate) mass spectra with the results of the maximum likelihood fit superimposed, for data acquired with the up (left) and down (right) polarities of the magnetic field.

Channel	Yield [10^6]	
	Magnet up	Magnet down
$D^0 \to \pi K$	21.0	32.8
$D^* \to D^0(K\pi)\pi$	2.14	5.38
$D^* \to D^0(KK)\pi$	0.405	0.671

Table 4.17: Summary of the signal yields, separately for the up and down polarities of the magnetic field.

and

$$A_{CP}(B_s^0 \to \pi K) = A_{CP}^{RAW}(B_s^0 \to \pi K)^{\uparrow\downarrow} + A_I(K\pi) + \alpha A_R(K\pi)^{\uparrow} - \kappa_s A_P(B_s^0), \tag{4.11}$$

where $A_{CP}^{RAW}(B^0 \to K\pi)^{\uparrow\downarrow}$ is the raw asymmetry averaged between magnet up and magnet down data, and the factor α measures the asymmetry of $B \to h^+h'^-$ yields in magnet up and magnet down data sets. Note that in the 2010 analysis the α factor has not been introduced since the yields in the magnet up and magnet down data samples where identical. We can estimate α by using the yields of the largest decay mode, i.e.:

$$\alpha = \frac{N(B^0 \to K\pi)^{\uparrow} - N(B^0 \to K\pi)^{\downarrow}}{N(B^0 \to K\pi)^{\uparrow} + N(B^0 \to K\pi)^{\downarrow}}. \tag{4.12}$$

In the limit of identical statistics in magnet up and magnet down data sets, the parameter α vanishes and consequently $A_R(K\pi)$ does not contribute in Eqs. (4.10) and (4.11).

Similarly, the observed raw asymmetry for the $B^0 \to J/\psi K^{*0}$ decay, averaged between up and down polarities of the magnetic field, can be written as

$$A_{CP}^{RAW}(B^0 \to J/\psi K^{*0})^{\uparrow\downarrow} = A_{CP}(B^0 \to J/\psi K^{*0}) + A_I(K\pi) + \alpha' A_R(K\pi)^{\uparrow} + \kappa' A_P(B^0), \tag{4.13}$$

where the parameters α' and κ' are the analogues of α and $\kappa_{d,s}$ for reconstructed $B^0 \to J/\psi K^{*0}$ decays and $A_{CP}(B^0 \to J/\psi K^{*0})$ is the corresponding time integrated CP asymmetry, assumed

Channel	A_{CP}^{RAW}	
	Magnet up	Magnet down
$D^0 \to K\pi$	-0.0184 ± 0.0002	-0.0148 ± 0.0002
$D^* \to D^0(K\pi)\pi$	-0.0254 ± 0.0008	-0.0113 ± 0.0005
$D^* \to D^0(KK)\pi$	-0.019 ± 0.002	-0.002 ± 0.002

Table 4.18: Summary of the raw asymmetries determined by the maximum likelihood fits, for the up and down polarities of the magnetic field.

Asymmetries	Values
$A_I(K\pi)$	-0.010 ± 0.002
$A_R(K\pi)^{\uparrow}$	-0.0018 ± 0.0002
$A_R(\pi_s)^{\uparrow}$	-0.0056 ± 0.0005

Table 4.19: Summary of relevant instrumental asymmetries. See text for their definition.

negligible in the following. Using Eq. (4.13), Eq. (4.10) finally becomes

$$A_{CP}(B^0 \to K\pi) = A_{CP}^{RAW}(B^0 \to K\pi)^{\uparrow\downarrow} - A_{\Delta}(B^0 \to K\pi), \tag{4.14}$$

where the quantity $A_{\Delta}(B^0 \to K\pi)$ is the correction due to instrumental and production asymmetries and is given by

$$\begin{aligned} A_{\Delta}(B^0 \to K\pi) &= A_I(K\pi) + \alpha A_R(K\pi)^{\uparrow} + \\ &+ \frac{\kappa_d}{\kappa'}\left[A_{CP}^{RAW}(B^0 \to J/\psi K^{*0})^{\uparrow\downarrow} - A_I(K\pi) - \alpha' A_R(K\pi)^{\uparrow}\right]. \end{aligned} \tag{4.15}$$

In the case of the $B_s^0 \to \pi K$ decay, we can write

$$A_{CP}(B_s^0 \to \pi K) = A_{CP}^{RAW}(B_s^0 \to \pi K)^{\uparrow\downarrow} - A_{\Delta}(B_s^0 \to \pi K), \tag{4.16}$$

where in the expression of the correction factor we can neglect the presence of a B_s^0 production asymmetry, due to the small value of the k_s parameter, i.e.:

$$A_{\Delta}(B_s^0 \to \pi K) = -A_I(K\pi) - \alpha A_R(K\pi)^{\uparrow}. \tag{4.17}$$

4.4.2.1 Determination of $A_{CP}^{RAW}(B^0 \to J/\psi K^{*0})$

The data sample is composed of about 120 pb^{-1} (magnet up) and 200 pb^{-1} (magnet down) of integrated luminosity in the full Reco10-Stripping13b DIMUON stream. The data are selected using the stripping line `BetaSBd2JpsiKstarUnbiasedLine`. In addition to the pre-selection, in order to further suppress the combinatorial background, an offline selection was applied using the following simple set of cuts:

- the minimum impact parameter χ^2 values of the two muons, the kaon and the pion, calculated with respect to all primary vertices, were requested to exceed 9;
- the proper decay time of the B candidate had to be larger than 0.2 ps.

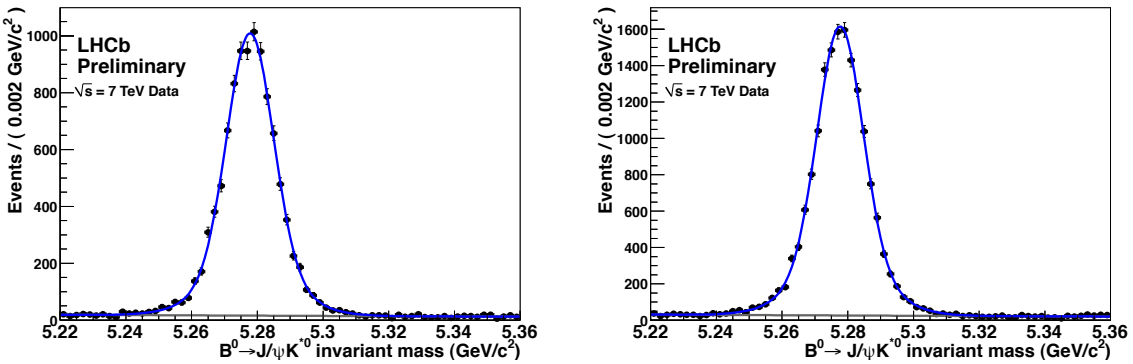

Figure 4.24: $B^0 \to J/\psi K^{*0}$ (plus charge-conjugate) invariant mass plots, for up (left) and down (right) polarities of the magnetic field.

	Magnet up	Magnet down
$B^0 \to J/\psi K^{*0}$ event yield	9800 ± 109	15607 ± 137
$A_{CP}^{RAW}(B^0 \to J/\psi K^{*0})$	-0.008 ± 0.011	-0.004 ± 0.008

Table 4.20: Signal yields and raw asymmetries determined by unbinned maximum likelihood fits to the $B^0 \to J/\psi K^{*0}$ reconstructed invariant mass spectra.

We perform an unbinned maximum likelihood fit of the $J/\psi(\mu^+\mu^-)K^{*0}(K^+\pi^-)$ and $J/\psi(\mu^+\mu^-)\bar{K}^{*0}(K^-\pi^+)$ mass spectra. The signal mass peak is modeled as the sum of two Gaussians with common mean, while the combinatorial background is modeled by means of an exponential p.d.f.. The mass plots with the result of the fit superimposed are shown in Fig. 4.24. Signal yields and raw asymmetries returned by the fit are reported in Tab. 4.20. Fig. 4.25 shows the reconstructed proper time distributions of $B^0 \to J/\psi K^{*0}$ decays in magnet up and magnet down data sets. The curves superimposed to the histograms are the results of maximum likelihood fits made using the following p.d.f.:

$$f(t) = A \exp(-\Gamma t') \otimes G(t - t'; \sigma_\tau) \frac{(at)^b}{1 + (at)^b}, \tag{4.18}$$

where A is a normalization factor, Γ is the B^0 decay width, G is a Gaussian resolution function of width $\sigma_\tau = 40$ fs (the precise value of the resolution width is not relevant for the aim of this study), and finally a and b are two free parameters describing the acceptance as a function of the proper time. The a and b acceptance parameters returned by the fits are reported in Tab. 4.21, together with the corresponding κ' factors calculated using Eq. (4.7). In the calculation of κ' we assume $\Delta\Gamma_d = 0$ and we use the central values of the current world averages for Γ_d and Δm_d [21].

4.4.3 Correction factors to the raw asymmetries

It is now possible to calculate the correction that must be applied to the raw asymmetry, defined in Eq. (4.15). By using the yields of reconstructed $B^0 \to K\pi$ in magnet up and down data sets

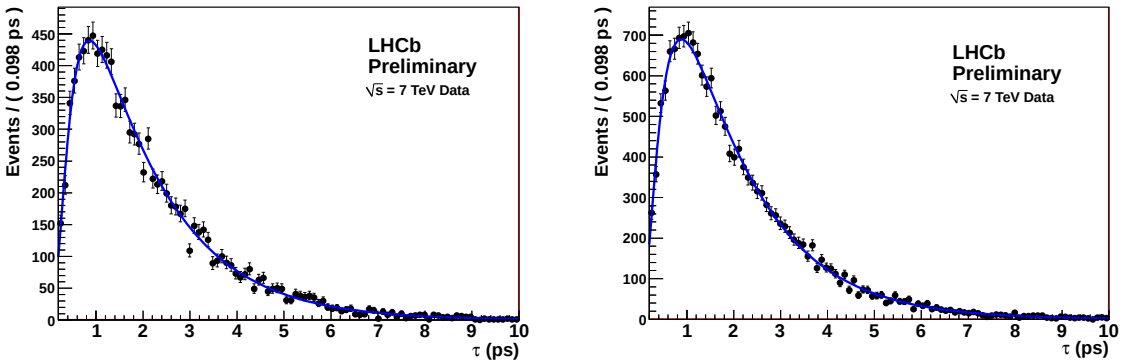

Figure 4.25: Proper time distributions of $B^0 \to J/\psi K^{*0}$ decays, for up (left) and down (right) polarities of the magnetic field.

Parameter	Magnet up	Magnet down
a	1.92 ± 0.09	1.75 ± 0.08
b	2.18 ± 0.14	1.91 ± 0.10
κ'	0.47	0.45

Table 4.21: Parameters governing the proper time acceptance function for reconstructed $B^0 \to J/\psi K^{*0}$ decays. The corresponding factors κ' are also shown.

given in Tab. 4.12, we determine the factor α to be

$$\alpha = \frac{N(B^0 \to K\pi)^{\uparrow} - N(B^0 \to K\pi)^{\downarrow}}{N(B^0 \to K\pi)^{\uparrow} + N(B^0 \to K\pi)^{\downarrow}} \simeq -0.20. \tag{4.19}$$

The analogue of α for $B^0 \to J/\psi K^{*0}$ decays can be as well calculated (the two values might slightly differ in case of different trigger conditions in magnet up and down data takings), and it is

$$\alpha' = \frac{N(B^0 \to J/\psi K^{*0})^{\uparrow} - N(B^0 \to J/\psi K^{*0})^{\downarrow}}{N(B^0 \to J/\psi K^{*0})^{\uparrow} + N(B^0 \to J/\psi K^{*0})^{\downarrow}} \simeq -0.22. \tag{4.20}$$

The correction to the raw asymmetry $A_{CP}^{RAW}(B^0 \to K\pi)$ is then given by

$$\begin{aligned} A_{\Delta}(B^0 \to K\pi) &= \left(1 - \frac{\kappa_d}{\kappa'}\right) A_I(K\pi) + \left(\alpha - \alpha' \frac{\kappa_d}{\kappa'}\right) A_R(K\pi)^{\uparrow} + \\ &+ \frac{\kappa_d}{\kappa'} A_{CP}^{RAW}(B^0 \to J/\psi K^{*0})^{\uparrow\downarrow} = 0.35 \cdot (-0.010 \pm 0.002) + \\ &+ (-0.20 + 0.22 \cdot 0.65) \cdot (-0.0018 \pm 0.0002) + \\ &+ 0.65 \cdot (-0.005 \pm 0.006) = -0.007 \pm 0.006. \end{aligned} \tag{4.21}$$

For the case of the $B_s^0 \to \pi K$ decay we have

$$\begin{aligned} A_{\Delta}(B_s^0 \to \pi K) &= -A_I(K\pi) - \alpha A_R(K\pi)^{\uparrow} = -(-0.010 \pm 0.002) + \\ &- (-0.20) \cdot (-0.0018 \pm 0.0002) = 0.010 \pm 0.002. \end{aligned} \tag{4.22}$$

Although we do not need to derive it explicitly, we obtain a value for $A_P(B^0)$:

$$\begin{aligned} A_P(B^0) &= \frac{1}{\kappa'}[A_{CP}^{RAW}(B^0 \to J/\psi K^{*0}) + \\ &- A_I(K\pi) - \alpha' A_R(K\pi)] = 0.010 \pm 0.013, \end{aligned} \tag{4.23}$$

where the error is statistical only.

4.5 Systematic errors

The systematic errors that we identify fall into the following main categories, related to:

1. PID calibration;
2. modelling of the signal and background components in the maximum likelihood fits;
3. instrumental and production asymmetries;
4. reconstruction efficiencies;
5. B-meson hadronization probabilities and reference branching fractions.

Categories (1), (2) and (3) affect the measurements of $A_{CP}(B^0 \to K\pi)$ and $A_{CP}(B_s^0 \to \pi K)$. Categories (1) and (2) also affect the determination of the relative yields needed to measure the branching fractions $\mathcal{B}(B^0 \to K^+K^-)$ and $\mathcal{B}(B_s^0 \to \pi^+\pi^-)$. In order to perform such measurements, we first determine the following ratios

$$\frac{f_d \cdot \mathcal{B}(B^0 \to K^+K^-)}{f_s \cdot \mathcal{B}(B_s^0 \to K^+K^-)} = \frac{N(B^0 \to K^+K^-)}{N(B_s^0 \to K^+K^-)} \cdot \frac{\varepsilon_{rec}(B_s^0 \to K^+K^-)}{\varepsilon_{rec}(B^0 \to K^+K^-)} \tag{4.24}$$

and

$$\frac{f_s \cdot \mathcal{B}(B_s^0 \to \pi^+\pi^-)}{f_d \cdot \mathcal{B}(B^0 \to \pi^+\pi^-)} = \frac{N(B_s^0 \to \pi^+\pi^-)}{N(B^0 \to \pi^+\pi^-)} \cdot \frac{\varepsilon_{rec}(B^0 \to \pi^+\pi^-)}{\varepsilon_{rec}(B_s^0 \to \pi^+\pi^-)}, \tag{4.25}$$

where ε_{rec} are the overall reconstruction efficiencies, f_d and f_s are hadronization probabilties of b-quarks into B^0 and B_s^0 mesons respectively, $N(B^0 \to K^+K^-)$, $N(B_s^0 \to K^+K^-)$, $N(B^0 \to \pi^+\pi^-)$ and $N(B_s^0 \to \pi^+\pi^-)$ are the event yields returned by the mass fits (see Tab. 4.14). Category (4) affects the evaluation of the various ε_{rec}. Then, by using external measurements of f_d/f_s, $\mathcal{B}(B^0 \to \pi^+\pi^-)$ and $\mathcal{B}(B_s^0 \to K^+K^-)$ we can derive the measurements of $\mathcal{B}(B_s^0 \to \pi^+\pi^-)$ and $\mathcal{B}(B^0 \to K^+K^-)$. This is where category (5) enters the scene.

4.5.1 PID calibration

As we have already seen in the previous chapter, PID efficiencies are necessary to compute the number of cross-feed background events affecting the mass fit of a given B decay channel. An imperfect PID calibration can lead to an incorrect estimate of the number of such background events, thus affecting the values of the direct CP asymmetries and the signal yields returned by the maximum likelihood fits. We perform unbinned maximum likelihood fits after having changed by 2% (see Sec. 4.2.4) the values of the relevant PID efficiencies, namely $\varepsilon(K\pi)$, $\varepsilon(\pi\pi)$, $\varepsilon(KK)$, $\varepsilon(pK)$ and $\varepsilon(p\pi)$, from the central values predicted by the calibration procedure. Four

modified sets of values are tried: in the first we increase by 2% the values of $\varepsilon(K\pi)$ and $\varepsilon(pK)$ while those of the other efficiencies are decreased by 2%; in the second we decrease by 2% the values of $\varepsilon(K\pi)$ and $\varepsilon(pK)$ and increase by 2% those of the other efficiencies; in the third and fourth we respectively increase and decrease the values of all the efficiencies by 2%. For each set we evaluate the shift of the relevant output quantities returned by the fits from those determined by the baseline fit. The systematic error is defined as the maximum observed shift.

4.5.2 Signal and background modelling

The signal p.d.f. used in the baseline fit to build the likelihood function for each $B \to h^+h'^-$ decay mode is given by a single Gaussian convolved with an additional component taking into account QED final state radiation processes. An estimate of the systematic error due to an incorrect description of the final state radiation is determined by varying in a wide range the value of the parameter governing the amount of emitted radiation. We also investigate the incorrect description of the core distribution in the signal mass model by replacing the single Gaussian function with the sum of two Gaussians with a common mean. We investigate the impact of the presence of a further component of 3-body B decays in the $K\pi$ spectrum, not accounted for in the baseline fit, e.g. due to $B \to \pi\pi\pi$ decays where one pion is not reconstructed and another one is misidentified as a kaon. We determine the mass lineshape of this background component from Monte Carlo simulations, and then we repeat the fit after having added it to the baseline model. For the modelling of the combinatorial background component we repeat the fit using a first order polynomial. For the case of the cross-feed backgrounds we estimate two distinct systematic errors: one due to a relative bias of the Monte Carlo mass distributions with respect to the signal distributions in data, and another one accounting for the difference in mass resolution between Monte Carlo and data. All the shifts from the relevant baseline values are accounted for as systematic errors.

4.5.3 Instrumental and production asymmetries

Instrumental and production asymmetries have been studied by means of charm control samples, as discussed in Sec. 4.4. We have determined the correction factors A_Δ, with their associated statistical errors, to be applied to the raw asymmetries of $B^0 \to K\pi$ and $B_s^0 \to \pi K$ decays measured in data. In order to take into account possible differences of the instrumental asymmetries, due to slightly different kinematic properties of charm and beauty two-body decays, as well as to different triggers and offline selections, we introduce a further systematic error of 0.005 (order of one half of the A_Δ corrections determined from the control samples).

4.5.4 Reconstruction efficiencies

The values of ε_{rec} obtained from Monte Carlo simulations are reported in Tab. 4.22. As is apparent, the efficiency for the $B_s^0 \to K^+K^-$ decay differs significantly from the other efficiencies, which in turn are in good agrement. This is because the lifetime of the $B_s^0 \to K^+K^-$ decay in the Monte Carlo is that of the short living B_s^0 eigenstate, roughly equal to 1.4 ps, as predicted by the Standard Model. Since in the offline event selection we apply a tight cut on the proper decay time at 2 ps, owing to this cut alone we expect a reduction in the value of the efficiency of a factor which is roughly given by $\exp(-2/1.5)/\exp(-2/1.4) \simeq 1.1$. However, albeit this was not taken into account in the simulation, also the $B_s^0 \to \pi^+\pi^-$ should exhibit the same reduced

Decay mode	$B^0 \to \pi^+\pi^-$	$B_s^0 \to \pi^+\pi^-$	$B^0 \to K^+K^-$	$B_s^0 \to K^+K^-$
ε_{rec}	0.64 ± 0.01	0.63 ± 0.01	0.63 ± 0.01	0.58 ± 0.01

Table 4.22: Absolute reconstruction efficiencies determined from Monte Carlo simulations for triggered, stripped and offline selected events passing the event selection for observing the rare decays $B^0 \to K^+K^-$ and $B_s^0 \to \pi^+\pi^-$. The errors are due to the limited Monte Carlo statistics available. The reason why the efficiency for the $B_s^0 \to K^+K^-$ decay differs significantly from the other efficiencies is discussed in the text.

lifetime. For this reason, also in this case we will consider a value of $\varepsilon_{rec} = 0.58 \pm 0.01$. Hence in the following we will use the following values for the ratios of efficiencies:

$$\varepsilon_{rec}(B_s^0 \to K^+K^-)/\varepsilon_{rec}(B^0 \to K^+K^-) = 0.92 \pm 0.02 \tag{4.26}$$

and

$$\varepsilon_{rec}(B^0 \to \pi^+\pi^-)/\varepsilon_{rec}(B_s^0 \to \pi^+\pi^-) = 1.10 \pm 0.03. \tag{4.27}$$

4.5.5 f_s/f_d and reference branching fractions

We will use the average value of f_s/f_d determined by LHCb [89]:

$$f_s/f_d = 0.267^{+0.021}_{-0.020}. \tag{4.28}$$

As values of the reference branching fractions, we will use the HFAG averages [58]:

$$\mathcal{B}(B^0 \to \pi^+\pi^-) = (5.16 \pm 0.22) \times 10^{-6} \tag{4.29}$$

and

$$\mathcal{B}(B_s^0 \to K^+K^-) = (26.5 \pm 4.4) \times 10^{-6}. \tag{4.30}$$

4.5.6 Summary of systematics

The systematic uncertainties for $A_{CP}(B^0 \to K\pi)$ and $A_{CP}(B_s^0 \to \pi K)$ are summarized in Tab. 4.23, while those for the ratios $N(B^0 \to K^+K^-)/N(B_s^0 \to K^+K^-)$ and $N(B_s^0 \to \pi^+\pi^-)/N(B^0 \to \pi^+\pi^-)$ are given in Tab. 4.24.

4.6 Final results and conclusions

4.6.1 $A_{CP}(B^0 \to K\pi)$ and $A_{CP}(B_s^0 \to \pi K)$

From Tabs. 4.12 and 5.7 we can determine the following values of the raw asymmetries, averaged between magnet up and magnet down data sets:

$$A_{CP}^{RAW}(B^0 \to K\pi)^{\uparrow\downarrow} = -0.095 \pm 0.011 \tag{4.31}$$

and

$$A_{CP}^{RAW}(B_s^0 \to \pi K)^{\uparrow\downarrow} = 0.28 \pm 0.08, \tag{4.32}$$

Systematic uncertainty	$A_{CP}(B^0 \to K\pi)$	$A_{CP}(B^0_s \to \pi K)$
PID calibration	0.0012	0.001
Final state radiation	0.0026	0.010
Signal model	0.0004	0.005
Combinatorial background model	0.0001	0.009
3-body background model	0.0009	0.007
Cross-feed background model (shift)	0.0009	0.005
Cross-feed background model (smearing)	0.0006	0.006
Instrumental and production asymmetries	0.0078	0.005
Total	0.0084	0.018

Table 4.23: Summary of systematic uncertainties on $A_{CP}(B^0 \to K\pi)$ and $A_{CP}(B^0_s \to \pi K)$. The total systematic uncertainties given in the last row are obtained by summing in quadrature all the contributions.

Systematic uncertainty	$\frac{N(B^0 \to K^+K^-)}{N(B^0_s \to K^+K^-)}$	$\frac{N(B^0_s \to \pi^+\pi^-)}{N(B^0 \to \pi^+\pi^-)}$
PID calibration	0.0005	0.0003
Final state radiation	0.0092	0.0013
Signal model	0.0011	0.0029
Combinatorial background model	0.0012	0.0004
Cross-feed background model (shift)	0.0008	0.0002
Cross-feed background model (smearing)	0.0002	0.0001
Total	0.0094	0.0032

Table 4.24: Summary of systematic uncertainties on the ratios of event yields $N(B^0 \to K^+K^-)/N(B^0_s \to K^+K^-)$ and $N(B^0_s \to \pi^+\pi^-)/N(B^0 \to \pi^+\pi^-)$. The total systematic uncertainties given in the last row are obtained by summing in quadrature all the contributions.

where the errors are statistical. By using Eqs. (4.14) and (4.16), with the central values of the correction factors given in Eqs. (4.22) and (4.23) and the total systematic uncertainties of Tab. 4.23, we obtain the following measurements of the physical CP asymmetries:

$$A_{CP}(B^0 \to K\pi) = -0.088 \pm 0.011 \pm 0.008 \tag{4.33}$$

and

$$A_{CP}(B^0_s \to \pi K) = 0.27 \pm 0.08 \pm 0.02. \tag{4.34}$$

The result for $A_{CP}(B^0 \to K\pi)$ constitutes the best measurement in the world, and is in good agreement with the current world average provided by HFAG [60]: $A_{CP}(B^0 \to K^+\pi^-) = -0.098^{+0.012}_{-0.011}$. The result for $A_{CP}(B^0_s \to \pi K)$ is the first evidence of CP violation in the $B^0_s \to \pi K$ decay, and is in agreement with the only measurement currently available, performed by CDF [48, 52]: $A_{CP}(B^0_s \to \pi^+K^-) = 0.39 \pm 0.15 \pm 0.08$. Both the results are also well compatible with those of the 2010 analysis.

4.6.2 $\mathcal{B}(B^0 \to K^+K^-)$ and $\mathcal{B}(B_s^0 \to \pi^+\pi^-)$

From Eqs. (4.24) and (4.25), using the relevant yields from Tab. 4.14, the values given in Eqs. (4.26), (4.27), (4.28), (4.29) and (4.30), and the total systematic uncertainties of Tab. 4.24, we obtain:

$$\mathcal{B}(B^0 \to K^+K^-) = (0.13^{+0.06}_{-0.05} \pm 0.07) \times 10^{-6} \tag{4.35}$$

and

$$\mathcal{B}(B_s^0 \to \pi^+\pi^-) = (0.98^{+0.23}_{-0.19} \pm 0.11) \times 10^{-6}. \tag{4.36}$$

In particular, using a likelihood ratio test and including the systematic uncertainties on the signal yields, we obtain a statistical significance of 5.3σ for the $B_s^0 \to \pi^+\pi^-$ signal, which is then observed for the first time. In the test the significance is estimated as $s_{stat} = \sqrt{-2\log\frac{L_B}{L_{S+B}}}$, where L_{S+B} and L_B are the values of the likelihoods at the maximum in the two cases of signal-plus-background and background-only hypotheses, respectively. The value of $s_{stat} = 5.5\sigma$ is then corrected by taking into account the systematic error on the signal yields as $s_{tot} \simeq s_{stat}/\sqrt{1+\sigma_{syst}^2/\sigma_{stat}^2}$, where σ_{stat} and σ_{syst} are the statistical and systematic errors on the ratios of the yields entering the computation of Eq. (4.24). Our values are in agreement with the recent CDF results [4]: $\mathcal{B}(B^0 \to K^+K^-) = (0.23 \pm 0.10 \pm 0.10) \times 10^{-6}$ and $\mathcal{B}(B_s^0 \to \pi^+\pi^-) = (0.57 \pm 0.15 \pm 0.10) \times 10^{-6}$.

Chapter 5

Measurements of the branching ratios of non-rare two-body modes

In this conclusive chapter we present the measurement of the branching fractions of $B^0 \to \pi^+\pi^-$, $B_s^0 \to K^+K^-$ and $B_s^0 \to \pi^+K^-$ decays. The current world average of the branching fraction of the $B^0 \to K^+\pi^-$ decay is used as a normalization. In addition we also report the measurement of the ratio of branching fractions between $\Lambda_b \to p\pi^-$ and $\Lambda_b \to pK-$ decays.

5.1 Data set and event selection

The data sample is composed of the full Reco10-Stripping13b BHADRON stream for both magnet polarities, and corresponds to an integrated luminosity of about 200 pb^{-1} for magnet down and 170 pb^{-1} for magnet up.

5.1.1 Trigger

In the analyses presented in the previous two chapters, no requirement on the trigger algorithms which selected the $B \to h^+h'^-$ decays was applied. In order to evaluate in a simpler way the trigger efficiencies for each decay mode, only the candidates triggered by a specific set of trigger algorithms have been used in the final analysis. In the LHCb jargon this requirement is defined as:

(**L0HadronTOS**)**AND**(**Hlt1TrackAllL0TOS**)**AND**(**Hlt2B2HHTOS**)

5.1.1.1 Trigger stripping and offline selection

The `L0Hadron` trigger algorithm selects events where the number of hits in the Scintillator Pad Detector (SPD) is less than 600 and where there is at least one cluster in the Hadronic Calorimeter (HCAL) with a transverse energy greater than 3.5 GeV/c.

The `Hlt1TrackAllL0` trigger algorithm is divided into three steps. In the first step it applies cuts on global event variables in order to reduce the time used for the online reconstruction of the events. The requirements are: the number of hits in the Outer Tracker (OTHits) less than 15000, the number of hits in the Inner Tracker (ITHits) less than 3000 and the number of hits in the Vertex Locator (VeloHits) less than 10000.

Efficiencies ratio	Value
$\varepsilon^{rec}(B^0 \to K^+\pi^-)/\varepsilon^{rec}(B^0 \to \pi^+\pi^-)$	0.98 ± 0.02
$\varepsilon^{rec}(B^0 \to K^+\pi^-)/\varepsilon^{rec}(B_s^0 \to K^+K^-)$	1.00 ± 0.02
$\varepsilon^{rec}(B^0 \to K^+\pi^-)/\varepsilon^{rec}(B_s^0 \to \pi^+K^-)$	0.98 ± 0.02
$\varepsilon^{rec}(\Lambda_b \to pK^-)/\varepsilon^{rec}(\Lambda_b \to p\pi^-)$	1.00 ± 0.02

Table 5.1: Ratios of reconstruction efficiencies of the various channel, escluding PID.

In the second steps the algorithm performs the reconstruction of the primary vertices and of the Velo Tracks. On the Velo Tracks the following requirements are applied:

- a difference between the expected and observed Velo hits less than 3;
- a number of hits in the Velo greater than 9;
- the minimum impact parameter with respect to all primary vertices less than 100 μm.

The Velo Tracks surviving to the second step are then fully reconstructed in the third step. These tracks are selected asking for:

- a number of total hits in the tracking system greater than 16;
- a transverse momentum greater than 1.7 GeV/c;
- a momentum grater than 10 GeV/c.

The selected tracks are then re-fitted using a BiDirectional Kalman filter and are required to have a χ^2 of the fit less than 3 and a χ^2 of the minimum impact parameter with respect to all the primary vertices greater than 16.
The trigger algorithm selects the events with at least one track surviving the three steps described above.

The HLT2 trigger and the stripping selections are the same already described in Secs. 4.1.1 and 4.1.2. For the measurement of the $\mathcal{B}$ of the dominant decay modes ($B^0 \to \pi^+\pi^-$ and $B_s^0 \to K^+K^-$) and the relative $\mathcal{B}$ between the two $\Lambda_b \to pK$ and $\Lambda_b \to p\pi$ decays we applied the same offline selection that we used for the measurement of $A_{CP}(B^0 \to K\pi)$, given in Tab. 4.3. In the case of the $\mathcal{B}$ of $B_s^0 \to \pi^-K^+$ decay we selected the sample by means of the tighter cuts used for the measurement of $A_{CP}(B_s^0 \to \pi K)$, given in Tab. 4.4.

The ratios between the reconstruction efficiencies $\varepsilon_{\rm rec}$ of the decays of interest and the reference $B^0 \to K^+\pi^-$ decay, are needed to calculate the $\mathcal{B}$ of a $B \to h^+h'^-$ decay. In order to evaluate such ratios, we applied stripping, kinematic selection and trigger requirements to full simulated events of each $B \to h^+h'^-$ decay. The results of this study are summarized in Tab. 5.1, where the errors are due to the limited statistics of simulated events available.

As usual each of the two $B \to h^+h'^-$ samples passing the two kinematic event selections is then subdivided into different final states using the PID capabilities of the two RICH subdetectors. In particular we employ the quantities $\Delta\log\mathcal{L}_{K\pi}$ and $\Delta\log\mathcal{L}_{p\pi}$, or their difference $\Delta\log\mathcal{L}_{Kp}$ when appropriate. The respective two sets of PID cuts are the same as those reported in Tabs. 4.6 and 4.7.

5.2 Particle identification

The PID efficiencies are determined by the using the same reweighting procedure described in Sec. 4.2.2, and are reported in Tabs. 5.2 and 5.3.

	$\pi^+\pi^-$	K^+K^-	$K^+\pi^-$	$p\pi^-$	pK^-
$B^0 \to \pi^+\pi^-$	43.1	0.33	28.6	1.53	0.13
$B_s^0 \to K^+K^-$	0.05	55.0	15.4	0.05	1.63
$B_{(s)}^0 \to K^+\pi^-$	1.40	4.17	67.9	0.72	0.06
$\bar{B}_{(s)}^0 \to \pi^+K^-$	1.40	4.17	2.09	0.02	0.85
$\Lambda_b \to p\pi^-$	1.93	0.92	16.8	35.4	3.16
$\bar{\Lambda}_b \to \pi^+\bar{p}$	1.93	0.92	0.95	0.03	0.18
$\Lambda_b \to pK^-$	0.06	12.2	1.92	1.18	40.2
$\bar{\Lambda}_b \to K^+\bar{p}$	0.06	12.2	4.51	0.03	0.18

Table 5.2: Efficiencies (in %) of PID cuts, for the various mass hypotheses, predicted for events passing the offline selection used for measuring the $\mathcal{B}$ of dominant $B \to h^+h'^-$ decays and the relative branching fraction of $\Lambda_b \to p\pi^-$ and $\Lambda_b \to pK^-$.

	$\pi^+\pi^-$	K^+K^-	$K^+\pi^-$	$p\pi^-$	pK^-
$B^0 \to \pi^+\pi^-$	42.8	0.33	2.06	1.51	0.13
$B_s^0 \to K^+K^-$	0.05	54.5	1.09	0.05	1.63
$B_{(s)}^0 \to K^+\pi^-$	1.38	4.12	35.7	0.72	0.06
$\bar{B}_{(s)}^0 \to \pi^+K^-$	1.38	4.12	0.02	0.02	0.84
$\Lambda_b \to p\pi^-$	1.90	0.90	6.01	35.4	3.16
$\bar{\Lambda}_b \to \pi^+\bar{p}$	1.90	0.90	0.03	0.03	0.17
$\Lambda_b \to pK^-$	0.06	11.8	0.09	1.19	40.2
$\bar{\Lambda}_b \to K^+\bar{p}$	0.06	11.8	0.88	0.03	0.17

Table 5.3: Efficiencies (in %) of PID cuts, for the various mass hypotheses, predicted for events passing the offline selection used for measuring the branching fraction of $B_s^0 \to \pi^+K^-$ decay.

The evaluation of systematic errors associated to the PID calibration has been discussed in Sec. 4.2.4, where we quoted an absolute systematic error on $\varepsilon_{\rm PID}$ of 2%. Using the values in Tabs. 5.2 and 5.3 we can determine the PID efficiency ratios needed to compute the final branching fractions. Such ratios are summarized in Tab. 5.4.

5.3 Fits to the $B \to h^+h'^-$ mass spectra

We perform unbinned maximum likelihood fits to the mass spectra of offline selected events, passing the kinematic selection with the PID cuts summarized in Tabs. 3.2 and 3.4 for the $\mathcal{BR}$ measurement of $B^0 \to \pi^+\pi^-$, $B_s^0 \to K^+K^-$ and $\Lambda_b \to p\pi/\Lambda_b \to pK$, and Tabs. 3.3 and 3.5 for the $\mathcal{BR}$ measurement of the $B_s^0 \to \pi^+K^-$ decay. The two samples have been refined requiring

PID ratio	Value
$\varepsilon^{PID}(K^+\pi^-)/\varepsilon^{PID}(\pi^+\pi^-)$	1.57 ± 0.09
$\varepsilon^{PID}(K^+\pi^-)/\varepsilon^{PID}(K^+K^-)$	1.23 ± 0.06
$\varepsilon^{PID}(pK^-)/\varepsilon^{PID}(p\pi^-)$	1.14 ± 0.05

Table 5.4: Ratio of PID efficiencies used to compute the $\mathcal{B}$ of $B \to h^+h'^-$ decays. The errors have been determined as described in the text.

Parameter	Fit result
$B^0 \to K\pi$ yield	9822 ± 122
$B_s^0 \to \pi K$ yield	608 ± 54
$B^0 \to \pi^+\pi^-$ yield	1667 ± 51
$B_s^0 \to K^+K^-$ yield	2523 ± 59
$\Lambda_b \to pK$ yield	372 ± 22
$\Lambda_b \to p\pi$ yield	279 ± 22
B^0 mass [GeV/c^2]	5.2717 ± 0.0003
B_s^0 mass [GeV/c^2]	5.3578 ± 0.0006
Λ_b mass [GeV/c^2]	5.6116 ± 0.0013
Mass resolution [MeV/c^2]	22.5 ± 0.2

Table 5.5: Relevant parameters determined by the unbinned maximum likelihood fit to the data sample surviving the event selection adopted for the $\mathcal{BR}$ measurement of $B^0 \to \pi^+\pi^-$, $B_s^0 \to K^+K^-$ and $\Lambda_b \to p\pi/\Lambda_b \to pK$. Only statistical errors are shown.

that each candidate is triggered by `L0Hadron`, `Hlt1TrackAllL0` and `Hlt2B2HH`. The modeling of signal and background components is the same as in the analysis described in the previous chapter.

5.3.1 $\mathcal{BR}$ measurement of $B^0 \to \pi^+\pi^-$, $B_s^0 \to K^+K^-$ and $\Lambda_b \to p\pi/\Lambda_b \to pK$

The $K^+\pi^-$ (plus charge-conjugate) mass spectrum is shown in Fig. 5.1. The dominant signal visible in the plot is due to the $B^0 \to K\pi$ decay. Below the $B^0 \to K\pi$ peak are visible three non negligible contributions from cross-feed backgrounds due to the mis identification of one or both final state particles: wrong sign $B^0 \to K\pi$ combination, $B^0 \to \pi^+\pi^-$ decays and $B_s^0 \to K^+K^-$ decays. A fourth component (green), due to the $B_s^0 \to \pi K$ signal decay, is also visible. Fig. 5.2 shows the $\pi^+\pi^-$ and K^+K^- invariant mass spectra. In both cases, the dominant cross-feed background comes from the $B^0 \to K\pi$ decay, where one of the two final state particles is mis-identified as a pion or a kaon. Fig. 5.3 shows the pK^- and $p\pi^-$ (plus charge conjugate) invariant mass spectra. The relevant parameters determined by the maximum likelihood fits are summarized in Tab. 5.5.

Using the values of Tab. 5.5 we can calculate the ratios between the relevant yields. In Tab. 5.6 such ratios with their statistical errors are reported.

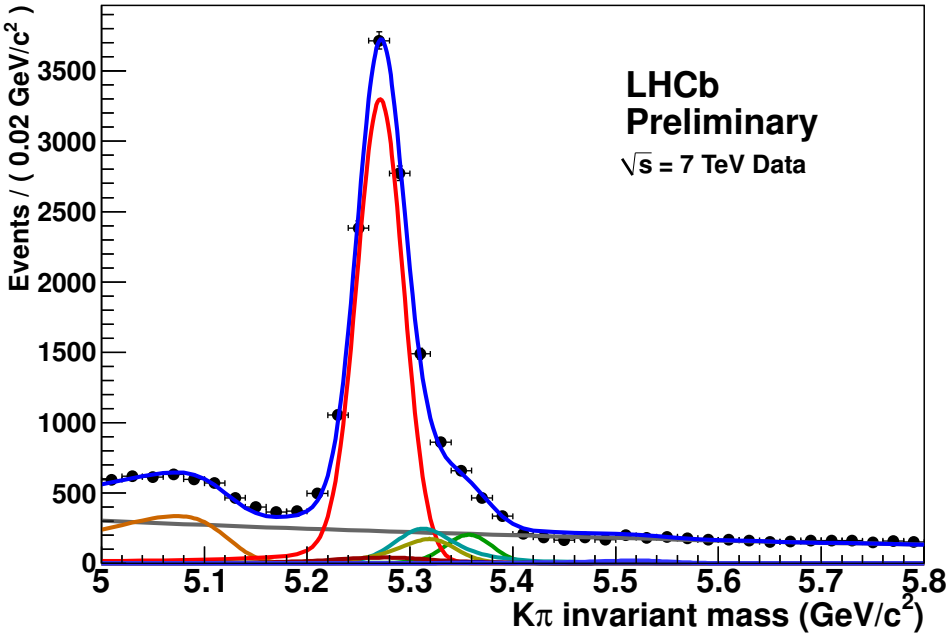

Figure 5.1: $K^+\pi^-$ (plus charge-conjugate) invariant mass spectrum for events surviving the event selection adopted for the relative $\mathcal{BR}$ measurement of $B^0 \to \pi^+\pi^-$, $B_s^0 \to K^+K^-$ and $\Lambda_b \to p\pi/\Lambda_b \to pK$. The result of the unbinned maximum likelihood fit is superimposed. The main components contributing to the fit model explained in the text are also visible: $B^0 \to K\pi$ (red), wrong sign $B^0 \to K\pi$ combination (dark red), $B^0 \to \pi^+\pi^-$ (light blue), $B_s^0 \to K^+K^-$ (dark yellow), $B_s^0 \to \pi K$ (green), combinatorial background (grey), 3-body partially reconstructed decays (orange).

Yield Ratio	Value
$N(B^0 \to \pi^+\pi^-)/N(B^0 \to K^+\pi^-)$	0.170 ± 0.006
$N(B_s^0 \to K^+K^-)/N(B^0 \to K^+\pi^-)$	0.257 ± 0.007
$N(\Lambda_b \to p\pi^-)/N(\Lambda_b \to pK^-)$	0.75 ± 0.07

Table 5.6: Relevant parameters determined by the unbinned maximum likelihood fit to the data sample surviving the event selection adopted for the $\mathcal{BR}$ measurement of $B^0 \to \pi^+\pi^-$, $B_s^0 \to K^+K^-$ and $\Lambda_b \to p\pi/\Lambda_b \to pK$. Only statistical errors are shown.

5.3.2 $\mathcal{BR}$ measurement of $B_s^0 \to \pi K$)

The π^+K^- (plus charge-conjugate) mass spectrum is shown in Fig. 5.4. The dominant signal visible in the mass spectrum is again due to the $B^0 \to K\pi$ decay, as it shares the same final state signature as the $B_s^0 \to \pi K$ decay and constitutes an irreducible background for the latter. The tighter selection adopted to select this data sample gives an high suppression both of the cross-feed backgrounds and of the combinatorial background. The relevant parameters determined by

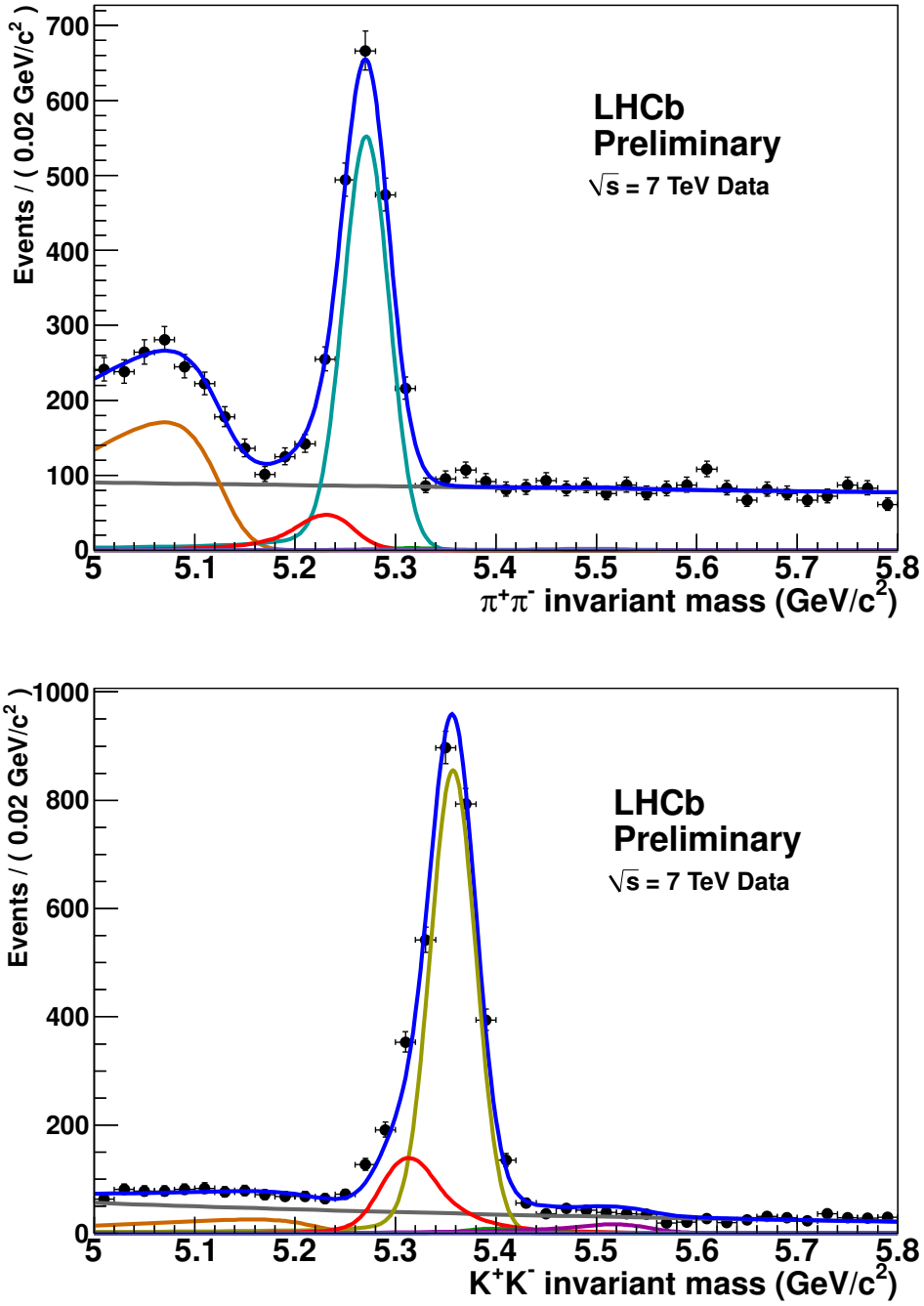

Figure 5.2: $\pi^+\pi^-$ (top) and K^+K^- (bottom) invariant mass spectra for events surviving the event selection adopted for the relative $\mathcal{BR}$ measurement of $B^0 \to \pi^+\pi^-$, $B_s^0 \to K^+K^-$ and $\Lambda_b \to p\pi/\Lambda_b \to pK$. The result of the unbinned maximum likelihood fit is superimposed. The main components contributing to the fit model explained in the text are also visible: $B^0 \to \pi^+\pi^-$ (light blue), $B_s^0 \to K^+K^-$ (dark yellow), $B^0 \to K\pi$ (red), combinatorial background (grey), 3-body partially reconstructed decays (orange).

Parameter	Fit result
$B^0 \to K\pi$ yield	3295 ± 59
$B_s^0 \to \pi K$ yield	249 ± 20
$B^0 \to \pi^+\pi^-$ yield	1120 ± 38
$B_s^0 \to K^+K^-$ yield	1624 ± 45
$\Lambda_b \to pK$ yield	241 ± 16
$\Lambda_b \to p\pi$ yield	174 ± 15
B^0 mass [GeV/c^2]	5.2717 ± 0.0004
B_s^0 mass [GeV/c^2]	5.3583 ± 0.0007
Λ_b mass [GeV/c^2]	5.6108 ± 0.0013
Mass resolution [MeV/c^2]	21.9 ± 0.3

Table 5.7: Relevant parameters determined by the unbinned maximum likelihood fit to the data sample surviving the event selection adopted for the $\mathcal{BR}$ measurement of $B_s^0 \to \pi K$. Only statistical errors are shown.

Systematic uncertainty	$N(B^0 \to \pi^+\pi^-)/N(B^0 \to K^+\pi^-)$	$N(B_s^0 \to K^+K^-)/N(B^0 \to K^+\pi^-)$
PID calibration	0.0002	0.0012
Final state radiation	0.0019	0.0043
Signal model	negligible	0.0001
Combinatorial background model	0.0013	0.0006
3-body background model	0.0018	0.0048
Cross-feed background model (shift)	0.0023	0.0044
Cross-feed background model (smearing)	0.0002	0.0010
Total	0.0038	0.0080

Table 5.8: Systematic uncertainties affecting the ratios of $B^0 \to \pi^+\pi^-$ and $B_s^0 \to K^+K^-$ yields with respect to the yield of the $B^0 \to K^+\pi^-$ decay.

the maximum likelihood fits are summarized in Tab. 5.7.

Using the values in Tab. 5.7 we can compute the ratio between yield of $B_s^0 \to \pi K$ and $B^0 \to K\pi$, that is:

$$\frac{N(B_s^0 \to \pi^+K^-)}{N(B^0 \to K^+\pi^-)} = 0.076 \pm 0.006. \tag{5.1}$$

5.4 Systematics on the ratios of the yields

In order to evaluate the systematic errors on the ratios of signal yields, we followed the same procedure that we used in the analysis presented in the previous chapter. A summary of such systematic errors is reported in Tabs. 5.8 and 5.9.

Systematic uncertainty	$N(B_s^0 \to \pi^+K^-)//N(B^0 \to K^+\pi^-)$	$N(\Lambda_b \to p\pi^-)/N(\Lambda_b \to pK^-)$
PID calibration	0.0013	0.0075
Final state radiation	0.0012	0.0140
Signal model	0.0052	0.0013
Combinatorial background model	negligible	0.0086
3-body background model	0.0011	0.0239
Cross-feed background model (shift)	0.0008	0.0013
Cross-feed background model (smearing)	0.0002	0.0040
Total	0.0056	0.0304

Table 5.9: Systematic uncertainties affecting the ratio between the $B_s^0 \to \pi^+K^-$ and the $B^0 \to K^+\pi^-$ yields, and the ratio between the $\Lambda_b \to p\pi$ and the $\Lambda_b \to pK$ yields.

Relative branching ratio	Result
$\frac{\mathcal{B}\left(B^0\to\pi^+\pi^-\right)}{\mathcal{B}(B^0\to K\pi)}$	$0.259 \pm 0.017 \pm 0.016$
$\frac{f_s}{f_d}\frac{\mathcal{B}\left(B_s^0\to K^+K^-\right)}{\mathcal{B}(B^0\to K\pi)}$	$0.347 \pm 0.020 \pm 0.021$
$\frac{f_s}{f_d}\frac{\mathcal{B}\left(B_s^0\to \pi K\right)}{\mathcal{B}(B^0\to K\pi)}$	$0.071 \pm 0.010 \pm 0.007$
$\frac{\mathcal{B}(\Lambda_b\to p\pi)}{\mathcal{B}(\Lambda_b\to pK)}$	$0.66 \pm 0.14 \pm 0.08$

Table 5.10: Measurements of relative branching ratios of B mesons decays with respect to $B^0 \to K\pi$ and the relative branching ratio between $\Lambda_b \to pK$ and $\Lambda_b \to p\pi$ decays as measured by CDF [3].

5.5 Final results

By using the values reported in Tabs. 5.1, 5.4 and 5.6, and Eq. (5.1) we can compute the following ratios:

$$\begin{aligned}
\frac{\mathcal{B}\left(B^0 \to \pi^+\pi^-\right)}{\mathcal{B}\left(B^0 \to K\pi\right)} &= 0.262 \pm 0.009 \pm 0.017, \\
\frac{f_s}{f_d}\frac{\mathcal{B}\left(B_s^0 \to K^+K^-\right)}{\mathcal{B}\left(B^0 \to K\pi\right)} &= 0.316 \pm 0.009 \pm 0.019, \\
\frac{f_s}{f_d}\frac{\mathcal{B}\left(B_s \to \pi K\right)}{\mathcal{B}\left(B^0 \to K\pi\right)} &= 0.074 \pm 0.006 \pm 0.006, \\
\frac{\mathcal{B}\left(\Lambda_b \to p\pi\right)}{\mathcal{B}\left(\Lambda_b \to pK\right)} &= 0.86 \pm 0.08 \pm 0.05,
\end{aligned}$$

where the first errors are statistical and the second systematic. Such results are compatible with those obtained by CDF, summarized in Tab. 5.10.

By using the current world average of $\mathcal{B}(B^0 \to K\pi)$ [58], that is

$$\mathcal{B}(B^0 \to K\pi) = (19.4 \pm 0.6) \times 10^{-6},$$

and the ratio between the hadronization probabilities f_s/f_d measured by LHCb [89]

$$f_s/f_d = 0.267^{+0.021}_{-0.020},$$

we can also derive measurements of $\mathcal{B}(B^0 \to \pi^+\pi^-)$, $\mathcal{B}(B_s^0 \to K^+K^-)$ and $\mathcal{B}(B_s^0 \to \pi K)$:

$$\begin{aligned}\mathcal{B}(B^0 \to \pi^+\pi^-) &= (5.08 \pm 0.17 \pm 0.37) \times 10^{-6},\\ \mathcal{B}(B_s^0 \to K^+K^-) &= (23.0 \pm 0.7 \pm 2.3) \times 10^{-6},\\ \mathcal{B}(B_s^0 \to \pi K) &= (5.38 \pm 0.44 \pm 0.62) \times 10^{-6}.\end{aligned}$$

These results are compatible with the world averages reported in Tab. 1.4. In particular, the measurements of $\mathcal{B}(B_s^0 \to K^+K^-)$ and $\mathcal{B}(B_s^0 \to \pi K)$ are the most precise available to date.

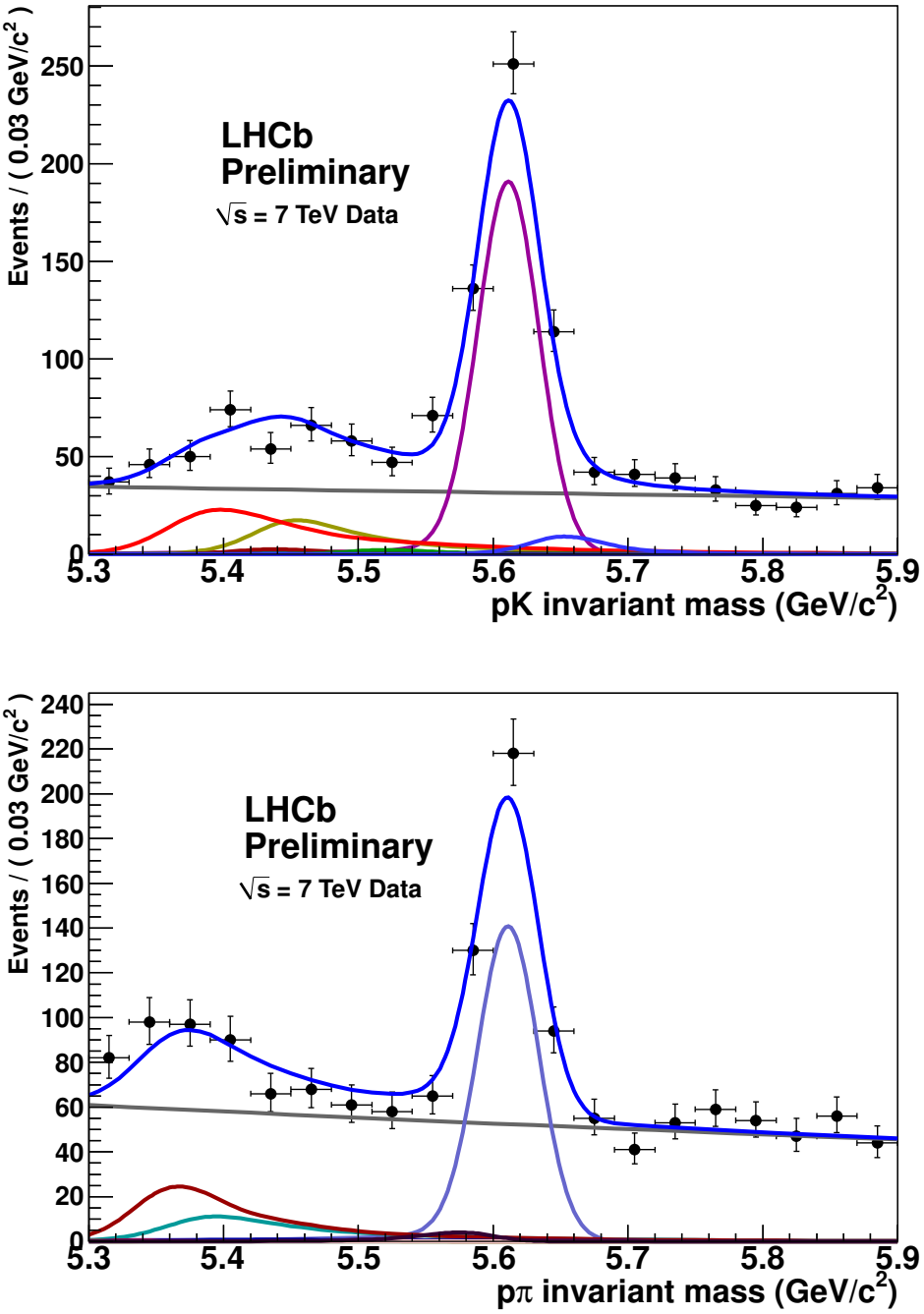

Figure 5.3: pK^- (plus charge conjugate, top) and $p\pi^-$ (plus charge conjugate, bottom) invariant mass spectra for events surviving the event selection adopted for the $\mathcal{BR}$ measurement of $B^0 \to \pi^+\pi^-$, $B_s^0 \to K^+K^-$ and $\Lambda_b \to p\pi/\Lambda_b \to pK$. The result of the unbinned maximum likelihood fit is superimposed. Clear signals of $\Lambda_b \to pK^-$ and $\Lambda_b \to p\pi^-$ decays are found.

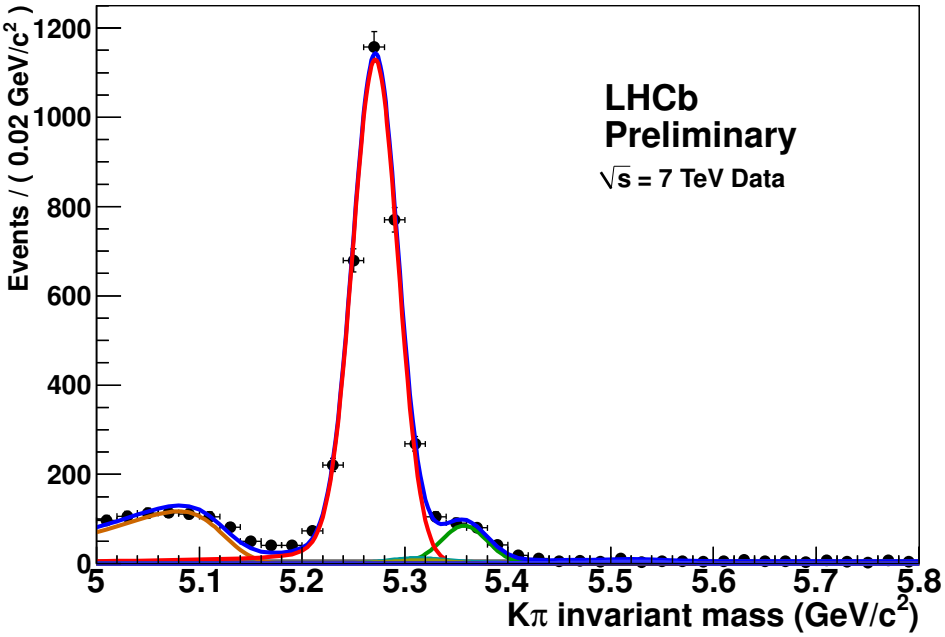

Figure 5.4: π^+K^- (plus charge-conjugate) invariant mass spectrum for events surviving the event selection adopted for the $\mathcal{BR}$ measurement of $B_s^0 \to \pi K$). The result of an unbinned maximum likelihood fit is superimposed. The main components contributing to the fit model explained in the text are also visible: $B^0 \to K\pi$ (red), $B^0 \to \pi^+\pi^-$ (light blue), $B_s^0 \to K^+K^-$ (dark yellow), $B_s^0 \to \pi K$ (green), combinatorial background (grey), 3-body partially reconstructed decays (orange).

Conclusions

This thesis provides the status-of-the-art of the LHCb measurements in the sector of charmless charged two-body B decays. The measurements of branching fractions and $\mathcal{CP}$ asymmetries of these decays realized using data collected during the 2010 and the 2011 data takings are presented. All the achievements here reported represent original contributions.

Analysing the data sample recorded during 2010, corresponding to an integrated luminosity of about 37 pb^{-1}, the following values of the direct $\mathcal{CP}$ asymmetries are obtained:

$$A_{CP}(B^0 \to K^+\pi^-) = -0.074 \pm 0.033 \pm 0.008$$

and

$$A_{CP}(B_s^0 \to \pi^+K^-) = 0.15 \pm 0.19 \pm 0.02.$$

These results are well compatible with the current world average $A_{CP}(B^0 \to K^+\pi^-) = -0.098^{+0.012}_{-0.011}$ and with the CDF measurement $A_{CP}(B_s^0 \to \pi^+K^-) = 0.39 \pm 0.15 \pm 0.08$.

Then, using a sub-sample of data collected during 2011, an updated analysis is performed, exploiting approximatively 320 pb^{-1} of integrated luminosity. Thanks to the increased statistics, the errors on the direct $\mathcal{CP}$ asymmetries are reduced. The final results are:

$$A_{CP}(B^0 \to K\pi) = -0.088 \pm 0.011 \pm 0.008$$

and

$$A_{CP}(B_s^0 \to \pi K) = 0.27 \pm 0.08 \pm 0.02.$$

The result for $A_{CP}(B^0 \to K\pi)$ constitutes the best measurement in the world, whereas that for $A_{CP}(B_s^0 \to \pi K)$ is the first evidence of CP violation in the $B_s^0 \to \pi K$ decay. Both the results are also well compatible with the current experimental knowledge and with the 2010 results quoted above. In addition to the direct $\mathcal{CP}$ asymmetries, also the measurement of the branching fractions of the rare decays $B^0 \to K^+K^-$ and $B_s^0 \to \pi^+\pi^-$ are performed. The results are:

$$\mathcal{B}(B^0 \to K^+K^-) = (0.13^{+0.06}_{-0.05} \pm 0.07) \times 10^{-6}$$

and

$$\mathcal{B}(B_s^0 \to \pi^+\pi^-) = (0.98^{+0.23}_{-0.19} \pm 0.11) \times 10^{-6}.$$

These values are in agreement with the recent CDF results $\mathcal{B}(B^0 \to K^+K^-) = (0.23 \pm 0.10 \pm 0.10) \times 10^{-6}$ and $\mathcal{B}(B_s^0 \to \pi^+\pi^-) = (0.57 \pm 0.15 \pm 0.10) \times 10^{-6}$. Using a likelihood ratio test and including the systematic uncertainties on the signal yields, we obtain a statistical significance of 5.3σ for the $B_s^0 \to \pi^+\pi^-$ signal. Hence this result represents the first 5σ observation of this decay mode.

Finally, using a sample corresponding to about 370 pb^{-1} of integrated luminosity acquired during 2011, the measurements of $\mathcal{B}(B^0 \to \pi^+\pi^-)$, $\mathcal{B}(B_s^0 \to K^+K^-)$, $\mathcal{B}(B_s^0 \to \pi^+K^-)$ and $\mathcal{B}(\Lambda_b \to p\pi^-)/\mathcal{B}(\Lambda_b \to pK^-)$ are performed. First of all the following ratios are determined:

$$\begin{aligned}
\frac{\mathcal{B}\left(B^0 \to \pi^+\pi^-\right)}{\mathcal{B}\left(B^0 \to K\pi\right)} &= 0.262 \pm 0.009 \pm 0.017, \\
\frac{f_s}{f_d}\frac{\mathcal{B}\left(B_s^0 \to K^+K^-\right)}{\mathcal{B}\left(B^0 \to K\pi\right)} &= 0.316 \pm 0.009 \pm 0.019, \\
\frac{f_s}{f_d}\frac{\mathcal{B}\left(B_s \to \pi K\right)}{\mathcal{B}\left(B^0 \to K\pi\right)} &= 0.074 \pm 0.006 \pm 0.006, \\
\frac{\mathcal{B}\left(\Lambda_b \to p\pi\right)}{\mathcal{B}\left(\Lambda_b \to pK\right)} &= 0.86 \pm 0.08 \pm 0.05,
\end{aligned}$$

where the first errors are statistical and the second systematic. Then, by using the current world average $\mathcal{B}(B^0 \to K\pi) = (19.4 \pm 0.6) \times 10^{-6}$ and the ratio between the hadronization probabilities $f_s/f_d = 0.267^{+0.021}_{-0.020}$ measured by LHCb, the measurements of $\mathcal{B}(B^0 \to \pi^+\pi^-)$, $\mathcal{B}(B_s^0 \to K^+K^-)$ and $\mathcal{B}(B_s^0 \to \pi K)$ are obtained:

$$\begin{aligned}
\mathcal{B}(B^0 \to \pi^+\pi^-) &= (5.08 \pm 0.17 \pm 0.37) \times 10^{-6}, \\
\mathcal{B}(B_s^0 \to K^+K^-) &= (23.0 \pm 0.7 \pm 2.3) \times 10^{-6}, \\
\mathcal{B}(B_s^0 \to \pi K) &= (5.38 \pm 0.44 \pm 0.62) \times 10^{-6}.
\end{aligned}$$

These results are compatible with the world averages. The measurements of $\mathcal{B}(B_s^0 \to K^+K^-)$ and $\mathcal{B}(B_s^0 \to \pi K)$ are the most precise available to date.

Bibliography

[1] J.H. Christenson *et al.*, Phys. Rev. Lett. **13**, 138 (1963).

[2] B. Aubert *et al.*, [BABAR Collaboration], arXiv:0807.4226v2 [hep-ex].

[3] T. Aaltonen *et al.*, [CDF Collaboration], *Phys. Rev. Lett.* **103**, 031801 (2009).

[4] T. Aaltonen *et al.*, [CDF Collaboration], arXiv:1111.0485v1 [hep-ex].

[5] R. Aaij *et al.*, [LHCb Collaboration], CERN-PH-EP-2011-206.

[6] B. Aubert *et al.*, [BABAR Collaboration], Phys. Rev. Lett. **87**, 091801 (2001)

[7] K. Abe *et al.*, [Belle Collaboration], Phys. Rev. Lett. **87**, 091802 (2001)

[8] H. Burkhardt *et al.*, [NA31 Collaboration], Phys. Lett. **B206**, 169 (1998)

[9] V.Fanti *et al.*, [NA48 Collaboration], Phys. Lett. **B465**, 335 (1999)

[10] A. Alavi-Harti *et al.*, [KTeV Collaboration], Phys. Rev. Lett. **83**, 22 (1999)

[11] B. Aubert *et al.*, [BABAR Collaboration], Phys. Rev. Lett. **93**, 131801 (2004)

[12] K. Abe *et al.*, [Belle Collaboration], arXiv:hep-ex/0507045.

[13] B. Aubert *et al.*, [BABAR Collaboration], Phys. Rev. **D72**, 072003 (2005)

[14] A. Garmash *et al.*, [Belle Collaboration], Phys. Rev. Lett. **96**, 251803 (2006)

[15] A. D. Sakharov, *Violation Of CP Invariance, C Asymmetry, And Baryon Asymmetry Of The Universe*, Pisma Zh. Exp. Theor. Fiz. **5**, 32 (1967),
English translation in JETP Lett. **5**, 24 (1967), reprinted in Sov. Phys. Usp. **34**, 392 (1991).

[16] N. Cabibbo, Phys. Rev. Lett. **10**, 531 (1963)

[17] M. Kobayashi and T. Maskawa, Prog. Theor. Phys. **49**, 652 (1973)

[18] B. J. Bjørken and S. L. Glashow, Phys. Lett. **B11**, 255-257 (1964)

[19] S. L. Glashow, J. Iliopoulos and L. Maiani, Phys. Rev. **D2**, 12851292 (1970)

[20] C. Jarlskog, Phys. Rev. Lett. **55**, 1039 (1985)

[21] K. Nakamura *et al.*, *JPG* **37**, 075021 (2010)

[22] L. Wolfenstein, Phys. Rev. Lett. **51**, 1945 (1983)

[23] UTfit Collaborataion web pages, *http://www.utfit.org/UTfit/.*

[24] M. Ciuchini et al., *JHEP* **0107**, 013 (2001), [arXiv:hep-ph/0012308].

[25] R. Fleischer, *B Physics and $\mathcal{CP}$ Violation*, *Lect. Notes Phys.* **647**, 42-77 (2004)

[26] G. Buchalla, A. J. Buras, M. E. Lautenbacher, *Weak decays beyond leading logarithms*, Rev.Mod.Phys. **68**, 1125-1144 (1996)

[27] A. J. Buras, R. Fleischer and T. Mannel, Nucl.Phys. **B533**, 3-24 (1998)

[28] A. J. Buras, M. Jamin, M.E. Lautenbacher and P. H. Weisz, Nucl.Phys. **B370**, 69-104 (1992)

[29] R. Fleischer, Phys. Rep. **370**, 531 (2002)

[30] A. J. Buras and R. Fleischer, Phys. Lett. **B341**, 379 (1995)

[31] M. Ciuchini *et al.*, Phys. Lett. **B515**, 33 (2001)

[32] N. G. Deshpande and X.-G. He, Phys. Rev. Lett. **74**, 26 (1995)

[33] M. Gronau *et al.*, Phys. Rev. **D52**, 6347 (1995)

[34] J. D. Bjørken, Nucl. Phys. (Proc. Suppl.) **B11**, 325 (1989);
M. Dugan and B. Grinstein, Phys. Lett. **B255**, 583 (1991);
H. D. Politzer and M. B. Wise, Phys. Lett. **B257**, 399 (1991).

[35] M. Beneke *et al.*, Phys. Rev. Lett. **83**, 1914 (1999);
M. Beneke *et al.*, Nucl. Phys. **B591**, 313 (2000);
M. Beneke *et al.*, Nucl. Phys. **B606**, 245 (2001).

[36] Y.-Y. Keum, H.-N. Li, and A. I. Sanda, Phys. Lett. **B504**, 6 (2001);
Y.-Y. Keum, H.-N. Li, A.I. Sanda, *Phys. Rev.* **D63**, 054008 (2001).

[37] C. W. Bauer, S. Fleming, and M. E. Luke, Phys. Rev. **D63**, 014006 (2001);
C. W. Bauer *et al.*, Phys. Rev. **D63**, 114020 (2001);
C. W. Bauer and I. W. Steward, Phys. Lett. **B516**, 134 (2001).

[38] A. Khodjamirian, T. Mannel, P. Urban, Phys.Rev. **D67**, 054027 (2003)

[39] M. Gronau and D. London, Phys. Lett. **B253**, 483 (1991);
M. Gronau and D. Wyler, Phys. Lett. **B265**, 172 (1991).

[40] D. Atwood, I. Dunietz and A. Soni, Phys. Rev. Lett. **78**, 3257 (1997);
D. Atwood, I. Dunietz and A. Soni, Phys. Rev. **D63**, 036005 (2001).

[41] S. Baek *et al.*, Phys. Rev. **D72**, 036004 (2005).

[42] R. Fleischer, Phys. Lett. **B459**, 306 (1999).

[43] V. Weisskopf and E. P. Wigner, Z. Phys. **63**, 54 (1930);
V. Weisskopf and E. P. Wigner, Z. Phys. **65**, 18 (1930).

[44] I. I. Bigi and A. I. Sanda, *CP violation*, *Cambridge University Press* , (2000).

[45] A. J. Buras, W. Słominski and H. Steger, Nucl. Phys. **B245**, 369 (1984).

[46] K. Abe *et al.*, [Belle Collaboration], Phys. Rev. Lett. **99**, 121601 (2007).

[47] H. Ishino *et al.*, [Belle Collaboration], Phys. Rev. Lett. **98**, 211801 (2007).

[48] A. Abulencia *et al.* [CDF Collaboration], Phys. Rev. Lett. **97**, 211802 (2006).

[49] [CDF Collaboration], CDF Public Note 9092.

[50] B. Aubert *et al.*, [BaBar Collaboration], Phys. Rev. **D69**, 091503 (2004).

[51] Y. T. Tsai *et al.*, [BELLE Collaboration], Phys. Rev. **D75**, 111101 (2007).

[52] T. Aaltonen *et al.*, [CDF Collaboration], Phys. Rev. Lett. **106**, 181802 (2011).

[53] [CDF Collaboration], CDF Public Note 10498.

[54] Belle Collaboration, *Nature* **452**, 332 (2008).

[55] R. Fleischer, Eur. Phys. J. **C52**, 267 (2007).

[56] B. Adeva *et al.*, [LHCb Collaboration], LHCb-PUB-2009-029, arXiv:0912.4179v3 [hep-ex].

[57] A. Khodjamirian, T. Mannel and M. Melcher, Phys. Rev **D70**, 094002 (2004).

[58] E. Barberio *et al.* [Heavy Flavor Averaging Group], *Charmless B Decays: August 2010 update*, `http://www.slac.stanford.edu/xorg/hfag/rare/ichep10/charmless/index.html`.

[59] E. Barberio *et al.* [Heavy Flavor Averaging Group], *Compilation of B_s Rare Branching Fractions*, `http://www.slac.stanford.edu/xorg/hfag/rare/ichep10/bs/index.html`.

[60] E. Barberio *et al.* [Heavy Flavor Averaging Group], *CP Asymmetries in Charmless B Decays: ICHEP 2010 update*, `http://www.slac.stanford.edu/xorg/hfag/rare/ichep10/acp/`.

[61] CDF collaboration, CDF Note 06-01-26 (2006).

[62] R. Aaij *et al.*, [LHCb Collaboration], CERN-PH-EP-2011-167

[63] S. Amato *et al.*, CERN-LHCb-2009-019;
LHCb Collaboration, CERN-LHCb-CONF-2011-004.

[64] Y. Grossman, *Phys. Lett.* **B380**, 99 (1996), [arXiv:hep-ph/9603244].

[65] R. Mohanta, *Phys. Rev.* **D63**, 056006 (2001), [arXiv:hep-ph/0005240].

[66] A. A. Alves *et al.* [LHCb Collaboration], *JINST* **3**, S08005 (2008).

[67] The CERN Large Hadron Collider: Accelerator and Experiments, *JINST* **3**, S08001 (2008)

[68] PYTHIA event generator web page, *http://home.thep.lu.se/ torbjorn/Pythia.html*.

[69] R. Aaij *et al.* [LHCb Collaboration], *Phys. Lett.* **B694**, 209 (2010), [arXiv:1009.2731 [hep-ex]].

[70] [LHCb Collaboration], CERN-LHCC-2001-011.

[71] [LHCb Collaboration], CERN-LHCC-2003-030.

[72] [LHCb Collaboration], CERN-LHCC-2002-029.

[73] [LHCb Collaboration], CERN-LHCC-2001-024.

[74] [LHCb Collaboration], CERN-LHCC-2000-007.

[75] M. Gersabeck [LHCb Collaboration], *LHCb Tracking, Alignment and Physics Performance*, *PoS (VERTEX 2010)* **Vol. 113**, p. 11 (2010).

[76] [LHCb Collaboration], CERN-LHCC-2000-037.

[77] [LHCb Collaboration], CERN-LHCC-2000-036.

[78] I. Machikhiliyan [LHCb Collaboration], *Current status and performance of the LHCb electromagnetic and hadron calorimeters*, *Journal of Physics: Conference Series (CALOR 2010)* , p. 6 (2010).

[79] [LHCb Collaboration], CERN/LHCC 2003-002.

[80] R. Aaij *et al.* [LHCb Collaboration], CERN-LHCb-CONF-2010-013.

[81] Worldwide LHC Computing Grid web page, *http://lcg.web.cern.ch/lcg/*.

[82] DIRAC web page, *http://diracgrid.org/*

[83] A. Carbone *et al.*, LHCb-ANA-2011-023.

[84] S. Chen *et al.* [CLEO Collaboration], *Phys. Rev. Lett.* **85**, 525 (2000), [arXiv:hep-ex/0001009].

[85] M. Pivk and F. R. Le Diberder, *Nucl. Instrum. Meth.* **A555**, 356 (2005), [arXiv:physics/0402083].

[86] E. Barberio *et al.* [Heavy Flavor Averaging Group], *CP asymmetries in D^0 decay modes: March 2010 update*, `http://www.slac.stanford.edu/xorg/hfag/charm/cp_asym/charm_asymcp_10mar10.html`.

[87] [CDF Collaboration], CDF public note 10296.

[88] T. Aaltonen *et al.*, [CDF Collaboration], arXiv:1111.5023v1 [hep-ph]

[89] R. Aaij *et al.*, [LHCb Collaboration], CERN-PH-EP-2011-172, [arXiv:1111.2357v1].

[90] E. Baracchini and G. Isidori, *Phys. Lett.* **B633**, 309 (2006), [arXiv:hep-ph/0508071].

[91] A. Carbone *et al.*, CERN-LHCb-PUB-2009-031.

[92] W. S. Hou, M. Nagashima and A. Soddu, arXiv:hep-ph/0605080.

[93] K. S. Cranmer, *Comput. Phys. Commun.* **136**, 198 (2001), [arXiv:hep-ex/0011057].

[94] W. Verkerke and D. Kirkby, *Proceedings of 2003 Conference for Computing in High-Energy and Nuclear Physics (CHEP 03), La Jolla, California, 2003* [arXiv:physics/0306116].

[95] F. James, Minuit Reference Manual, `http://wwwinfo.cern.ch/asdoc/minuit/minmain.html`.